Alma Mater Studiorum - Università di Bologna

Dipartimento di Fisica e Astronomia

DOTTORATO DI RICERCA IN ASTRONOMIA

CICLO XXV

THE UNIVERSE 10 BILLION YEARS AGO:

MORPHOLOGIES, STAR-FORMATION RATES AND GALACTIC-SCALE WINDS IN $z \sim 2$ GALAXIES

Tesi di Dottorato di

MARGHERITA TALIA

COORDINATORE	RELATORI
Prof. **Lauro MOSCARDINI**	Prof. **Andrea CIMATTI** Dr. **Marco MIGNOLI**

Esame finale anno 2013

SCUOLA DI DOTTORATO IN SCIENZE MATEMATICHE, FISICHE E ASTRONOMICHE

Settore concorsuale: 02/C1 - Astronomia, Astrofisica, Fisica della Terra e dei Pianeti

Settore scientifico-disciplinare: FIS/05 - Astronomia e Astrofisica

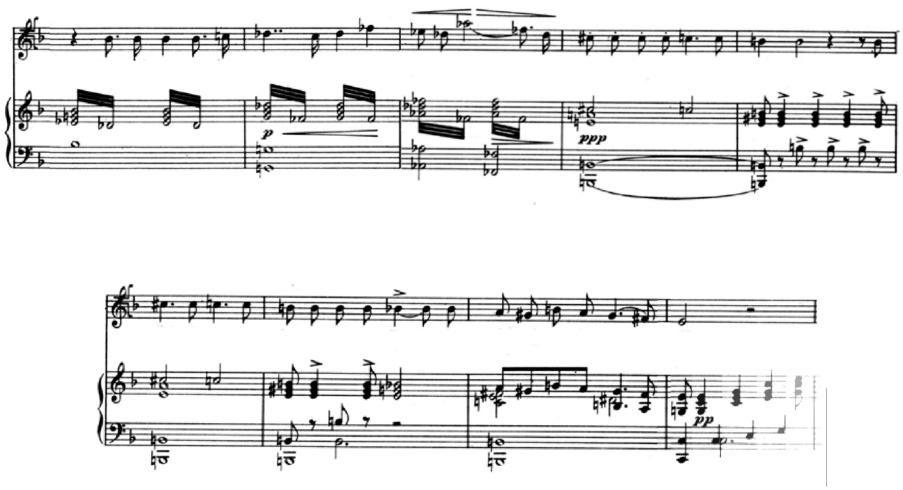

Otello
G. Verdi

Table of Contents

List of Figures . . . . . **xii**

List of Tables . . . . . **xiii**

Preface **1**

1 Thesis project **3**

2 Introduction **6**

2.1 Cosmological framework 6

2.2 Galaxy formation and evolution 10

2.3 Morphologies 15

2.3.1 Sérsic profile 16

2.3.2 CAS and G-M20 parameters 17

2.3.3 The merger fraction 19

2.3.4 Morphologies and physical properties of galaxies 21

2.4 Star-formation rate and dust extinction 23

2.4.1 Kennicutt et al. (1998) relations: assumptions on SFGs 24

2.4.2 SED fitting 24

2.4.3 The relation between UV continuum slope and attenuation 26

2.4.4 Nebular emission lines 28

2.5 Galactic-scale outflows 29

2.5.1 The role of "superwinds" in galaxy evolution 29

2.5.2 UV inter-stellar absorption lines . . . 30
2.5.3 The structure of star-formation driven winds . . . 33

3 The sample . . . 35
3.1 Data description . . . 35
3.1.1 The GMASS survey . . . 35
3.1.2 Other spectroscopic data in the CDF-S . . . 40
3.1.3 The CANDELS survey . . . 40
3.1.4 The PEP-HerMES merged catalogue . . . 41
3.2 Selection criteria: the final samples . . . 42

4 Morphologies . . . 44
4.1 Introduction . . . 44
4.2 The data sample . . . 45
4.3 Visual morphological analysis . . . 46
4.3.1 Fraction of morphological types as a function of redshift . . . 49
4.4 Quantitative morphological analysis . . . 51
4.4.1 The segmentation map . . . 51
4.4.2 Parameters definitions . . . 54
4.4.3 The CvsA plane . . . 55
4.4.4 The GvsM20 plane . . . 57
4.5 Morphological *k*-correction . . . 60
4.5.1 $ACS - z_{850}$ images degradation . . . 60
4.5.2 Visual appearance . . . 61
4.5.3 Quantitative changes . . . 64
4.6 Colour bimodality . . . 68
4.6.1 The blue *spheroidal* population . . . 76

4.7 Conclusions 79

5 Star-formation rate and dust extinction 82

5.1 Introduction 82

5.2 The data sample 83

5.3 The infrared luminosity (LIR) 89

5.3.1 IR SED libraries: description 89

5.3.2 Testing the IR SED libraries 90

5.3.3 LIR from 24 μm flux only: CE01 and DH02 calibration 96

5.4 Comparing different estimates of SFR 100

5.4.1 SFR_{SED} vs. SFR_{IR+UV} 102

5.4.2 SFR_{UV} vs. SFR_{IR+UV}: the IR excess and dust obscuration 105

5.4.3 $SFR_{[OII]}$ vs. SFR_{IR+UV} 113

5.5 Conclusions 116

6 Galactic-scale outflows 119

6.1 Introduction 119

6.2 The data sample: selection criteria and redshift refinement 120

6.3 Rest-frame UV spectroscopic features 124

6.3.1 Photospheric absorption stellar lines 125

6.3.2 Nebular emission lines 125

6.3.3 Low- and high-ionization absorption lines associated with the ISM 130

6.3.4 Other notable spectral lines 131

6.4 Outflows 133

6.4.1 Velocity offset measurements 134

6.4.2 Uncertainties 136

6.4.3 Results 136

6.5 Searching for correlations between UV spectroscopic properties and galaxy physical properties . . . 139

6.5.1 Outflow velocities . . . 145

6.5.2 Equivalent widths of outflow-related absorption lines . . . 145

6.6 Conclusions . . . 146

7 Brief summary and future prospects . . . 148

Bibliography . . . 152

Appendix: the morphological atlas . . . 161

List of Figures

2.1 CMB anisotropy map from COBE 8

2.2 Planck first-year all-sky survey map. 10

2.3 Hubble's tuning fork diagram 11

2.4 $M_\star/L_R$ as function of redshift, for ETGs in the *K20* survey 12

2.5 Possible evolutionary paths for the formation of massive spheroidal galaxies. 14

2.6 Distribution of Sérsic indices for a sample of WCF3/UDF galaxies. 17

2.7 Test galaxy morphological measurements C, A, S, G, and M20. 18

2.8 Merger candidates in the G-M20 plot. 20

2.9 Merger fraction as a function of redshift. 21

2.10 Distribution of IEROs in the Gini - M20 diagram. 22

2.11 Comparison between different synthetic SED libraries. 25

2.12 Ratio of FIR to UV flux 27

2.13 R-band image of the Cosmic Horseshoe. 30

2.14 UV spectrum of the Cosmic Horseshoe. 31

2.15 The dependence of W_{LIS} on W_{Ly_α} and E(B-V), in LBGs. 32

2.16 Schematic diagram of a super-wind 33

3.1 Location of the GMASS field. 36

3.2 Histogram of redshifts in the GMASS catalogue. 37

3.3 Rest-frame composite spectra of galaxies in the blue and red masks. . . . 38

3.4 K band counts for the GMASS field. 39

4.1 Redshift distribution of the *GMASS-wfc3 sample* 45

4.2 The rest-frame wavelength probed by the four ACS and the two WFC3-IR filters, as a function of redshift. 46

4.3 The morphological visual classification scheme. 47

4.4 Physical properties of *GMASS-wfc3 sample* as a function of redshift and morphological type. 48

4.5 Relative fraction of morphological types as a function of redshift. 50

4.6 S/N as a function of H-band magnitude 51

4.7 Concentration vs. Asymmetry. 56

4.8 Gini coefficient vs. M20. 58

4.9 Relative fraction of morphological types as a function of redshift (ACS_{deg} sample). 62

4.10 Galaxies showing the strongest *k*-correction from optical to UV band. . . 63

4.11 Distribution of redshift, mass and SFR of faint objects in ACS_{deg} with a morphological classification in H_{160}. 65

4.12 Concentration vs. Asymmetry in z_{850}. 66

4.13 Gini coefficient vs. M20 in z_{850}. 67

4.14 Rest-frame (U-B) colour distribution. 70

4.15 Rest-frame colour vs. stellar mass, in 3 redshift bins: lowest z bin. 71

4.16 Rest-frame colour vs. stellar mass, in 3 redshift bins: intermediate z bin. . 72

4.17 Rest-frame colour vs. stellar mass, in 3 redshift bins: highest z bin. 73

4.18 Distribution of morphological parameters for the "blue cloud" and the "red sequence". 74

4.19 Distribution of physical properties for the "blue cloud" and the "red sequence". 75

4.20 $R_{80\%}$ of spheroidal galaxies in the sample. 77

5.1 Examples of different spectral types: early type and intermediate. 84

5.2 Examples of different spectral types: star-forming. 85
5.3 Examples of different spectral types: AGN. 86
5.4 Examples of optical-to-IR SEDs. 87
5.5 Redshift distribution. 88
5.6 Success rate of different IR libraries in achieving the best χ^2. 91
5.7 Some examples of best-fit IR SEDs. 92
5.8 Comparison between LIR from SED fitting using all the available IR libraries together as templates, and LIR obtained using the different libraries separately. 93
5.9 Comparison between different IR SED libraries. 94
5.10 Best-fit IR SEDs of three peculiar galaxies. 95
5.11 Calibration of LIR_{MIPS} recovered by CE01 library. 97
5.12 Calibration of LIR_{MIPS} recovered by DH02 library. 98
5.13 LIR computed using CE01 libraries vs. LIR computed using DH02 libraries. 99
5.14 LIR distribution over the sample, as a function of redshift. 100
5.15 SFR_{IR+UV}/SFR_{IR} vs. SFR_{IR} 101
5.16 SFR_{IR+UV} vs. SFR_{SED} 102
5.17 SFR_{IR+UV} vs. SFR_{SED} - Constant SFH. 103
5.18 $\log(SFR_{IR}/SFR_{UV})$ vs. $\log(SFR_{SED}/SFR_{IR+UV})$. 104
5.19 UV continuum slope fit. 107
5.20 UV continuum slope distribution 108
5.21 $SFR_{UV-corr}$ vs. SFR_{IR+UV} 109
5.22 A_{IRX} vs. β. 110
5.23 SFR_{IR+UV} vs. stellar mass. 111
5.24 $sSFR_{IR+UV}$ vs. stellar mass. 112
5.25 A_{IRX} vs. β. 113

5.26 SFR_{IR+UV} vs. $SFR_{[OII-uncorr]}$. 114

5.27 SFR_{IR+UV} vs. $SFR_{[OII]}$ - 1. 115

5.28 SFR_{IR+UV} vs. $SFR_{[OII]}$ - 2. 116

6.1 BzK plot for the objects in the GMASS total sample. 121

6.2 Redshift distribution. 122

6.3 Distributions of stellar age, stellar mass, and SFR. 123

6.4 Percentage of contributing objects per wavelength unit to the composite spectrum. 124

6.5 Average spectrum of the 74 SFGs. 128

6.6 Average spectrum of the 74 SFGs - Zoom. 129

6.7 Composite spectrum of 74 SFGs: regions close to the C IV and the Si IV doublets. 130

6.8 Average spectrum of the six galaxies with Lyα line in emission. 131

6.9 Comparison of a composite spectrum and the spectrum of a single galaxy. 134

6.10 Composite spectrum of 74 SFGs: detectable stellar photospheric absorption lines. 135

6.11 Composite spectrum of 74 SFGs: strongest low-ionization interstellar absorption lines. 137

6.12 Distribution over the sample of stellar mass, SFR, and E(B-V) 140

List of Tables

3.1 Extended GMASS spectroscopic high-z sample: distribution of spectra between different surveys 42

3.2 Extended GMASS spectroscopic high-z sample: IR bands 43

4.1 Visual morphological classification: number of galaxies for each type. . . 46

4.2 Morphological parameters. 53

4.3 Visual morphological classification in WFC3-IR H_{160} vs. ACS deg z_{850} . . 62

4.4 Average change in morphological parameters between H_{160} and z_{850} images. 64

6.1 Spectral lines in a SFG rest-frame UV spectrum (1000-2000Å). 126

6.2 Spectral lines in a SFG rest-frame UV spectrum (2000-3000Å). 127

6.3 Velocity offsets and EWs of strong low-ionization lines. 138

6.4 Equivalent widths and velocity offsets of the strongest interstellar absorption lines. 141

6.5 Equivalent widths and velocity offsets of the strongest interstellar absorption lines. 142

6.6 Equivalent widths and velocity offsets of the strongest interstellar absorption lines. 143

6.7 Mean measured equivalent widths and velocity offsets. 144

Preface

The job of an astronomer is very similar to the one of an economist, or a social scientist. What does an astronomer do? He looks. Just that. He cannot make experiments. He works in a lab that is self-managed, and has only one way to understand what is happening inside: looking, and taking notes. The same thing is true for a sociologist, whose object of study, the society, cannot be manipulated to verify this or that theory, as well as galaxies. With a little bit of imagination, it is easy to identify sociologists or anthropologists among the astronomers that study the objects populating that portion of the Universe which is closer to as, the Local Universe; and we could as well call archaeologists the astronomers who try to reconstruct the evolutionary history of these objects studying the fossils inside them: old stellar populations, for example.

But there is a category of astronomers that has no corresponding in other disciplines: the time travellers. Maybe the term is not the most appropriate, since astronomers do not actually travel through time: it is the past that comes to meet us. The electro-magnetic radiation, emitted by objects that are distant from us in time and space, travelling at finite speed, allows us to see things that happened in ancient times as if we were watching a real-time coverage.

The present time is a very special moment to be a time traveller. Theoretical and technological developments, during the last decades, allowed astronomers to investigate truly in depth the great issues of how our Universe formed and which is its structure. In particular, the topic of galaxy evolution made a great leap forward with the advent of many surveys, aimed to discover and study the nearby and far galaxies. A great effort is being devoted in particular to the study of the Universe in the redshift range $1 < z < 3$, since several studies have shown that this is the epoch when a substantial fraction of galaxy mass assembly took place, and when there is a peak in the evolution of the star-formation

rate (SFR) density through cosmic time (Lilly et al. 1996; Madau et al. 1996; Dickinson et al. 2003; Hopkins & Beacom 2006; Daddi et al. 2007).

This thesis is devoted to the study of the properties of galaxies in this crucial redshift range, following a multi-perspective approach and using the most recent and high-quality high-redshift galaxy data (spectra, photometry and imaging).

CHAPTER 1

Thesis project

At high redshift, the galaxies are very different from their local siblings, and one of the major goals of extragalactic astronomy is to understand the evolutionary processes that are responsible for such differences. The most evident difference between distant and local galaxies is their appearance: in the local Universe they have quite defined morphologies, while at $z > 1$ the majority of galaxy population has more irregular shape. When did the irregular high-redshift galaxies turn into the ellipticals and spirals that today constitute the well known Hubble sequence? And how did they? The shape of a galaxy can be modified in many ways: through interaction with neighbour galaxies, merging, or infall of cold gas from the intergalactic medium. But also internal activities, such as star-formation or an active nucleus, are responsible for shaping the galaxy. The estimate of the SFR, at high-redshift, is not straightforward, since the relations used to convert fluxes into SFRs are all calibrated on local galaxies, that have very different properties with respect to high-redshift ones, especially the dust content and geometry. Another fundamental question to be answered is then: which are the star-formation histories of distant galaxies?

Motivated by the need of investigating these open issues, this thesis project was devoted to the study of the properties of high-redshift galaxies, in particular in the range $1 < z < 3$, the epoch when a substantial fraction of galaxy mass was assembled, and when the evolution of the star-formation rate density peaked. The thesis focused on two main aspects: the built up of the main sequence, and the estimate of the SFR at high-redshift.

Chapter 2: Introduction

In the introduction, the state of current research on many aspects of the topic of galaxy formation and evolution is outlined.

Chapter 3: The sample

The analysed sample of galaxies was drawn from the ultra-deep optical spectroscopic survey called GMASS (Galaxy Mass Assembly ultra-deep Spectroscopic Survey), which

was an ESO VLT Large Program project. To draw a picture as complete as possible of the galaxy population in the distant Universe, the GMASS photometric catalogue was taken as a starting point, but also other multi-wavelength archive data were collected: rest-frame UV and optical spectra (ESO surveys), imaging (HST/WFC3 - CANDELS), optical to near infrared broad-band photometry, and infrared (IR) data (HERSCHEL - PEP consortium).

Chapter 4: Morphologies

To address the first issue, a detailed morphological analysis was performed on a sub-sample of $z > 1$ galaxies, for which both HST/ACS and HST/WFC3-IR imaging were available, sampling respectively the rest-frame UV and optical wavelength regimes. Galaxies were first classified by eye. Non-quantitative statistics methods were also used (CAS and G-M20), and their robustness was tested in segregating different morphological types. The morphological classification of galaxies, and the analysis of the evolution with redshift of the fraction of different morphological types, led to the result that the build-up of the Hubble sequence, as we see it in the local Universe, happened around $z \sim 2.5$. By comparing HST/WFC3-IR with HST/ACS imaging, the role of the morphological *k*-correction between the rest-frame UV and optical appearance of galaxies was also explored. The main result is that, at $1 < z < 3$, there is no evidence of a significant morphological *k*-correction. The correlation between rest-frame colour and morphology was finally investigated. In our sample, the existence was confirmed of a rest-frame colour bi-modality, holding up to redshift $z \sim 2.3$: morphologies tend to follow this bi-modality in the sense that almost all ellipticals fall under the red peak, while irregulars and compacts under the blue one. Disks are a mixed category: they show a blue and a red peak in their distribution, but they also populate the intermediate region.

An interesting population have of blue, star-forming galaxies with the same morphological properties of red ellipticals have been discovered.

Chapter 5: Star-formation rate and dust extinction

Star-formation was the second main topic addressed in this work. Different estimators were compared, to study how they are related to one another. SED fitting to broad band photometry, in the optical and in the far IR regimes, and spectral analysis were used in the investigation. The different SFR estimators were found not to agree very well, due to the difficulties in properly accounting for the effects of dust extinction. In particular, SFR_{SED} is correlated to SFR_{IR+UV} for the majority of galaxies, but there is also a tail

toward lower SED-modelled SFRs. Changing the star-formation history in the models, from exponentially decaying to constant, improves the situation, but does not entirely cancels the differences. SFR_{SED} is also systematically higher than SFR_{IR+UV}. This result suggests that the treatment of dust obscuration in SED modelling also needs to be refined. The comparison between SFR_{IR+UV} and $SFR_{correctedUV}$ gives better results. The two estimates agree reasonably well, though with a large scatter. This scatter depends on the scatter in the relation between the ratio of IR over UV flux (A_{IRX}) and the rest-frame UV spectral slope (β). This relation is very tight, in the local Universe, but it becomes much more scattered at $z > 1$. This is another prove that the traditional way of addressing the dust obscuration is problematic, at high-redshifts, and new models of dust geometry and composition are required.

The conversion from LIR to SFR relies on great extrapolations, due to the lack of the far IR data needed to well constrain the galaxy SED. HERSCHEL data, that cover the observed IR regime up to 500 μm, were used to test the robustness of different SED libraries in recovering LIR, when only the MIPS 24 μm flux was available. The result of these tests is that the best choice of SED library is the set of Chary and Elbaz, 2001; but, at high luminosities ($LIR_{MIPS} \geq 12.2(log(L/L_{\odot}))$, a correction must be applied, computed and presented in chapter 5.

Chapter 6: Galactic-scale outflows

Galactic winds, a phenomenon strictly related to star-formation activity, was investigated by means of ultra-deep spectroscopy and stacking techniques. Analysing the spectra of a sub-sample of SFGs with very high-quality spectra, evidence of escaping gas at velocities of $\sim$ 100 km/s was found. No significant correlation was observed between the gas velocity and other properties of the galaxies. A positive trend between the equivalent width of the interstellar absorption lines and SFR, stellar mass, and E(B-V) was found instead. The most significant of the three correlations appears to be with E(B-V), suggesting that the equivalent widths of the absorption interstellar lines are probably related to the velocity dispersion of the gas, to its geometry, or to a combination of the two effects.

Chapter 7: Brief summary and future prospects

In the last chapter, the main results obtained from this work are summarized, along with some future prospects of continuations of the presented research.

CHAPTER 2

Introduction

In this chapter, a brief introduction of the theories about the origin of the Universe and structure formation is given. Then, the most recent results will be reviewed related to the Hubble sequence at high-redshift, the various estimators, at different wavelengths, used to derive the star-formation rate of galaxies, and galactic-scale outflows in star-forming galaxies (SFGs).

2.1 Cosmological framework

Today, the most reliable theory to describe the origin of the Universe is the *Big Bang* theory, with the addition of an inflationary phase (see, for example Mukhanov (2005)). The ultra-relativistic perfect gas of non-degenerate particles, constituting the expanding primordial Universe, underwent a series of phases, or "epochs" during which its temperature went down and its composition changed. When the temperature reached the value of $T \sim 5 \times 10^9 K$, the radiative epoch began: at that time the Universe, made of photons, neutrinos, and baryons, was dominated by radiation.

Matter energy density and radiation energy density evolved separately, due to the expansion of the Universe: $\rho_{rad} \propto (1+z)^4$ and $\rho_{matter} \propto (1+z)^3$. At some point the two densities were equal. The estimated redshift for this event, called *equivalence*, is $z \sim 5000$. After equivalence, the epoch dominated by matter started. When the temperature fell below $10^4 K$ electrons and protons began to combine to create hydrogen atoms. The name that has been given to this phase of the life of the Universe is *recombination*. Up to this moment radiation and matter were coupled, i.e. they were in equilibrium at the same temperature. This was granted by the fact that the dominant interaction mechanism between radiation and matter, Thomson scattering, occurred on time scales much shorter than that of the expansion of the Universe. After recombination, electrons found themselves trapped inside hydrogen atoms, that have a smaller cross section than the one

typical of the Thomson scattering. The decrease of the cross section meant a decrease in the number of targets for the photons. Matter and radiation ceased to be in equilibrium: it is the moment of *decoupling*. From then on, those two components of the Universe would have evolved independently. It is known that radiation went on cooling down, and today we can still see it in the Cosmic Microwave Background (CMB).

What about the matter? If the fluid constituting the primordial Universe was perfectly homogeneous and isotropic, matter would have followed an evolution similar to that of radiation, and probably we would not be here trying to answer this kind of questions. To explain the birth of cosmic structures, it is assumed that, during the inflation phase, some perturbations have originated in the primordial fluid. Perturbations evolved following random processes, but their growth, at the beginning, was inhibited due to radiation that, in its dominant epoch, freezes the perturbations. After decoupling, however, any primordial fluctuation of the matter component that had succeeded to survive the radiation dominated epoch, was free to grow to form eventually structures. The evolution of perturbations is treated with the Jeans gravitational instability theory, in a first approximation. According to this theory, density inhomogeneities, in an almost homogeneous and isotropic fluid, can grow in time when the pressure support is weak compared to the gravitational pull. This criterion may be expressed in terms of a critical length. The Jeans length is defined as: $\lambda_J = c_s(\pi/G\rho_0)^{1/2}$, where c_s is the sound speed, G is the gravitational constant, and ρ_0 is the density of the unperturbed fluid. If the typical length scale of a fluctuation is greater than the Jeans length, the perturbation growths. This treatment is valid for a generic fluid. In order to apply it to the cosmological case, some corrections are needed, to take into account the expansion of the Universe, but the basic idea remains the same.

Once the model has been defined, it is possible to estimate the size of the primordial fluctuations. In a Universe made only of baryons and photons, the initial amplitude of the fluctuations, in terms of temperature, should have been $\delta T/T \approx 10^{-3} - 10^{-4}$, in order to give the fluctuations time enough to grow to the produce the large-scale structure that is now observed in the distribution of galaxies. As previously stated, matter and radiation were subject to the same perturbations before decoupling. This is the reason why we can read the amplitude of primordial fluctuations in the CMB. The first data coming from the COBE (*COsmic Background Explorer*) satellite, launched by NASA in 1989, undermined the theoretical model, since the satellite measured fluctuations by the order of $\delta T/T \approx 10^{-5}$ (Mather et al. 1994) (Fig. 2.1).

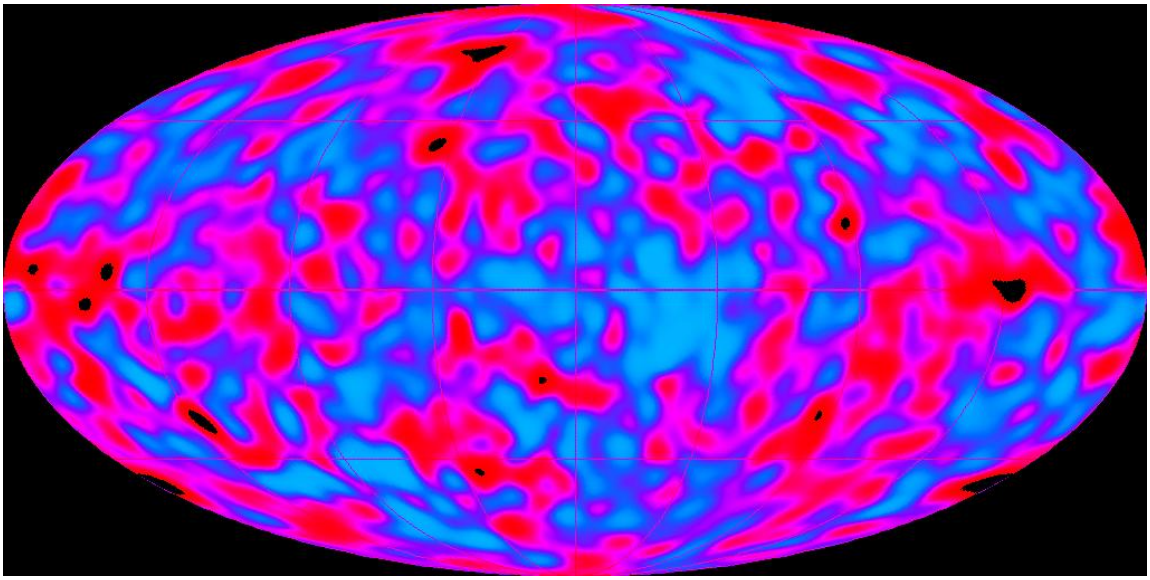

Fig. 2.1: Map of the CMB anisotropy formed from data taken by the COBE spacecraft. Credit: NASA

The model was then revised, with the addition of a third ingredient in the recipe of the first constituents of the Universe: non-baryon dark matter, quite an undefined component that manifests its presence only by gravitational interactions. According to the modified theory, the decoupling of dark matter happened earlier than the other two components, during the radiation dominated epoch. While the perturbations in the photons-baryons plasma were frozen until recombination, dark matter fluctuations had time to grow. Once baryons were decoupled from radiation, they were free to fall into dark matter potential wells and in turn collapse to form the first cosmic structures.

The Jeans instability theory in case of non-collisional matter is applied to the growth of dark matter perturbations; here the resistance to the gravitational attraction is given by the motion of the particles, that provides an effective pressure. The equivalent of the Jeans length, the free streaming length, is defined as $\lambda_{FS} = v_d(\pi/G\rho_0)^{1/2}$, where v_d is the velocity dispersion of the dark matter particles. Only perturbations with a length scale greater than the free streaming length can survive, while the one with a smaller length scale are deleted. The perturbation spectrum at the time of recombination depends on the free streaming length, that depends in turn on v_d. The velocity dispersion is determined by the thermodynamic state of dark matter particles at the time of their decoupling from the other primordial components. With respect to the nature of dark matter particles, there are two possibilities: relativistic particles (*Hot Dark Matter - HDM*) and non-relativistic particles (*Cold Dark Matter - CDM*).

The two type of particles define two different free streaming lengths, from which it is possible to derive an lower limit to the mass able to collapse. The mass limit for the HDM case is $M_{lim} \sim 10^{15} M_{\odot}$; for the CDM it is $M_{lim} \sim 10^{5} - 10^{6} M_{\odot}$ instead: these are, respectively, typical masses of galaxy clusters and globular clusters. In a HDM scenario, the first objects to be formed were galaxy clusters, then fragmenting into smaller structures such as galaxies (*top-down scenario* or *monolithic collapse*). In a CDM scenario, the formation of galaxies preceded that of clusters: small dark matter halos formed, that constituted the potential wells inside which baryon matter fell; these small halos then merged into increasingly large ones (*bottom-up scenario* or *hierarchical merging*). Observational evidences led to the rejection of the monolithic scenario in favour of the hierarchical one. In particular, the *top-down* model is not able to reproduce the observed large-scale structure of the Universe.

The addition of a set of cosmological parameters able to define the geometry and the global evolution of the Universe (total density, density of each component, deceleration parameter, cosmological constant, Hubble constant and so on) completes the models. Currently, the most reliable theory is the so-called ΛCDM model, according to which the Universe is flat with a non-null cosmological constant Λ and whose mass is dominated by cold dark matter.

In principle, cosmological parameters can be determined accurately studying the spectrum of the temperature fluctuations in the CMB. The most accurate measurements now available are the ones provided by the NASA satellite WMAP (*Wilkinson Microwave Anisotropy probe*) (Jarosik et al. 2011; Komatsu et al. 2011), that will be soon outweighed by the cosmology results by PLANCK (Fig. 2.2).

Though the Big Bang theory still has many problems to be solved, today we can say that this theory gives us roughly quite a complete picture of what happened in the Universe, from its birth up to the moment when the first clouds of baryon gas fell in the dark matter potential wells. The idea on what happened next, how the first collapsed structures managed to turn into the large variety of galaxies observed today in the local Universe are not so well understood.

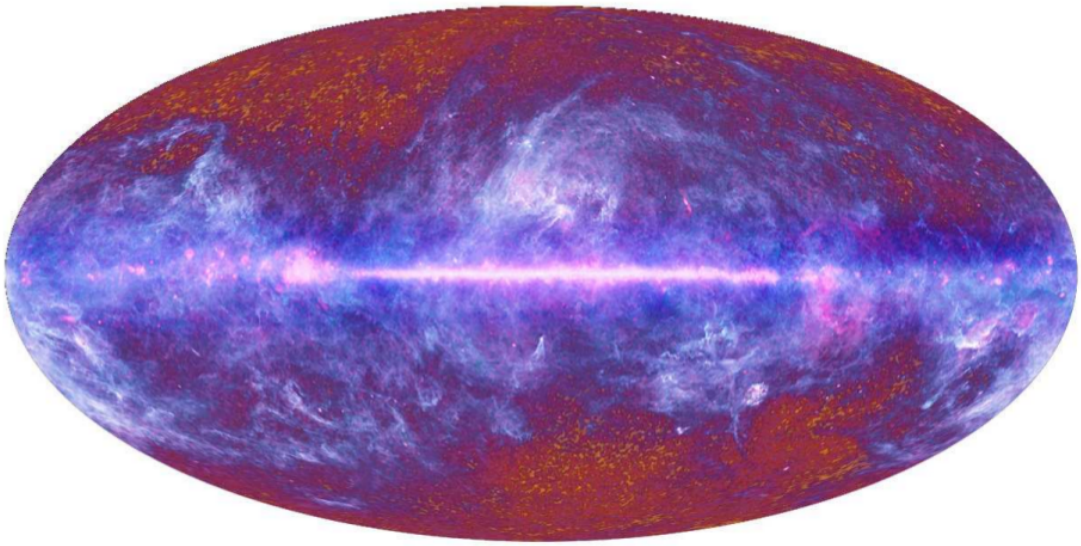

Fig. 2.2: Planck first-year all-sky survey map. It is possible to see, below the Galactic emission in blue, the anisotropies of the CMB. Credit: ESA, LFI and HFI consortia.

2.2 Galaxy formation and evolution

In the local Universe, the different morphological types of galaxies are summarized in the tuning fork diagram known as the *Hubble sequence* (Fig. 2.3). Formerly the diagram was interpreted as an actual evolutionary sequence in which a spheroidal galaxy evolves in time into a spiral. This model had some problems. For example, it did not explain how galaxies rich in inter-stellar matter, as spirals, should have formed from ellipticals, which are generally gas poor systems. A trace of this failed attempt of reading the Hubble diagram as an evolutionary sequence, from left to right, still remains in the traditional nomenclature which defines ellipticals and spirals, respectively, as *early-type* and *late-type* galaxies.

The opposite reading direction was then considered: ellipticals could originate from spirals and irregular galaxies as a consequence of the merging of two or more galaxies belonging to these latter categories. Massive ellipticals should be the objects that formed more recently, but they are characterized by old stellar populations that had evolved in the parent galaxies before the merging event (Blumenthal et al. 1984; White & Rees 1978). This theory is the natural continuation of the hierarchic scenario previously introduced with respect to dark matter halos, but it has some problems too. The key point is if the

observed merger rate can reproduce the abundance of elliptical galaxies as a function of their mass, age metallicity, and so on. There are different scenarios, depending on the kind of merging process is considered. In particular, it has been suggested that massive ellipticals can be the remnants of a dissipationless merger event (*dry merging*) between elliptical progenitors, while less massive ones can be described by dissipation mergers (*wet mergers*). Many of the observed properties of *early-type galaxies* (ETGs) can be reproduced and predicted within the hierarchical merging scenario, given that some feedback process, like the presence of an AGN, is provided to prevent the formation of stars in these systems. However some discrepancy between models and theory remains. The detailed process with which ETGs assemble their mass is still unclear. On the one hand, dissipationless *dry merging* of ETGs has been suggested to build up the masses of massive ETGs, reproducing results that are consistent with the high central densities of ellipticals, their old stellar populations, and the strong correlations of their properties (van Dokkum 2005; Bell et al. 2006); on the other hand, arguments based on the evolution of the shape of the stellar mass function and on the very small scale clustering of local SDSS ETGs arise some problems in this scenario (Bundy et al. 2006; Masjedi et al. 2006).

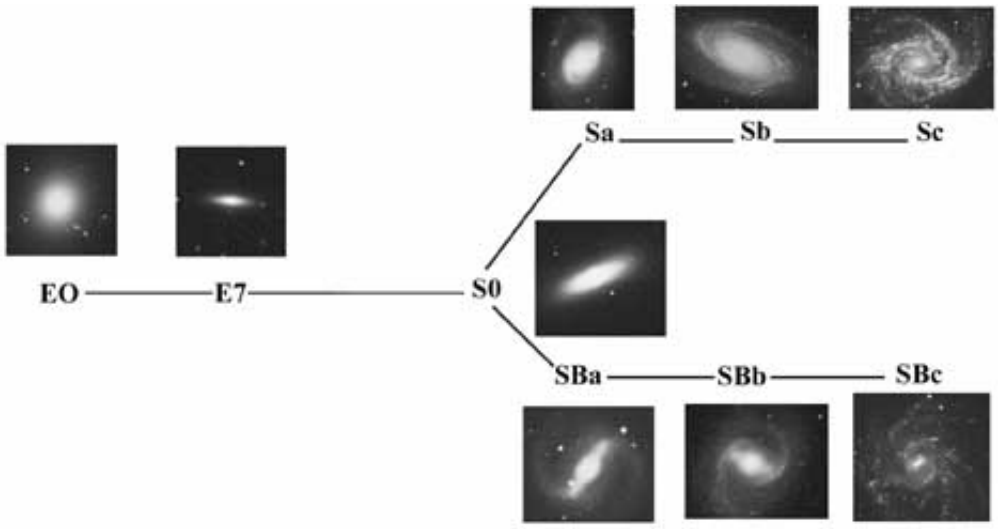

Fig. 2.3: Hubble's tuning fork diagram of galaxy classification. Credit: NASA

Near infrared surveys, sensitive to stellar mass, and therefore particularly suitable for studying elliptical galaxies, revealed that the number density of more massive objects ($M > 10^{11} M_{\odot}$ decreases only slightly going back from $z \sim 0$ to $z \sim 1$ (Fontana et al. 2004; Glazebrook et al. 2004; Drory et al. 2005; Caputi et al. 2005; Bundy et al. 2006). This means that most of the massive galaxies we see in the local Universe were already formed between $z \sim 0.7$ and $z \sim 1$. Furthermore, there was the discovery of massive

ETGs showing signs of an old stellar populations of ages between 1 and 4 Gyrs, in even more ancient times, between $z \sim 1$ and $z \sim 2$ (Cimatti et al. 2004; Glazebrook et al. 2004). Less massive galaxies show the opposite tendency: the number density grows more rapidly from $z \sim 0$ to $z \sim 1$, suggesting an evolution of this objects more prolonged in time (Fontana et al. 2004; Glazebrook et al. 2004; Drory et al. 2005; Caputi et al. 2005; Bundy et al. 2006). With the vast majority of massive ETGs being already in place by $z \sim 0.8$, there seemed to be no much room left for any major contribution of dry merging events in increasing the number of the most massive ETGs. This appeared to be in a agreement with the very low rate of dry merging events estimated from SDSS data (Masjedi et al. 2006).

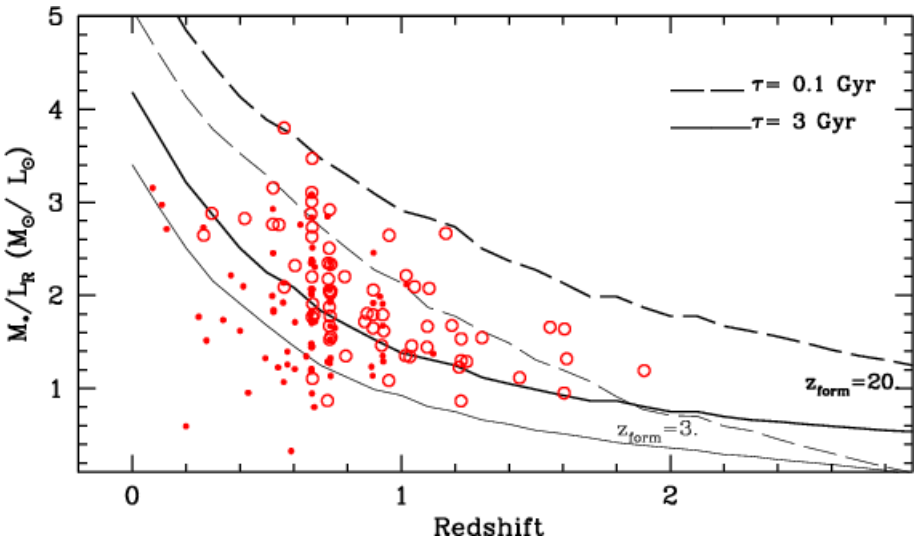

Fig. 2.4: $M_\star/L_R$ ratios as a function of redshift for spectroscopically early and early emission spectral type galaxies of the K20 sample.Large hollow circles are for bright ($M_R < 22$) objects, small filled circles for fainter ($M_R > 22$) ones. Lines show the $M_\star/L_{IR}$ values computed with a set of single-exponential models with $z_{form} = 3$ (thin lines) or $z_{form} = 20$ (thick lines) and star-formation time-scales ranging of $\tau = 0.1Gyr$ (dashed lines) and $\tau = 3Gyr$ (solid lines), all drawn with a Salpeter IMF and no dust extinction. Credit: Fontana et al. (2004)

Another piece of the puzzle was given by the stellar mass over luminosity ratio. This parameter shows a decreasing trend with increasing redshift but, at all times, its value is larger for more luminous galaxies, with respect to less luminous ones (Fig. 2.4). This collection of information can be interpreted assuming that the formation of stars happened on very short time-scales or in ancient epochs (or both things together) for more luminous galaxies galaxies, while on longer time-scales and in more recent epochs for less luminous systems. The just drawn picture was first introduced by Cowie et al. (1996)

to solve all the open issues of the standard hierarchical scenario, and is known as *downsizing*. On the basis of many recent observational evidences, it has been proposed that the downsizing scenario should apply not only to star formation (i.e. stars in more massive galaxies are older), but also to the stellar mass assembly, with more massive galaxies that have assembled before less massive ones. This is often referred as *mass-downsizing*. Although hierarchical models are able to successful reproduce the star-formation downsizing, a coherent explication of the latter one within theoretical models still lacks.

The properties of distant massive ETGs seem to imply that their precursors were characterised by a strong ($SFR > 100 M_{\odot} yr^{-1}$) and short-lived ($\tau \sim 0.1 - 0.3 Gyrs$)[1] starburst, an onset of star formation occurring at high redshift ($1.5 < z < 3$), a passive-like evolution after the major starburst, and the strong clustering expected in the ΛCDM models for the populations located in massive dark matter halos and strongly biased environments Kurk et al. (2013). However, recent studies suggest that stars in these galaxies were formed instead by a quasi-steady star-formation histories, increasing with time and extending over time-scales of order a few billion years (Daddi et al. 2007; Genzel et al. 2008; Renzini 2009). HERSCHEL observations indeed show that starbursts contribute only $\sim$ 10% to the total SFR density at $z \sim 2$ (Rodighiero et al. 2011).

A possible picture for the formation and evolution of massive ETGs is given by Cimatti (2009); in the following, is reported the basic scheme (see also Fig. 2.5):

1. a large fraction of massive SFGs selected in the optical/near-IR are gas-rich disky systems characterized by a âquietâ evolution with long-lived star formation (e.g. $\sim$ 0.5 - 1 Gyr) supported in some cases by âsmooth accretionâ of cold gas streams. These massive systems may later evolve into spheroids through disk instabilities and/or merging processes;

2. the submillimetre galaxy (SMG) phase corresponds to the cases of rapid, highly dissipative, gas-rich major mergers characterized by short-lived ($\sim$ 0.1 Gyr) starbursts. It is intriguing to notice that SMGs are the only star-forming systems at $z > 2$ having the same small sizes and high (gas) mass surface density of ETGs at $1 < z < 2$. If the compact superdense ETGs at $1 < z < 2$ are the descendants of SMGs, the duty cycle time-scale of the SMG phase can be estimated as the ratio of the comoving number densities of the SMGs ($\sim$ 10 - 5 Mpc_{-3}) and ETGs ($\sim$ 10 - 4 Mpc_{-3}) and the amount of cosmic time available from $z \sim 2.5$ to $z \sim 1.5$

[1] τ indicates the scale time of star formation where its rate is $SFR \propto exp(-t/\tau)$.

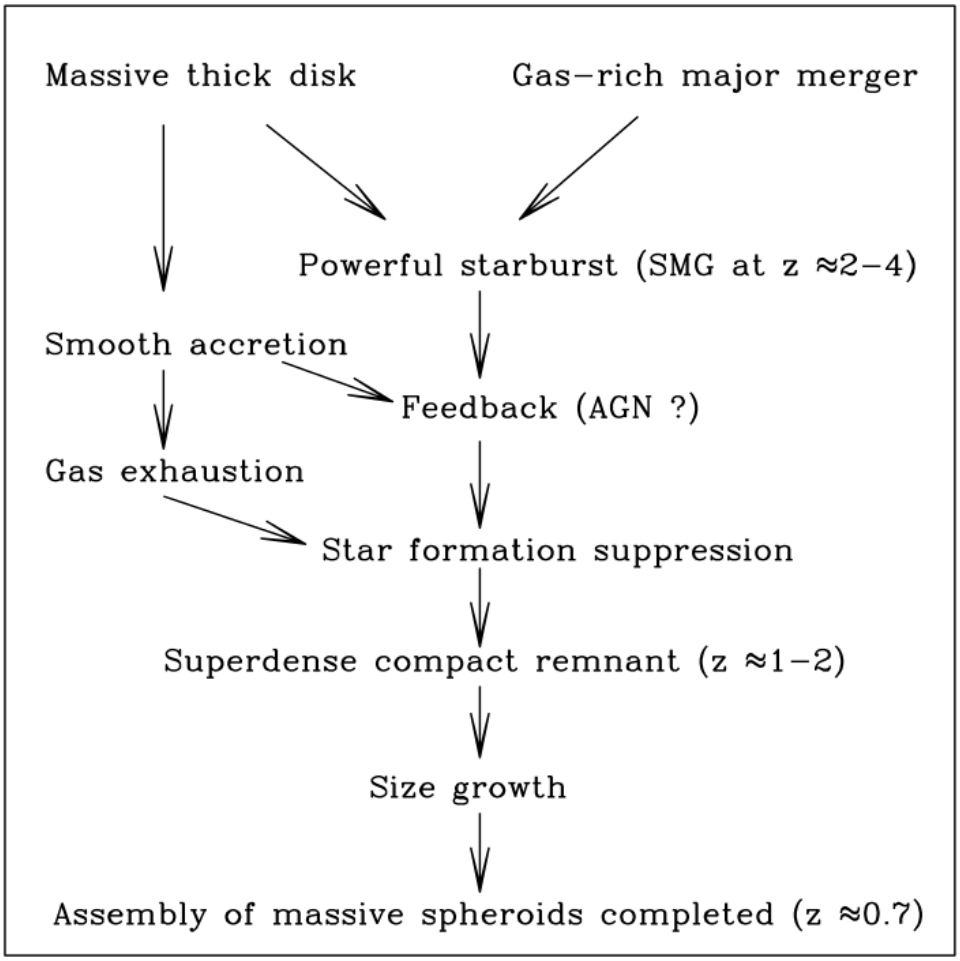

Fig. 2.5: Reproduced from Cimatti (2009): the variety of possible evolutionary paths for the formation of massive spheroidal galaxies.

($\sim$ 1.5 Gyr), i.e. $\sim$ 0.15 Gyr. This is broadly consistent with the e-folding timescale derived independently from the SED fitting and from the SMG molecular gas. AGN feedback would then be required to âquenchâ the star formation. This could also explain the origin of the relation between super-massive black hole and galaxy masses. Although the involved physical processes are different, this scenario is somehow reminiscent of the âold-fashionedâ monolithic collapse;

3. the compact, superdense ETGs at $1 < z < 2$ evolve by increasing gradually their sizes. A possible mechanism is major dissipationless (âdryâ) merging. However, it is unclear how the âdryâ merging scenario can be reconciled with the properties of the small-scale clustering of low-z ETGs and with the weak evolution of the high-mass end of their stellar mass function at $0 < z < 0.7$. Other processes which may

increase the sizes at z < 1 are the smooth envelope accretion and multiple frequent minor mergers;

4. the majority of most massive ETGs reaches the assembly completion around $z \sim 0.7 - 0.8$, while lower mass ETGs continue to assemble down to lower redshifts (downsizing).

To answer the main questions about galaxy evolution, the critical epoch in the redshift range of $1 < z < 3$ must be explored. Two of the most important processes that govern galaxy assembly are the conversion of in-situ initial gas into stars in a galaxy, over time, and merging with existing galaxies. The merger rate is a quantity rather complex to be measured, especially at high redshift (see also section 2.3 of this chapter). A deep understanding of the morphological properties of galaxies is necessary.

The morphological analyses of high-redshift galaxies, and the study of the link between galaxy physical and spectral properties and the morphologies is important not only to discover and study merger candidates, but firstly to investigate the built-up of the Hubble sequence and how the evolution in time of a galaxy may affect its visual appearance.

Driven by these motivations, a part of this thesis project was devoted to the analyses of morphologies of a sample of high-redshift galaxies.

2.3 Morphologies

As already said in the previous section, it is by now quite established that galaxies in the local Universe may be well classified, according to their visual appearance, along the so-called Hubble sequence. At $z > 1$ things work in a different way: the majority of the galaxy population at high redshift consists of objects with peculiar and irregular morphologies, visually very dissimilar from their low redshift descendants (Abraham et al. 1996; Cassata et al. 2005; Conselice et al. 2008).

How and when did these objects turn into the ellipticals and spirals that we see today? The structures of galaxies have been proven to correlate with formation modes, such as star formation and galaxy mergers (Conselice et al. 2003), therefore classifying morphologies at different redshifts, studying how they change through cosmic time and how they relate to other physical and spectral properties, is of fundamental importance in the understanding of galaxies formation and evolution processes.

Assigning a galaxy to a particular morphological class is a 'by-eye' job that relies much on human subjectivity, especially in the case of faint high-redshift galaxies. The Hubble types are still used in the morphological classification at high-redshift, even if galaxies shapes do not fit perfectly in the 'traditional' classes. However, in last years some authors have also developed simpler visual classification schemes based on the apparent nucleation of galaxies light profiles and the number and definition of distinct clumps (Law et al. 2012b,a).

Alongside visual classification, other parametric and non-parametric methods have been conceived to quantify morphological properties.

2.3.1 Sérsic profile

One widely used approach is to fit the light distribution of galaxies to analytic laws; the most used model is a single Sérsic profile[2], which is characterized by an effective radius and the radial index of the profile characterizing the shape of the light distribution. In the nearby Universe, the most commonly observed values of the Sérsic index are $n = 1$ and $n = 4$, which describe respectively an exponential disk profile and a classical de Vaucoulers profile typical of ellipticals and galactic bulges (Peng et al. 2002).

Though useful to provide some description of the characteristic sizes of the studied objects and a rough guide to the overall shape of their light distribution, this approach suffers from the fact that the light distribution in high-redshift galaxies hardly follows regular ellipsoidal models (Cassata et al. 2005; Law et al. 2012b). In the far Universe galaxies may be still roughly divided into bulge- and disk-dominated, according to their Sérsic index: $n < 2$ and $n > 2$ respectively (Ravindranath et al. 2004; Trujillo et al. 2007; Buitrago et al. 2008; Conselice et al. 2011), but the contamination between the two groups is high enough that the Sérsic index alone is not sufficient to correctly classify the structural type of a galaxy (Fig. 2.6) (see also Abraham et al. (1996); Cassata et al. (2005)). The sizes of the galaxies obtained from this kind of approach are traditionally indicated in terms of circularized effective radius ($r_{circ} = r_e \sqrt{b/a}$, where b/a is the minor/major axis ratio) (Shen et al. 2003; Trujillo et al. 2007; Toft et al. 2009). Typical sizes of SFGs at $z \sim 2$, in their optical rest-frame, are $r_e \sim 0.7 - 3$ kpc (Law et al. 2012b; Kriek et al. 2009).

[2]The Sérsic profile: $\Sigma(r) = \Sigma_e exp(-\kappa[(r/r_e)^{1/n} - 1])$, where Σ is the surface brightness, r_e is the effective half light radius and n is called the Sérsic index.

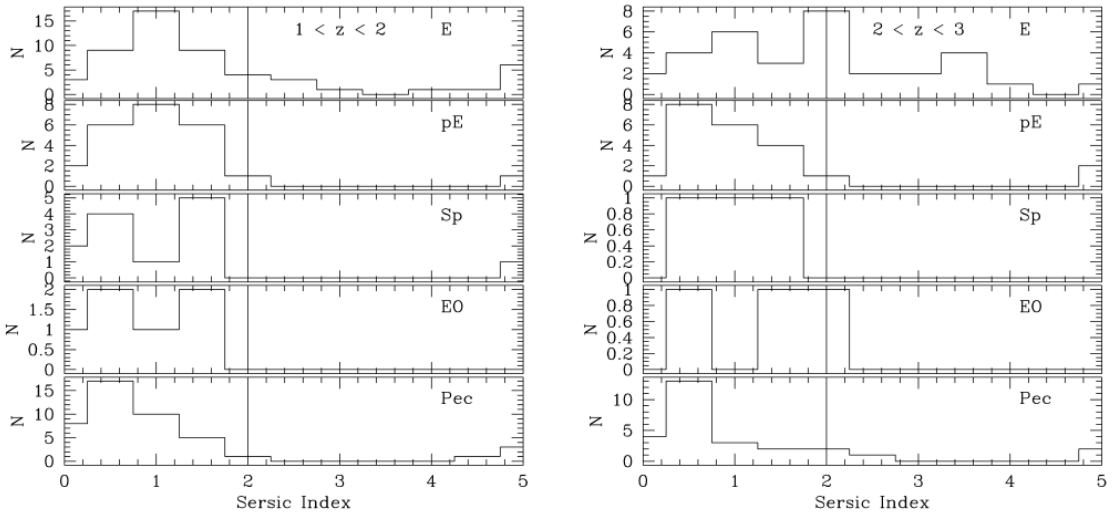

Fig. 2.6: Reproduced from Conselice et al. (2011): distribution of Sérsic indices for a sample of WCF3/UDF galaxies. The Sérsic indices distribution is shown for each visually determined galaxy type (elliptical (E), peculiar elliptical (pE), spiral/disc (Sp), edge-on disc (EO) and peculiar (Pec)). The vertical lines at $n = 2$ demonstrate the separation between galaxies that are "disc like" with $n < 2$ and those that are "elliptical like" with $n > 2$ (see Ravindranath et al. (2004); Buitrago et al. (2008).

2.3.2 CAS and G-M20 parameters

The most used non-parametric approaches are the CAS system (concentration - asymmetry - clumpiness), and the G-M_{20} system (Gini coefficient - second order moment) (Fig. 2.7) (Abraham et al. 1994; Abraham et al. 1996; Abraham et al. 2003; Lotz et al. 2004). In high-redshift galaxies the clumpiness is the less defined parameter, due to the small size and faintness of the galaxies and poor resolution of the images with respect to the local Universe case (Lotz et al. 2004; Law et al. 2012b; Bluck et al. 2012). Though the definition of the various parameters is quite established in the literature, the same cannot be said for the segmentation maps that are needed to compute the morphological statistics; therefore caution is needed when comparing different studies. However, Law et al. (2012b) demonstrated that the results obtained from the most commonly adopted segmentation maps are correlated with each other and systematic offsets between the different systems may be computed.

At low redshift, the position of a galaxy in the C-A and G-M_{20} planes have been associated to the different morphological classes (Bershady et al. 2000; Conselice et al. 2003; Lotz et al. 2008), but high-redshift galaxies of different morphologies do not fall precisely in the same regions of their local equivalents, suggesting an evolution of morphological

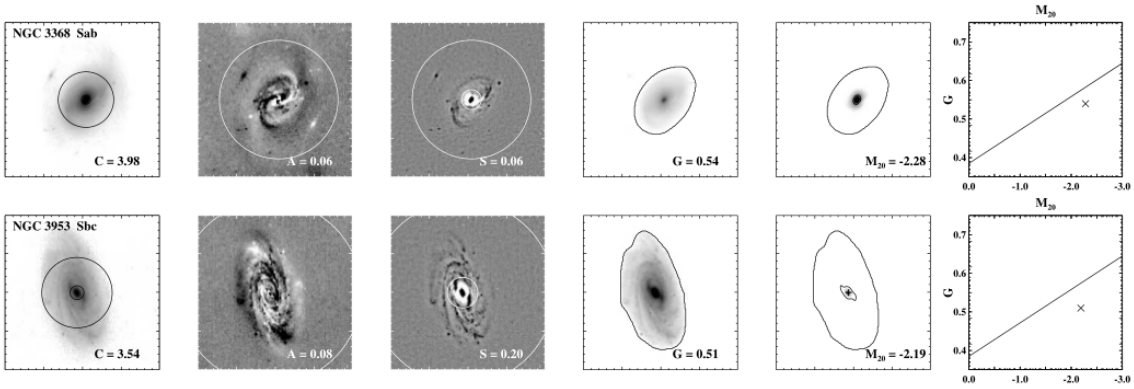

Fig. 2.7: Reproduced from Lotz et al. (2004): test galaxy morphological measurements C, A, S, G, and M20 for rest-frame $\sim$ 6500 Å images of a sample of local galaxies. In the first panel inner and outer circles enclose 20% and 80% of the flux within 1.5 r_p. The second panel shows the residual I - I_{180} image, with the circle at 1.5 r_p. The third panel shows the residual I - I_S image, with the inner and outer circles at 0.25 and 1.5 r_p. The fourth panel images are the original galaxy images scaled such that the minimum surface brightness matches that used to create the galaxy segmentation maps. The outer edge of the segmentation map are the outer contour plotted in the fourth and fifth panels. The inner contours plotted in the fifth panel trace each galaxy's brightest 20% of it flux, while the crosses indicate each galaxyâs centre. The final panel plots each galaxyâs G and M20, where the solid line is for reference.

parameters with redshift. In particular, early-type galaxies show a higher general level of asymmetry (Conselice et al. 2008, 2011), with respect to their local siblings. It is important to stress that the redshift evolution of morphologies, regardless the way in which they are defined, has to be studied in the same 'rest-frame' band for all redshifts, that means using different appropriate 'observed' bands. Morphological features can strongly depend on the rest-frame wavelength: since at different wavelengths different gas phases and stellar populations are probed, also the structure of a galaxy may change depending on the wavelength at which the galaxy is seen. However, the occurrence of this so-called morphological k-correction is not so easy to establish and quantify, since the different PSFs of the instruments used to take the images may play a role in mimicking an actual change in visual morphology and/or morphological parameters.

In the rest-frame ultra-violet (UV) to B-band images of high-redshift galaxies, the C-A plane segregates quite well the ellipticals, which are characterized by the highest concentrations along with the lowest asymmetries, while irregulars and disks span a larger range in the parameters space (Conselice et al. 2008; Cassata et al. 2005). Something similar happens when looking at the optical rest-frame (Conselice et al. 2011; Law et al. 2012b), but with a larger scatter and some interesting differences. In particular, com-

paring ACS and WFC3 imaging for the same sample of galaxies, Conselice et al. (2011) find that high-redshift irregular galaxies are, in their rest-frame UV, more asymmetric and clumpy, compared to rest-frame optical bands; both elliptical and irregular morphologies show, instead, lower concentration values at shorter wavelengths.

Also in the G-M_{20} plane, ellipticals are confined in a precise region, with $M_{20} \sim -1.5 - -2.0$ both in rest-frame UV and optical imaging, and G values spanning a ~ 0.2 range between 0.5 and 0.8, depending on the study (therefore the chosen segmentation map). Disky and irregular morphologies lie more scattered, but are better confined with respect to what happens in the C-A plane. Conselice et al. (2008), studying the rest-frame UV of galaxies in the Hubble Ultra-Deep Field (UDF), with the Advanced Camera for Surveys (ACS), find irregulars to have, on average, higher values of both G and M_{20} parameters than ellipticals galaxies, and lie in the region of the G-M_{20} plane where Lotz et al. (2008) find ULIRGs merger candidates in the local Universe. In the rest-frame optical samples analysed by Law et al. (2012b) and Wang et al. (2012) with the Hubble Wide-Field Camera 3 (HST/WFC3) most of the irregular galaxies (Type III in the Law et al. (2012b) paper) are characterized by lower Gini values than ellipticals/spheroids (Type I).

2.3.3 The merger fraction

Morphological analyses is also the tool to estimate the fraction of merger episodes. This task is very challenging, especially at high redshift. Merger candidates are usually found either searching for close galaxy pairs (Patton et al. 1997; Le Fèvre et al. 2000; Carlberg et al. 2000) or by looking at the position of a galaxy in the CAS plane (Conselice et al. 2003) or in the G-M20 diagram (Lotz et al. 2008) (Fig. 2.8).

At low to intermediate redshifts ($0 < z1.4$), close pair methods and morphological approaches find close accord in estimating the major merger history of massive galaxies (Bluck et al. 2009; Conselice et al. 2009). At the highest redshifts ($z > 1.5$), studies have concentrated primarily on close pair methods, as opposed to morphological approaches, due to restrictions on the resolution of imaging of very high redshift objects (Bluck et al. 2009). These studies find rough agreement in identifying a positive evolution of the major merger fraction with redshift, with an estimate for the most massive galaxies (with $M_{star} > 10^{11} M_{\odot}$) of evolution such that $f_m \propto (1 + z)^{3.0 \pm 0.4}$ (where f_m is the merger fraction), with no sign of this monotonic increase in merger fraction with redshift abating at higher redshifts (Fig. 2.9) (Bluck et al. 2009, 2012).

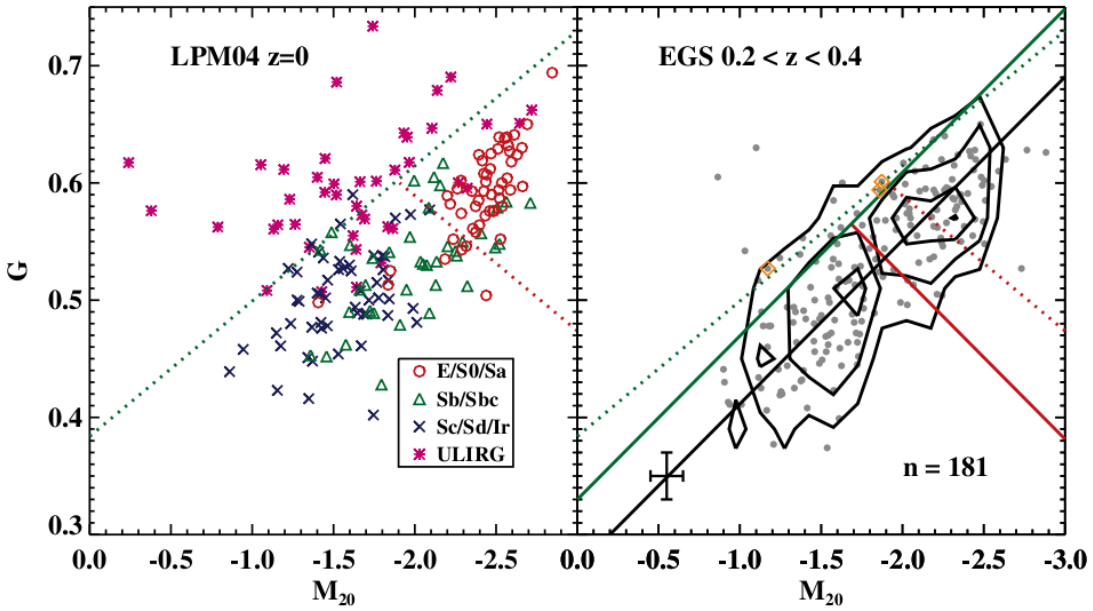

Fig. 2.8: Reproduced from Lotz et al. (2008). Left: rest-frame *B-band* G vs. M20 morphologies for local galaxies from Lotz et al. (2004). The upper green dotted line divides merger candidates (ULIRGS) from normal Hubble types. The lower red dotted line divides normal early-types (E-Sa) from late-types (Sb-Ir). Right: rest-frame *B-band* G vs. M20 morphologies for Extended Groth Strip $0.2 < z < 0.4$ sample (grey points and contours).

For lower mass systems there is an observed peak in the merger fraction history at $z \sim 1-2$, as seen in Conselice et al. (2007), but to date no similar peak is observed for the most massive galaxies in the universe (with even out to $z = 3$. This disagrees with predictions from semi-analytical interfaces with the Millennium Simulation, where a turnaround in merger fraction is expected for massive galaxies by $z \sim 2$ (Bertone & Conselice 2009). At some point the merger fractions must turn over, but this has yet to be observed or constrained for very massive galaxies.

It has to be stressed that the merger-rate issue at high-redshift is still difficult to address with rest-frame optical imaging, especially when using quantitative morphologies, since merger candidates loci in the parameter space have not been yet identified for the PSF and depth of the NIR-imaging survey. Some authors have also pointed out that irregular morphologies may arise from dynamical instabilities within gas-rich systems, instead of being related to merger processes (Bournaud et al. 2008; Genzel et al. 2011).

Though there is evidence that the major merger fraction of massive galaxies increases with redshift, the accurate estimate of this fraction is still an open issue, that has to be addressed combining different approaches: close pairs identification, calibration of the

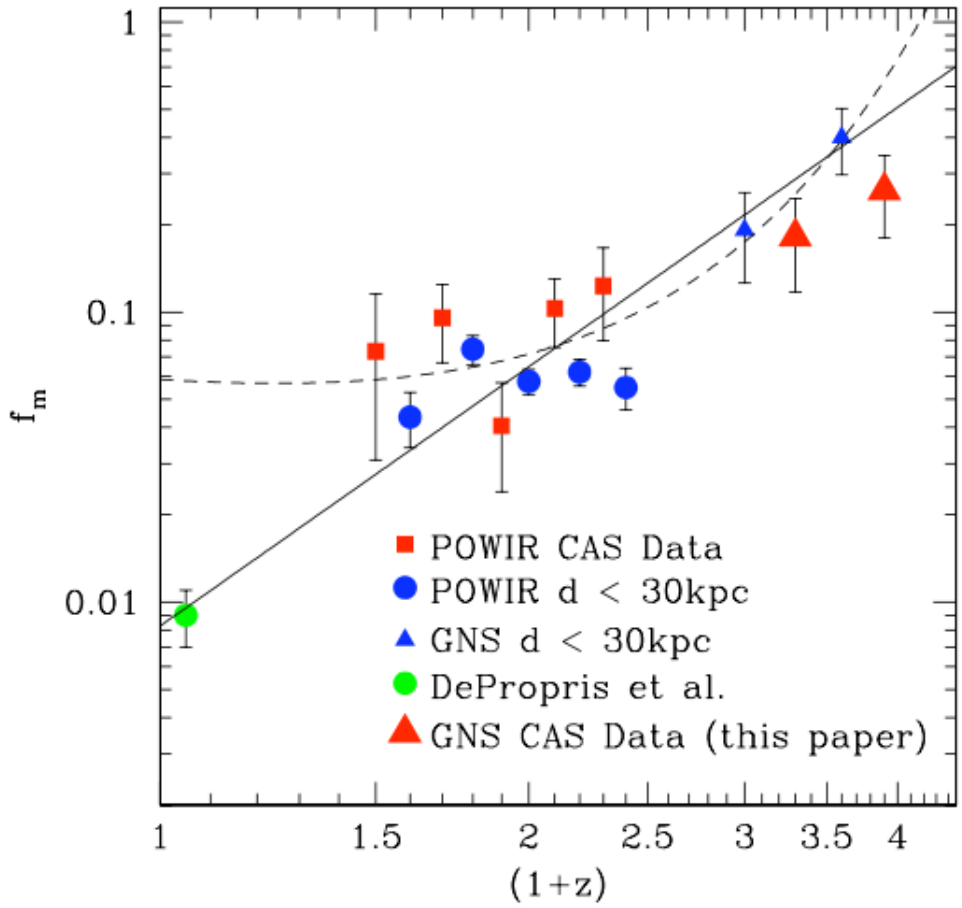

Fig. 2.9: Reproduced from Bluck et al. (2012): the major merger fraction evolution of $M_{star} > 10^{11} M_{\odot}$ galaxies. The red squares are taken from POWIR data, with merger fractions calculated via CAS morphologies (Conselice et al. 2007). The blue circles are taken from POWIR data, with merger fractions calculated via close-pair methods. Blue triangles are taken from the GNS, with merger fractions calculated via close-pair methods. The green circle represents the local universe value (calculated in De Propris et al. (2007)). Large red triangles represent CAS morphology determined major merger fractions for the two highest redshift ranges, up to $z = 3$ (Bluck et al. 2012). Solid line is a best fit power law, to the high z data, of the form $f_m = 0.008(1+z)^3$, with dotted line being a best fit power law exponential, to the high z data, of the form $f_m = 0.008(1+z)^3\ exp(1.0(1+z)^2)$.

CAS plus G-M20 parameter space at high redshift, and semi-analytical simulations.

2.3.4 Morphologies and physical properties of galaxies

Another interesting issue to address is the correspondence between the visual classification of high-redshift galaxies and their physical properties, such as spectral type (as

inferred by spectra or by fitting SEDs to broad-band photometry), rest-frame and/or observed colours and star-formation history. The correlation between morphologies and star-formation, observed in low redsfhit galaxies, still holds at high-redshift, but is not so tight (Cassata et al. 2011; Wuyts et al. 2011; Bell et al. 2012). In general, quiescent galaxies are the ones with the most specific appearance, while SFGs show a large variety of morphologies (Law et al. 2012b).

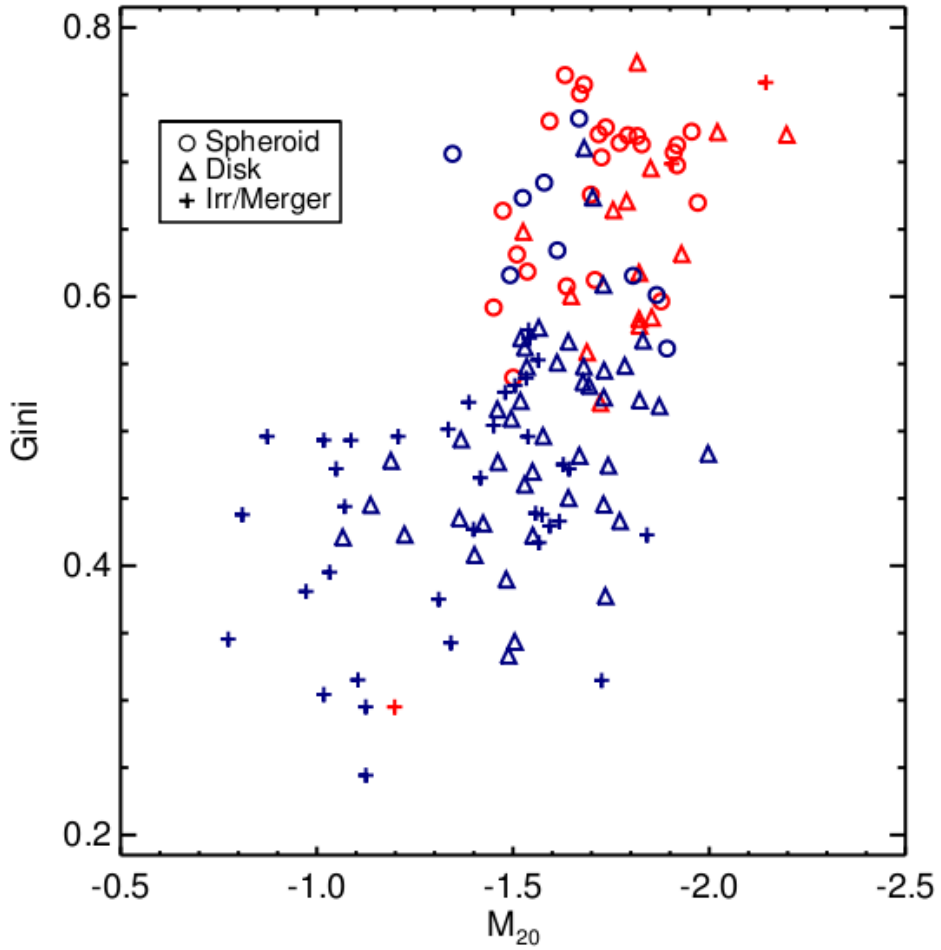

Fig. 2.10: Reproduced from Wang et al. (2012): distribution of IEROs, with different visual morphological types, in the Gini - M20 diagram. Quiescents, based on *UVJ* colours, are denoted with red points, while dSFGs are in blue.

Rest-frame colours have also been proven to correlate with morphological properties. Wang et al. (2012), for example, find that massive IRAC-selected Extremely Red Objects (IEROs), classified as quiescent or dusty SFGs, according to their IR colours, are well separated in the *UVJ* diagram and in the G-M_{20} plane (Fig. 2.10); the implied relation

between these quantities may indicate that the quenching process for star formation may occur along with (or be the cause of) an increase of galaxy concentration.

Morphologies are closely related to the star-formation status of a galaxy, in a double way: the star-formation activity has a role in the shaping of a galaxy, and morphological features may give information about the triggering mechanism of the star-formation (a merger event, for example).

As well as morphologies, however, the star-formation is still a difficult issue to address, at high-redshift, because local relations and calibrations have to be used to analyse the star-formation activity in distant galaxies, and we have been aware for a while that SFGs, in the past, were different from their local siblings. In particular, it seems clear that the role of dust in affecting the observables used to derive the star-formation rate in high-redshift galaxies, is yet to be fully understood.

The problem of correctly deriving the star-formation rate in high-redshift galaxies, and the calibration of multi-wavelength estimators, is another one of the hot topics of modern extragalactic astrophysics.

2.4 Star-formation rate and dust extinction

Determining when the stars were formed is one of the main goals in galaxy evolution. Two widely adopted approaches to this question are to measure the assembled stellar mass at various look-back times (Cole et al. 2001; Bell et al. 2003; Bundy et al. 2006; Pozzetti et al. 2007; Fontana et al. 2004) or to quantify the rate of on-going star formation over cosmic time (Madau et al. 1996; Lilly et al. 1996; Steidel et al. 1999; Bouwens et al. 2011). While the latter should in principle integrate up to the former, modulo stellar mass loss, it is currently heavily debated whether or not the data, or rather the physical quantities estimated from them, satisfy this continuity equation (Hopkins & Beacom 2006; Reddy & Steidel 2009). Critical to these investigations are the assumptions made in translating fluxes and colours to an estimate of the SFR. Especially the presence of dust greatly impacts the interpretation of multi-wavelength data. It is known, in fact, that dust grains absorb the flux emitted by stars at UV and optical wavelength, and re-emit it at longer wavelength, in IR bands. There are many ways of deriving the rate of star-formation in a galaxy, depending on the wavelength of the available data. From the UV to the far IR (FIR), we can distinguish between two main cases: either the luminosity

coming from dust emission is directly converted into the rate of obscured star formation, or the rate of unobscured star formation is scaled up by a dust correction factor (SED fitting, UV flux, nebular emission lines flux). The former requires knowledge of the total IR luminosity (LIR) emitted in the rest-frame $8 - 1000\mu m$ range by dust that was heated by young stars, often extrapolated from the observed 24 μm photometry. The latter requires knowledge of how the observed colours break down in intrinsic colours of the stellar population and dust reddening, which are both model dependent.

2.4.1 Kennicutt et al. (1998) relations: assumptions on SFGs

Apart from the dust-extinction problem that affects UV and optical SFR estimators, the model dependencies of the conversions from IR luminosity, UV flux, or nebular emission lines flux, to SFR have to be taken into account. The most widely used relations, that are described in Kennicutt (1998), are theoretical relations based on the starburst synthesis models of Leitherer & Heckman (1995) obtained for a continuous burst, solar abundances and a Salpeter (1955) IMF, assuming that young stars dominate the radiation field throughout the UV-visible, and that the FIR luminosity measures the bolometric luminosity of the starburst. This physical situation holds in dense circumnuclear starbursts that power many IR-luminous galaxies. In the disc of normal galaxies or early-type galaxies, the situation is much more complex as dust heating from the radiation field of older stars may be very important.

2.4.2 SED fitting

A commonly used way of recovering the instantaneous star-formation of a galaxy, is by fitting its spectral energy distribution (SED) with a library of theoretically modelled synthetic spectra.

SED fitting strongly depends on the availability of broad band photometry on a large wavelength base, and on the reliability of the theoretical models. Different sets of evolutionary population synthesis models are fitted to broad-band galaxy SEDs using a χ^2 minimization; a best-fit model for each galaxy is derived, providing estimates for age, stellar mass, extinction A_V, and SFR (Bolzonella et al. 2000; Pozzetti et al. 2007).

Today, the most widely used libraries of synthetic spectra are Maraston (2005) (M05) and Bruzual & Charlot (2003) (BC03). The main difference among these sets of models

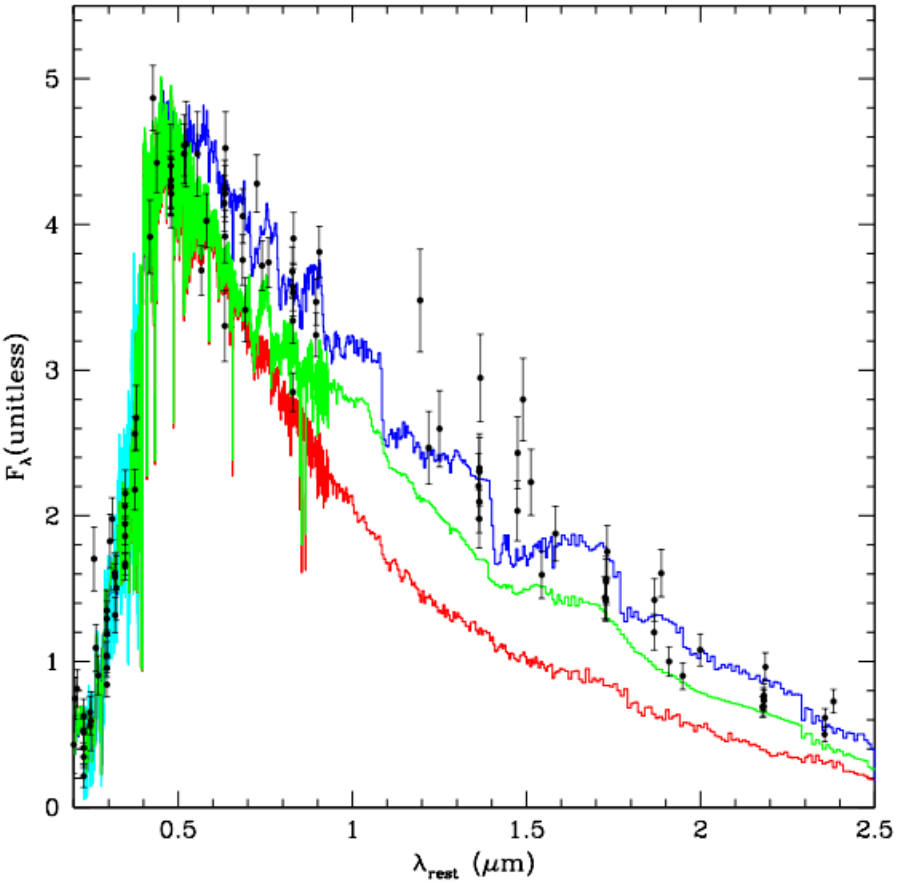

Fig. 2.11: Reproduced from Cimatti et al. (2008): the observed stacked spectrum of GMASS (see Chapter 3) passive galaxies (cyan) and two synthetic spectra which provide the formal best fit in the range of 2480-3560 Å for solar metallicity and age of 1.0 Gyr for BC03 (red) and M05 (blue) models (Charlot & Bruzual (2007) model is also shown, in green). The black dots are the rest-frame photometry of the galaxies normalized at $\lambda_{rest} = 0.5\mu m$.

is in the treatment of the thermally pulsing asymptotic giant branch (TP-AGB) phase of stellar evolution, which for intermediate age SSPs can contribute up to $\sim 50\%$ to the total bolometric light, radiated mostly in the NIR. In M05 models the TP-AGB contribution was calibrated using Magellanic Cloud globular clusters of various ages, whereas BC03 models had a negligibly small contribution of the TP-AGB at all ages. Fig. 2.11 shows how the templates differ with each other at long wavelengths. Usually, star-formation histories (SFHs) are parametrized by exponentials ($e^{\frac{-t}{\tau}}$) with e-folding time-scales τ of between 100 Myr and 30 Gyr, plus the case of constant SFR. For the dust extinction, the Calzetti law (Calzetti et al. 2000) is the most widely extinction law assumed, in the case of high-redshift SFGs. Moreover, a solar metallicity is almost always assumed, al-

though many studies have shown that, at high-redshift, SFGs have sub-solar metallicities (Halliday et al. 2008).

Alternative star-formation histories have been proposed, recently. Several authors have argued, both on observational (Renzini 2009; Maraston et al. 2010; Papovich et al. 2011) and on theoretical (Finlator et al. 2007; Lee et al. 2010) grounds, that galaxies may undergo increasing, rather than decreasing, SFHs during parts of their life, specifically at early times ($z \geq 3$). Alongside these so-called inverted-τ models, Wuyts et al. (2011) propose also delayed τ models, that use the following form of SFHs: $SFR(t) = te^{-t/\tau}$. This formulation allows for solutions with increasing SFRs (for ages $< \tau$) as well as solutions in which the SFR is decreasing after a prior phase during which it was increasing (for ages $> \tau$).

2.4.3 The relation between UV continuum slope and attenuation

Not always all the photometric bands needed to well constraint the SED of a galaxy may be available. Another way to derive the SFR of a galaxy is from its UV flux. The UV part in the spectrum of SFGs is dominated by emission from young stars and provides strong constraints on the ongoing SFR. The availability of many SFR tracers diminishes at moderately-high redshifts ($z > 1$), where nebular lines are red shifted into the near-infrared and spectroscopy becomes increasingly difficult, while the availability of deep mid and far infrared (MIR and FIR) photometry is limited to a few deep extragalactic fields. In contrast, at these redshifts the UV band shifts into the optical range, which makes it possible to observe from the ground to very high depths, often making it the most accessible SFR indicator for large samples. UV radiation is susceptible to attenuation by dust in the host galaxy. In many examples, only a few percent of the UV photons escape the host galaxy. It is therefore vital to correct UV luminosities for dust attenuation. The estimation of the attenuation normally relies on measuring the change in some photometric colours, often at wavelengths other than the ones to be corrected. This estimation also requires assumptions on the extinction curve and the geometrical arrangement of the UV sources and dust. In particular, Calzetti et al. (1994) showed that the shape of the continuum can be fairly well-approximated by a power law $F_\lambda \propto \lambda^\beta$, where F_λ is the observed flux ($erg\ s^{-1}\ cm^{-2}\ \text{Å}^{-1}$) and β is the continuum slope, and that there is a strong correlation between the slope and nebular extinction measured in the optical using the Balmer decrement.

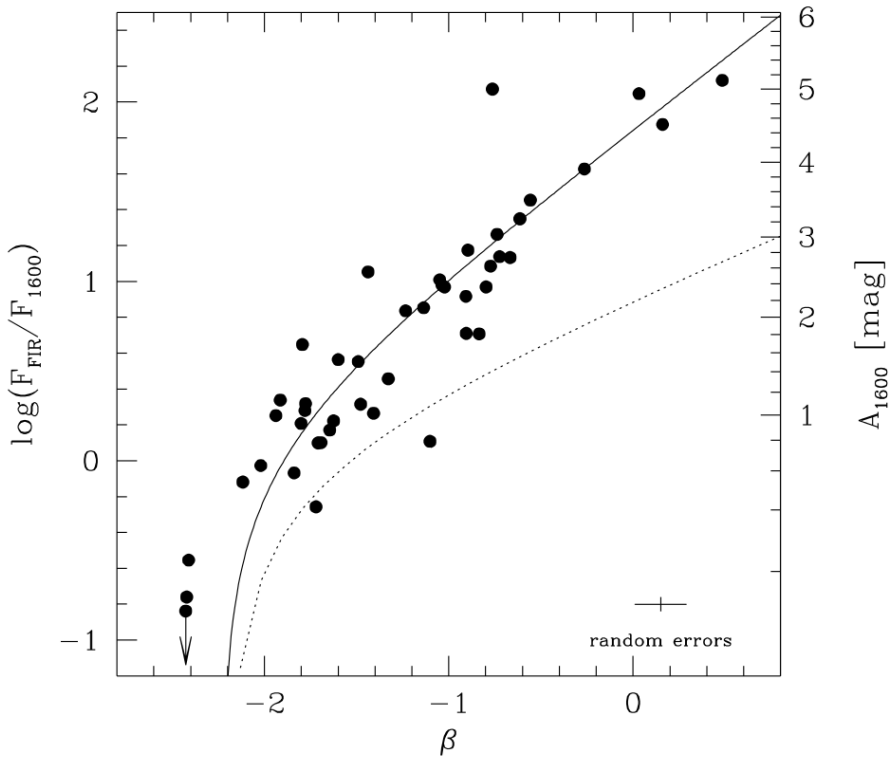

Fig. 2.12: Reproduced from Meurer et al. (1999): ratio of FIR to UV flux at 1600 Å compared to UV spectral slope β for UV-selected starburst galaxies. The right axis converts flux ratio to 1600 Å absorption A_{1600}. The solid line shows the linear fit to the $A_{1600}-$ relationship by Meurer et al. (1999). The dotted line shows the proposed dust-absorption/population model of Pettini et al. (1998).

Meurer et al. (1999) found a linear relation between the UV continuum slope, parametrized by β, and dust extinction at 1600 Å, expressed in magnitudes (Fig. 2.12). This relation, which was calibrated for a sample of local starburst galaxies, has also been used in $z > 1$ studies. The calibrations used the ratio of the FIR luminosity (representing the UV radiation reprocessed by dust) to the UV luminosity (escaped light) as an indicator of the UV attenuation. The FIR/UV ratio is often referred to as the infrared excess or IRX, and the UV attenuation derived from the FIR/UV ratio is referred to as A_{IRX}.

The need for far infrared luminosities in order to determine A_{IRX} significantly limited earlier studies to low redshifts. At redshifts of $z > 1$ such studies were limited to very FIR-bright objects, or to use alternative methods for determining the UV attenuation. The situation improved with the advent of Spitzer and Herschel (Pilbratt et al. 2010) infrared space telescopes. The latter in particular performed deep extragalactic surveys that detect normal SFGs at $z \sim 2$ and more in six bands that cover the peak of the FIR emission in

SFG. Studies regarding the UV attenuation at high-redshift report significant scatter in the A_{IRX} vs. β relation (Nordon et al. 2010, 2012; Reddy et al. 2012), with different galaxy populations tending to lie on different relations. This may indicate different dust properties, different stellar populations that dominate the UV, or different star and dust geometry in these populations. Some authors favour a dust screen in the foreground with the UV emitting stars behind it. Others find better agreement with a mix of dust and stars in the same volume, or combinations of both possibilities.

2.4.4 Nebular emission lines

Another very important estimator is the H_α emission line flux. The SFR derived from H_α is calibrated on the physical basis of photo-ionization. The nebular lines effectively re-emit the integrated stellar luminosity of galaxies shortwards the Lyman limit, so they provide a direct, sensitive probe of the young massive population. Only stars with masses $> 10 M_\odot$ and lifetimes < 20 Myr contribute significantly to the integrated ionizing flux, so the emission lines provide a nearly instantaneous measure of the SFR, independent of the previous star formation history. However, a large part of the light emitted by young stars, which mostly reside within or behind clouds of gas and dust, is absorbed by dust and then re-emitted at longer wavelengths. To properly calculate the SFR from H_α emission line an extinction correction must be applied to take this effect into account. A method to measure the extinction is to compare the observed ratio of the H_α and H_β emission lines (R_{obs}) with the theoretical value ($R_{th} = H_\alpha/H_\beta = 2.86$). Then the reddening towards the nebular regions, E(B - V), can be derived from a chosen extinction law, for example the one by Calzetti et al. (2000).

For a comprehensive review of SFR estimators, see Kennicutt (1998) and its more recent update Kennicutt & Evans (2012).

Star-formation is also responsible of a very interesting phenomenon, long known (Lynds & Sandage 1963), but that only recent observational facilities have allowed us to study in depth: galactic-scale outflows.

2.5 Galactic-scale outflows

Galaxies are known to affect their environment by expelling gas and metals into the intergalactic medium (IGM) via "superwinds" (Heckman et al. 1990). These outflows may contribute to the limiting of black hole and spheroid growth (possibly resulting in the correlation between black hole and bulge mass; Ferrarese & Merritt (2000), the enrichment of the IGM (Oppenheimer & Davé 2006), and the regulation of star formation through the ejection of cold gas (Scannapieco et al. 2005). Two are the processes responsible of galactic-scale outflows: AGN activity and star-formation, but here we shall concentrate only on star-formation driven winds.

2.5.1 The role of "superwinds" in galaxy evolution

At high redshifts, winds may have played a critical role in reionization by clearing paths for ionizing radiation to escape from galaxies (Dove et al. 2000; Heckman et al. 2001a). The kinematics of interstellar absorption lines provide one of the key probes of outflowing gas in galaxies. Observations of blueshifted interstellar absorption lines at a variety of rest wavelengths and ionization states have been observed in both local and high-redshift samples (Heckman et al. 2000; Shapley et al. 2003; Steidel et al. 2010; Coil et al. 2011; Kulas et al. 2012; Law et al. 2012a). The presence of outflows with blueshifted velocities relative to stars and H II regions appears to be associated with objects undergoing starbursts: UV-selected star-forming galaxies at $z = 2 - 3$ with large star-formation rates (SFRs) (Pettini et al. 2002; Shapley et al. 2003; Steidel et al. 2010), local ULIRGs (Heckman et al. 2000; Rupke et al. 2005), and local dwarf starbursts (Heckman et al. 2001b; Schwartz & Martin 2004). Studies of X-ray and H_α emission in local samples have focused on correlating outflows with spatially resolved properties such as star-formation rate surface density, morphology, and galaxy inclination (Heckman 2002; Strickland et al. 2004). Only recently, however, have absorption-line studies of winds at higher redshifts begun similar investigations, thanks to the advent of 8-10 m class telescopes (Weiner et al. 2009; Rubin et al. 2010; Steidel et al. 2010; Talia et al. 2012; Kornei et al. 2012; Law et al. 2012a), that have made available deep spectroscopy of the UV spectrum of galaxies at $z > 1$.

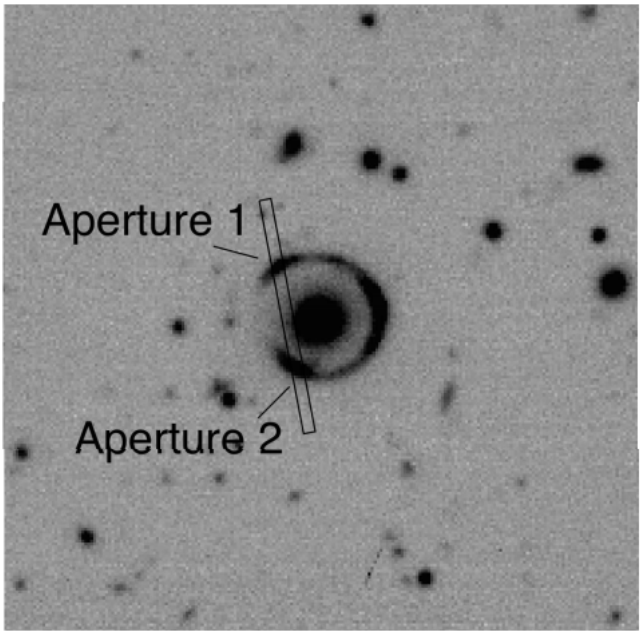

Fig. 2.13: Reproduced from Quider et al. (2009): R-band image of the Cosmic Horseshoe obtained with FORS2 on the Very Large Telescope of the European Southern Observatory (courtesy of L. J. King). North is up and East is to the left. Superposed on the image is the 1.0×20 arcsec entrance slit of ESI used for the observations reported in Quider et al. (2009).

2.5.2 UV inter-stellar absorption lines

The UV spectrum of a SFG, in the wavelength range between 1100 Å and 3000 Å, is characterized by strong absorption lines, which originate from absorption of the stellar radiation by the interstellar medium (ISM) surrounding the regions of intense star-formation. These lines come from different elements, predominantly carbon, silicon, and iron, at different ionization stages. Some of them are the result of the combination of various mechanisms, such as stellar winds, in addition to the interstellar component, and therefore their profiles may be quite complicated to analyse (see chapter 6 for further details). As previously said, a common property of these lines is that they have been found to be blue-shifted to velocities of about ~ 100 km/s, with respect to the galaxy rest-frame, in the spectra of galaxies in the local universe as well as at higher redshifts, suggesting that the gas is flowing out from the galaxy.

The study of outflows in $z > 1$ objects to date has relied primarily on composite spectra. The measurement of the outflow velocity requires a very high precision in the determination of the systemic redshift of the galaxy. In the wavelength range where the ISM

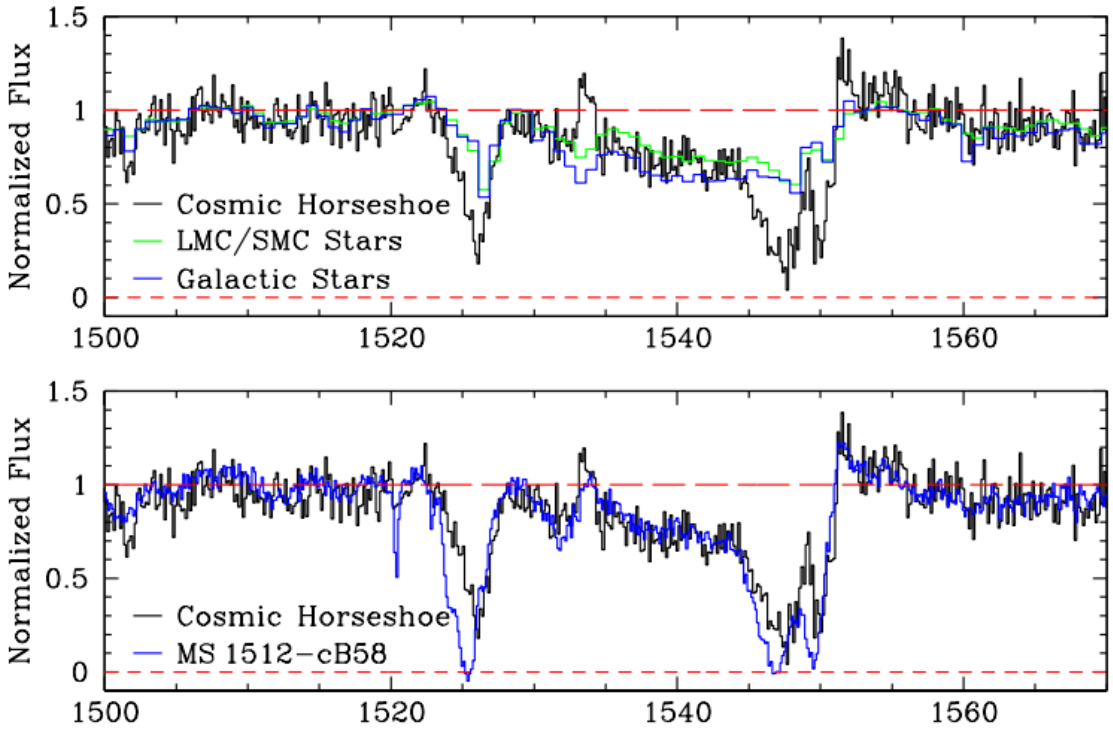

Fig. 2.14: Reproduced from Quider et al. (2009): Upper panel: Comparison between the ESI spectrum of the Cosmic Horseshoe in the region encompassing the C IV line and model spectra computed with *Starburst99* and empirical libraries of Galactic and Magellanic Clouds stars, as indicated. The model spectra were generated assuming a 100 Myr old continuous star formation episode with a Salpeter IMF. Lower panel: The stellar spectra of the Cosmic Horseshoe and of MS 1512-cB58 are remarkably similar in the wavelength region shown. The ESI spectrum of cB58 is reproduced from Pettini et al. (2002), and has been reduced to its rest wavelengths. The systemic redshift of the Cosmic Horseshoe spectrum is $z_{star} = 2.38$.

absorption lines are found (between 1000 and 3000 Å), where there are no strong nebular lines, the systemic redshift has to be determined from stellar absorption lines, that are too weak to be reliably measured in single spectra. Hence the need to use stacking techniques. However, some studies have also been conducted on lensed single objects (Pettini et al. 2000, 2002; Quider et al. 2009, 2010) (Fig. 2.13, 2.14).

The equivalent width (EW) of UV inter-stellar absorption lines has been found to be correlated with several galaxy properties (Heckman et al. 1998; Shapley et al. 2003; Weiner et al. 2009); in particular, the lines are stronger in galaxies characterized by higher SFRs, higher masses, and higher dust extinctions, but it is not yet clear on which property the outflow parameters are most strongly dependent. Shapley et al. (2003) also found a

correlation between the EW of low-ionization lines, the EW of Ly$_\alpha$, and other spectral properties of Lyman Break Galaxies (LBGs): LBGs with stronger Ly$_\alpha$ emission have bluer UV continua, weaker low-ionization interstellar absorption lines, smaller kinematic offsets between Ly$_\alpha$ and the interstellar absorption lines, and lower star-formation rates (Fig. 2.15).

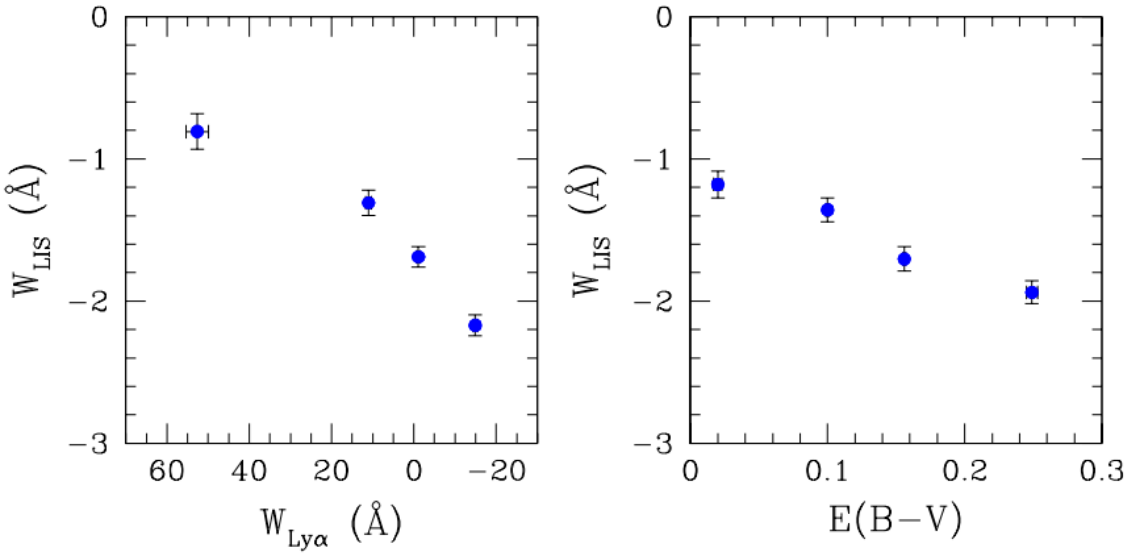

Fig. 2.15: Reproduced from Shapley et al. (2003): the dependence of low-ionization interstellar absorption strength, W_{LIS}, on both Ly$_\alpha$ equivalent width and dust reddening. These plots show the results of dividing LBG spectroscopic sample into quartiles, according to either Ly$_\alpha$ equivalent width (left) or E(B-V) (right).

The UV interstellar absorption lines have been shown to be saturated, hence they cannot be used to infer chemical abundances (though, in some cases, lower limits to the column density can be estimated). Heckman et al. (1998) pointed out that, in the case of a saturated line, the EW is only weakly dependent on the ionic column density, and more strongly dependent on the velocity dispersion of the absorbing gas. Therefore, the correlation between EW and dust extinction might imply that the velocity dispersion in the absorbing gas is larger in galaxies with higher dust extinction. By analysing the Na $\lambda\lambda 5890, 5896$ Å doublet in 32 far-IR selected galaxies, Heckman et al. (2000) concluded that winds with larger velocity spreads are driven by galaxies with higher SFRs, that contain more dust. Shapley et al. (2003) alternatively proposes that the correlation between the EW of interstellar absorption lines and dust extinction can be more directly explained by considering the covering fraction of dusty clouds.

2.5.3 The structure of star-formation driven winds

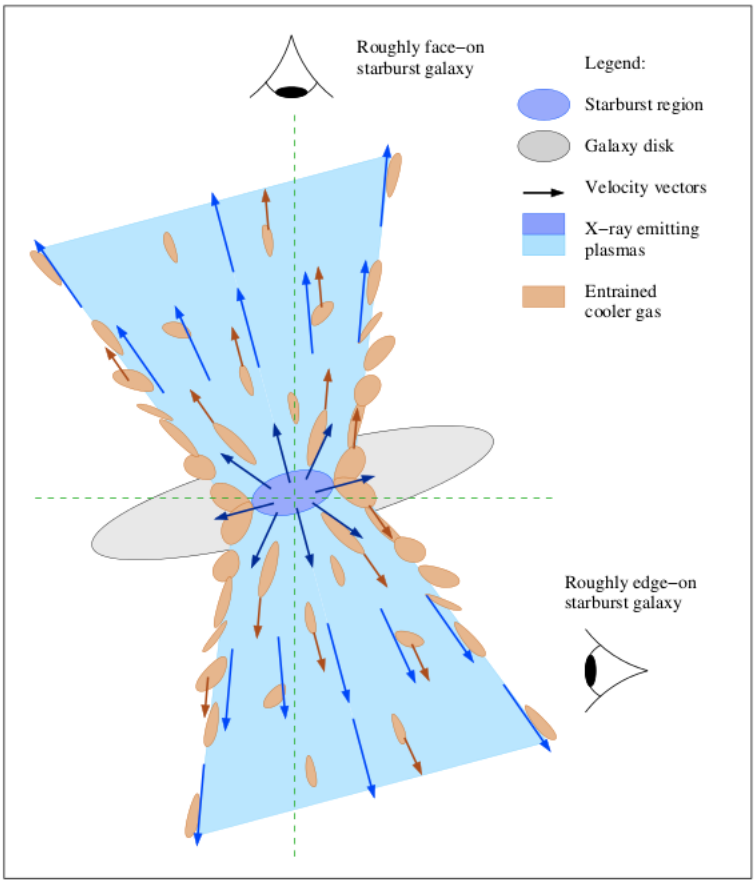

Fig. 2.16: Reproduced from Strickland & Stevens (2000): schematic diagram of a super-wind viewed from different angles, with phase-dependent velocity vectors added to illustrate the line of sight velocity components expected. The combination of galaxy inclination and geometrical divergence within the wind leads to velocity shifts in the line centroids and line broadening or splitting. The resulting velocity components along the line of sight are significant fractions of the intrinsic velocity even in roughly edge-on starbursts. This diagram is simplified in that no acceleration or deceleration or change of geometry of the flow with position is shown.

Different models of galactic-scale winds in SFGs have been proposed over the years (Chevalier & Clegg 1985; Tenorio-Tagle et al. 1999; Strickland & Stevens 2000; Nath & Silk 2009; Strickland et al. 2009; Steidel et al. 2010), but a general consensus remains to be found. It is generally accepted that galactic-scale winds originate in the disruption of bubbles of hot gas, created by a combination of the effects of supernovae and stellar winds in actively star-forming regions. Galactic winds are also believed to have a multi-phase gas structure, in principle providing observables at all wavelengths from X-ray to

optical. The blue-shifted absorption features that can be found in the wavelength range between 1100 Å and 3000 Å, originate in the warm phase of the outflow. The hot phase ($10^7 - 10^8$ K), emitting in the X-ray regime, is the "engine" of the wind and carries most of the energy. The precise role of the warm phase in the general structure of a galactic-scale outflow remains unclear. In some models, the expanding hot gas entrains fragments of the cooler ambient gas, leading to the formation of clouds moving at lower velocities than the main flow, in which the UV blue-shifted absorption lines originate (Fig. 2.16). In other models, the UV lines originate in ambient gas pushed by the expanding bubble in the pre-wind phase. It is uncertain whether the gas, though flowing out from the galaxy, is able to reach the IGM or whether it is instead trapped in the extended haloes and then accreted back onto the galaxy. To help discriminate between the different models, X-ray observations would be useful. Evidence of out-flowing gas has often been detected in SFGs, but only in the UV and optical regimes.

For a comprehensive review of galactic winds, see Veilleux et al. (2005).

CHAPTER 3

The sample

In this chapter, the data sample used in this study is presented. After a brief description of the surveys from which the different wavelengths data were taken, the selection criteria used to select the final sample for each of the performed analyses will be reviewed.

3.1 Data description

The core of our data was the photometric catalogue of the Galaxy Mass Assembly ultra-deep Spectroscopic Survey (GMASS survey). The GMASS spectroscopic sample was expanded thanks to the publicly available spectra of other spectroscopic campaigns in the GOODS-South. The photometric information available in the GMASS field extends from U band to 500 μm band, with data coming from both ground-based and space-based telescopes. Finally, imaging from HST-ACS and HST-WFC3/IR in the GMASS field was used too in the analyses.

3.1.1 The GMASS survey

The GMASS[3] survey is an ESO VLT large program project based on data acquired using the FOcal Reducer and low dispersion Spectrograph (FORS2) (Kurk et al. 2013). The project's main science driver is to use ultra-deep optical spectroscopy to measure the physical properties of galaxies at redshifts $1.5 < z < 3$.

The first step in the definition of the sample was to define a region of 6.8×6.8 arcmin^2 (matching the field of view of FORS2) in the GOODS-South public image taken at 4.5μm with the *Infrared Array Camera* (IRAC) mounted on the *Spitzer Space Telescope* (Fig. 3.1). The sample included all the sources with $m_{4.5} < 23.0$ (AB system).

[3]GMASS public data release: http://www.mpe.mpg.de/~kurk/gmass/

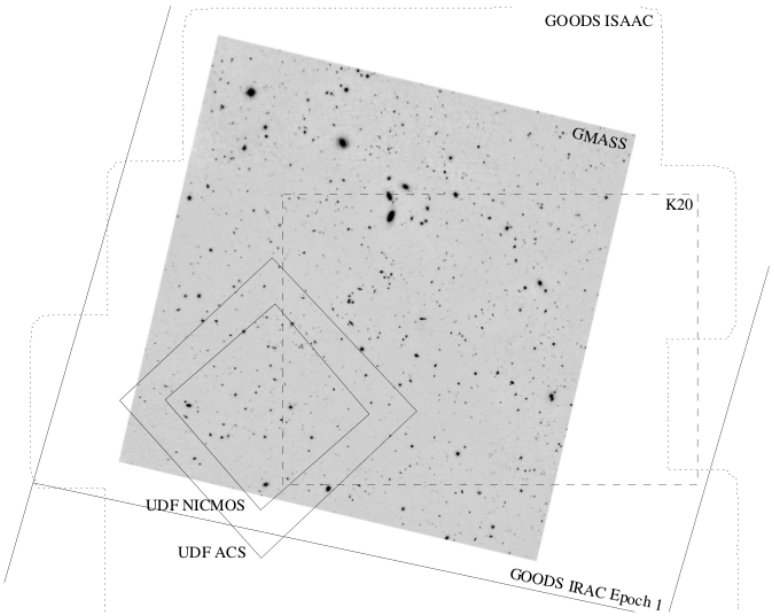

Fig. 3.1: Reproduced from Kurk et al. (2013): location of the GMASS field (greyscale, Ks band) compared to other fields (K20, dashed) and instrument imaging (UDF NICMOS and ACS, diamonds; GOODS ISAAC, dotted; GOODS IRAC, large rectangular, with Epoch 1 indicated) coverages. North is up, east to the left.

The choices of photometric band and limiting magnitude were imposed by several considerations. Among the IRAC bands, the 4.5μm one provides the optimal compromise in terms of sensitivity, PSF, and image quality. In addition, it samples the rest-frame near infrared up to $z \sim 3$, thus allowing a selection that is more sensitive to stellar mass. This is also the band into which the rest-frame 1.6 μm peak of the stellar SEDs is redshifted for $z > 1.5$. The limiting magnitude was mainly dictated by the observational constraints imposed by the spectrograph, in particular by the number of available slits with respect to the surface density of targets at $z > 1.4$ detected in the field. Moreover, at $m_{4.5} < 23.0$ the selection is sensitive to stellar masses down to $\log(M/M_{\odot}) \approx 9.8$, 10.1, and 10.5 for $z = 1.4$, 2, and 3, respectively. This ensures that it is possible to investigate the evolution of the galaxy mass assembly for a wide range of masses. The photometric selection led to the construction of a catalogue of 1277 objects, the *GMASS total sample*. From this catalogue, 221 objects with photometric redshift $z_{phot} \geq 1.4$ were selected as targets for ultra-deep spectroscopy. The total allocated observational time (145 hours) was distributed over six masks: three observed through the 300V grism (the blue masks) and three observed through the 300I grism (the red masks).

Among the 221 objects, 170 could be placed in the masks. To fill the masks, we also

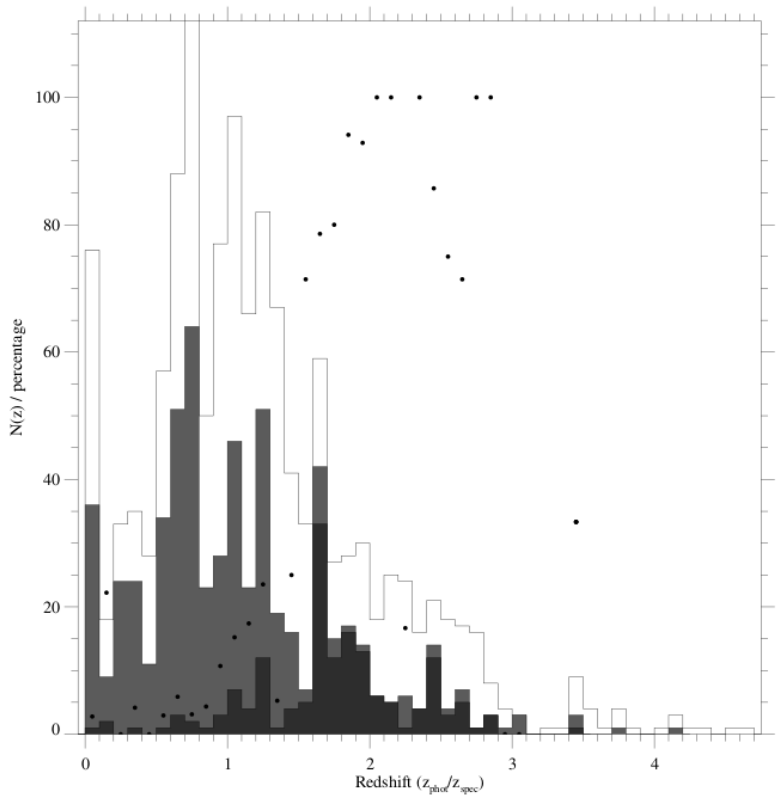

Fig. 3.2: Reproduced from Kurk et al. (2013): histogram of redshifts in the GMASS catalogue. The open histogram represents photometric redshifts. The light grey histogram represents archive spectroscopic redshifts in the GMASS field, while the dark grey histogram represents secure spectroscopic redshifts from the GMASS survey. The dots indicate the percentage of secure redshifts determined by the GMASS survey.

observed objects not included in the spectroscopic target list, obtaining a final *GMASS spectroscopic sample* of 250 unique objects. To ensure the feasibility of the spectroscopy, it was necessary to set magnitude limits B < 26.0 and I < 26.0 for the blue and red masks, respectively. The assignment of each object to either category was made according to colours and photometric redshifts: red objects at intermediate redshift ($(z - K) \geq 2.3$, $z_{phot} \leq 2.5$) were listed as primary targets to be included in the red masks, while objects that are blue ($(z - K) < 2.3$) or have UV absorption lines that have been redshifted into the optical domain ($z_{phot} > 2.5$) were allocated as primary targets for the blue masks. The actual wavelength coverage for a certain slit depends, apart from the grism and order separation filter, on its position in the mask in the dispersion direction. The maximum wavelength range covered for central slits was 3300-6500 Å for the blue masks and 6000-11000 Å for the red masks. To be able to include enough background for subtraction of the sky, minimum slit lengths were constrained to be 9″ and 8″ for the

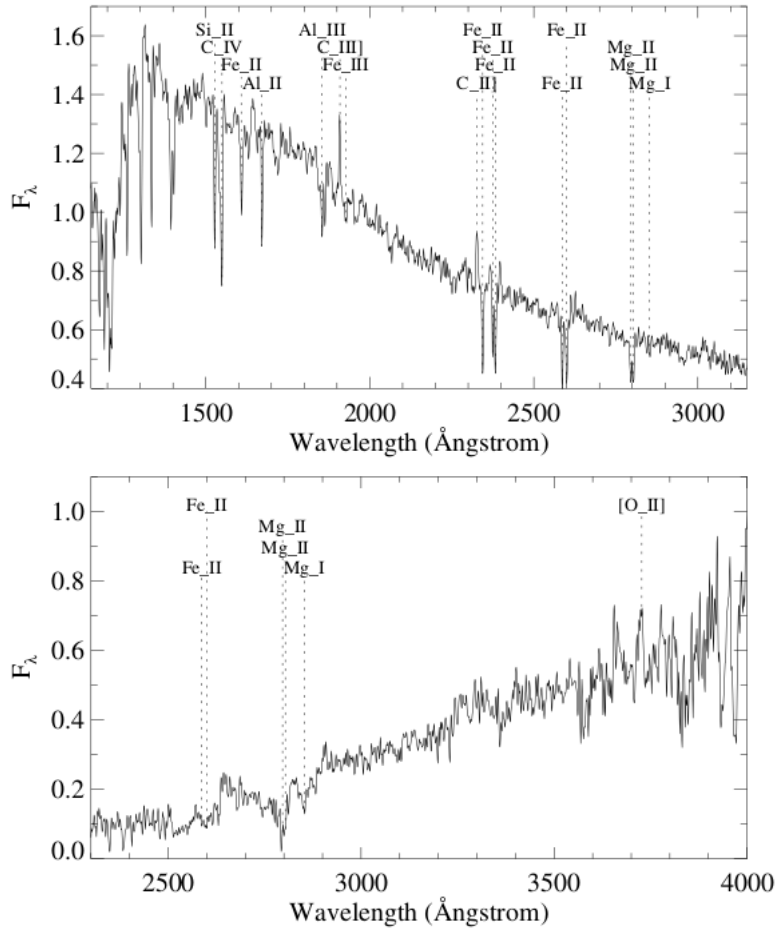

Fig. 3.3: Reproduced from Kurk et al. (2013): rest-frame composite spectra of galaxies in the blue (top) and red (bottom) masks. The most important absorption lines and one emission line ([O II]λ3727) are indicated. Note the clear difference in slope and strength of the FeII and MgII, MgI absorption lines.

red and blue masks, respectively, while the slit width was 1″ for both the grisms. Fig. 3.3 shows rest-frame composite spectra of galaxies in the blue and red masks. The spectral resolution of $\lambda/\Delta\lambda \approx 600$ was chosen because of the large wavelength coverage that it provides and is high enough to enable us to resolve and identify spectral features for redshift determination. In total, it was possible to determine secure spectroscopic redshifts for 131 objects included in the spectroscopic target list, and for another 16 galaxies we obtained at least a redshift estimate (Fig. 3.2).

The GMASS photometric catalogue includes optical and NIR data derived from publicly available images provided by several institutes. The ground-based data includes observations in the U, B, V, R, I, J, H, and Ks bands, some provided by ESO as part of its

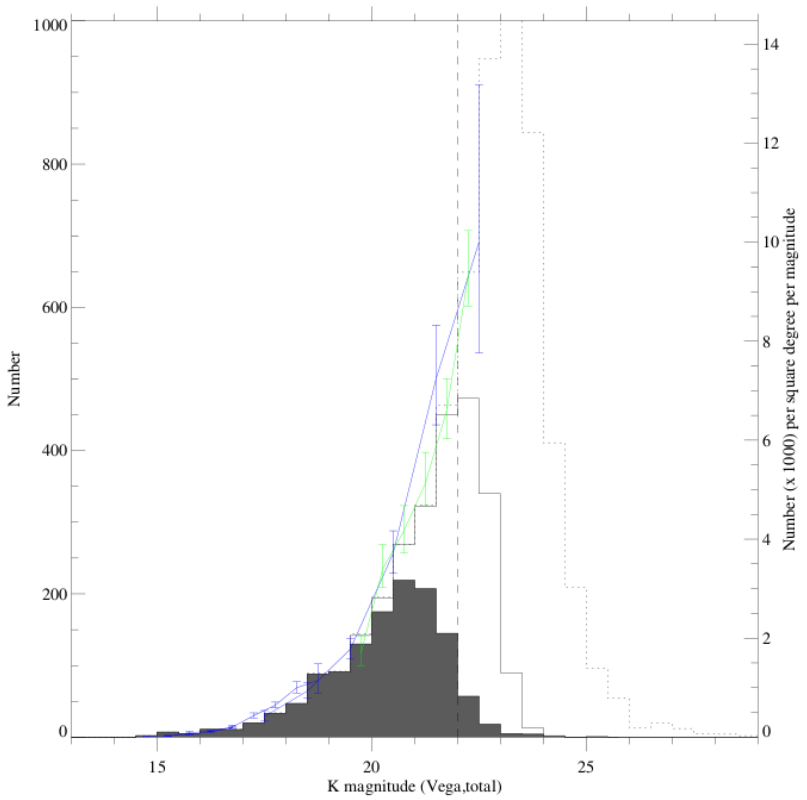

Fig. 3.4: Reproduced from Kurk et al. (2013): K band counts for the 49.75 arcmin^2 GMASS field. Also indicated on the right-hand axis are counts/mag/arcmin^2 . The solid histogram is for the 3.3σ K band catalogue, while the dashed histogram is for the (faint) 2.2σ catalogue. The filled histogram indicated which objects are in the GMASS catalogue (i.e., are counterparts of an unblended 4.5 μm source). The vertical dashed line indicated the completeness limit for the 3.3 σ catalogue. Further details may be found in Kurk et al. (2013).

participation in the GOODS project. The space-based data includes optical observations taken with the Advanced Camera for Surveys (ACS) and NIR observations taken with the Near Infrared Camera and Multi Object Spectrometer (NICMOS), both aboard the Hubble Space Telescope (HST). To construct the final multi-band catalogue, i.e. the GMASS photometric catalogue, covering wavelengths from the UV to the MIR, the optical-NIR catalogue and the IRAC catalogue were combined by matching both catalogues. Fig. 3.4 shows the K band counts for the GMASS field. For further details about the photometric ancillary data, we invite the reader to refer to the Kurk et al. (2013) paper.

The physical properties of the galaxies belonging to the entire GMASS total sample were estimated by fitting different sets of evolutionary population synthesis models to broad-band SEDs (extending from U band to the IRAC 8μm band) derived from photometric

data. In particular, we used the results obtained with the synthetic spectra of Maraston (2005), adopting a Kroupa IMF (Kroupa 2001) and fixed solar metallicity. Star-formation histories were parametrized by exponentials ($e^{\frac{-t}{\tau}}$) with e-folding time-scales τ of between 100 Myr and 30 Gyr, plus the case of constant SFR. For the dust extinction, a Calzetti law (Calzetti et al. 2000) was assumed.

3.1.2 Other spectroscopic data in the CDF-S

The non-GMASS spectra were selected from the ESO-GOODS/FORS2 v3.0 (Vanzella et al. 2008) and ESO-GOODS/VIMOS 2.0 (Popesso et al. 2009; Balestra et al. 2010) surveys, the VVDS v1.0 (Le Fèvre et al. 2005) survey, and the K20 (Mignoli et al. 2005) survey, through the compilation of GOODS/CDF-S spectroscopy master catalogue (v2.0), from the ESO website. The first two surveys are part of the ESO-GOODS spectroscopic campaign, that was carried out with FORS2 and VIMOS (VIsible Multi-Object Spectrograph) at the VLT. FORS2 observations have a limiting AB magnitude of ∼26 in the z band and an observed resolution of R ∼660. For the VIMOS survey, two grism have been used: a low-resolution blue grism (LR), providing an observed R ∼180, for galaxies with magnitudes of ∼24-25 in the B band, and a medium-resolution orange grism (MR), R ∼580, for galaxies with a limiting magnitude of ∼24-25 in the R band. Other VIMOS spectra come from the VIMOS VLT Deep Survey (VVDS), targeting galaxies with $17.5 \leq I_{AB} \leq 24$ with an observed R ∼230. Finally, the K20 survey is a near infrared selected survey targeting galaxies as faint as K_s ∼20. The observed resolution of the spectra is R ∼260, 380, 660, depending on the grism.

3.1.3 The CANDELS survey

The Cosmic Assembly Near-IR Deep Extragalactic Legacy Survey (CANDELS; see Grogin et al. (2011); Koekemoer et al. (2011)) is a 902-orbit Multi-Cycle Treasury program on the HST. The project aims at document galaxy evolution up to redshift z ∼8 using deep imaging data collected with the IR and UVIS channels of the WFC3, together with the ACS. Two different mini-surveys are planned to target five existing survey fields on the sky, more specifically the CANDELS/Deep survey covers ∼130 arcmin^2 within GOODS-N and GOODS-S, while the CANDELS/Wide survey covers a total of ∼720 arcmin^2 in GOODS, COSMOS, EGS and UKIDSS/UDS. The survey is still ongoing. Science

drizzled images, along with weight images, are being publicly released as long as the observations are carried on. The exposure depth in the two WFC3/IR filters, F125W (J band) and F160W (H_{160}), is of 1000s and 1100s, respectively, while the PSF FWHM is 0".12 and 0".18. At the time this work was carried out, the most recent releases in the GOODS-S field were the Deep epoch 6 images.

3.1.4 The PEP-HerMES merged catalogue

The GOODS-South field has been observed with the Photodetector Array Camera and Spectrometer (PACS; Poglitsch et al. (2010)) on board the Herschel Space Observatory as part of the PACS Evolutionary Probe (PEP; Lutz et al. (2011)). PEP is a Herschel guaranteed time key programme survey of the extragalactic sky, aimed to study the rest-frame far infrared emission of galaxies up to redshift $z \sim 3$, as a function of environment. With 5σ depths for prior extraction of 1.8 mJy, 1.9 mJy, and 3.3 mJy at 70 μm, 100 μm, and 160 μm, respectively, GOODS-S is the only PEP field to be imaged at 70 μm, and a factor 2.5 - 4.5 deeper than the other PEP blank fields at 100 μm and 160 μm. For an in depth description of the observations, data reduction, and catalogue building, we refer to Berta et al. (2010) and Lutz et al. (2011). The PACS photometry used in this work was obtained by point-spread function fitting using the positions of MIPS 24 μm detected sources from Magnelli et al. (2009) as priors. Adopting this positional prior reduces the effects of confusion and is justified by the relative depths of the MIPS and PACS imaging.

HerMES is the Herschel Multi-tiered Extragalactic Survey, an astronomical project to study the evolution of galaxies in the distant Universe. It is the largest project on ESA's Herschel Space Observatory, and consists of a survey of many well-studied extra-galactic fields at various depths (Oliver et al. 2010). The observations that are part of the HerMES program were carried out using the Spectral and Photometric Imaging REceiver (SPIRE). The SPIRE instrument, its in-orbit performance, and its scientific capabilities are described by Griffin et al. (2010), and the SPIRE astronomical calibration methods and accuracy are outlined in Swinyard et al. (2010).

On SPIRE maps made using 250, 350 and 500 μm filters, photometry has been performed by using the known positions of 24 μm sources as a prior, thus leading to the creation of a PEP-HerMES merged catalogue (version 1.0; not public) that contains MIPS 24 μm, PACS 70, 100, and 160 μm, SPIRE 250, 350 and 500 μm fluxes.

3.2 Selection criteria: the final samples

Since the aim of this work is to study galaxies at high-redshift, only galaxies at $z \geq 1$ were selected for the analysis. This *GMASS high-z sample* counts 761 objects, whose redshift is either photometric (596 objects) or spectroscopic, from the *GMASS spectroscopic catalogue* (165 objects).

The compilation of GOODS/CDF-S spectroscopy master catalogue (v2.0), from the ESO website, was used to search for spectra of the galaxies listed in the *GMASS high-z sample*, but with no GMASS spectrum taken. Through a nearest algorithm, coordinates from the master catalogue and the GMASS catalogue were matched, and sources within 1" angular separation were selected. When more than one spectrum was available, the one with the highest reliability redshift flag was taken. Also GMASS sources with a photometric redshift $z_{phot} < 1$ where checked, to ensure not to loose $z \geq 1$ galaxies with an incorrect photometric redshift. The total number of galaxies with an available spectrum is 407, the *extended GMASS spectroscopic high-z sample*. All the spectra not belonging to the GMASS survey were re-classified, and their redshifts were checked. Table 3.1 summarizes the distribution of spectra from the different surveys.

Table 3.1: *Extended GMASS spectroscopic high-z sample*: number of spectra collected from the different surveys.

*G*MASS	ESO-FORS2	VIMOS$_{LR}$	VIMOS$_{MR}$	VVDS	K20
165	120	45	14	16	47

The photometric information from U band to the IRAC 8.0 μm band, in the *GMASS photometric catalogue*, was extended up to observed 500 μm band. The *extended GMASS spectroscopic high-redshift sample* catalogue was matched to the MIPS 24 μm source list in the GOODS-S by Magnelli et al. (2011) (see also Magnelli et al. (2009)), with a nearest algorithm. GMASS catalogue positions come from Ks band images, while IRAC 3.6 μm positions were used by Magnelli et al. (2011). We found 196 24 μm counterparts for our galaxies, all of them with a flux $S/N \geq 3$, within an angular separation of 1.4". This angular separation was chosen as the most conservative not to lose real counterparts, while minimizing the selection of false pairs. Available PEP-PACS fluxes (70, 100 and 160 μm) and HerMES-SPIRE fluxes (250, 350, 500 μm), from the PEP-HerMES merged catalogue (version 1.0), obtained using the positions from the MIPS 24 μm source list by Magnelli et al. (2011) (see also Magnelli et al. (2009)) as priors, were then added

to our catalogue. We also supplemented our catalogue by adding 52 more MIPS 24 μm counterparts with flux $S/N \geq 3$ (Daddi, private communication), not present in the MIPS 24 μm source list by Magnelli et al. (2011) and therefore with no HERSCHEL detection. Finally, IRS 16 μm fluxes from the catalogue by Teplitz et al. (2011) were also added for a sub-sample of galaxies. Only detections with a significance limit $S/N > 3$ were added to the catalogue. Table 3.2 summarizes the number of detections for each of the eight IR bands available (from IRS, MIPS and HERSCHEL). 91 out of 407 galaxies have at least a detection in one of the six HERSCHEL bands.

Table 3.2: *Extended GMASS spectroscopic high-z sample*: number of detections for each IR photometric band.

16 μm	24 μm	70 μm	100 μm	160 μm	250 μm	350 μm	500 μm
74	248	18	60	77	21	11	4

For all objects in the *GMASS high-z sample*, images from the Advanced Camera for Surveys (ACS) mounted on the Hubble telescope are available (Giavalisco et al. 2004). In addition, cutouts for 494 objects included in the *GMASS high-z sample* were extracted from the most recent available public images obtained with the HST-WFC3 in the H_{160} band, within the CANDELS survey (the *GMASS-wfc3 sample*).

Summarizing, these are the samples to which we will refer in this thesis:

1. *GMASS high-z sample*: 761 galaxies with $z_{phot/spec} \geq 1$, U band to IRAC 8.0 μm band photometry, and HST-ACS imaging;

2. *extended GMASS spectroscopic high-z sample*: 407 galaxies with $z_{spec} \geq 1$, and U band to IRAC 8.0 μm band photometry; some of them also have IRS 16 μm band to HERSCHEL-SPIRE 500 μm band photometry;

3. *GMASS-wfc3 sample*: 494 galaxies with $z_{phot/spec} \geq 1$, HST-ACS imaging, and HST-WFC3/IR imaging.

CHAPTER 4

Morphologies

4.1 Introduction

In this chapter, the rest-frame optical morphology of galaxies at intermediate to high redshift will be studied, using the most recent IR images from HST/WFC3-IR, which sample the rest-frame optical regime, in order to relate the morphological features to the physical properties of the galaxies, such as mass and star-formation rate.

First the galaxies of our sample will be visually classified and the basic morphological statistics (C-A and G-M_{20}) will be computed. Information about the galaxies physical properties, drawn from SED fitting to broad-band photometry, will be used to link the star-formation status of our sample of galaxies to the different morphological types. A visual classification and morphological parameter calculation, performed for rest-frame UV images of our sample, will be compared with rest-frame optical to investigate the morphological *k*-correction issue at redshift $z > 1$. Then we shall study how morphologies fit into the well established bimodal colour distribution of galaxies, by examining the colour-mass diagram.

4.2 The data sample

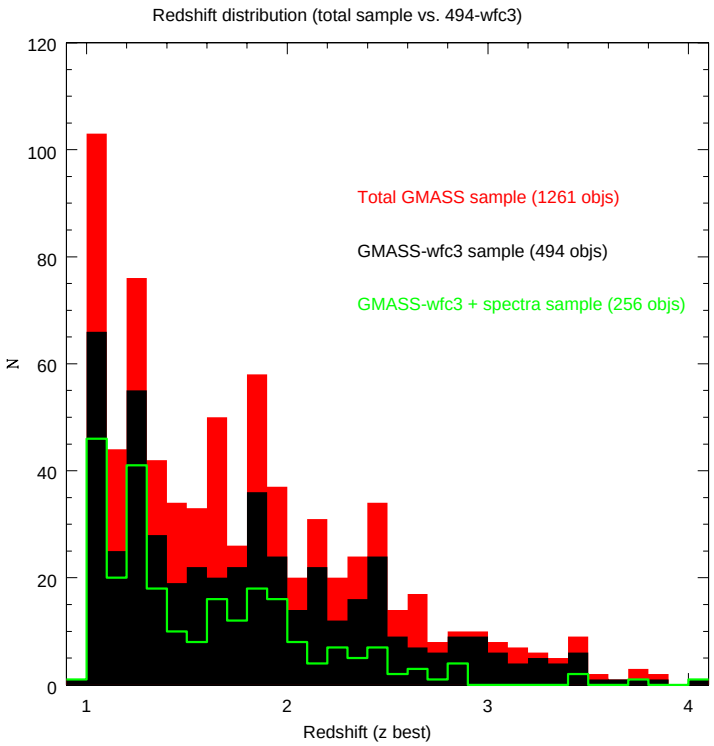

Fig. 4.1: Redshift distribution. The red histogram represents best-redshift (spectroscopic or photometric) distribution of the GMASS sample at $z \geq 1$; the black histogram represents best-redshift distribution of the 494 galaxies from the *GMASS-wfc3 sample*; the green histogram represents spectroscopic redshift distribution of the 257 galaxies from the *GMASS-wfc3 spec sample*.

The morphological analyses was performed on a galaxy sample drawn from the *photometric catalogue* of GMASS. The GMASS field partially overlaps the CANDELS field. Cutouts for 494 objects at $z > 1$ were extracted from the most recent available public images in the H_{160} band (6th epoch). These sample, that has been already introduced in chapter 3, will be referred to as the *GMASS-wfc3 sample*, from now on.

For all the objects of the photometric GMASS catalogue, images from the Advanced Camera for Surveys (ACS) mounted on the Hubble telescope are also available (Giavalisco et al. 2004).

Fig.4.1 shows the redshift distribution of the *GMASS-wfc3 sample*. Fig.4.2 shows the rest-frame wavelength probed by the four ACS and two WFC3-IR filters, as a function of redshift: at $z > 1$, ACS and WFC3 images may be used to study the structures of galaxies

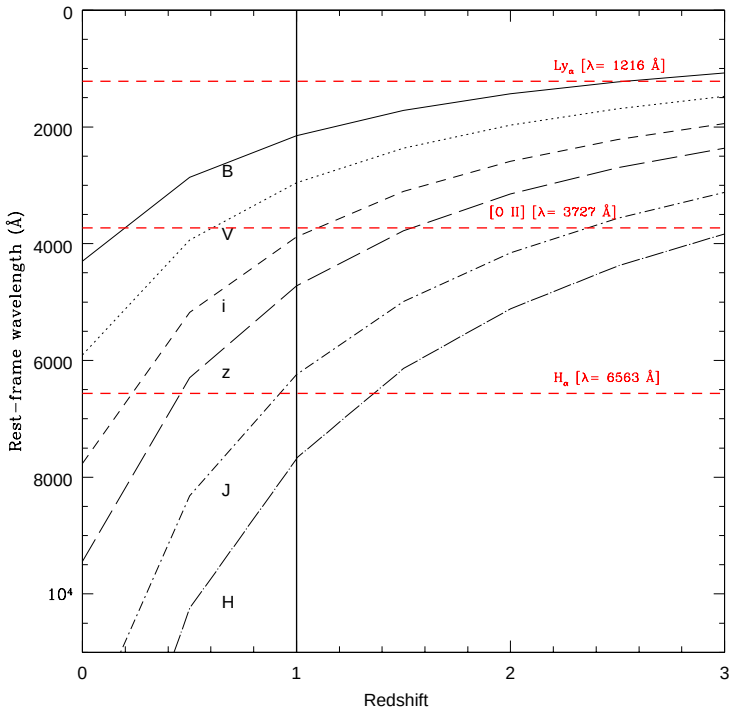

Fig. 4.2: The rest-frame wavelength probed by the four ACS and the two WFC3-IR filters, as a function of redshift. The vertical line indicates the redshift cut applied to our sample of galaxies, while horizontal red lines mark the wavelength of three UV and optical spectroscopic lines: Ly$_\alpha$, [OII] and H$_\alpha$.

in two distinct wavelength regimes, UV and optical, respectively.

4.3 Visual morphological analysis

The morphological analysis of H_{160} images was done using two different methods: a visual classification was done, following traditional Hubble types, and a quantitative analysis, using parameters that quantify the concentration of light and the galaxy asymmetry. The sample was divided into five main types, based on the appearance of our galaxies in the H_{160} band imaging.

Table 4.1: Visual morphological classification: number of galaxies for each type.

Ellipticals	Compact	Disk-like	Irregulars	(Multiples)	Faint Objects
75	36	157	199	(68)	27

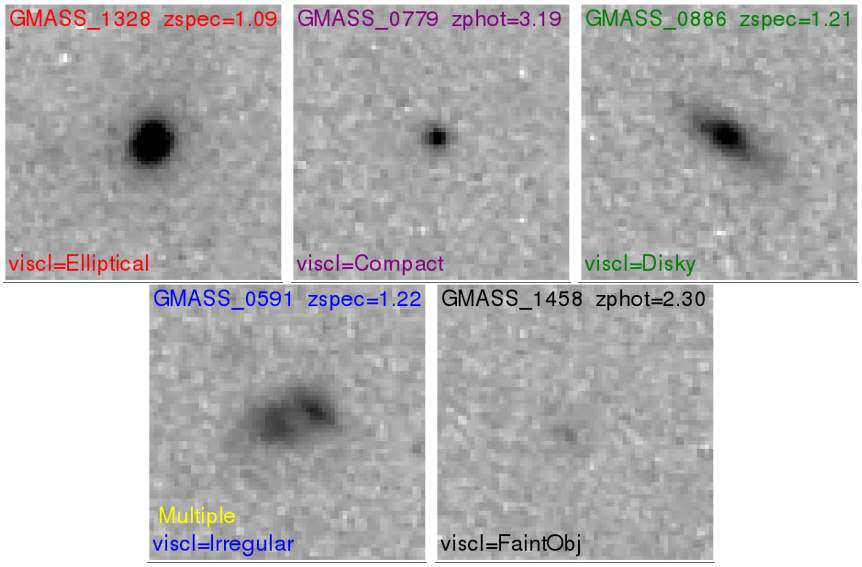

Fig. 4.3: Sample snapshots of galaxies to illustrate the visual classification scheme.

Ellipticals: single centrally concentrated source with no evidence for low surface brightness, outer structures. In this category were also included galaxies defined as *peculiar ellipticals* by some authors (Conselice et al. 2011), i.e. galaxies that appear elliptical but have some minor morphological peculiarity, such as offset isophotes or low surface brightness asymmetries in their outer parts.

Compact: single centrally concentrated source, very smooth and symmetric, without evidence of any substructure. Similar to the elliptical classification, it differs from it in that a compact galaxy contains no features such as an extended light distribution or a light envelope.

Disk-like: undisturbed source with a disk-like shape.

Irregulars: galaxy morphology that does not fall in any of the previous classes. These systems are possibly in some phase of a merger (Conselice et al. 2003). Some of them show evidence of two or more distinct nucleated sources of comparable magnitude. These galaxies were sub-classified as *Multiples*.

Faint objects: objects too faint to allow any reliable classification.

It should be stressed that the classification by eye is based only on appearance as seen in the observed H_{160} filter: no additional information such as colour, optical spectrum, mass, SFR was used to assign a morphological type to a galaxy. Fig. 4.3 shows sample snapshots of galaxies to illustrate the classification scheme, while Table 4.1 summarizes

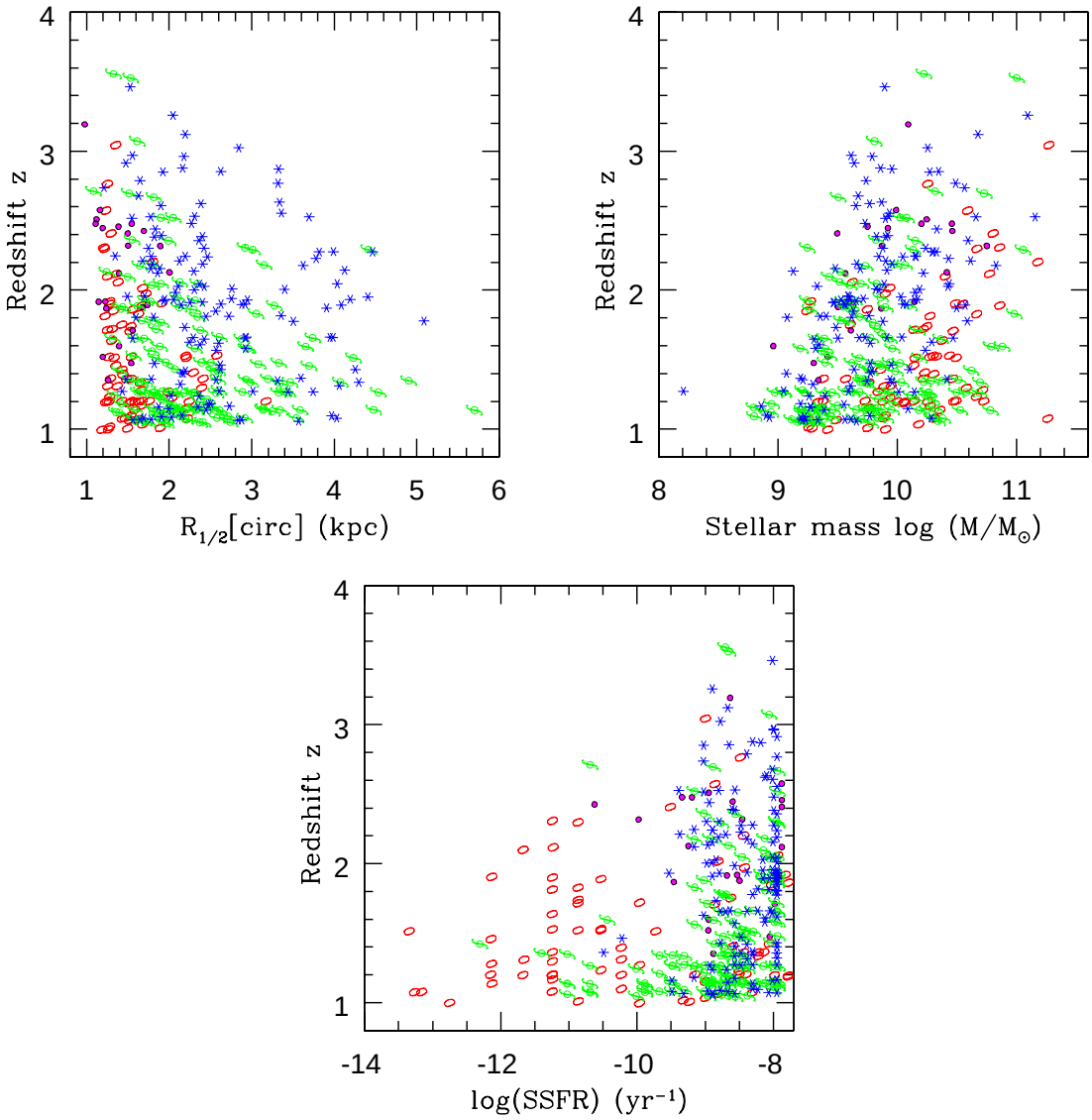

Fig. 4.4: Clockwise, from upper left: Half-light radius (computed on WFC3-IR H_{160} images), stellar mass, and sSFR as a function of the redshift. Points colours and shapes are as in Fig. 4.5 legend. Only galaxies with a visual classification, i.e. not classified as *Faint objects*, and a signal-to-noise ratio $S/N > 50$ are plotted.

the number of galaxies in each class. A morphological atlas with all the 494 galaxies of the sample is presented at the end of this chapter.

The various physical properties in different morphological class are plotted in Fig. 4.4 as a function of redshift. The stellar mass and SFR were computed through a SED fitting

procedure, as described in Chapter 3. Galaxies classified as *Faint objects* are not plotted. The half-light radius $R_{1/2[circ]}$ is used as a measure of the physical size of our galaxies. $R_{1/2[circ]}$ is the radius of the ellipse enclosing the 50% of the total flux of the galaxy: it was derived from the curve of growth and then circularized ($R_{1/2[circ]} = R_{1/2[ell]} \sqrt{(b/a)}$, where b/a is the minor/major-axis ratio)[4]. Looking at the entire sample, we see that typical sizes of the ellipticals range between 1 and 2.5 kpc, while disks and irregulars go up to $\sim$ 5 kpc. It is interesting to notice that irregular and compact galaxies do not show an evolution in size with redshift. On the other hand, disks at redshift $z > 2$ appear to be, on average, smaller than at lower redshift, as well as ellipticals at redshift $z > 1.5$.

For what concerns the correspondence between visual morphological types and the star-formation modes of galaxies, Fig. 4.4 shows that galaxies with little to no sign of star-formation have quite a defined morphology, almost all of them being ellipticals, though a fraction also show a disk-like appearance. Galaxies with higher sSFR ($log(sSFR) > -10$ yr^{-1}), on the other hand, display a wider range of morphologies; in particular, almost all irregular galaxies have $log(sSFR) \gtrsim -9$ yr^{-1}. We can conclude that non-SFGs at $z > 1$ are generally ellipticals (with some disk-like exceptions), while an irregular morphology is synonymous of a galaxy experiencing an intense episode of star-formation. There is also a broad distribution of types over the entire stellar mass range of our sample of galaxies, as observed also by Conselice et al. (2011) in the HST-UDF, though it can be seen that the largest fraction of irregulars have the lowest masses $M_{\odot} < 10^{10}$.

4.3.1 Fraction of morphological types as a function of redshift

The relative fraction of the different morphological visual types, as a function of redshift, is shown in Fig. 4.5: starting from $z = 1$ and going backward to higher redshifts, the fraction of ellipticals and disks drops, ending with the majority of galaxy population, at redshift $z \sim 2$ and higher, to have an irregular structure. The fraction of compact galaxies, on the other hand, stays quite constant (~ 0.1) between redshift 1 and 3, and has a peak around $z \sim 2.5$. The sub-category of *Multiple* follows the same trend of irregulars, growing going back in time, and with a peak at $z \sim 3$.

Comparing these trends with the literature, we can explore the full range of redshift, down to $z \sim 0$: below the limit of our sample, $z < 1$, disks and spheroids are the dominant

[4]To avoid confusion, please notice that this radius basically comes from aperture photometry, and is not the effective radius derived from models by fitting the light distribution with a given function.

population, with about 20% of irregulars (Conselice et al. 2005). At redshift $z \sim 1 - 1.5$, the fraction of irregulars and compact starts to grow, while disks and ellipticals fractions go down (Conselice et al. 2005; Conselice et al. 2008). Though the trends are generally similar, the relative fraction of each morphological type, at high redshift, changes from field to field, probably a selection effect due to different magnitude limits in the various samples.

The general conclusion is that the build up of the Hubble sequence seems to take place around $z \sim 2.5 - 2.7$, when there is still 20% of galaxies that show some regular morphology (elliptical or disky), while at redshifts higher than $z \sim 3$ almost all galaxies have an irregular appearance.

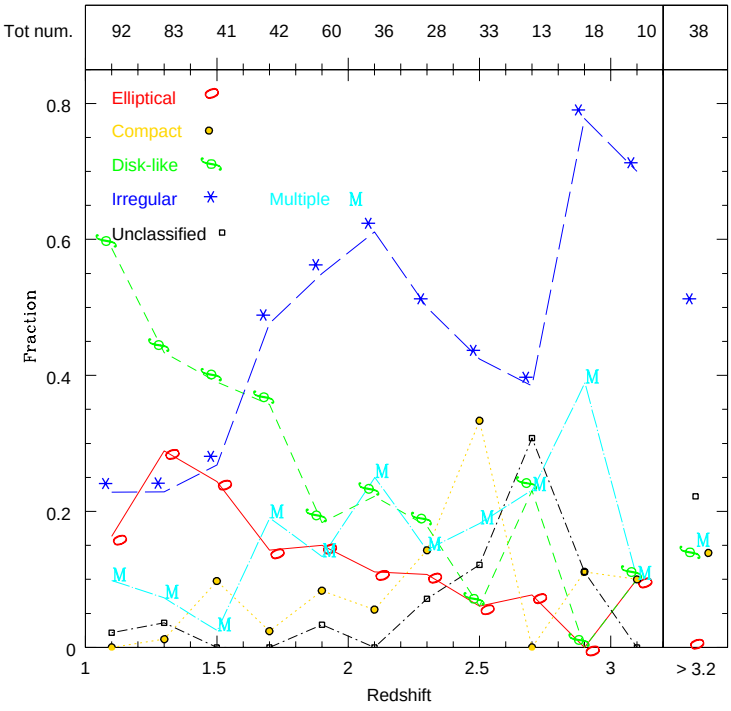

Fig. 4.5: The relative fraction of galaxy morphological types as a function of redshift. In the upper panel the total number of galaxies in each redshift step ($\Delta z = 0.2$) between $z = 1$ and $z = 3.2$ is written. The last step includes all galaxies at $z > 3.2$.

4.4 Quantitative morphological analysis

Another approach for the galaxy morphological classification is to use non-parametric statistics. We concentrated on the four most used parameters: the Concentration C, the rotational Asymmetry A, the Gini coefficient G and the second order moment of the light distribution M_{20}. Another frequently used parameter in the local Universe studies is the smoothness parameter, which has been proved to be not robustly defined for galaxies as small and poorly resolved as high redshift ones (Lotz et al. 2004), and was therefore not calculated here.

4.4.1 The segmentation map

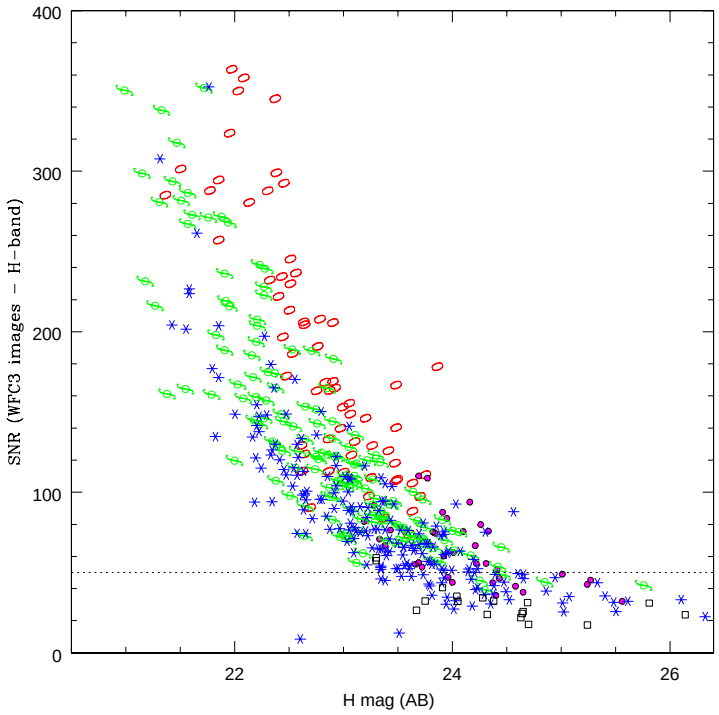

Fig. 4.6: Signal-to-noise ratio of the galaxies as a function of H-band magnitude (taken from the GMASS photometric catalogue). Points are shape and colour coded with respect to the morphological visual class (see Fig. 4.5).

The first procedure in the computation of the morphological parameters is the creation of a segmentation map, i.e. to establish which image pixels actually belong to the analyses galaxy and which ones are background noise. This is not straightforward, especially

when irregular structures are involved, with low surface brightness extended features. The first step is the preliminary selection of pixels belonging to the galaxy, using Source Extractor (Bertin & Arnouts 1996). Then, two methods may be used to refine the segmentation map. Authors like Conselice et al. (2008) and Lotz et al. (2004) apply either a circular or elliptical Petrosian (Petrosian 1976) selection technique to select pixels independent of total galaxy flux. Briefly, the Petrosian selection technique consists in including all pixels within a certain radius, defined as the radius at which the surface brightness is some fraction η of the enclosed surface brightness. On the other hand, Abraham et al. (2007) modified the Petrosian pixel selection method to work also for galaxies whose flux components are not necessarily contiguous. The pixels in the preliminary Source Extractor segmentation map are sorted in decreasing order of flux into an array f_i, which is then used to construct a cumulative flux array. The so-called quasi-Petrosian isophote is then set by determining the pixel index at which the pixel flux is equal to some fraction (called the quasi-Petrosian threshold η) of the cumulative mean surface brightness.

Here we adopt the quasi-Petrosian method of Abraham et al. (2007), with a threshold $\eta = 0.3$, following the prescriptions of Law et al. (2012b) who found this to be the best choice to maximize the advantages of the method. These segmentation maps were also used to compute the curve of growth from which the $R_{1/2[circ]}$ used in the previous section were derived. In this part of the analysis, following the literature, only images with $SNR > 50$[5] were used, since a low S/N does not allow a correct galaxy mapping over the image pixels (Law et al. 2012b). This S/N cut, that roughly corresponds to a cut in H_{160} magnitude: $H_{AB} < 24$ (Fig. 4.6), left out 106 objects from the following analysis.

To allow a rough quantitative comparison of our results with parameters obtained using different segmentation maps, in Table 4.2 we report, for each morphological visual type, the mean values of the four parameters in three different choices of segmentation maps: our own, plus the other two more frequently used in the literature. The change in segmentation maps does not affect significantly the determination of M20 and A, while Gini does. In the rest of this study, when discussing about the comparison of our results with previous works, the different choice of segmentation maps will always be taken into account.

[5] $S/N = F/sqrt(A) * rms$, where F is the total flux of the galaxy, A is the total number of pixels and rms is the average r.m.s. of the background over all sky pixels.

Table 4.2: Boundaries for the total sample (minimum and maximum) and mean values (with r.m.s.) for each morphological type of the morphological parameters, computed using three different choices of segmentation maps[a].

	Minimum	Maximum	Ellipticals	Compact	Disk-like	Irregulars
QP3[b] Concentration	1.53	2.98	2.41 ± 0.19	2.38 ± 0.21	2.24 ± 0.21	2.10 ± 0.20
QP3[b] Asymmetry	0.00	0.58	0.19 ± 0.08	0.17 ± 0.07	0.12 ± 0.06	0.17 ± 0.10
QP3[b] Gini	0.21	0.49	0.41 ± 0.02	0.39 ± 0.03	0.37 ± 0.04	0.34 ± 0.04
QP3[b] M20	-2.29	-0.78	-1.64 ± 0.17	-1.63 ± 0.19	-1.67 ± 0.19	-1.51 ± 0.26
CPL[c] Concentration	1.76	2.98	2.49 ± 0.16	2.47 ± 0.17	2.35 ± 0.17	2.23 ± 0.17
CPL[c] Asymmetry	0.02	0.49	0.18 ± 0.06	0.16 ± 0.06	0.13 ± 0.05	0.16 ± 0.08
CPL[c] Gini	0.18	0.68	0.54 ± 0.04	0.50 ± 0.05	0.47 ± 0.06	0.41 ± 0.07
CPL[c] M20	-2.41	-0.84	-1.74 ± 0.17	-1.72 ± 0.20	-1.76 ± 0.19	-1.60 ± 0.27
CPC[d] Concentration	2.04	3.14	2.71 ± 0.14	2.69 ± 0.16	2.58 ± 0.16	2.47 ± 0.15
CPC[d] Asymmetry	0.00	0.40	0.13 ± 0.05	0.12 ± 0.05	0.09 ± 0.04	0.12 ± 0.07
CPC[d] Gini	0.52	0.77	0.70 ± 0.02	0.68 ± 0.02	0.66 ± 0.03	0.63 ± 0.04
CPC[d] M20	-2.57	-0.94	-1.88 ± 0.18	-1.86 ± 0.21	-1.90 ± 0.20	-1.73 ± 0.29

[a] The default segmentation map used in this study is QP3. We follow the Law et al. (2012b) nomenclature to indicate different segmentation maps and use the relations in their Appendix A.1 to convert QP3 values.

[b] QP3: quasi-Petrosian segmentation map with threshold $\eta = 0.3$ (this work).

[c] CPL: elliptical Petrosian segm. map ($\eta = 0.2$) that includes all pixels with flux grater than the surface brightness at the Petrosian radius (Lotz et al. 2004).

[d] CPC: circular Petrosian segm. map ($\eta = 0.2$) that includes all pixels within 1.5 Petrosian radii irrespective of flux (Conselice et al. 2008).

4.4.2 Parameters definitions

Briefly, these are the definitions of the four morphological parameters that were used in the analysis.

Concentration (C). The concentration index C measures the intensity of light contained within a central region, compared to an outer larger one. Among the mostly used definitions of concentration, here we apply the Bershady et al. (2000) one (see also Conselice et al. (2003)):

$$C = 5log\left(\frac{r_{80}}{r_{20}}\right) \tag{4.1}$$

r_{80} and r_{20} were derived interpolating the curve of growth obtained using 30 aperture radii. A higher value of C indicates that a larger amount of light in a galaxy is contained within a central region.

Asymmetry (A). The asymmetry index was first defined by Schade et al. (1995) as a measure of the asymmetry of a galaxy to a 180° rotation. The mathematical definition is[6]:

$$A = \frac{\sum |I_{0^\circ} - I_{180^\circ}|}{\sum I_{0^\circ}} \tag{4.2}$$

where I_{0° represents flux in the original image pixels and I_{180° flux in the rotated image pixels. The image centre was first taken as the position of the maximum pixel value. Then the rotational centre was determined by iterating the computation of the asymmetry inside a 5x5 pixels box around the image centre, until converging on the point of minimum asymmetry. A correction term must be added to the asymmetry, to remove the background asymmetry. Here we used the statistical correction defined by Lauger et al. (2005). Lower values of A imply that a galaxy is largely symmetric, which tends to be found in early-type galaxies. Higher values of A indicate an asymmetric light distribution, which are usually found in spiral galaxies or in merger candidates.

Gini (G). The *Gini* coefficient (Abraham et al. 2003; Lotz et al. 2004) is a statistical tool that measures the cumulative flux distribution of a population of pixels and is insensitive to the actual spatial distribution of the individual pixels. It is defined as:

$$G = \frac{1}{\overline{f}N(N-1)} \sum_{i=1}^{N} (2i - N - 1) f_i \tag{4.3}$$

[6]Please notice that some authors include a factor two in the denominator. Here we follow the convention of the most recent literature.

where $\overline{f}$ is the average flux and the f_i pixel fluxes are sorted in increasing order before the summation over all N pixels in the segmentation map. Higher values of the *Gini* coefficient indicate that the majority of the total flux is concentrated in a small number of pixels, while lower values represent a more uniform distribution of flux.

M_{20}. The second order moment of the light distribution, M_{20} (Lotz et al. 2004) is defined as the second order moment of the brightest pixels that constitute 20% of the total flux in the segmentation map, normalized by the second order moment of all the pixels in the segmentation map.

$$M_{20} = log\left(\frac{\sum M_i}{M_{tot}}\right), while \sum f_i < 0.2 f_{tot} \tag{4.4}$$

The total moment of light (M_{tot}) is calculated by summing the flux of each pixel multiplied by the square of its distance from the centre. More negative values of M_{20} are typical of most regular morphologies, while less negative values characterize most irregular galaxies, often with multiple clumps. Given that the spatial variations in the concentration of light strongly affect M20, this parameter is also very sensitive to merger signatures, such multiple nuclei (Lotz et al. 2004).

4.4.3 The CvsA plane

Fig. 4.7 shows the Concentration vs. Asymmetry plane, for WFC3-IR H_{160} images. Mean values of all parameters for each morphological types were given in 4.2 There is some segregation of different morphological types. It is worth noticing that the type segregation regions found in the parameter's plane are independent of redshift, between $z = 1$ and $z = 4$: we searched for a possible evolution of Concentration and Asymmetry with cosmic time, founding any.

Type segregation

In the CvsA plane ellipticals and compact galaxies are characterized by higher concentration values, while almost all irregular galaxies have $C < 2.2$. However, the separation is not very sharp. There is not such a segregation in asymmetry. In the optical rest-frame, high-redshift ellipticals are often in the form of *peculiar ellipticals*, i.e. they show some minor morphological peculiarities, and are likely experiencing an episode of star-formation.

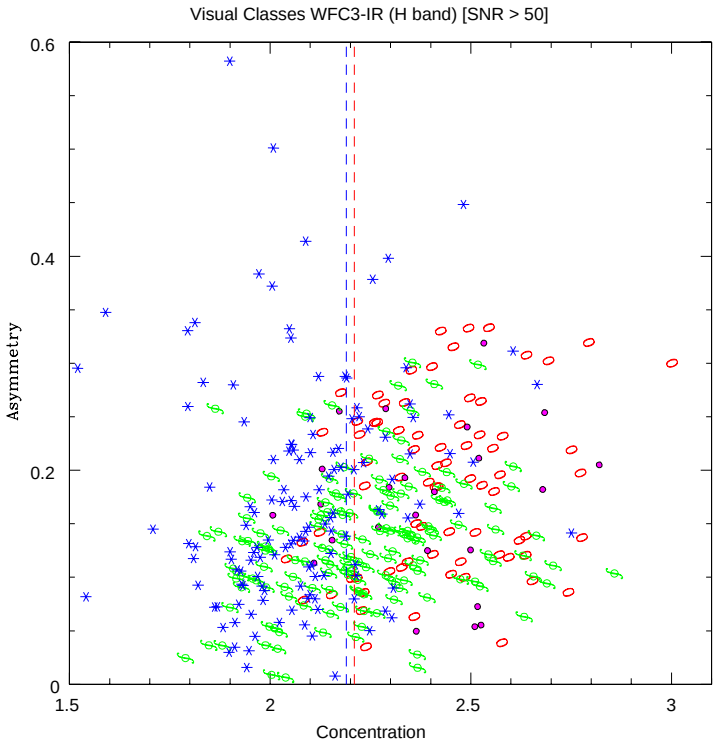

Fig. 4.7: Concentration vs. Asymmetry. The parameters were computed on WFC3-IR - H_{160} images. Dashed lines mark the regions populated by the different morphological classes (red: ellipticals; blue: irregulars), when a clear type segregation occurs. Points are shape and colour coded with respect to the morphological visual class (see Fig. 4.5).

Disk-like galaxies, on the other hand, do not show any kind of segregation, spanning a very large range of values both in concentration and asymmetry, though they never reach very high asymmetries ($A < 0.3$): the *Disk-like* category gathers spirals with different bulge to disk ratios, therefore with different concentrations and asymmetries, as well as galaxies with different inclinations, on which the asymmetry strongly depends; also, particularly in the disk galaxies experiencing episodes of star-formation, there may be multiple clumps.

Comparison with the literature

Comparing our results with the ones by other authors at lower z, in the same wavelength rest-frame range, the greatest difference is found in terms of asymmetry, with all the morphological types at high-redshift having larger asymmetries than their local siblings (Bershady et al. 2000; Conselice et al. 2003; Conselice et al. 2011). In particular, this is

true for elliptical systems, whose mean asymmetry at $z \sim 2$, which is $< A > \ 0.2$, is about one dex higher than what is measured in the local Universe ($< A > \ 0.02$).

Our results were also compared with other high-redshift studies in the same wavelength rest-frame range. There is a general agreement in the qualitative picture: galaxies have always quite sharp boundaries in terms of both concentration and asymmetry, generally with $A < 0.4$ and $1.5 < C < 3.5$ (Conselice et al. 2011; Law et al. 2012b). Below $A = 0.4$ the different morphological types do not have a sharp separation in Asymmetry, though in Conselice et al. (2011) ellipticals appear to be better segregated at lower asymmetries, with respect to irregular galaxies, than in the other works. The separation between ellipticals and irregulars that is found in our sample is almost absent in the UDF sample of Conselice et al. (2011). Law et al. (2012b) reports a separation between their classes of single nucleated (that include our *Ellipticals*, *Compact* as well as some *Disk-like*) and irregular galaxies, though there is a high contamination of the first type in the low-concentration region of the plot. Disks do not populate a limited region in any sample, but this morphological type is always reported to disappear at the highest redshifts ($z > 2.5$).

In conclusion, apart from small differences between various samples, that may depend by technical factors, the general picture is that high-redshift galaxies are, on average, much more asymmetric than low-redshift ones. However, the CvsA plane proves to be a tool not very well suited for the morphological analysis of high-redshift galaxies, at least not at the resolution currently provided by WFC3 images. We will return on this point later, when discussing about the morphological *k*-correction issue.

4.4.4 The GvsM20 plane

Fig. 4.8 shows the Gini vs. M20 plane, for WFC3-IR H_{160} images. Mean values of all parameters for each morphological types were given in 4.2. In this plane there is a clearer segregation of different morphological types, with respect to the previously analysed CvsA plane. Type segregation regions are independent of redshift, between $z = 1$ and $z = 4$: we searched for a possible evolution of the parameters with cosmic time, founding any, with the only exception of irregular galaxies that have less negative M20 and lower Gini values, with increasing redshift.

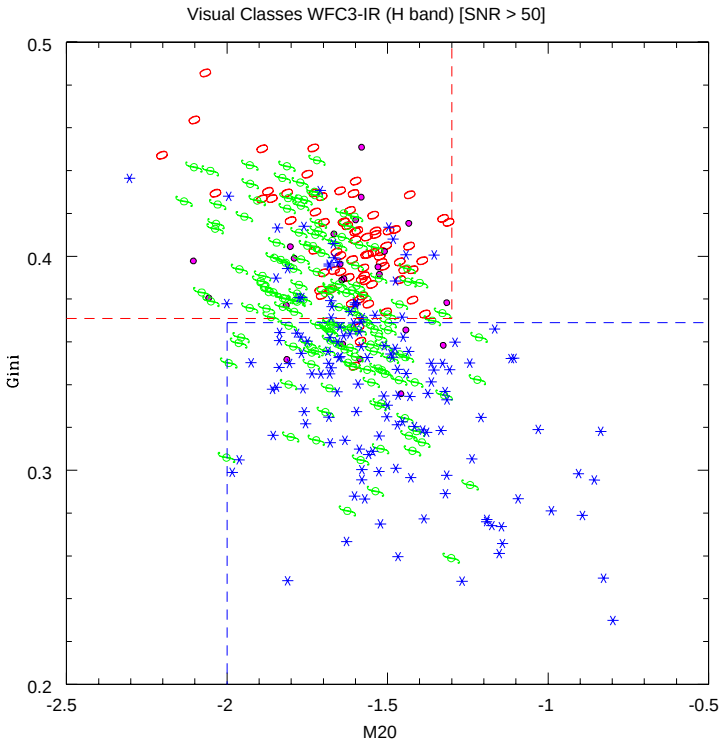

Fig. 4.8: Gini coefficient vs. M20. The parameters were computed on WFC3-IR - H_{160} images. Dashed lines mark the regions populated by the different morphological classes (red: ellipticals; blue: irregulars), when a clear type segregation occurs. Points are shape and colour coded with respect to the morphological visual class (see Fig. 4.5).

Type segregation

The GvsM20 distribution shows an evident bimodality, for all types but disks, with the two peaks corresponding respectively to the regions where elliptical/compact and irregular galaxies fall. In the plot of Fig. 4.8 these two regions have been marked: ellipticals and compact galaxies lie in the "regular and compact region" delimited by $M20 < -1.3$ and $G > 0.37$, while irregulars have $M20 > -2$ and $G < 0.37$ as boundaries.

In general, we find that all galaxies lie along a quite defined sequence in *G-M20*, regardless their type. Objects in the *Disk-like* category cover a large portion of the parameters space, though we find the vast majority of disks to have $G > 0.35$, meaning that most of the flux is distributed in a small number of pixels, and $M20 < -1.4$, that places galaxies with this morphological classification in the region of objects with quite a regular appearance.

Comparison with the literature

The GvsM20 plane always allows a quite good separation between the two extreme classes of ellipticals/compact and irregulars. Also in other works (Law et al. 2012b; Wang et al. 2012) the region of the plane with highest Gini and more negative M20 values is populated by ellipticals and compact galaxies, while irregulars are found in the opposite angle, the contamination between the two zones being very low.

From a quantitative point of view, we found a very good agreement in $M20$ between different studies: $< M20 >\sim 1.5$ is the average M20 value in all samples: from this point ellipticals/compact depart going towards more negative values, up to $M20 \sim -2.3$, while irregulars span the opposite range, down to $M20 \sim -0.7$. More differences were found in the Gini parameter. Though there is always quite a sharp separation between ellipticals and irregulars, with disks spanning a wide range in the parameter space, in the study by Law et al. (2012b), who examine a sample of star-forming galaxies, they report Gini values that are, on average, consistent with our own findings, while Wang et al. (2012) report much higher Gini values for their IEROs sample ($0.2 < G < 0.7$) and also the separation threshold between different morphologies is shifted from our $G \sim 0.4$ to $G \sim 0.7$.

The overall appearance of the GvsM20 plane does not change much from the local Universe to higher redshift, in the sense that there is a general trend between G and M20, with ellipticals and irregulars always being well separated and falling on the opposite angles of the plane, while disk galaxies span a larger range in values. From a quantitative point of view, however, some differences emerge. In particular, local ellipticals have much more negative M20 values[7]: $M20 < -2$ (Lotz et al. 2004). There are some differences across the literature, with this respect: for example, the HST-UDF galaxies analysed by Conselice et al. (2008) show $-1.3 < M20 < -1.8$.

The conclusion is that the GvsM20 plane allows, especially at high redshift, a better segregation of morphological types than the CvsA plane. However, the regions where different morphological classes are segregated are different at low and high redshift.

[7]Numbers are given with respect to our chosen segmentation map.

4.5 Morphological k-correction

An important issue to address in the morphological study of galaxies is how much the morphological features change as a function of the rest-frame band in which the galaxies are observed. As already reported in the data sample description, for all galaxies in the *GMASS-wfc3 sample*, images from the Advanced Camera for Surveys (ACS) mounted on the Hubble telescope are also available. As shown in Fig. 4.2, the H_{160} of the WFC3 probes the rest-frame optical regime for galaxies at redshift $z > 1$. To study how the optical morphologies differ from the UV ones, ACS imaging in z_{850} was used, which sample the UV rest-frame.Images with the same angular size of the WFC3 ones (4"x 4") were cut from the public ACS image of the GOOODS-South field, and the previously described morphological analyses was done on them. Finally, these rest-frame UV results were compared with the rest-frame optical ones.

4.5.1 $ACS - z_{850}$ images degradation

ACS and WFC3 images have different resolution and PSF. This may heavily affect both the visual assignment of a morphological type to a galaxy and the morphological non-parametric statistics. Therefore, before going on with the analysis, the ACS images were degraded to match the pixel size and PSF of WFC3: first, we registered ACS images to the pixel size of WFC3; then we convolved the registered images with the WFC3-IR PSF. The resulting images will be referred to as the "ACS_{deg} sample" (ACS degraded).

Comparing original ACS images with ACS_{deg} sample we verified that a worst resolution and larger PSF can indeed mimic a morphological k-correction, and this effect has to be taken into account when searching for differences in images at different wavelengths. In general, the elliptical classification is quite robust against the change in PSF, in fact we verified that almost all of the galaxies classified as ellipticals in original ACS images have the same appearance in ACS_{deg}. Only one third of the compact galaxies in original ACS images are recovered as such also in ACS_{deg}, while the majority is re-classified as elliptical or irregular. ∼70% of disks in original ACS has the same classification in ACS_{deg}, but the remaining ∼30% is re-classified as irregular. Almost all original ACS irregulars are recovered as such in the degraded images, while ∼20% changes morphological type. Finally, one third of *Faint Objects* in ACS sort of acquires a morphological type (mainly *Irregular*) in the degraded images. This is not strange: pixels are merged

in the re-pixelization process and smoothed in the convolution of the image with a larger PSF, but the total flux is conserved, therefore structures previously confused with the background noise may become "classifiable".

Quantitative morphological parameters in the two sets of images were also compared. Using parameters computed on original ACS images, ellipticals and irregulars are quite well separated in the CvsA plane (see also Cassata et al. (2005)), while in ACS_{deg} case there is not a sharp segregation between different morphological types. This means that C and A parameters are not robust against changes in pixel sampling and PSF, at least for high-redshift galaxies.

Comparing original ACS and ACS_{deg} values, G and M20 are more stable in elliptical and compact galaxies, while they are sensitive to the change in image quality for irregular and disk galaxies. This depends on the definitions of the two parameters: in galaxies where the light is distributed in a well defined region (contiguous pixels), the re-pixelization and the smoothing do not affect much G and M20; on the other hand, when galaxy's light has a more uneven space distribution, the effects of change resolution and PSF are perceived more strongly by the two parameters.

4.5.2 Visual appearance

Fig. 4.9 shows the relative distribution of galaxy morphological types, as a function of redshift, in ACS_{deg} images. This plot has to be compared with the analogous one for the H_{160} band (Fig. 4.5).

162 out of 494 objects have different H_{160} and ACS_{deg} visual classifications (see Table 4.3). In most cases, the change is from elliptical in H_{160} to compact or irregular in ACS_{deg}.

Two thirds of H_{160} ellipticals have the same ACS_{deg} classification. The remaining galaxies change type, mainly to compact. The fraction of ellipticals is lower, in the UV range with respect to the optical, at all redshifts, as also reported by Conselice et al. (2011). In the optical there is evidence of an evolution of the ellipticals fraction with cosmic time, while in the UV the fraction drops soon before $z = 1$ and stays quite constant going backwards. The fraction of compact galaxies is similar in the two bands at all redshift but $z \sim 2.5$, when only in the optical regime there is a peak. The same thing can be said of the disk category.

80% of H_{160} compacts do not change morphology with wavelength, but another 20%

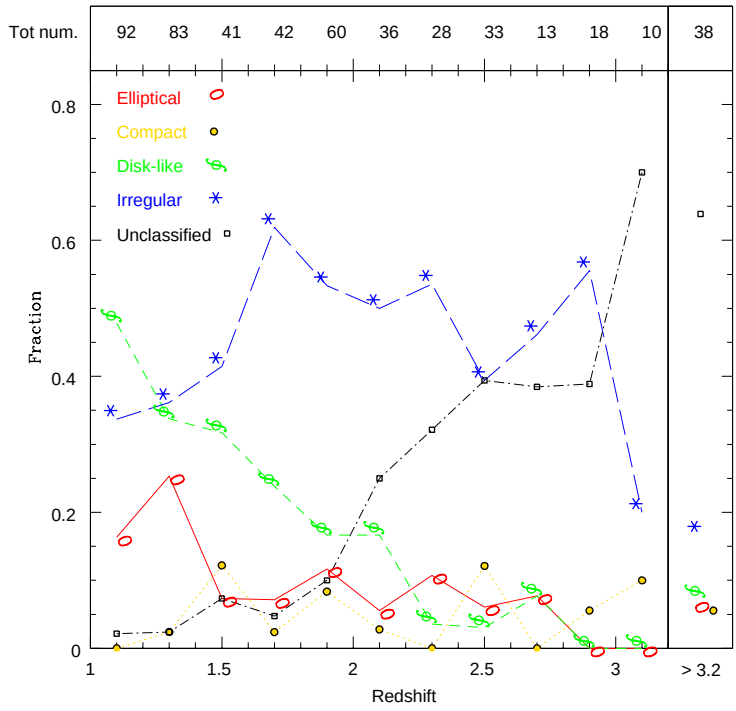

Fig. 4.9: The relative fraction of galaxy morphological types as a function of redshift, for ACS_{deg} images. In the upper panel the total number of galaxies in each redshift step ($\Delta z = 0.2$) between $z = 1$ and $z = 3.2$ is written. The last step includes all galaxies at $z > 3.2$.

appears as a faint object in the UV band. Also 80% of optical disks are recovered as such in ACS_{deg} images, while the remaining fraction changes type to irregular.

Table 4.3: Visual morphological classification in WFC3-IR H_{160} vs. ACS deg z_{850}. (Example. The number in Row 1 / Column 2 means that 6 galaxies are classified as ellipticals in H_{160} and as compact in z_{850}. In parenthesis the total number of galaxies belonging to each type is reported.

		degz_{850}				
		Ell(59)	Comp(22)	Disk(117)	Irr(208)	Faint(88)
H_{160}	Ell (75)	53	6	5	8	3
	Comp(36)	3	16	2	6	9
	Disk(157)	0	0	103	49	4
	Irr(199)	3	0	7	137	51
	Faint(27)	0	0	0	6	21

Some of the galaxies that show the strongest k-correction between H_{160} and ACS_{deg} images are presented in Fig. 4.10, where also original ACS images. These images show

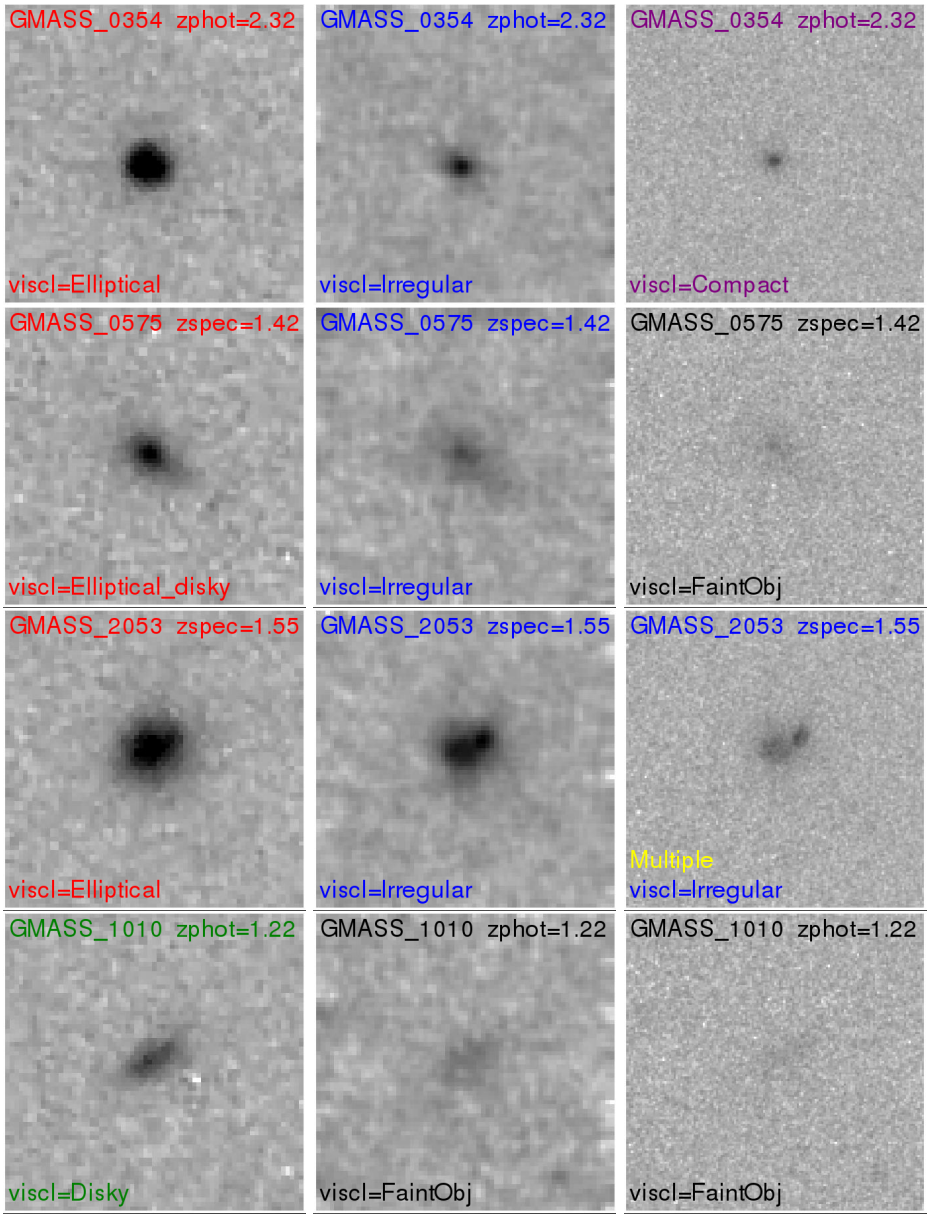

Fig. 4.10: Some examples of galaxies showing the strongest k-correction from optical to UV band. Each group of three images shows H_{160}, ACS_{deg} and original ACS images. On each snapshot, galaxy ID, redshift and classification are reported.

both the effect of the change in PSF and pixel sampling and and the occurrence of an actual change in morphology between the two wavelength bands. In general, galaxies appear more regular and less compact in H_{160}, with respect to z_{850}, but differences are very small. It may be notices, however, that in some cases original ACS images show evidence of sub-structures that are lost in the degraded images: in these cases it is not possible to determine if such structures do not exist in H_{160} images or if they are just

smoothed by the larger PSF, an effect described in the previous section.

We have already pointed out, in the previous section, that the change in resolution and PSF may allow structures, which are confused with the background noise in high-quality images, to become "classifiable" in lower-quality images. But this effect does not account for all the galaxies: there is still a fraction of galaxies whose structure is only observable in the optical rest-frame, and not in the UV. In particular, there are 67 objects with a H_{160} morphological classification but faint appearance in ACS_{deg} imaging. Since they have intermediate to high masses, with respect to the total sample, and high SFRs (Fig. 4.11), these objects are probably dusty star-forming galaxies, in which the UV signal coming from young stars is almost entirely absorbed, while what we see in the optical regime is a mixture of nebular emission and light from older stellar populations.

4.5.3 Quantitative changes

Non-parametric statistics were also computed for the ACS_{deg} images and compared with H_{160} values, to assess in a quantitative way the presence or absence of a morphological k-correction at high-redshift. Table 4.4 shows the average change in morphological parameters (in units of μm^{-1}), for the total sample and for each morphological type, taking as reference the H_{160} visual classification.

Table 4.4: Average change (and r.m.s.) in morphological parameters, from the rest-frame optical to near-UV, for the total sample and for each morphological visual type, as classified on WFC3-IR - H_{160} images. $\Delta P = P(H_{160}) - P(z_{850})$, where P stands for each of the four measured parameters. $\Delta\lambda$ is the change in rest-frame wavelength at $z \sim 2$.

$H_{160}-$ deg z_{850}	Total sample	Ell	Comp	Disk	Irr
$\frac{\Delta C}{\Delta\lambda}$ (μm^{-1})	-0.05 ± 1.04	-0.19 ± 1.26	-0.10 ± 1.20	0.11 ± 0.98	-0.16 ± 0.95
$\frac{\Delta A}{\Delta\lambda}$ (μm^{-1})	-0.13 ± 0.58	-0.01 ± 0.63	0.01 ± 0.46	-0.09 ± 0.37	-0.24 ± 0.71
$\frac{\Delta G}{\Delta\lambda}$ (μm^{-1})	0.03 ± 0.21	-0.02 ± 0.20	-0.04 ± 0.13	0.07 ± 0.20	0.01 ± 0.21
$\frac{\Delta M20}{\Delta\lambda}$ (μm^{-1})	-0.04 ± 1.38	0.58 ± 1.15	0.50 ± 0.96	-0.33 ± 1.27	-0.08 ± 1.57

The CvsA plane

Fig. 4.12 shows the CvsA plane in the UV rest-frame.

Comparing the CvsA plane for H_{160} (Fig. 4.7) and ACS_{deg} images, we found that, apart

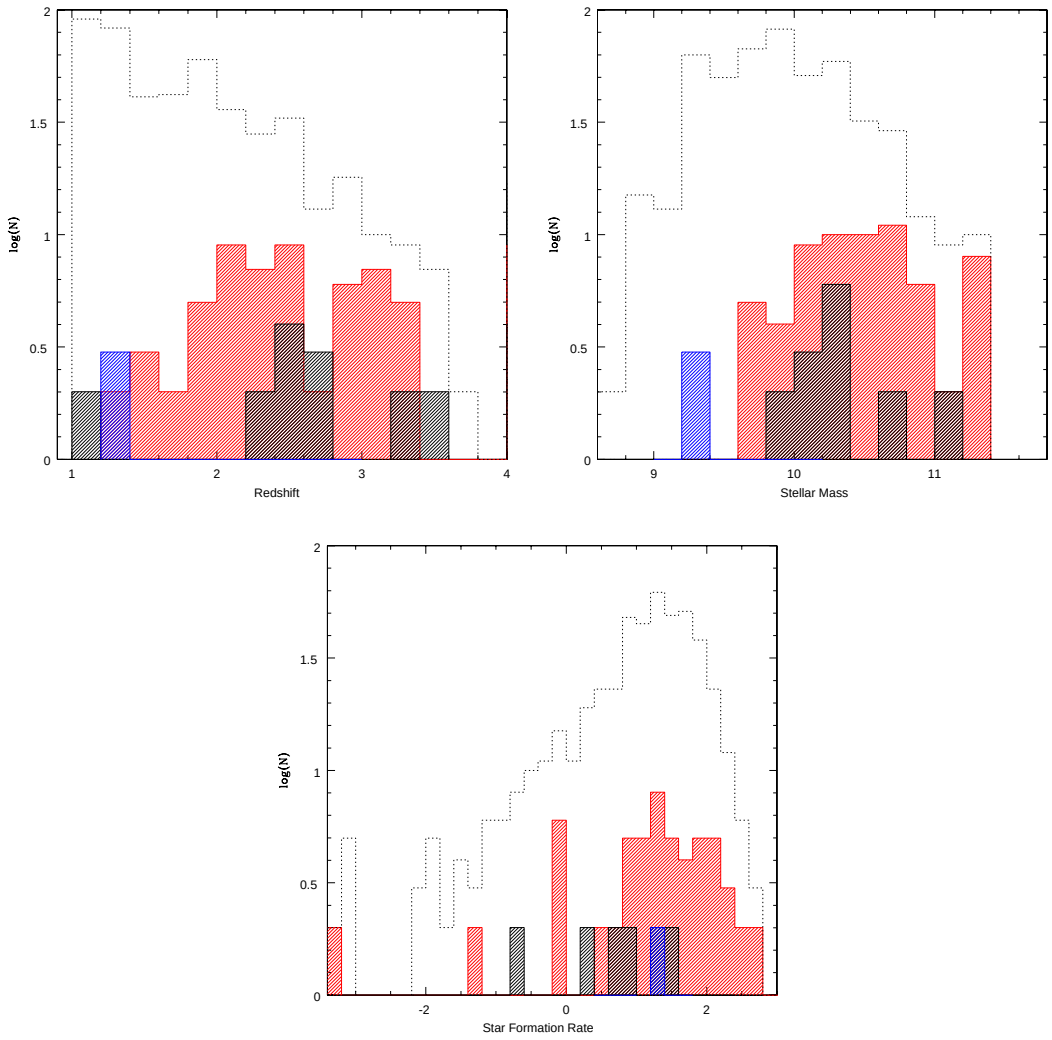

Fig. 4.11: Distribution of redshift, mass and SFR of faint objects in ACS_{deg} with a morphological classification in H_{160}. Empty black histograms represent the entire $GMASS - wfc3sample$. Histograms are in logarithmic scale.

from a slightly higher scatter in asymmetry of the irregular galaxies, the two plots are very similar.

Though the UV and optical CvsA planes look quite similar, quantitatively there are still some differences (see also Table 4.4). Ellipticals appear more concentrated at shorter wavelengths compared to optical ones. This confirms a similar result by Conselice et al. (2011), though we find for our galaxies a smaller difference between the two bands. The opposite case happens in the local Universe ($z < 0.75$), where early types become more concentrated at longer wavelengths (Conselice et al. 2008; Taylor-Mager et al. 2007).

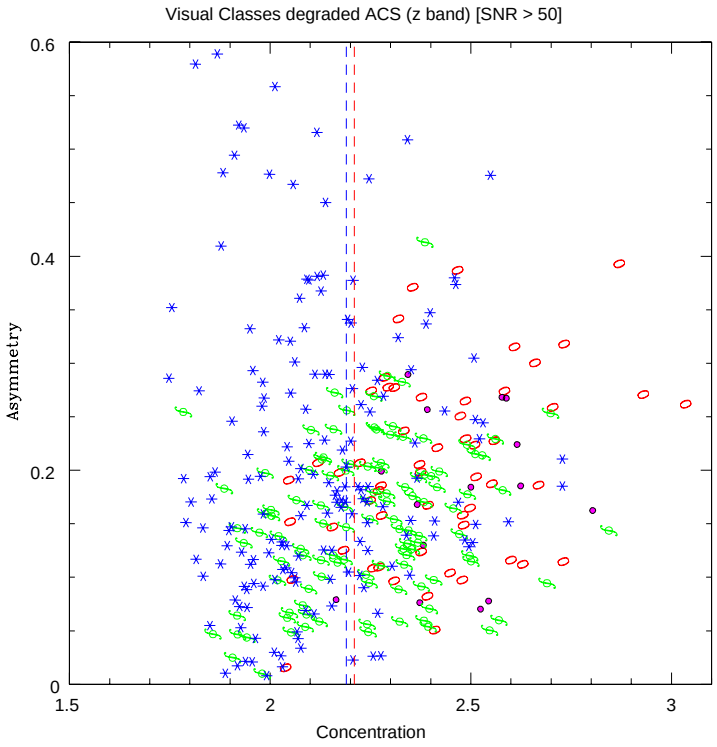

Fig. 4.12: Concentration vs. Asymmetry. The parameters were computed on ACS deg z_{850} images. Dashed lines mark the regions populated by the different morphological classes (red: ellipticals; blue: irregulars), when a clear type segregation occurs. Points are shape and colour coded with respect to the morphological visual class (see Fig. 4.5).

Lanyon-Foster et al. (2012) found that morphological early type galaxies are less concentrated in terms of their stellar mass distribution than in z_{850} band light, which is explainable by the fact that central star-formation may be dominating the morphologies of these systems; we recall that there is evidence that a fraction of morphological ellipticals are not passive galaxies but, in fact, star-forming ones. The likely reason for the change in the concentration gradient with redshift is that the SFR of these galaxies is declining. This results in the differences between a blue and a UV band becoming even more pronounced, as there is not as much star-formation to create a large signal in the UV.

Also compact and irregulars have lower concentration at redder bands, while disks are more concentrated in H_{160} imaging. Irregular galaxies are, on average, more asymmetric in z_{850} band, as would be expected since they are actively star-forming galaxies (see also Conselice et al. (2011)), and so are disks, though only very slightly. Compact and ellipticals, on the other hand, do not show differences in asymmetry between the two bands.

The GvsM20 plane

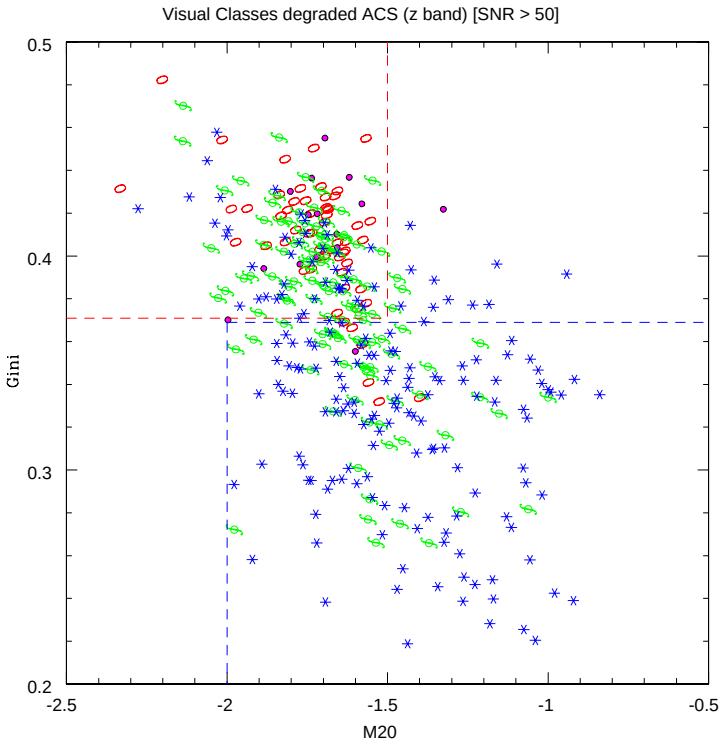

Fig. 4.13: Gini coefficient vs. M20. The parameters were computed on ACS deg z_{850} images. Dashed lines mark the regions populated by the different morphological classes (red: ellipticals; blue: irregulars), when a clear type segregation occurs. Points are shape and colour coded with respect to the morphological visual class (see Fig. 4.5).

In the ACS_{deg} GvsM20 plane there are quite defined boundaries for the ellipticals region, though with some contamination of irregulars. In the optical plane all galaxies tend to aggregate around $M20 \sim -1.5$, while in the UV plane the trend between G and M20 has a flatter slope; in fact, the boundaries of the elliptical region are slightly different in the two plots: $M20 < 1.3$ in the optical and $M20 < 1.5$ in the UV.

Optical ellipticals have, on average, higher M20 values, meaning that eventual signs of mergers would be more likely to be found in longer wavelength imaging. The Gini coefficient, on the other hand, does not show any significant variation. Galaxies classified as compact show the same behaviour in M20, but have a larger difference in Gini.

Note that all *DeltaP* must be read considering the dynamical range of each parameter. For example, Gini has a range of ~ 0.3, while C has a range of ~ 1.5.

Table 4.4 shows that optical disks have significantly more negative M20 values (for the el-

lipticals is exactly the opposite), and a the largest difference in the Gini coefficient. Since M20 is a measure of the concentration of light sensitive to spatial variations, the GvsM20 k-correction indicates that, in high-redshift disk galaxies, very young stars responsible for the production of UV light have a more irregular spatial distribution with respect to the totality of stellar populations that make up the light originating in the rest-frame optical.

* * *

The overall conclusion of this section is that, taking into account the difference in resolution and PSF of WFC3-IR H_{160} and ACS z_{850} images, at $z > 1$, there is no significant morphological k-correction in the visual appearance of galaxies.

However, looking at morphologies in a quantitative way, some differences arise. In particular, ellipticals, compact and irregular galaxies appear slightly more concentrated at shorter wavelengths compared to optical ones, while disks show the opposite trend. The change in the concentration of light is confirmed also by the Gini parameter. All types, but irregulars, show no difference in asymmetry with wavelength. For irregulars, a negative asymmetry gradient is expected since they are actively star-forming galaxies. The greatest difference with wavelength is found in the M20 parameter, with ellipticals and compact showing a positive gradient, meaning that eventual signs of mergers would be more likely to be found in longer wavelength imaging, while disks have a negative gradient, indicating that very young stars responsible for the production of UV light have a more irregular spatial distribution with respect to the totality of stellar populations that make up the light originating in the rest-frame optical.

4.6 Colour bimodality

Galaxy rest-frame colours show a bimodal distribution, as it has been well established by several studies (Strateva et al. 2001; Hogg et al. 2002; Cassata et al. 2007, 2008; Bell et al. 2004; Weiner et al. 2005; Whitaker et al. 2011; Bell et al. 2012). There is also a relation between colour and stellar mass: when plotted on a rest-frame colour vs. stellar mass diagram, galaxies tend to segregate in a so-called "red sequence", with higher masses, and a less massive "blue cloud". This bimodality, observed in the local Universe, has been proven to hold also at higher redshifts. The population in the red peak of the distribution is dominated by galaxies with an early-type morphology and old stellar

populations, though there is also a contamination of star-forming galaxies reddened by dust, while the blue cloud contains mainly late-type morphologies, meaning spirals and irregulars.

Here we wanted to test the behaviour of the different morphological types with respect to the colour bimodality. To do this, rest-frame magnitudes were computed. Our method consists of computing the absolute magnitude in a given filter X using the observed apparent magnitude in the filter Y, which is chosen to be $\lambda(Y) \sim \lambda(X)*(1+z)$. The advantage of this method with respect to other ones is that it limits the template dependency. We computed the absolute magnitudes through U and B Johnson filters. Fig. 4.14 shows the rest-frame (U-B) colour distribution for the *GMASS-wfc3 sample* vs. the total GMASS sample, and the distribution for each morphological class of galaxies. The WFC3 subsample shows the same colour bimodality already observed in the total GMASS sample by Cassata et al. (2008). The colour distribution was also checked in four redshift bins, and we verified that the bimodality may still be seen clearly up to $z \sim 2.3$, while at even higher redshifts the distribution is smoother and there is a larger fraction of galaxies in the "valley" between the blue and the red tails of the distribution (see also Cassata et al. (2008)).

We took the minimum between the red and the blue peaks, $(U-B)_{restframe} \sim 1$, as the separation value between the red sequence and the blue cloud, which is consistent to threshold values usually reported in the literature (Cassata et al. 2008; Kriek et al. 2009). There is a tight correspondence between the belonging of a galaxy to a colour group and its morphological type. In fact, compact and irregular galaxies generally fall under the blue peak, while ellipticals mainly populate the red sequence. However, there are also a group of red irregulars on one side and blue ellipticals on the other one. Disk galaxies have a slightly different behaviour: two peaks are distinguishable, a blue one around ~ 0.75 and a red one around ~ 1.25. The main characteristic of disks colour distribution is that they populate also the intermediate region between the red and the blue peak.

In Fig. 4.15, 4.16 and 4.17, the rest-frame colour vs. stellar mass diagram is shown, for each morphological type.

In Fig. 4.18 and 4.19 we also plot the distribution of some physical and quantitative morphological properties of the two groups. In the redshift distribution, blue galaxies of each type are found in the entire range covered by that type. Red ellipticals and irregulars also span the entire redshift range of their own parent group, while red disks are found predominantly at $z < 1.5$ and red compact around $z \sim 2.5$, where there is also the peak in

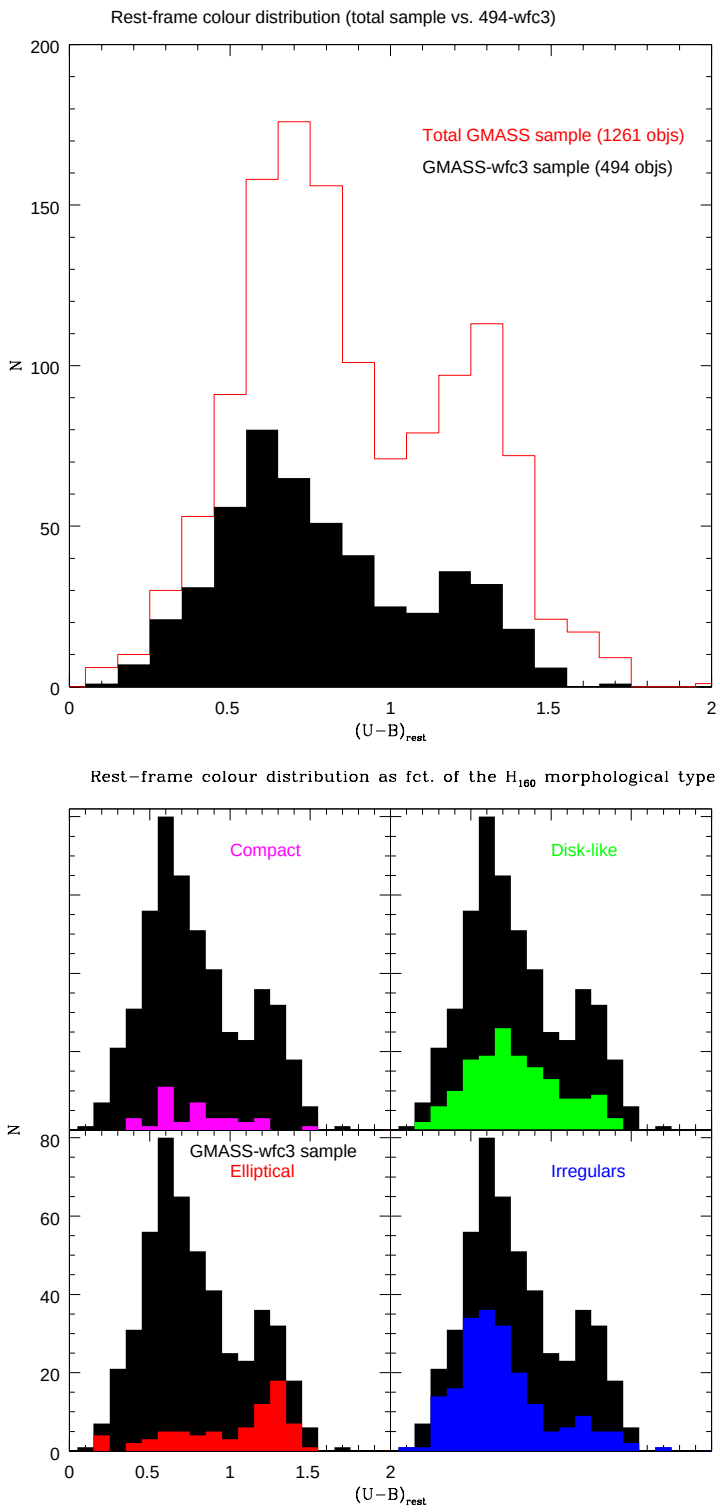

Fig. 4.14: *Upper panel*: rest-frame (U-B) colour distribution for the *GMASS-wfc3 sample* vs. the total GMASS sample. *Bottom panel*: rest-frame (U-B) colour distribution for each morphological visual class.

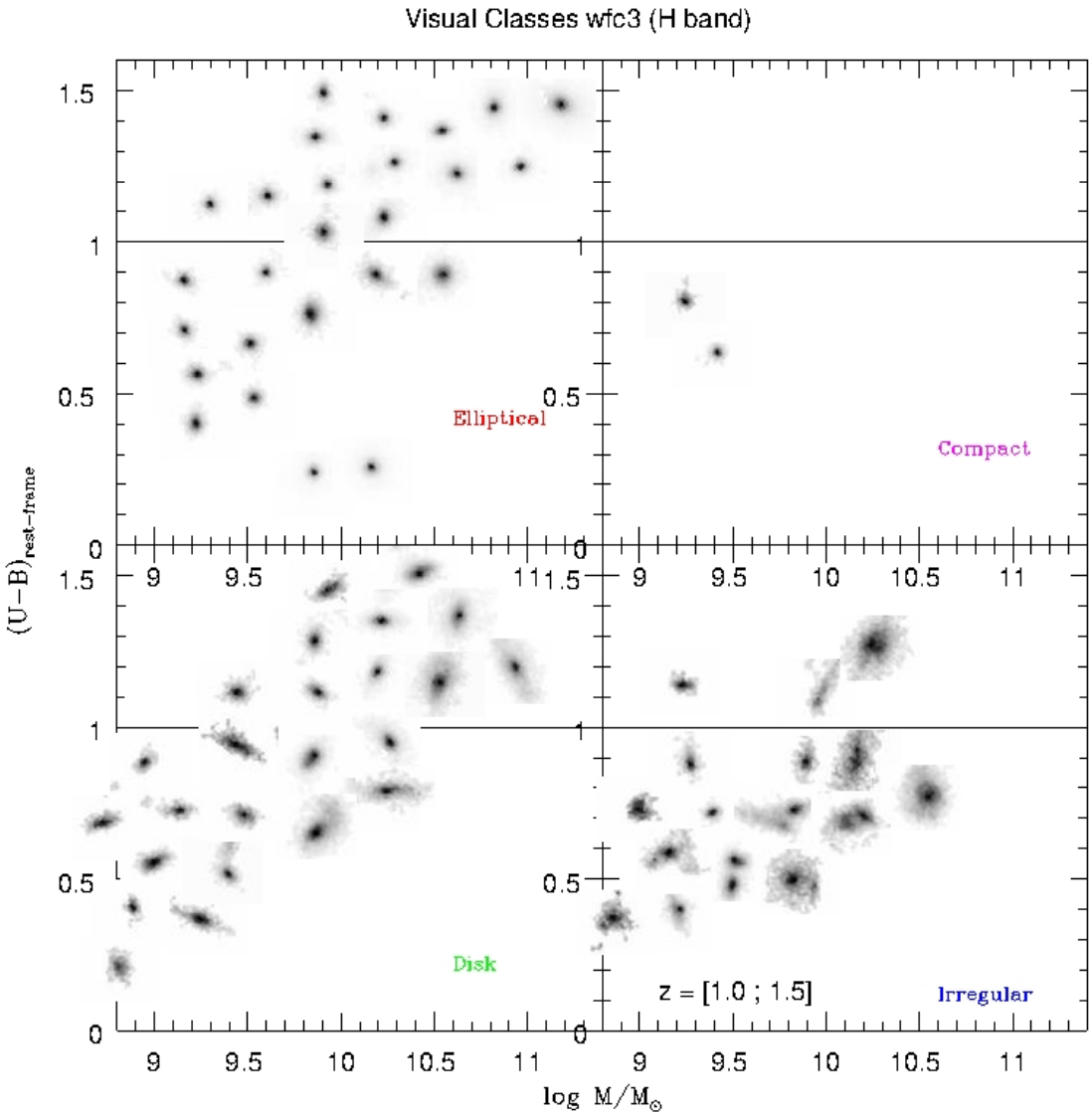

Fig. 4.15: Rest-frame colour vs. stellar mass for each morphological type, in three redshift bins. Instead of symbols, randomly selected H_{160} 4"x 4" cutouts from our sample images are used. Lowest redshift bin.

their total distribution.

With respect to the size, compact and ellipticals have the smallest size, in both the red and the blue sample. Red disks and irregulars also have the smallest $R_{1/2}$, while blue late-types reach larger radii.

The morphological parameters (we choose to use only G and M20, that were proved to be the more robust of the set) show little differences in each class between the red and

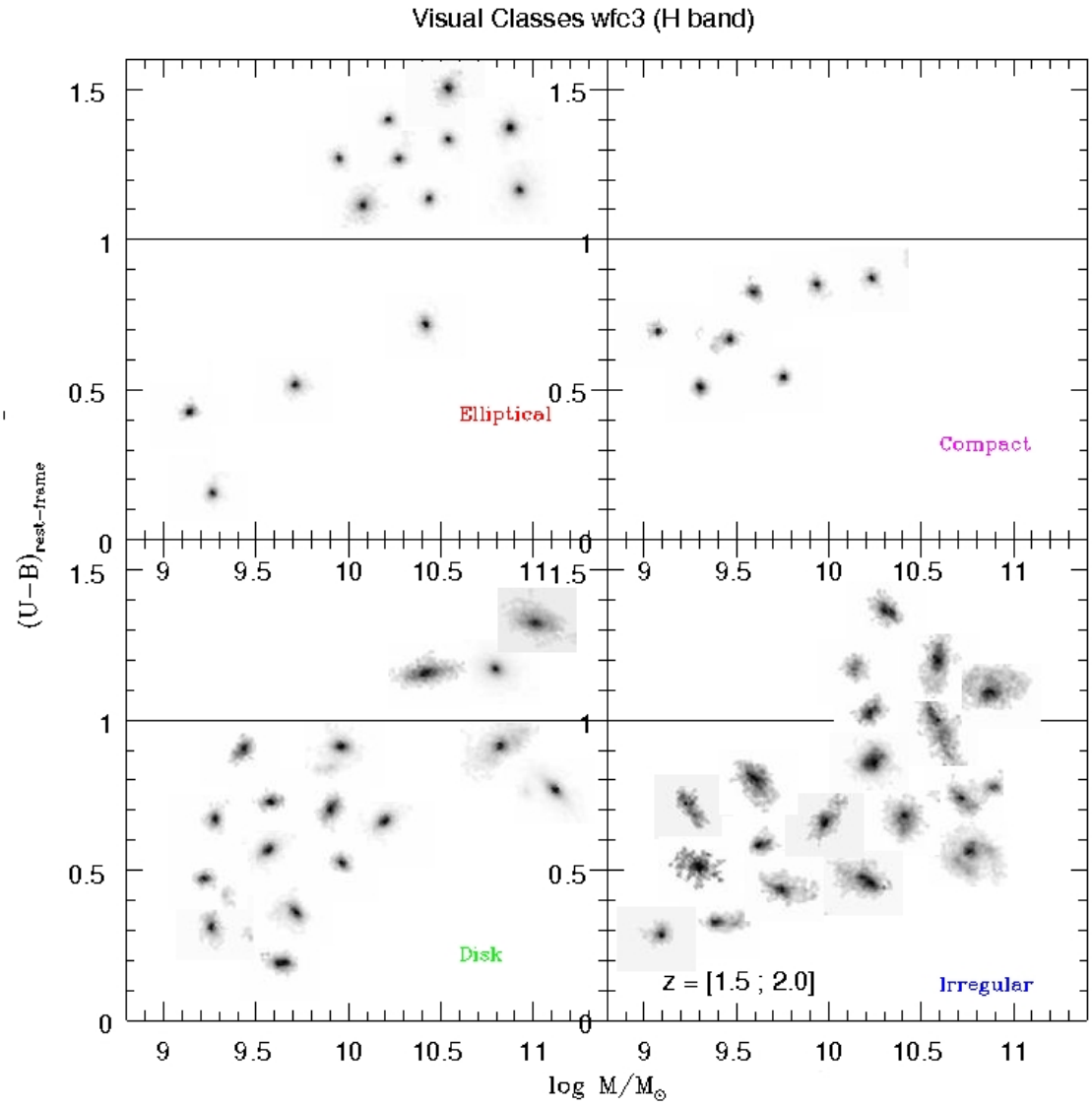

Fig. 4.16: Rest-frame colour vs. stellar mass for each morphological type, in three redshift bins. Instead of symbols, randomly selected H_{160} 4"x 4" cutouts from our sample images are used. Intermediate redshift bin.

the blue group. Again, the red group is the one that shows the greatest consistency, with galaxies belonging to each morphological type having similar values of both G and M20. In the categories of disks and compact we find the largest differences between red and blue galaxies: red disks are more concentrated and regular than blue disks, and the same holds for the compact. In the ellipticals group there is a strong correspondence between the red and blue distributions, though blue elliptical are a bit less concentrated that the red one. Moreover, blue ellipticals are also more regular than the red ones, at odds with

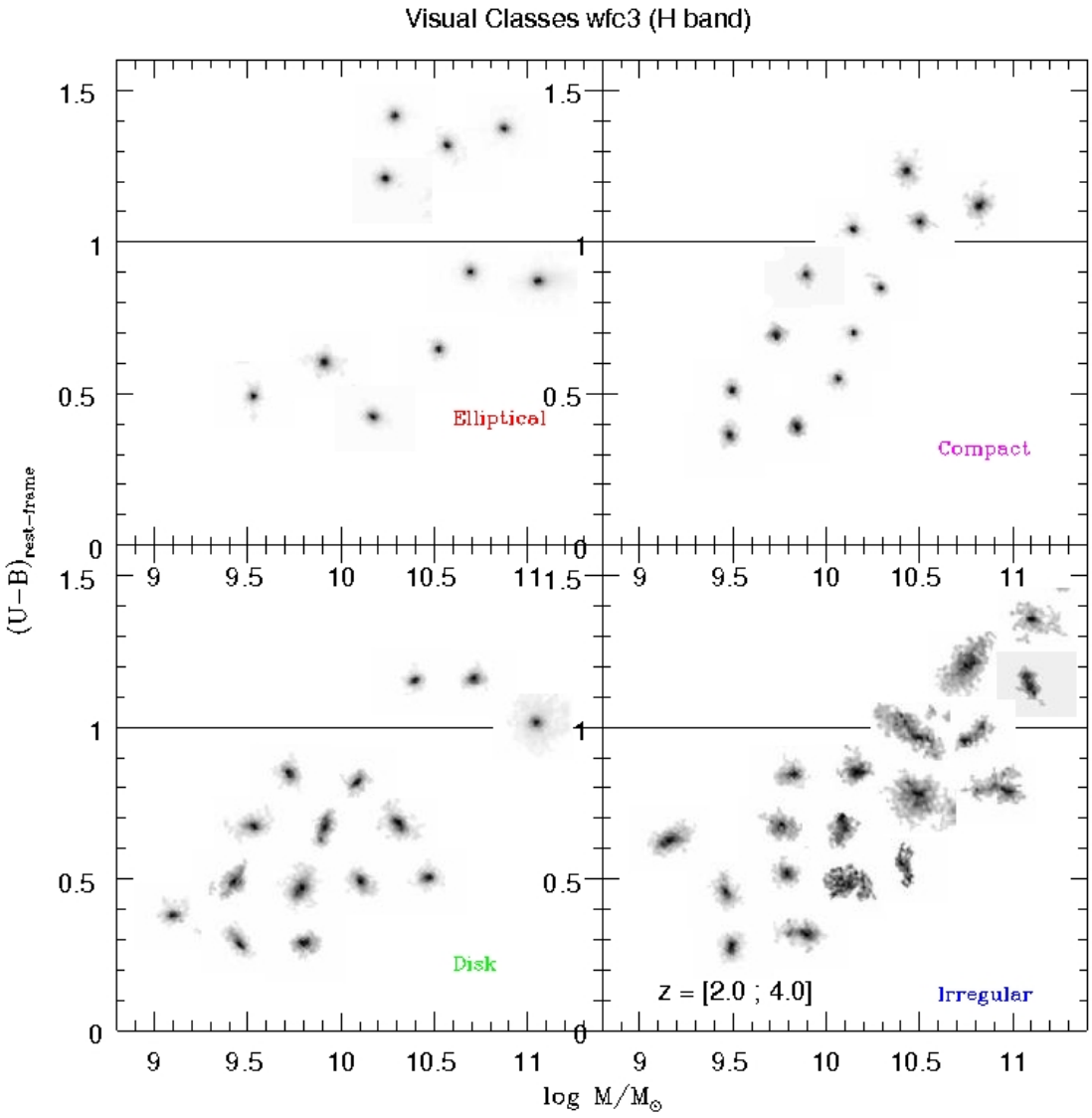

Fig. 4.17: Rest-frame colour vs. stellar mass for each morphological type, in three redshift bins. Instead of symbols, randomly selected H_{160} 4"x 4" cutouts from our sample images are used. Highest redshift bin.

what happens for the other types.

Looking at the physical properties of the galaxies, all red objects have the highest masses, regardless their morphological type. While almost all red ellipticals are actually passive galaxies, showing little to no sign of star-formation activity, most of the red disks and irregulars are star-forming galaxies, probably with different levels of dust extinction. The red colour of these late-type galaxies may depend by a combination of factors. Some of

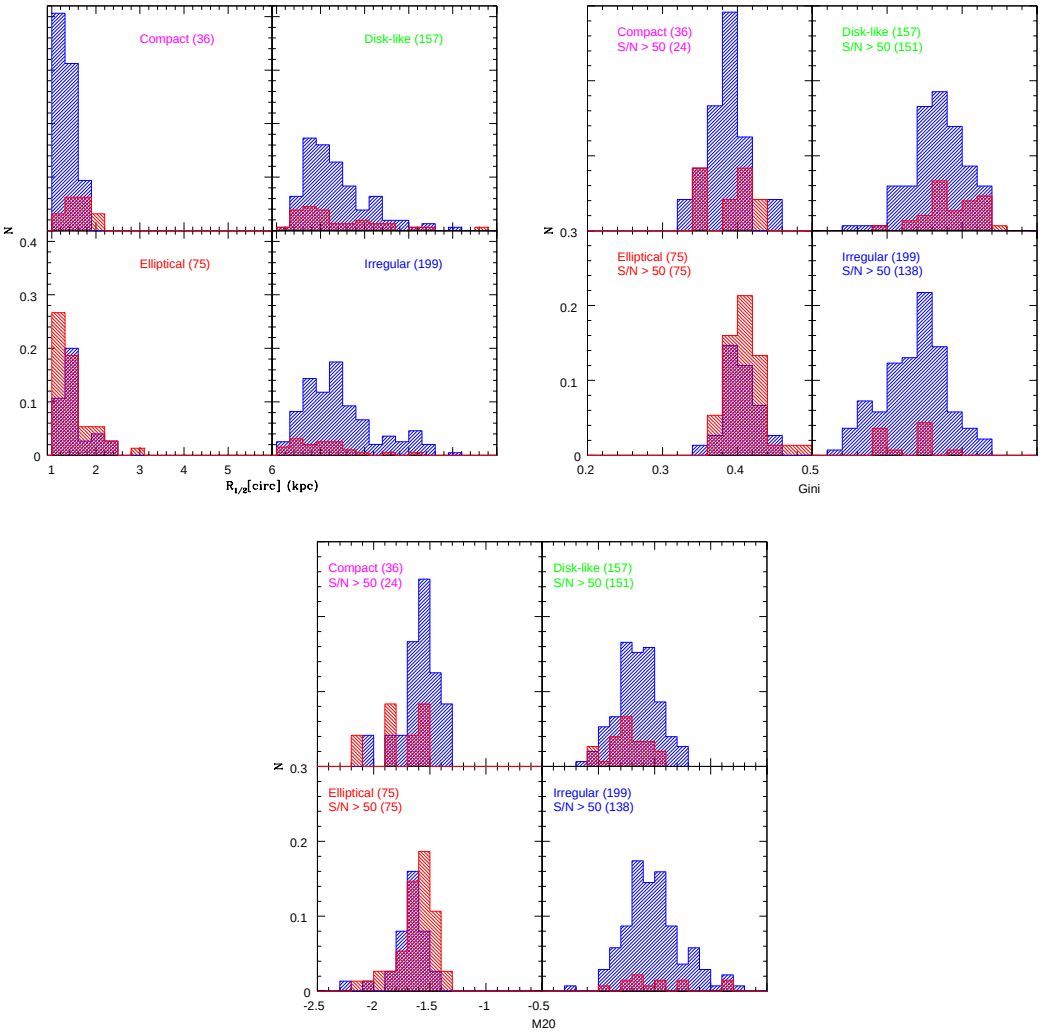

Fig. 4.18: Distribution of (clockwise):$R_1/2$, Gini and M20 for the "blue cloud" (blue histogram) and the "red sequence" (red histogram) in the $(U-B)_{rest}$ vs. Mass diagram, for each morphological type. Histograms are normalized to the total number of galaxies in each morphological class (indicated in parentheses): in each box the sum of the blue and the red histograms is 1. For the Gini and the M20 distribution only galaxies with H_{160} image S/N > 50 were used.

them are simply highly star-forming galaxies which are heavily obscured by dust. The bimodality in mass for compact, disks and irregulars, along with that in colour, may also suggest that the metallicity plays a role too in determining the colour. (Cassata et al. 2007), for a sample of $z \sim 0.7$ red late-type galaxies in the COSMOS field propose the inclination of the disk as the dominant effect in determining the measured colour, finding all their red late-type objects to be edge-on or very inclined spirals, with a distribution of

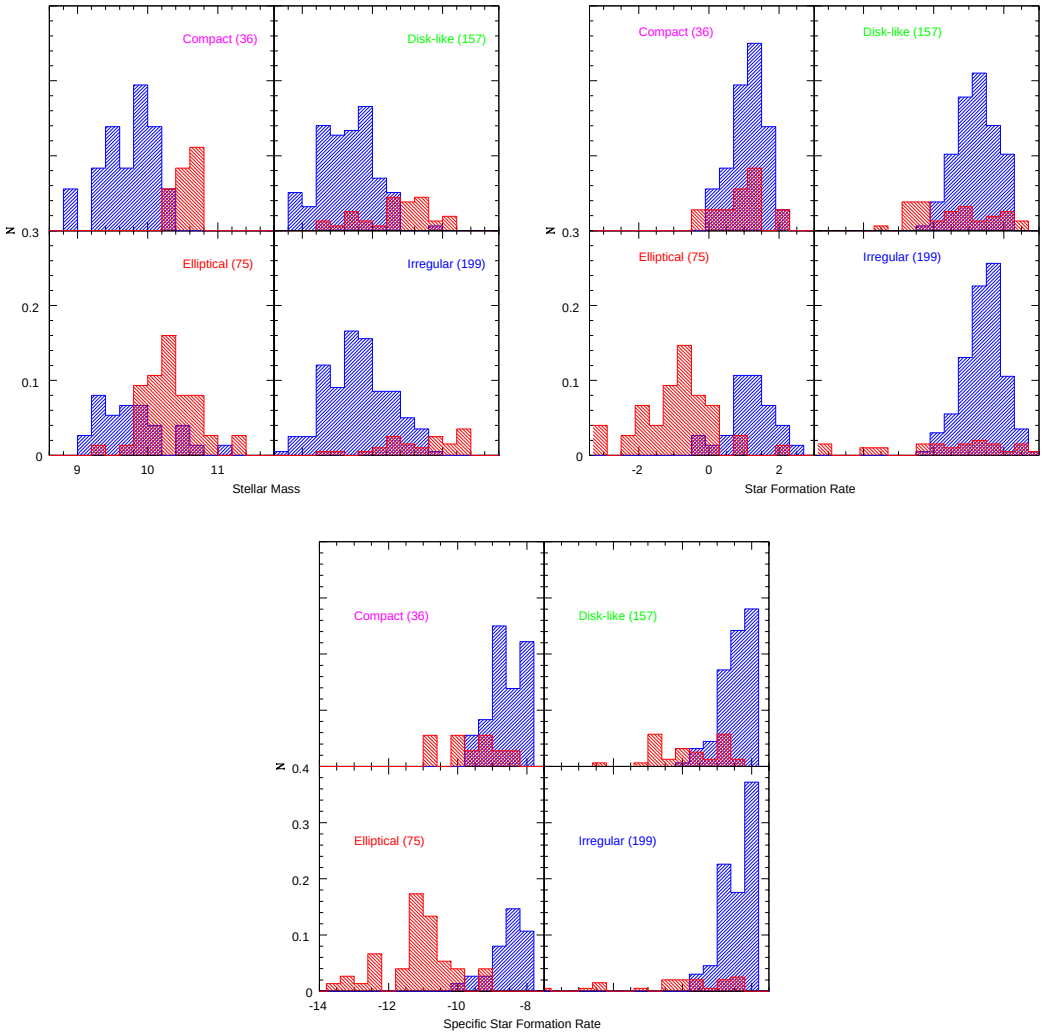

Fig. 4.19: Distribution of (clockwise): stellar mass, star-formation rate, specific star-formation rate for the "blue cloud" (blue histogram) and the "red sequence" (red histogram) in the $(U\text{-}B)_{rest}$ vs. Mass diagram, for each morphological type. Histograms are normalized to the total number of galaxies in each morphological class: in each box the sum of the blue and the red histograms is 1.

ellipticity skewed toward higher value than the blue late-type population. We checked the inclination of the red and blue disks in our sample, but comparing the two distributions we did not find a significant difference. We conclude that the dominant reddening effect for red late-type galaxies in our sample is likely that they are spirals and peculiar spirals dominated by a bright bulge, as it may be inferred by a visual check of the red disks in Fig. 4.15, 4.16, and 4.17.

4.6.1 The blue *spheroidal* population

The most interesting result of the morphological analysis of the colour-mass diagram is the presence, in the blue cloud, of a group of 30 galaxies with low to intermediate masses and high SFRs, that were classified by eye as ellipticals, and have the same morphological properties of ellipticals in the red sequence. We called these galaxies "blue spheroidals" and examined their properties more in depth.

The remarkable similarity between morphological characteristic of the red ellipticals and the blue spheroidals, shown in Fig. 4.18, should guarantee that the blue ellipticals are truly relaxed objects, from a morphological point of view. However, the separation between ellipticals and compact, with respect to morphological parameters, is no so sharp. This means that may be the possibility that some of the galaxies in the blue spheroidals group were misclassified as ellipticals, instead of compact star-forming.

First, we verified that all ellipticals, blue spheroidals, and compact are resolved objects: all our galaxies have $FWHM \geq 0.2$", which is the PSF of WFC3-IR H_{160} images. The morphological types of the 30 blue spheroidals where also checked in ACS z_{850} images (not degraded): 23 out of 30 galaxies are classified as ellipticals also in their UV rest-frame, 2 are compact and only 4 have a late-type morphology.

If we consider all the red ellipticals, blue spheroidals, and compact together, they all have similar half-light radii, and this is true in H_{160} and z_{750} images as well. Examining a different scale parameter, in particular $R_{80\%}$ (radius that encloses 80% of the total luminosity), the values are still quite the same for all the red ellipticals, blue spheroidals, and compact, in H_{160} and degraded z_{750} images (Fig. 4.20). But, if we consider original z_{750} images, there is a clear separation between the compact on one hand, and red ellipticals and blue spheroidal on the other. In particular, almost all ellipticals and blue spheroidals have $R_{80\%} \geq 1.2$ kpcs, while compact have $R_{80\%} \leq 1.2$ kpcs. The comparison between the three sets of images tells us that both ellipticals and blue spheroidals have larger $R_{80\%}$ than compact, but the resolution and PSF of WFC3 images smooths the compacts with the result that they end up having larger $R_{80\%}$, more similar to those of ellipticals, both in H_{160} and degraded z_{750} images.

A higher Gini coefficient would be also expected in ellipticals, hence in blue spheroidals, with respect to compact. In our sample, ellipticals have $0.38 < G < 0.44$: half of the compact have the same range of Gini values, the other half have lower Gini.

Finally, $R_{80\%}$ seems to be the only parameter, at $z > 1$ able to sharply separate ellipticals

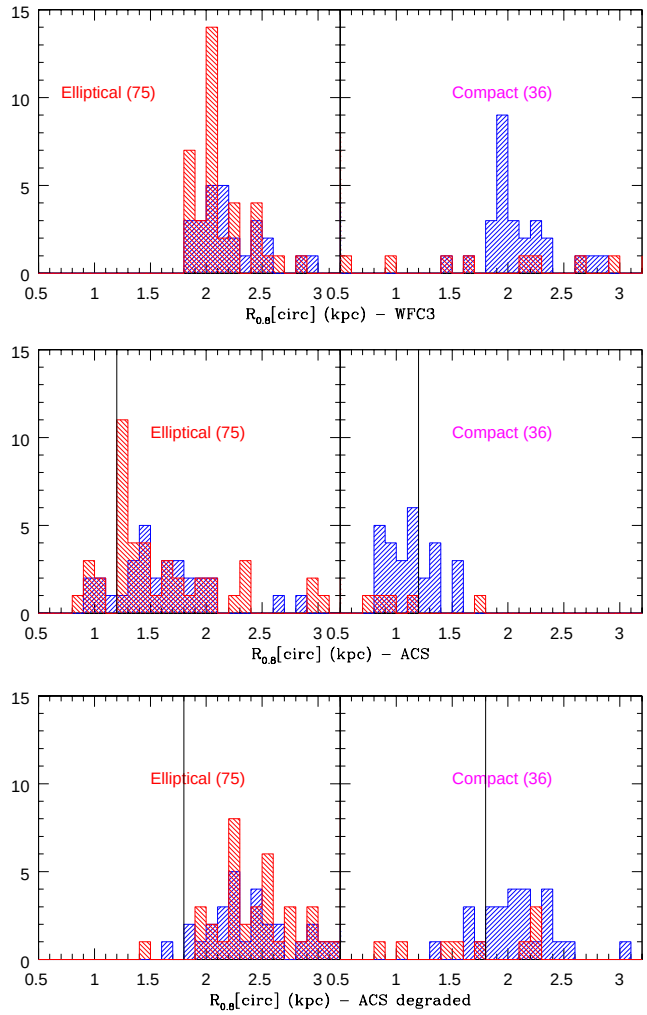

Fig. 4.20: Distribution of $R_{80\%}$ for the "blue cloud" (blue histogram) and the "red sequence", for galaxies morphologically classified as ellipticals and compact. Values are shown for: H_{160}, z_{750}, degraded z_{750} images. Histograms are normalized to the total number of galaxies in each morphological class: in each box the sum of the blue and the red histograms is 1.

and compact, on a pure morphological basis.

After all these considerations, we can conclude that the galaxies that we called "blue spheroidals" are, on a pure morphological base, more similar (in fact, practically indistinguishable) to red ellipticals than to compact objects. Of course, more checks of other morphological features will have to be done in order to strengthen the classification.

Blue galaxies with an elliptical appearance, in the local Universe and up to redshift $z \sim 1$, have been already discovered (Kannappan et al. 2009; Cassata et al. 2007; Im et al. 2001;

Lee et al. 2006; Huertas-Company et al. 2010), though the recognition of these galaxies as a "population" is quite recent. At high-redshift, we notice that, in the star-forming galaxies sample analysed by Law et al. (2012b), a fraction of their Type I galaxies (single, nucleated sources) shows an elliptical morphology, according to our classification. Conselice et al. (2011), for a sample of HUDF galaxies, compared the morphological classification to the spectral type obtained from SED fitting to broad-band photometry. They found that there is a significant difference in the population of galaxies classified as early/mid/late types as defined by spectral-types and those defined through visual estimates. The most common difference is found for galaxies classified as elliptical: a significant fraction of theese have a disk spectral type, suggesting a mixture of old and young stars, or even a starburst spectral type. However, the properties of these galaxies were not examined in the Conselice et al. (2011) paper. This is, to our knowledge, the first time that a sample of blue spheroidals is recognized as such and studied, at high-redshift.

The distribution of the physical properties of the samples of red ellipticals and blue spheroids shows that, though sharing similar morphological features, they are two very distinct classes of objects. In particular, red ellipticals have all the characteristics of quiescent or passive galaxies: high stellar masses ($log(M_{\odot}) \geq 10$) and low to null star-formation activity ($log(sSFR) < -10$). On the other hand, the blue spheroids are in the low mass end of the total mass distribution ($log(M_{\odot}) \leq 10$), have SFRs going from tens to hundreds $M_{\odot}yr^{-1}$ and also show a wide range of dust extinction ($0 < E(B-V) < 0.5$). 24 galaxies out of 30 also have a spectrum, and are all spectroscopically classified as star-forming galaxies. Three objects make an exception, being spectroscopically identified AGNs: two of them are the two great outliers from the blue sequence that may be seen in the lowest z bin in Fig. 4.15.

Kannappan et al. (2009), in their study of local blue ellipticals, find that the occurrence of this category of galaxies is related to the mass, with blue ellipticals becoming more common with decreasing stellar mass. They also establish threshold masses marking the appearance (($M \sim 10^{11} M_{\odot}$)) and the growth in number fraction (($M \sim 4-6\times10^{9} M_{\odot}$)) of these galaxies, with which our sample is fairly consistent. They also analyse the sSFRs of blue ellipticals, finding that they are comparable to those of spirals, something that we observe too in our sample. cassata2010 report that $z \sim 0.7$ blue ellipticals have smaller physical half-light radii than red early-type, while we found that the two populations, in our sample, have comparable sizes.

Blue spheroidals are likely objects in a transitional state of evolution. For example, they

could be non-interacting low mass galaxies that are building up their stars and then will slowly passively evolve into local ellipticals. Or they could be post-merger galaxies eventually destined to fall in the red sequence, or disk-building systems. Kannappan et al. (2009) propose both latter options to be valid, with the mass being the dominant characteristic to separate the two scenarios: higher mass galaxies in their blue elliptical sample resemble major-merger remnants, while most low mass galaxies show signs of disk building, which may be enhances by companion interactions.

4.7 Conclusions

The aim of this section was to study the rest-frame optical morphology of galaxies at intermediate to high redshift, using mainly the most recent IR images from HST WFC3, which sample the rest-frame optical regime, and to relate the morphological features to the physical properties of the galaxies.

The results of our analyses my be summarized as follows:

1. The fraction of elliptical galaxies drops going from $z = 1$ to $z \sim 4$; so does the fraction of disks. The high redshift galaxy population is, in fact, dominated by irregular galaxies. Up to $z \sim 2.5 - 2.7$, Hubble morphological types are still recognizable, while this is no more true at $z \sim 3$. Therefore we can place the build up of the Hubble sequence around $z \sim 2 - 3$.

2. Typical sizes of the ellipticals, parametrized by $R_{1/2}$, are between 1 and 2.5 kpc, while disks and irregulars go up to ~ 5 kpc. Disks and ellipticals have smaller sizes at higher redshift.

3. Galaxies with little to no star-formation have quite a defined morphology, almost all of them being ellipticals. Star-forming galaxies, on the other hand, show a wide range of morphologies, as it happens at $z \sim 0$. In particular, an irregular appearance is always associated to star-formation activity.

4. Between the most commonly used non-parametric statistics, the GvsM20 plane proves to be the more effective in segregating different morphological type: ellipticals and irregulars occupy quite defined regions, with ellipticals having higher G and more negative M20, meaning that they are the more concentrated and regular objects. The asymmetry is not as good in separating different morphologies

at high-redshift as it is in the local Universe. High redshift galaxies, in general, are much more asymmetric than local ones, regardless their morphological type. Disk galaxies do not have a preferential region in neither of the planes that were explored, spanning a wide range in all parameters.

5. By comparing WFC3 with ACS imaging, we explored the role of the morphological k-correction between the rest-frame UV and optical appearance of our galaxies. We concluded that, at $1 < z < 3$, there is no evidence of a significant morphological k-correction.

6. Though, looking at morphologies in a quantitative way, some differences arise. In particular, ellipticals, compact and irregular galaxies appear slightly more concentrated at shorter wavelengths compared to optical ones, while disks show the opposite trend. The greatest difference with wavelength is found in the M20 parameter, with ellipticals and compact showing a positive gradient, meaning that eventual signs of mergers would be more likely to be found in longer wavelength imaging, while disks have a negative gradient, indicating that very young stars responsible for the production of UV light have a more irregular spatial distribution with respect to the totality of stellar populations that make up the light originating in the rest-frame optical.

7. Some objects with a H_{160} morphological classification but faint appearance in ACS_{deg} imaging were found in the sample. Since they have intermediate to high masses, with respect to the total sample, and high SFRs, these objects are probably dusty star-forming galaxies, in which the UV signal coming from young stars is almost entirely absorbed, while what we see in the optical regime is a mixture of nebular emission and light from older stellar populations.

8. In our sample we confirm the existence of a rest-frame colour bimodality, holding up to redshift $z \sim 2.3$, with galaxies segregating in a red sequence and a blue cloud when put in a colour-stellar mass diagram. Morphologies tend to follow the bimodality in the sense that almost all ellipticals fall under the red peak, while irregulars and compacts inhabit the blue one. Disks are a mixed category, showing a blue and a red peak in their distribution, but also populating the intermediate region.

9. The colour of the fraction of irregulars and disks in the red sequence may depend by a combination of factors, such as reddening by dust, or inclination effects. In

our sample we found that the large majority of red late-type galaxies are likely spirals dominated by a bright bulge.

10. We discovered a population of blue, star-forming galaxies with the same morphological properties of red ellipticals. The physical properties of these "blue spheroidals" make them an entirely different population with respect to the red ellipticals. They have low masses, high star-formation rates and display a wide range of extinction values, though showing morphological features undistinguishable to those of red ellipticals. The true nature, and possible evolution, of these objects is yet to be understood: they could be non-interacting low mass galaxies that are building up their stars and then will slowly passively evolve into local ellipticals, or major-merger remnant or disk-building systems.

CHAPTER 5

Star-formation rate and dust extinction

5.1 Introduction

In this chapter we study the star-formation of galaxies from intermediate up to high redshift and the effects of dust extinction, by comparing different star-formation rate indicators. The sample consists of galaxies which were all observed spectroscopically. Our analysis benefits from the wealth of information available in the GOODS-South field: optical and near infrared photometric data (from U to Ks bands, plus the four IRAC bands), optical spectra from ESO public surveys, ultra-deep optical spectra from the GMASS survey. Above all, we will use far infrared data coming from two HERSCHEL projects: PEP and HerMES. HERSCHEL observations cover far infrared bands up to 500 μm, thus allowing us to better constrain the integrated infrared luminosity than ever done before.

Before focusing on the SFR, the HERSCHEL IR data will be used to infer IR luminosities (LIR), for our sample of galaxies, by fitting the photometric data with semi-empirical synthetic SED libraries.

5.2 The data sample

The *extended GMASS spectroscopic high-z sample*, introduced in chapter 3, was used as starting point. We choose to concentrate on a spectroscopic sample in order to achieve the highest possible precision in the redshift determination. This requirement allows us to rule out at least one source of uncertainty in the interpretation of the analysed observables. This also introduces a bias towards brightest (in the rest-frame UV) and more star-forming objects, that will be taken into account in the interpretation of the results.

Since our aim is to study the star-formation in normal galaxies at $z \geq 1$, the *extended GMASS spectroscopic high-z sample* had to be cleaned of non star-forming galaxies and of active galactic nuclei (AGNs). We notice that the properties of passive galaxies belonging to the GMASS survey were already discussed in Cimatti et al. (2008) and Cappellari et al. (2009). All the spectra not belonging to the GMASS survey were re-classified, and their redshift were checked. 19 galaxies were found to have unreliable redshift and classification, and were subsequently excluded from the sample. 35 galaxies with an early-type spectrum were also excluded. Intermediate objects, i.e. with a spectrum showing a red continuum but also emission lines, were kept, but with a specific flag. Fig. 5.1 to 5.3 show examples of the different spectral types identified in our sample.

To ensure as much as possible the exclusion of all active galaxies from the sample, the AGN identification was conducted using three different classification methods: spectra, X-ray detections and optical to near-IR SED fitting. The spectral identification was done searching for broad emission lines, typical of Type 1 AGNs, or narrow CIV λ1549 Å, typical of Type 2 AGNs. 10 objects were found that showed such features in their spectra, and were excluded from the sample.

For the remaining 343 objects, all spectroscopically classified as intermediate (33 objects) or star-forming (310 objects) galaxies, the Chandra 4Ms catalogue *(xue2011)* was checked, searching for X-ray counterparts. Within an angular separation of 2", 32 X-ray counterparts were found. In the Chandra catalogue the absorption-corrected, rest-frame 0.5-9 kev luminosities are also reported. A threshold of $L_x = 3x10^{42}$ was chosen to separate secure AGNs from doubtful cases, following the AGN identification criteria given by Xue et al. (2011). 14 objects with an X-ray luminosity $L_x > 3x10^{42}$ erg/s were excluded from the sample. The 18 objects with an X-ray detection, but $L_x < 3x10^{42}$ erg/s were kept with a specific flag.

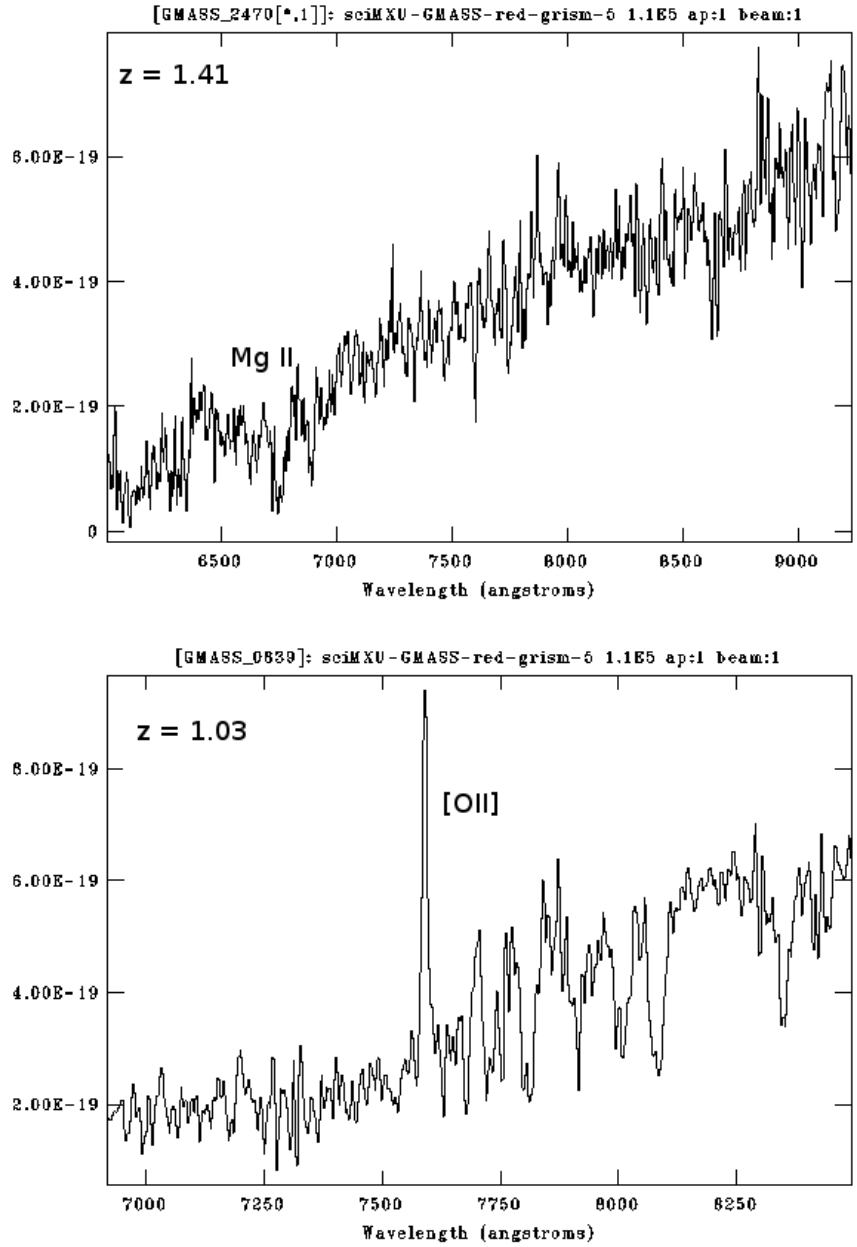

Fig. 5.1: Examples of different spectral types identified in our sample. Spectra are shown in observed wavelengths and fluxes in units of erg/s/cm^2/Hz. For each spectrum the spectroscopic redshift of the galaxy is indicated. Main identification features are also marked. Top: early-type spectrum (characterized by a very red continuum and rich of metal absorptions); bottom: intermediate spectrum (red UV continuum and [OII]λ3727 emission line).

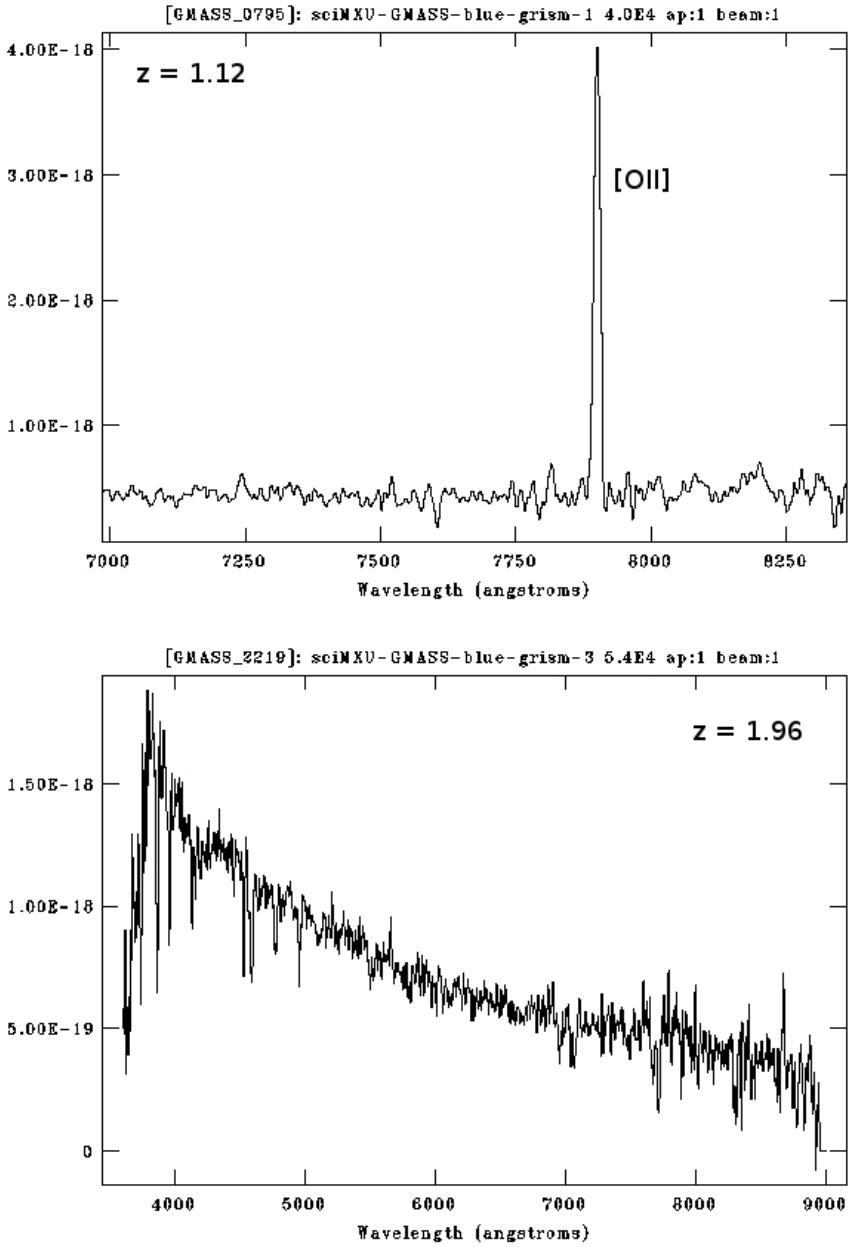

Fig. 5.2: As in Fig. 5.1. Top: SFGs at $z < 1.4$ (strong [OII] emission line); bottom: SFGs at $z > 1.4$ (ISM absorption lines: see chapter 6 of this thesis for more details).

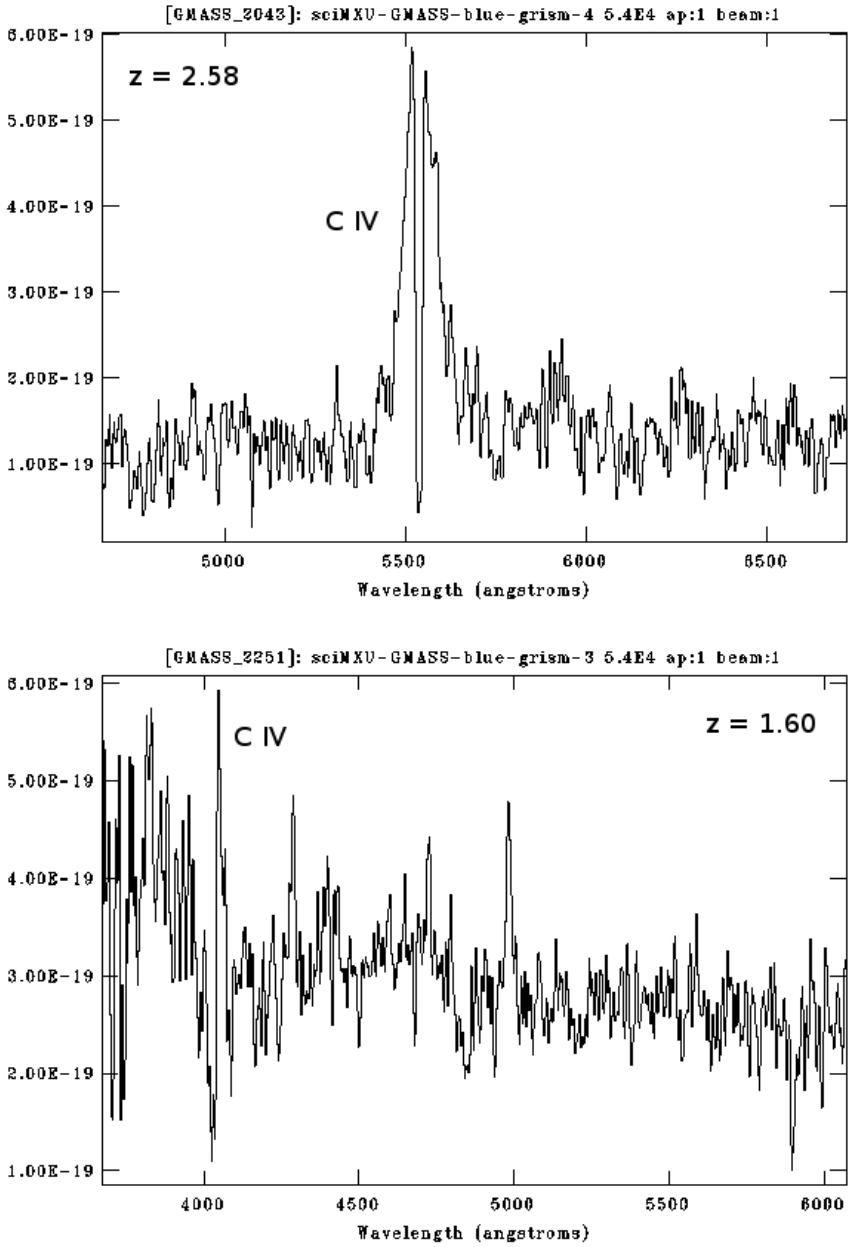

Fig. 5.3: As in Fig. 5.1. Top: type 1 AGN (broad emission lines); bottom: type 2 AGN (narrow CIV λ1549 Å emission line).

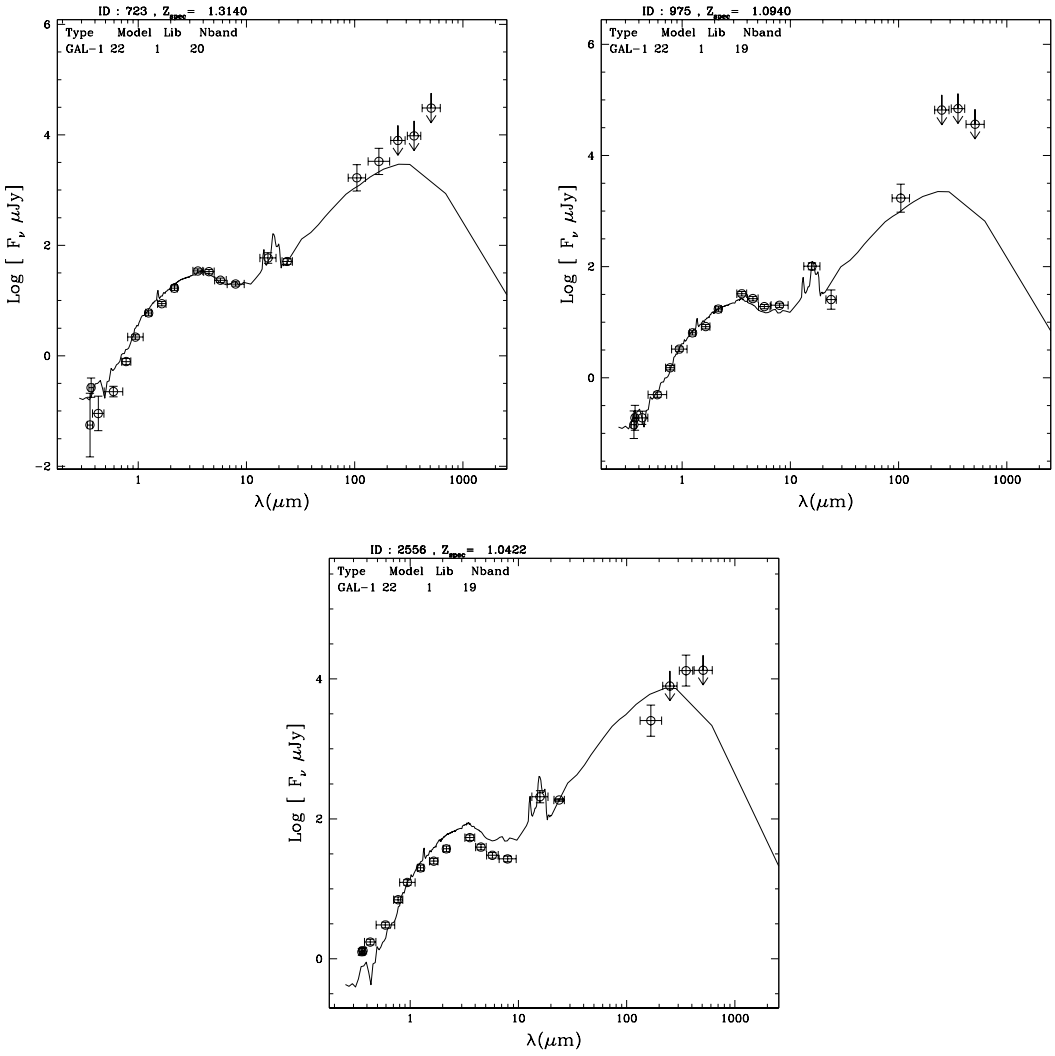

Fig. 5.4: Fit of optical-to-IR SED to Polletta et al. (2007) templates for the three galaxies identified as AGNs. The points are the photometric data, with their errors. Arrows mark upper limits. The line is the best-fit template from Polletta et al. (2007) library.

The last search for AGN was done in the IR regime, by fitting the photometric data from U band to the furthest IR band with a library of template SEDs of local objects by Polletta et al. (2007). This library includes elliptical, spiral, starburst, AGN and composite starburst-plus-AGN templates. 2 objects were found to be best fitted by an AGN (Seyfert 2) template, and were excluded from the sample. We also excluded a third object identified as an AGN, though with a poor fit, to be as much conservative as possible (see Fig. 5.4). 5 galaxies SED were fitted by a composite starburst-plus-AGN template, and were kept in the sample, with a specific flag. This AGN identification method, at least for galaxies at $z > 1$, is the less reliable among the ones here proposed, and must be

used with caution. For many of our galaxies, Polletta et al. (2007) templates could not provide a goof fit (or any fit, in some cases) to the photometric data. In general, in some cases Polletta et al. (2007) templates may give a hint on the spectral type of a galaxy at high-redshift, but in many other cases they are not able to correctly reproduce the optical-to-IR SED. Some modifications to this library, to try to better reproduce the SED of high-redshift galaxies, have been proposed, for example by Gruppioni et al. (2010).

Given the aforementioned caveats, though all our efforts to clean the sample from active galaxies, it must be noticed that some obscured AGN may be left in the final sample.

The described selection criteria led to the creation of a final sample of 326 SFGs (*326-SFGs sample*). In Fig. 5.5 the redshift distribution of the final sample, compared to the parent ones, is shown.

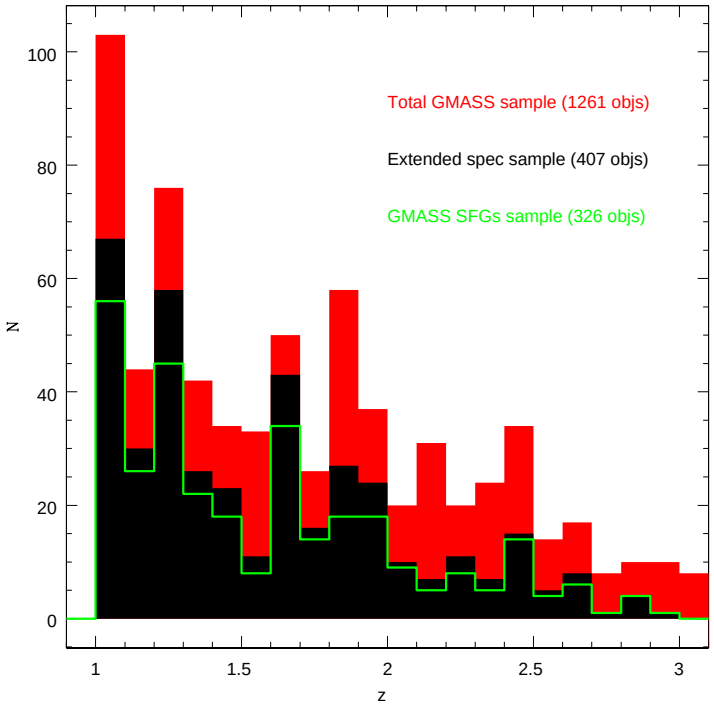

Fig. 5.5: Redshift distribution. The red histogram represents best-redshift (spectroscopic or photometric) distribution of the GMASS sample at $z \geq 1$; the black histogram represents the spectroscopic redshift distribution of the extended spectroscopic sample. The green empty histogram represents the spectroscopic redshift distribution of the SFGs sample.

5.3 The infrared luminosity (LIR)

The first SFR estimator to be analysed, against which the other estimates will be compared, is based on the total IR luminosity (LIR), which is defined as the integrated luminosity between 8-1000 μm. The conversion from LIR to SFR, for high-redshift galaxies, relied since now on great extrapolations, due to the lack of far infrared data needed to better constrain the galaxy SED. When only one photometric band is available, usually the MIPS 24 μm, the LIR of a galaxy is recovered by fitting the flux measured in the single photometric band to different sets of SED libraries: the SED models are shifted according to the redshift of the source, and then the one is chosen which matches better the observed flux in the selected band. Finally, the template is normalized to perfectly match the observed flux.

This method is of course severely model dependent. Moreover, for high-redshift galaxies ($z \sim 2$), 24 μm fluxes probe a wavelength range far from the SED peak, making these estimates sensitive to extrapolation errors. In addition, at the rest-frame wavelengths corresponding to the 24 μm band, polycyclic aromatic hydrocarbon (PAH) emissions contribute significantly and the ratio of their fluxes to LIR may create significant scatter (Nordon et al. 2010).

HERSCHEL data allow us now to begin to discriminate between the different SED libraries and to partially solve the limitations in recovering the total LIR of a galaxy when only a single photometric point is available.

5.3.1 IR SED libraries: description

Five sets of libraries, among those most commonly used in the literature, were considered at the beginning: Chary & Elbaz (2001) (CE01), Dale & Helou (2002) (DH02), Lagache et al. (2004) (L04), Polletta et al. (2007) (P07) and Rieke et al. (2009) (R09). For a complete description of the different libraries, we refer to the cited papers. Briefly, these are the main characteristics of the libraries.

CE01 library is a set of 105 synthetic template SEDs built to reproduce the observed mid infrared vs. far infrared luminosities correlations for local galaxies; their shape is luminosity dependant.

DH02 library is a set of 64 semi empirical SEDs, with the shape and normalization of

each determined by the intensity of the interstellar radiation field, normalized to the local interstellar radiation field.

L04 library is a set of 46 template SEDs of normal and starburst galaxies constructed from a phenomenological galaxy evolution model to fit the local IR luminosity function. A single form of SED is associated with each activity type and luminosity.

P07 library was already introduced in a previous section: it is a set of 25 templates constructed composing synthetic models and real data, including different types of galaxies, from ellipticals up to starbursts and AGNs. The templates cover the entire optical-to-IR wavelength range, but for this analyses we used only the IR range, i.e. $\lambda \geq 5\mu m$.

R09 library is a set of 25 SEDs: 11 of them are real SED of local IR-luminous galaxies, while the others are synthesized SEDs of 14 average templates in a sequence of increasing infrared luminosity.

It is important to notice here that CE01 have a physically realistic calibration for wavelengths longer than $\lambda_{rest} > 6\mu m$, while the validity range of DH02 and L04 libraries starts for wavelengths longer than $\lambda_{rest} > 3\mu m$. Due to this fact, the photometric points sampling a wavelength regime shorter than the cited ones, depending on the redshift of the source and the selected library, were not used in the analysis.

5.3.2 Testing the IR SED libraries

To establish which is the set of models that better reproduces the observed SEDs, an SED fitting procedure based on χ^2 minimization was applied to the galaxies of our sample with a MIPS 24 μm detection plus at least one other photometric point in the far infrared regime, using as templates all the available sets of IR libraries together. The 5σ flux thresholds from PEP and HerMES surveys where imposed as upper-limits for the non-detected PACS and SPIRE bands. LIR errors were determined by randomizing the observed fluxes, according to their errors, and assuming a normal distribution for the flux distribution, then repeating the template fitting to derive a new luminosity. This step is repeated a large number of times and the r.m.s. of the measured luminosities is adopted as the error on LIR (see Nordon et al. (2012)).

Fig. 5.6 shows the success rate of each set of libraries in achieving the best χ^2: for galaxies with at least two photometric points in the IR regime, though DH02 library has the lowest success rate, while CE01 and L04 have the highest, there is not a strong

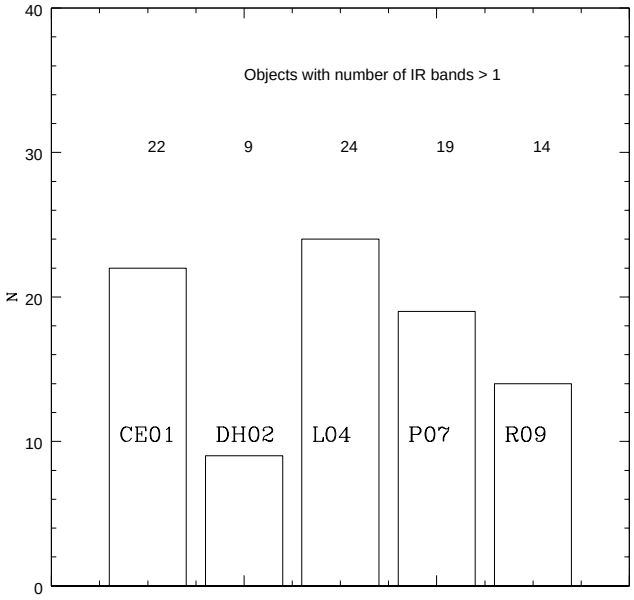

Fig. 5.6: Results of the SED fitting procedure applied to the *326-SFGs sample* using all the available sets of IR libraries together. The histogram shows the "success rate" of each set of libraries (i.e. achieving the best χ^2).

favourite template library. Fig. 5.7 shows some examples of IR SED for galaxies with at least one HERSCHEL photometric point.

The SED fitting procedure was then applied to the sample using the available sets of libraries separately. The recovered LIR were then compared with the ones computed using all the IR libraries together. Fig. 5.8 shows that, when more than one IR photometric point is available, the mean scatter from the 1-to-1 relation is below 0.3 dex for all the sets of templates, apart from a couple of strong outliers ($\sigma > 1$ dex). The fact that some of these galaxies are also X-ray sources, or have an intermediate spectrum, is not correlated to the distance from the 1-to-1 relation. In Fig. 5.9 we show some examples of the results obtained by fitting the IR photometry of a galaxy with the five different sets of model libraries.

The conclusion is that, to recover the LIR of a galaxy, the analysed libraries are almost interchangeable, for practical purposes, if at least 24 μm plus another redder photometric point are available.

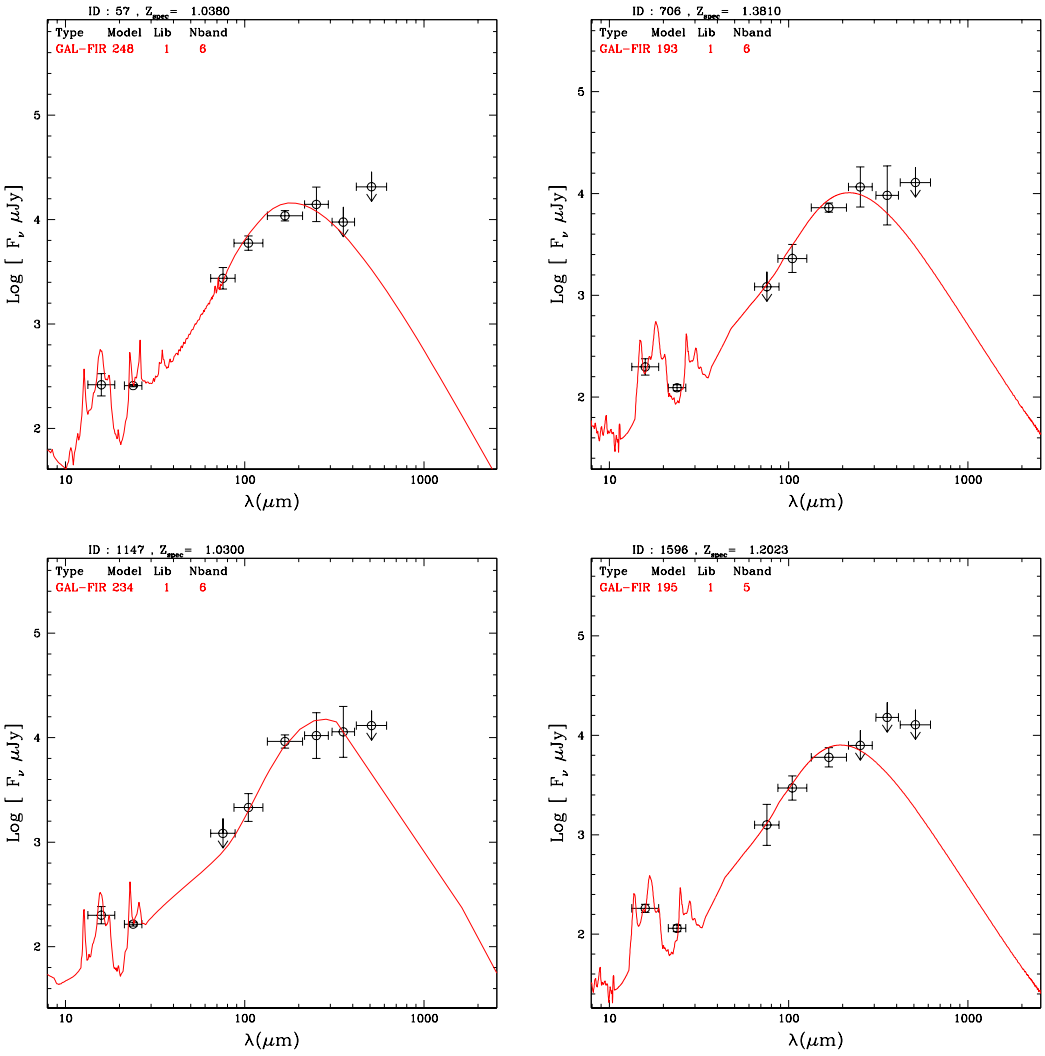

Fig. 5.7: Some examples of best-fit IR SEDs. The continuous red line is the best-fit model, respectively from R09 library (GMASS 0057), L04 library (GMASS 0706, GMASS 1596) and P07 library (GMASS 1147). The points are the photometric data, with their errors. Upper limits are marked with arrows.

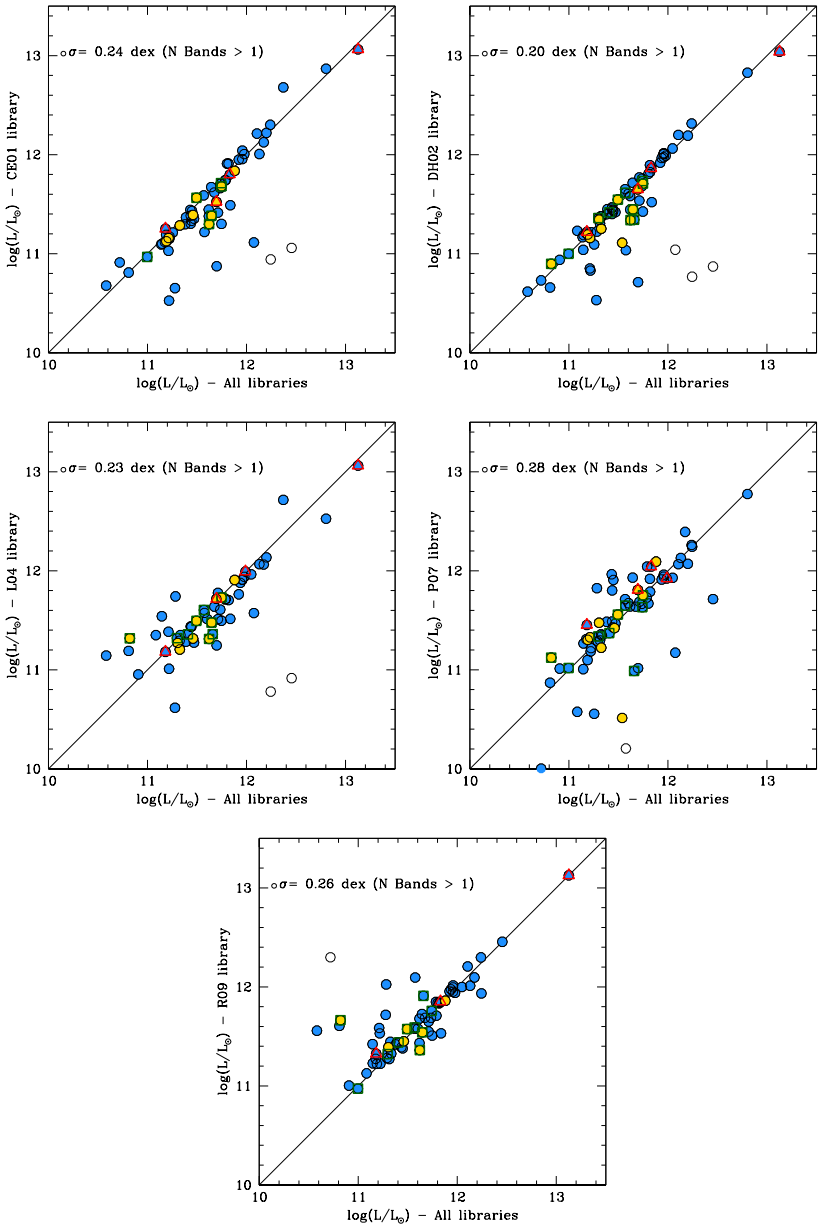

Fig. 5.8: Comparison between LIR from SED fitting using all the available IR libraries together as templates, and LIR obtained using the different libraries separately. Galaxies whose LIR lies on the 1-to-1 relation by construction are not shown. The standard deviation of the points from the 1-to-1 relation is also indicated (strong outliers are not considered). Strong outliers ($\sigma > 1$ dex) are indicated by empty points. Colour and shape legend - Blue points: galaxies with star-forming spectrum; gold points: galaxies with intermediate type spectrum; dark green squares: galaxies with X-ray detection ($L_x < 3x10^{42}$ erg/s); red triangles: galaxies with composite SB+AGN UV to IR SED.

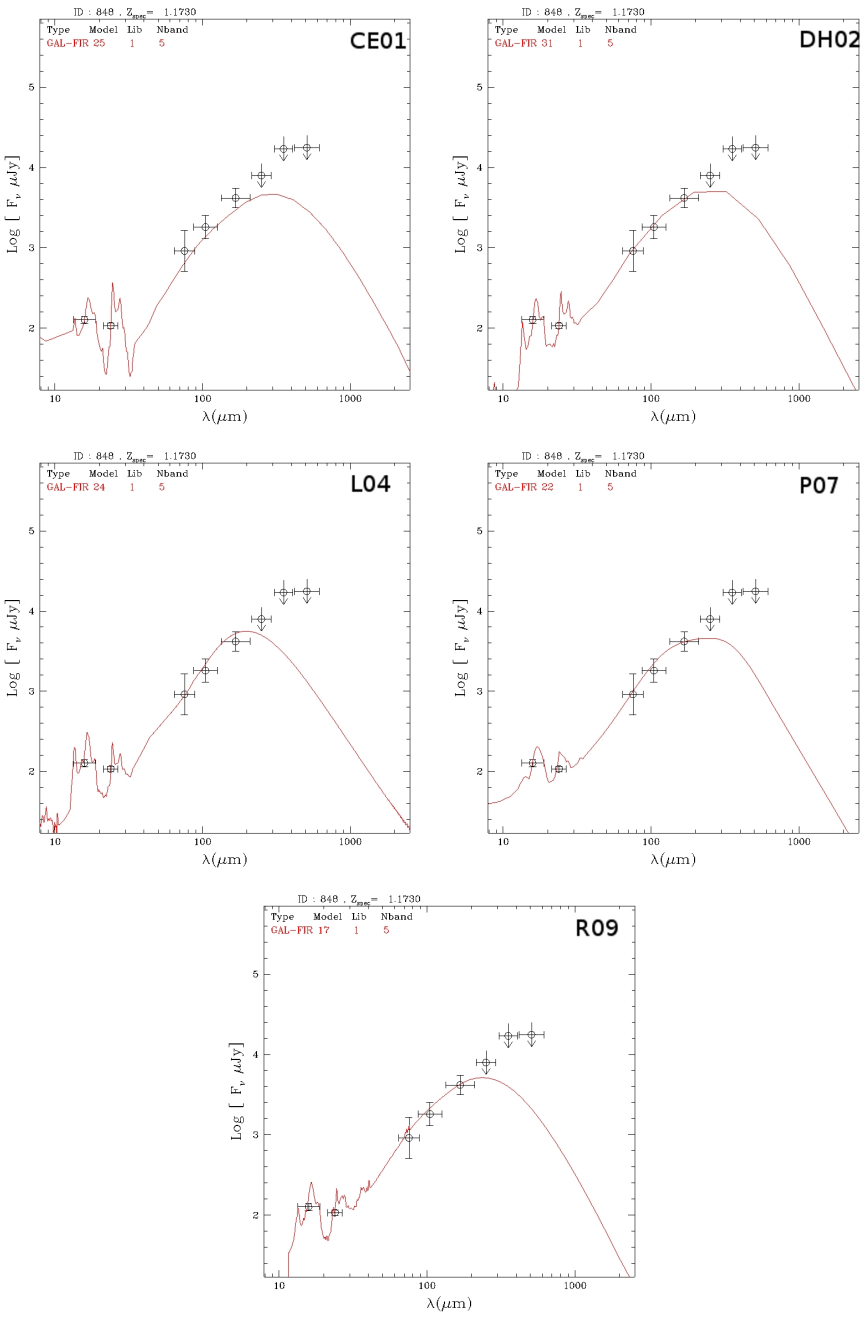

Fig. 5.9: Best-fit SEDs for galaxy GMASS 0848. The best-fit SEDs obtained using separately the five IR libraries are shown. In each plot, the red line is the best-fit model; the points are the photometric data, with their errors. Upper limits are marked with arrows. The best χ^2, in this case, is achieved with R09 library.

Peculiar objects

Three galaxies in our sample were found whose SED non of the model libraries were able to correctly reproduce. These galaxies are presented in Fig. 5.10. The SPIRE data, that sample the peak of IR emission, seem to suggest that dust in these galaxies might be colder than the predictions of the models. These three galaxies will be the subjects of a deeper investigation, to establish if they really have unpredicted dust properties and which exactly these properties are, but this is beyond the scope of this work.

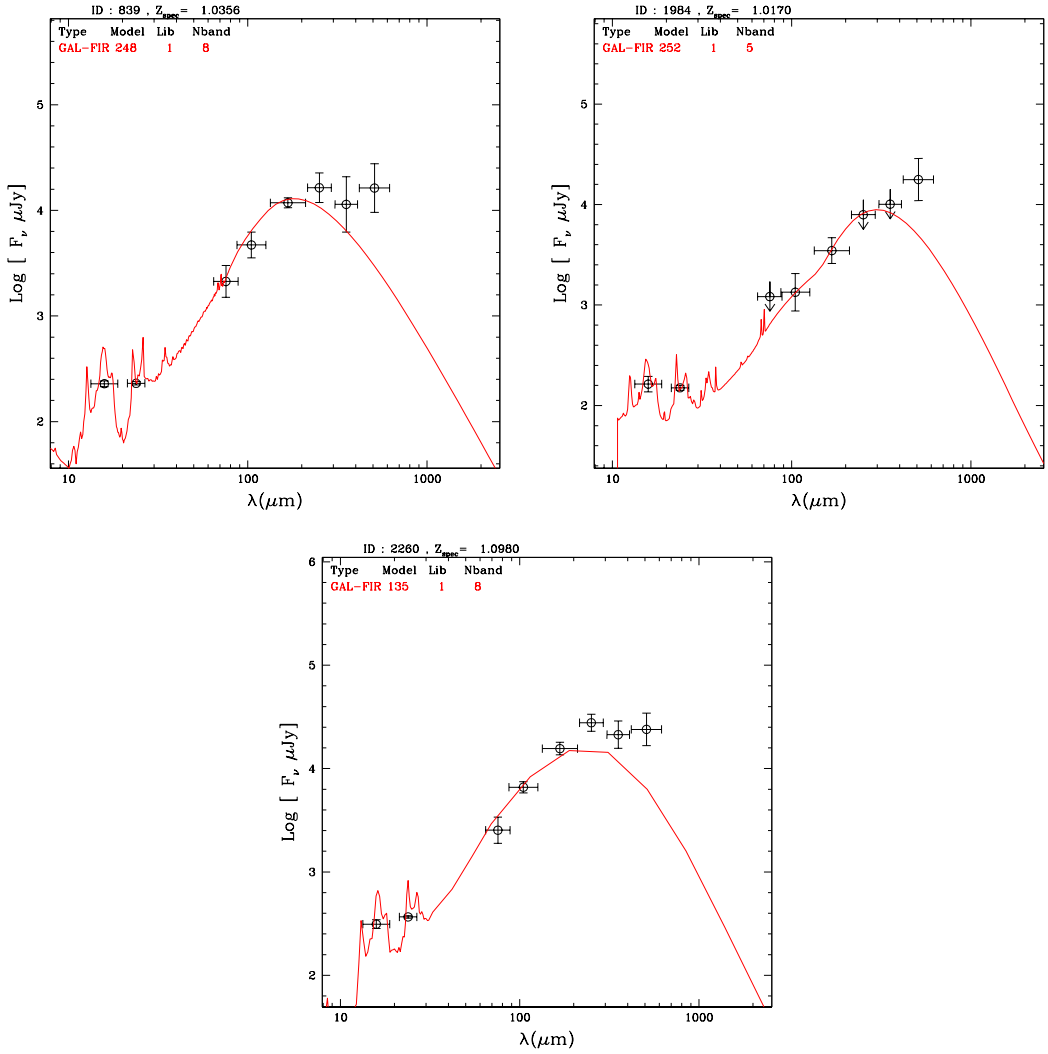

Fig. 5.10: Best-fit SEDs of three peculiar galaxies, with at least one SPIRE photometric point, whose SED no model library was able to correctly reproduce. The red line is the best-fit model; the points are the photometric data, with their errors. Upper limits are marked with arrows.

In the sample here analysed, these three galaxies are one seventh of the galaxies with at least one SPIRE point, which are the data needed to constrain the peak of the IR emission, given the redshift of our sample galaxies. Therefore it would be also very useful to search for similar cases in larger samples of SFGs, with available SPIRE data, to check if these peculiarities are common at high redshift, or not.

5.3.3 LIR from 24 μm flux only: CE01 and DH02 calibration

As previously described, when only the 24 μm points is available, the traditional way of recovering the total LIR is to shift the SED models according to the redshift of the source, then choosing the one that matches better the observed flux in the selected band; finally, normalizing the template to perfectly match the observed flux. The libraries most widely used in the literature are CE01 and DH02. Here, by using HERSCHEL data, we want to test the robustness of these two libraries in the extrapolation of the total LIR when only the 24 μm is available.

To do this, the galaxies with at least two photometric points in the IR regime (i.e. 24 μm plus at least one HERSCHEL band) were selected. The LIR was computed using only the 24 μm and the traditional method. These LIR_{MIPS} values were then compared with the ones computed with the same library, but using all the available IR photometric points (MIPS+PACS+SPIRE; $\mathrm{LIR}_{allbands}$) and a χ^2 minimization fitting procedure. The results are shown in the first panels of Fig. 5.11 and 5.12.

CE01 library has a very robust LIR extrapolation from the single 24 μm band up to $\mathrm{LIR}_{MIPS} \sim 12.2$, that means for galaxies at redshift $z \leq 1.7$, while for LIR_{MIPS} above 12.2 (and $z \geq 1.7$), using only one band, leads to a systematic overestimate of the total IR luminosity, as already noted by other authors (Nordon et al. 2010; Elbaz et al. 2010, 2011). On the other hand, DH02 library show a constant offset with quite a small scatter. For both CE01 and DH02 libraries the results obtained for galaxies with more than one photometric point were used to get relations to correct LIR_{MIPS}. One single linear fit was applied to calculate the calibration relation for the DH02 libraries, while a two linear fits were used for the CE01 case. The second panels of Fig. 5.11 and 5.12 show the fits and the corresponding calibration relations.

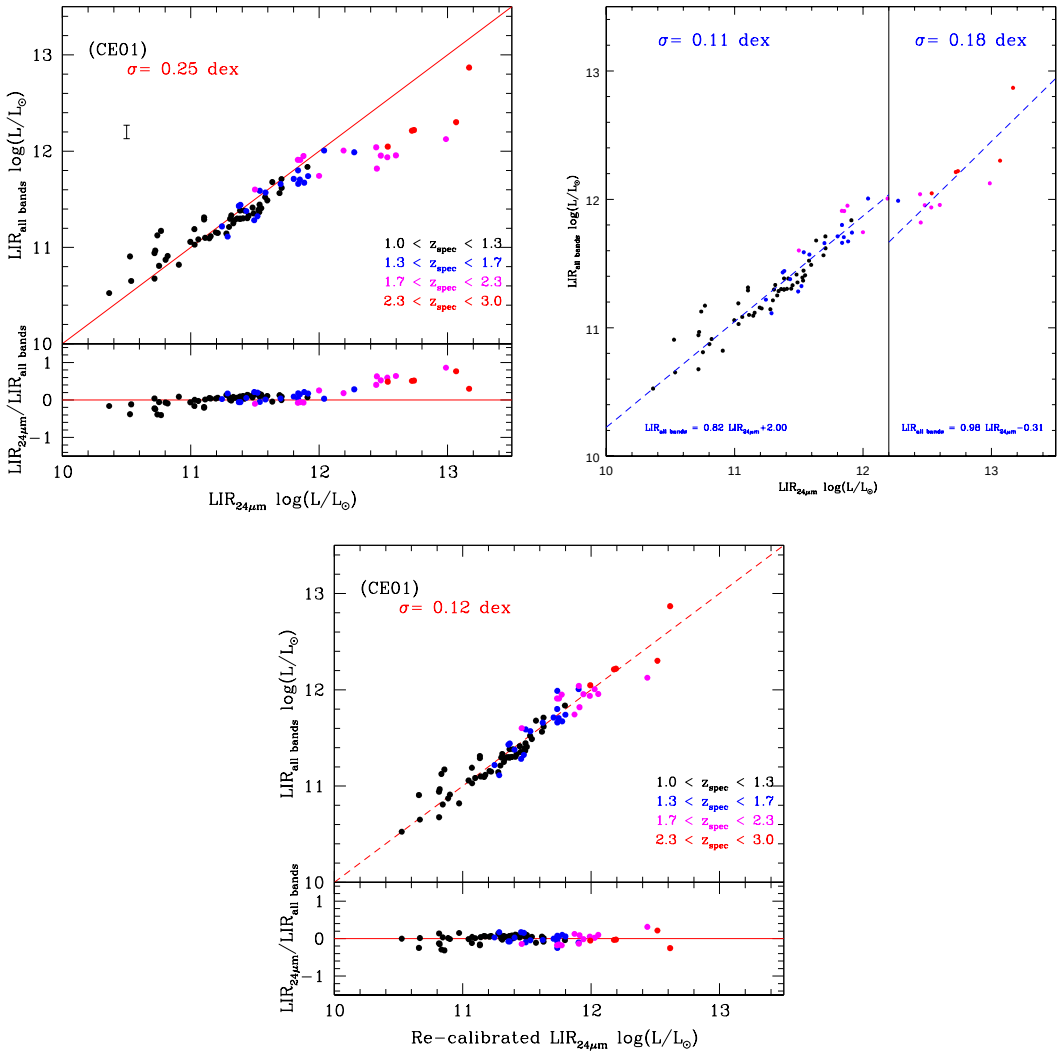

Fig. 5.11: Clockwise. First panel: comparison between LIR computed using all the available bands ($LIR_{allbands}$) and LIR computed using only the 24 μm flux (LIR_{MIPS}), for galaxies with at least two IR photometric points. In the insets, ratio between $LIR_{allbands}$ and LIR_{MIPS}. Second panel: linear fits to the points. The black vertical line indicates $LIR_{MIPS} = 12.2\ \log(L/L_{\odot})$. Standard deviations of the points from the shown relations are also indicated. Third panel: same as in the first panel, but using re-calibrated LIR_{MIPS}. Standard deviation of the points from the 1-to-1 relation is also indicated. Points are colour coded with respect to the redshift of the galaxies.

For CE01 libraries these relations are:

LIR = 0.82 LIR_{MIPS} + 2.00 [$LIR_{MIPS} \leq$ 12.2] (3.1a)

LIR = 0.98 LIR_{MIPS} - 0.31 [$LIR_{MIPS} >$ 12.2] (3.1b)

Where all LIR are given in units of $log(L/L_{\odot})$.

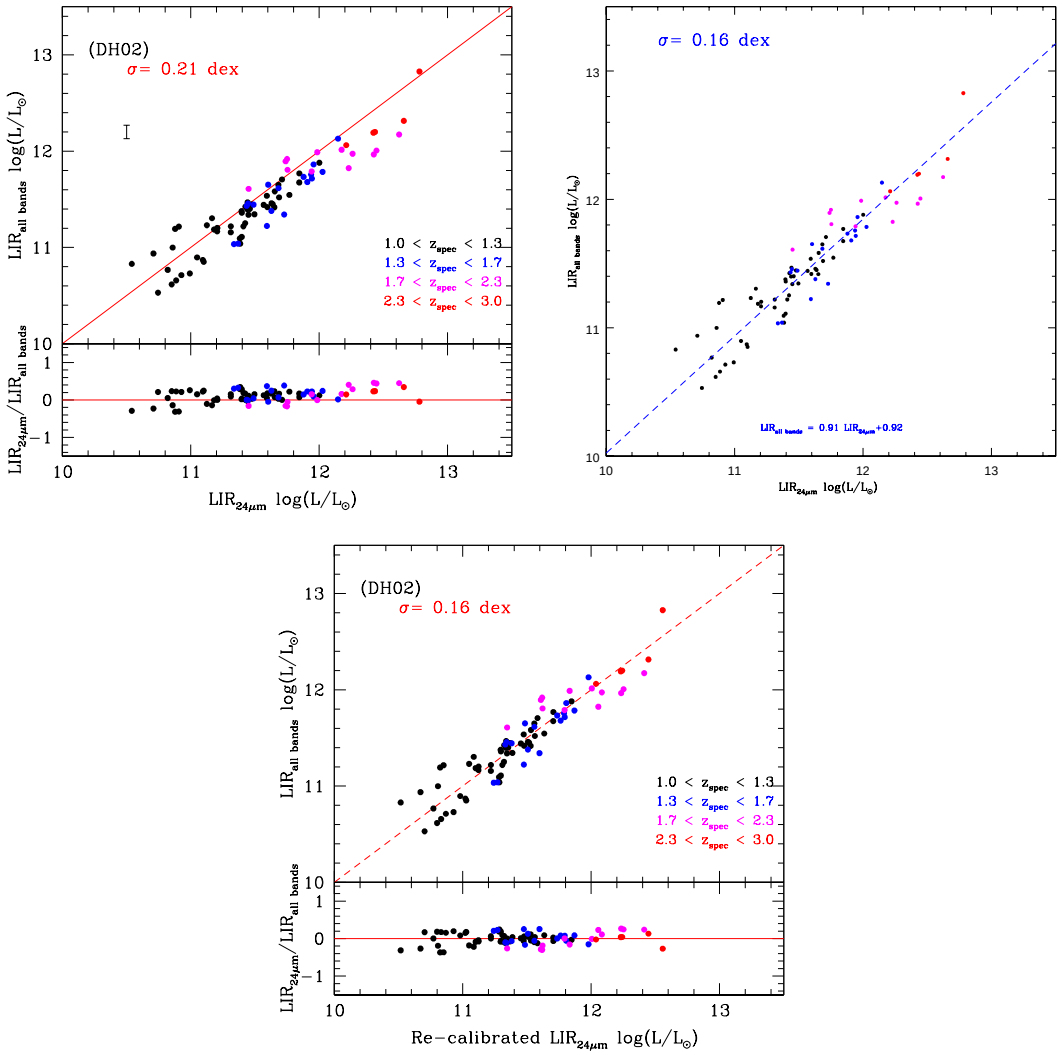

Fig. 5.12: Clockwise. First panel: comparison between LIR computed using all the available bands ($LIR_{allbands}$) and LIR computed using only the 24 μm flux (LIR_{MIPS}), for galaxies with at least two IR photometric points. In the insets, ratio between $LIR_{allbands}$ and LIR_{MIPS}. Second panel: linear fits to the points. Standard deviations of the points from the shown relations are also indicated. Third panel: same as in the first panel, but using re-calibrated LIR_{MIPS}. Standard deviation of the points from the 1-to-1 relation is also indicated. Points are colour coded with respect to the redshift of the galaxies.

For DH02 the relation is:

LIR = 0.91 LIR_{MIPS} + 0.92 (3.2)

for all LIR_{MIPS}.

The results of the comparison between $LIR_{allbands}$ and LIR_{MIPS}, after applying the aforementioned calibrations, are shown in the third panels of Fig. 5.11 and 5.12: after the

calibration, LIR_{MIPS} by both libraries show a much better agreement with $LIR_{allbands}$, but CE01 library is the most robust in recovering the total LIR, since it offers the smaller scatter from the 1-to-1 relation.

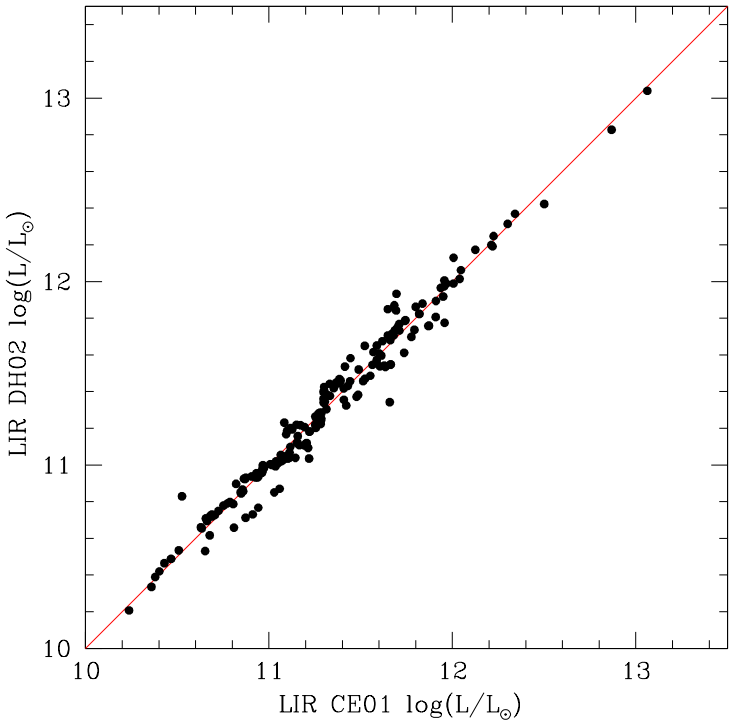

Fig. 5.13: LIR computed using CE01 libraries vs. LIR computed using DH02 libraries. $LIR_{allbands}$ (i.e. LIR computed using all the available IR bands) is plotted for the galaxies with more than one photometric point, while the LIR_{MIPS}, corrected following (3.1)-(3.2) calibrations, is plotted for the galaxies with only a 24 μm detection.

Using the our calibration relations, LIR_{MIPS} of the galaxies for which only the 24 μm is available were corrected. In the rest of this chapter, when talking about LIR, we will refer to $LIR_{allbands}$ (i.e. LIR computed using all the available IR bands and all the available libraries) for the galaxies with more than one photometric point, and to the LIR_{MIPS}, corrected following (3.1)-(3.2) calibrations, for the galaxies with only a 24 μm detection. In particular, in this chapter we will use the calibrated LIR_{MIPS} obtained by using the CE01 libraries, since we have verified them to be the most robust in recovering the total LIR, provided that the appropriate calibration is applied. We notice that the use of DH02 libraries would also be a good choice, since LIR computed using CE01 or DH02 libraries, correcting the LIR_{MIPS} with our proposed relations, are strongly consistent with one another (see Fig. 5.13).

5.4 Comparing different estimates of SFR

The LIR for 201 out of 326 galaxies in our sample were estimated. The LIR distribution obtained, as a function of redshift, is shown in Fig. 5.14. The points are colour and shape coded with respect to their inclusion flag in the *326-SFGs sample* (see legend of Fig. 5.8). Galaxies whose LIR was recovered only by MIPS-24 μm flux are also marked.

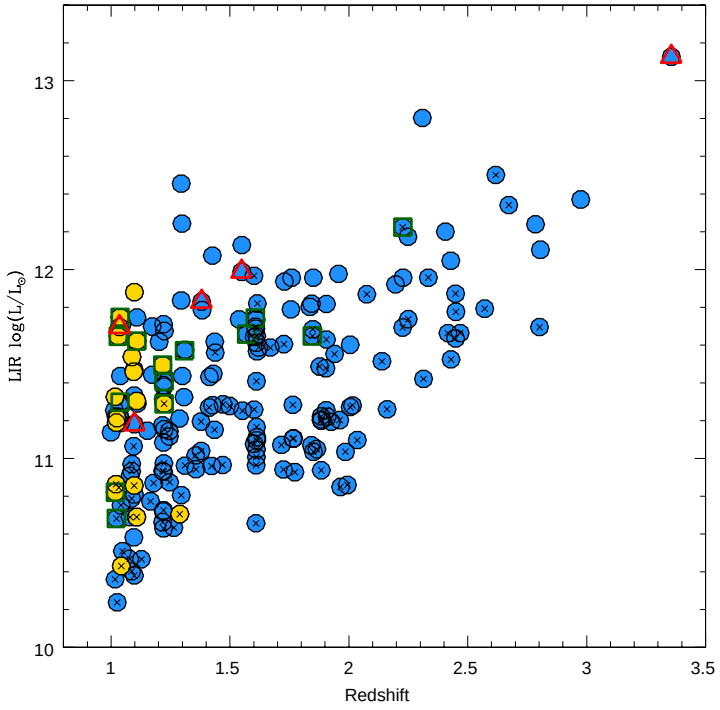

Fig. 5.14: LIR distribution over the sample, as a function of redshift. The points are shape and colour coded as in Fig. 5.8. Small crosses mark galaxies whose LIR was recovered only by MIPS-24 μm flux, with CE01 libraries and our (3.1) calibration.

LIR was then converted into SFR according to Kennicutt (1998), scaling the appropriate relation for a Kroupa IMF[8]:

SFR_{IR} ($M_\odot$ yr^{-1}) = 2.9×10^{-44} LIR (erg/s)

The conversion from LIR to SFR assumes that LIR represents the bolometric luminosity of the young stars. Since UV is detected anyway, this indicated that some radiation escapes and is not reprocessed into the IR. Therefore, a more correct estimate of the SFR should be obtained by adding to the SFR_{IR} a contribution derived from the observed UV

[8] $SFR_{Kroupa} = SFR_{Salpeter}/1.55$

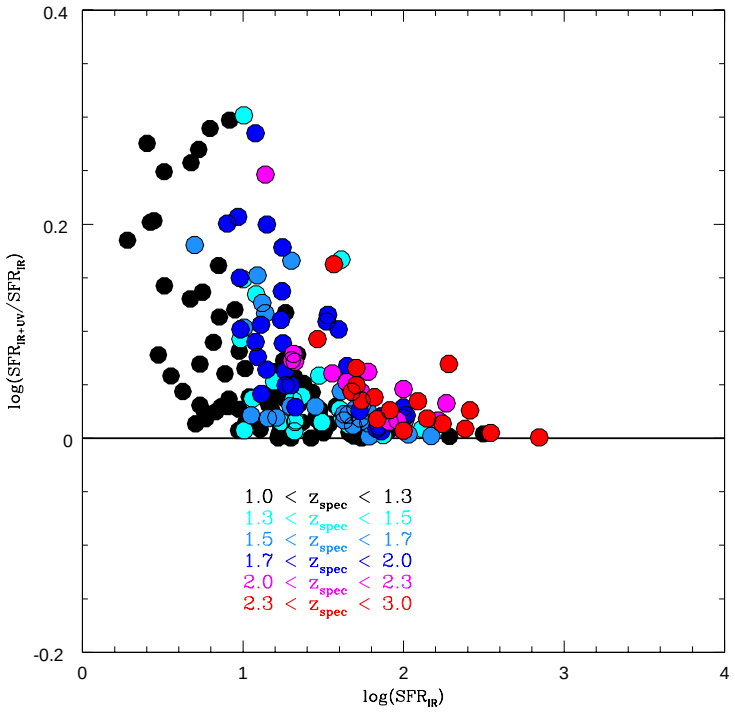

Fig. 5.15: SFR_{IR+UV}/SFR_{IR} vs. SFR_{IR}. Points are colour coded with respect to the redshift of the galaxies.

flux, not corrected for dust extinction (Wuyts et al. 2011; Nordon et al. 2012; Kennicutt & Evans 2012). Rest-frame flux at 1500Å was computed for all the galaxies in the sample[9] and converted into SFR using again the appropriate Kennicutt (1998) relation, without correcting in any way for dust extinction:

SFR_{UV} ($\mathrm{M}_\odot$ yr^{-1}) = $0.9 \times 10^{-28} \times \mathrm{L}_{1500\ \text{Å}}$ [erg s^{-1} Hz^{-1}]

We define $SFR_{IR+UV} = SFR_{IR} + SFR_{UV}$ and will take it as our main estimator against which compare the other ones available for our sample.

The contribution of SFR_{UV} to the total SFR is smaller in galaxies with high SFRs, where the quantity and distribution of dust is supposed to be as such to allow almost a complete reprocessing of star light, but in galaxies with low SFRs it may equal the contribution of SFR_{IR}: in these cases, considering the SFR_{IR} alone would lead to an underestimate of the total SFR (see Fig. 5.15).

[9]Our method consists of computing the absolute magnitude in a given filter X using the observed apparent magnitude in the filter Y, which is chosen to be the closest one to $\lambda(X) * (1 + z)$. The advantage of this method with respect to other ones is that it limits the template dependency. We computed the absolute magnitudes a square filter 300Å wide, centred on 1500Å.

5.4.1 SFR_{SED} vs. SFR_{IR+UV}

The physical properties of the galaxies belonging to the entire GMASS total sample, including SFR, A_v and stellar masses, were estimated by fitting the photometric data (extending from U band to the IRAC 8μm band) to the synthetic spectra of Maraston (2005) evolutionary population synthesis models (see Kurk et al. (2013) for further details); a Kroupa IMF (Kroupa 2001) and fixed solar metallicity were adopted. Star-formation histories were parametrized by exponentials ($e^{\frac{-t}{\tau}}$) with e-folding time-scales τ of between 100 Myr and 30 Gyr, plus the case of constant SFR. For the dust extinction, a Calzetti law (Calzetti et al. 2000) was assumed.

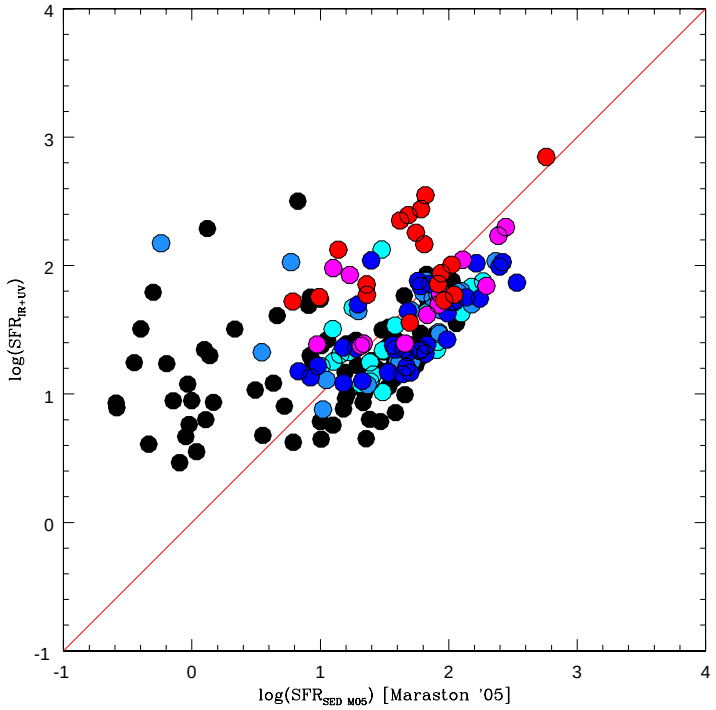

Fig. 5.16: SFR_{IR+UV} vs. SFR_{SED}. SFR_{SED} is computed using the evolutionary population synthesis models by Maraston (2005). Points are colour coded with respect to the redshift of the galaxies. See Fig. 5.15 for the legend. The red line marks the 1-to-1 relation.

In Fig. 5.16 we show the comparison between SFR_{SED} and SFR_{IR+UV}. For the majority of galaxies, the relation between the two estimates is quite tight, though M05 models tend to systematically overestimate the SFR, with respect to SFR_{IR+UV}. We note also a tail toward lower SED-modelled SFRs. This behaviour is consistent with the findings of Wuyts et al. (2011) for a K_s-selected sample of galaxies in the fields covered by HER-

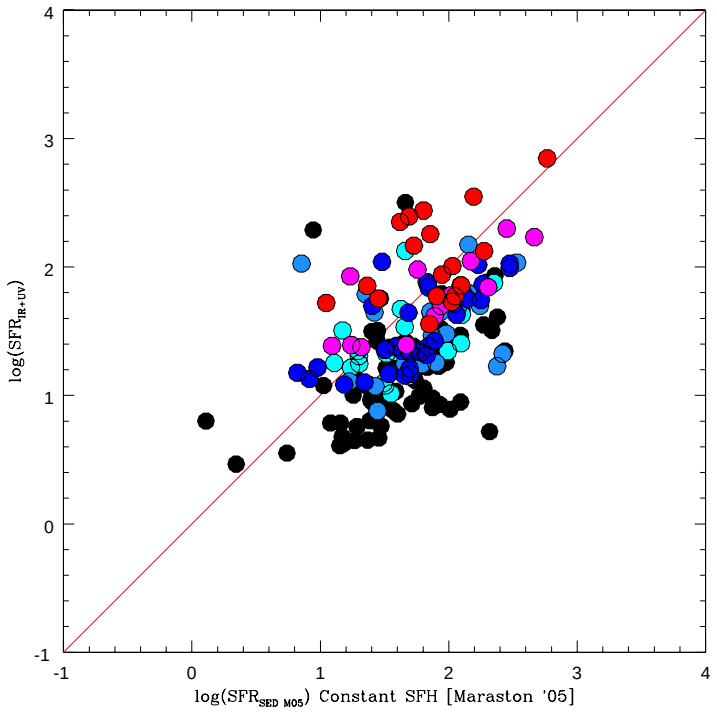

Fig. 5.17: SFR_{IR+UV} vs. SFR_{SED}. SFR_{SED} is computed with evolutionary population synthesis models by Maraston (2005), assuming a constant SFH. Points are colour coded with respect to the redshift of the galaxies. See Fig. 5.15 for the legend. The red line marks the 1-to-1 relation.

SCHEL observations, but making use of PACS data only. Galaxies lying more closely to the 1-to-1 relation have e-folding time-scales that range from $\tau = 0.1$ to $\tau = 20$ or constant star-formation, but all the galaxies with $SFR_{IR+UV} > SFR_{SED}$, and intermediate to low SFR_{SED}, have a very small e-folding time-scale: $\tau < 1.0$. The SED fitting procedure was then redone, this time assuming the extreme case of a constant star-formation history for all galaxies. In Fig. 5.17 it can be seen that the correspondence between the two estimators improves, in the sense that the tail at very low SFR_{SED} disappears, at the cost of a larger scatter in the overall relation between the two estimates. Wuyts et al. (2011) found the best correspondence between SFR_{SED} and SFR_{IR+UV} when forcing the e-folding time to be $\tau_{min} = 0.3$ Gyr, therefore adopting a strong fine-tuning in the SED fitting procedure.

Wuyts et al. (2011) found that the distance from the 1-to-1 relation between SFR_{IR+UV} and SFR_{SED} is a function of the relative ratio of emission from young stars that is reprocessed by dust vs. UV light escaping. This means that a simplistic dust correction method

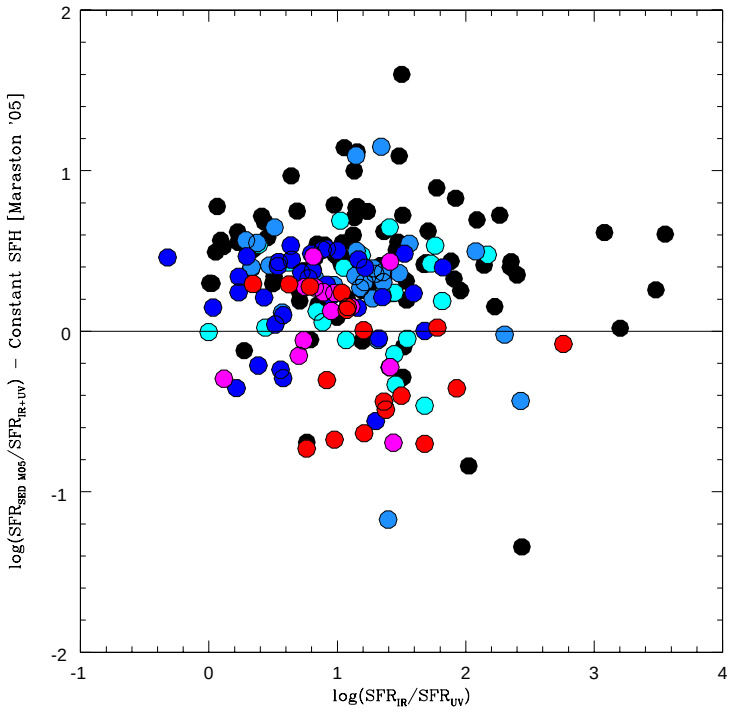

Fig. 5.18: $\log(SFR_{IR}/SFR_{UV})$ vs. $\log(SFR_{SED}/SFR_{IR+UV})$. SFR_{SED} is computed with evolutionary population synthesis models by Maraston (2005), assuming a constant SFH. SFR_{UV} is not corrected for extinction. Points are colour coded with respect to the redshift of the galaxies. See Fig. 5.15 for the legend.

based on a uniform foreground screen does not account properly for optical depth effects. Reddening only translates linearly to extinction when the obscuring material has the configuration of a foreground screen, but it saturates as a traces of extinction when patchy configurations are considered.

In our sample we were not be able to confirm the Wuyts et al. (2011) trend between SFR_{IR+UV}/SFR_{SED} and SFR_{IR}/SFR_{UV}. Comparing our Fig. 5.18 with Fig. 4 in Wuyts et al. (2011) paper, we notice that the majority of the galaxies in our sample have low values of the ratio between SFR_{IR} and SFR_{UV} ($log(SFR_{IR}/SFR_{UV}) < 1.8$): we are sort of missing the galaxies, at $z \geq 2$, with a very low contribution of unattenuated UV emission to the total SFR, which are the galaxies for which the trend between the SFR ratio and the flux ratio is more evident. We attribute this to the selection bias due to request of having a spectroscopy redshift, while almost all (73%) Wuyts et al. (2011) galaxies at $z > 1.5$ have only a photometric redshift.

However, the relation between SFR_{IR+UV}/SFR_{SED} and SFR_{IR}/SFR_{UV} in our sample, and

the causes of the systematic underestimate of SFR_{SED}, with respect to SFR_{IR+UV}, will need further investigation.

5.4.2 SFR_{UV} vs. SFR_{IR+UV}: the IR excess and dust obscuration

The next SFR estimate we examined was the one obtained from the rest-frame UV flux, corrected for dust extinction. In a previous section, the Kennicutt (1998) relation to convert UV flux to SFR was already recalled:
SFR_{UV} ($M_\odot$ yr^{-1}) = $0.9 \times 10^{-28} \times L_{1500\ Å}$ [erg s^{-1} Hz^{-1}].

Rest-frame flux at 1500Å computed for all the galaxies in the sample had now to be corrected for the effects of dust extinction.

The UV flux emitted by young stars is severely extinct by the dust surrounding star-forming regions, therefore the measured rest-frame UV luminosity must be corrected before being converted into SFR. Empirical recipes are usually applied for this purpose, but since they are calibrated on local galaxies, they often rely on the assumption that the dust composition and distribution in high-redshift galaxies is the same that in their local counterparts. One of the most widely used recipes is the Meurer et al. (1999), that links the UV spectral slope to dust extinction at 1600 Å. Under the assumption, which is quite robust when considering galaxies dominated by a young stellar population, that the shape of the UV continuum can be fairly accurately approximated by a power law $F_\lambda \propto \lambda^\beta$, where F_λ is the observed flux ($erg\ s^{-1}\ cm^{-2}$ $Å^{-1}$) and β is the continuum slope, Meurer et al. (1999) derived the aforementioned relation from an observed correlation between the ratio of IR luminosity over UV luminosity (not corrected for extinction) and the continuum slope.

Making use of the LIR information obtained thanks to HERSCHEL data, we tested the validity of the Meurer et al. (1999) for our high-galaxy sample. LIR and uncorrected UV fluxes were computed as explained in the previous sections. The next step was to compute the UV continuum slope.

The UV continuum slope

The spectra of our galaxies sample different wavelength ranges, depending on the redshift and on the survey from which they were selected, and therefore they show different

"classes" of spectral features. On this basis we may divide the sample roughly into two sub-samples: galaxies, whose spectra include the [OII]λ3727 line ([OII] sample), and galaxies whose spectra sample the UV regime, in the wavelength range 1000Å $< \lambda <$ 3000Å, often including the Lyα lines (*Lyα* sample). All galaxies at $z \leq 1.4$ fall into the [OII] sample, while all galaxies at $z \geq 1.7$ fall into the *Lyα* sample. Galaxies at intermediate redshifts may be included into one sample or the other, or in same cases even both, depending on the covered wavelength range.

Since spectra from the Lyα sample cover the wavelength range over which the UV continuum slope is defined, in this part of the analysis we concentrated on this sub-sample of galaxies.

The continuum of each spectrum was fitted with a least squares minimization procedure, in the $log(F_\lambda) - log(\lambda)$ plane, of ten average fluxes measured in wavelength windows in the range between $\sim$ 1250 Å and 2600 Å, as defined by Calzetti et al. (1994). These windows were chosen to avoid the strongest spectral features.

In Figure 5.19, we present a spectrum from our sample, as an example. The range covered by the fitting windows is indicated by the vertical dotted lines in the upper panel, while the final fit is superimposed on the spectrum in red. The two lower panels show zoomed-in regions of the same spectrum, where the ten fitting windows (in the $F_\lambda - \lambda$ plane) are indicated. To ensure the reliability of the fit, and since the wavelength baseline may influence the slope, we used only the 122 galaxies with at least 7 out of 10 windows available. The UV continuum slope (β) distribution over this sample can be seen in Figure 5.20. The mean value for the sample is $< \beta >= -1.11 \pm 0.57$ (r.m.s.).

The definition of β is not unique across the literature. First of all, it can be calculated directly in spectra, as we did, or determined from the photometry (Bouwens et al. 2009; Nordon et al. 2012). The range over which β is defined also changes from one work to another: when defined over a shorter wavelength range than that defined by Calzetti et al. (1994), the quoted slope is systematically redder (see Calzetti 2001).

Keeping all this in mind, we compared the results of our analysis with others, for both local and high redshift galaxies, taken from the literature. The mean value of β over our sample is in good agreement with the $< \beta > \; = -1.13 \pm 0.12$ measured by Heckman et al. (1998) from the spectra of 45 local SFGs observed with the *IUE* satellite. For high redshift galaxies, Noll & Pierini (2005) analysed the spectra of 34 SFGs at $2 < z < 2.5$ from the FORS Deep Field (FDF) spectroscopic survey (Noll et al. 2004).

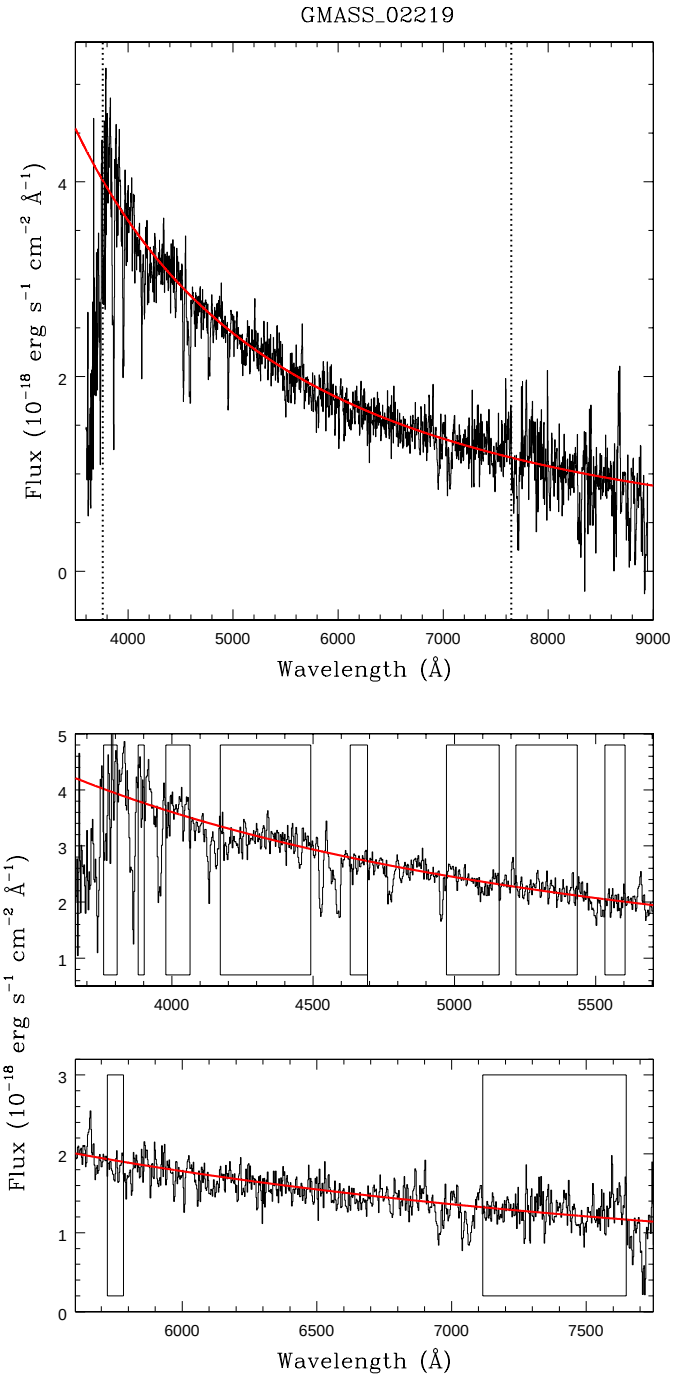

Fig. 5.19: Top panel: an observed spectrum with corresponding fit of the continuum superimposed in red. The vertical dashed lines delineate the range covered by the windows defined by Calzetti et al. (1994) and used in the fitting procedure. Bottom panels: zoom over the wavelength range used in the fitting routine, with the ten fitting-windows indicated.

The measured mean value of the continuum slope for the sub-sample of galaxies with bluer spectra is $< \beta > \ = -1.01 \pm 0.11$, with which the mean value over our sample is fairly consistent, taking into account the different wavelength baseline ($\sim 1200 - 1800$ Å in their analysis, compared to $\sim 1200 - 2600$ Å in this work).

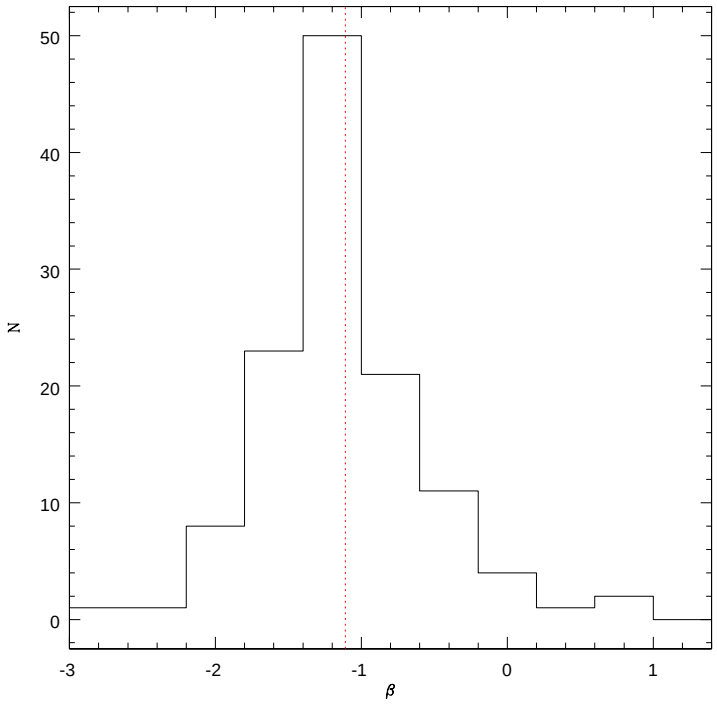

Fig. 5.20: UV continuum slope distribution over the sample. The vertical red line indicates the mean value for the sample: $< \beta >= -1.11$, with $r.m.s. = 0.57$.

Bouwens et al. (2009) presented a systematic measurement of the UV continuum slope over a wide range in redshift, using photometry. For galaxies at redshift $z \sim 2$, they found that $< \beta > \ \sim -1.5$, a result with a scatter of ~ 0.30 (see Bouwens et al. 2009, Figure 5), with which our results agree reasonably well, again considering the differences in methods and wavelength baselines used. Finally, also Nordon et al. (2012), for their sample of PACS detected sources, found a distribution of β, computed from photometry, peaked around $\beta \sim -1$, which is in good agreement with our own findings.

The A_{IRX} vs. β relation

The extinction derived from β was used to correct the flux at 1500 Å (see Section 5.4). The unextinct flux was in turn converted into $SFR_{UV-corr}$ using the appropriate Kennicutt

(1998) relation. Fig. 5.21 shows the comparison between $SFR_{UV-corr}$ and our reference estimator, SFR_{IR+UV}, for the 68 galaxies with at least 7 UV continuum fitting windows and an available LIR. The two estimates agree reasonably well, but there is a large scatter in the relation, as also reported by other authors (Nordon et al. 2010; Reddy et al. 2012).

The origin of the scatter has to be searched in the Meurer et al. (1999) relation, i.e. in the relation between the UV continuum slope and the ratio between IR flux and unextinct UV flux. The flux ratio may be expressed in terms of effective UV attenuation A_{IRX} (Nordon et al. 2012). SFR_{UV} uses the observed UV luminosity and hence is missing a significant fraction of the luminosity which was attenuated by the dust.

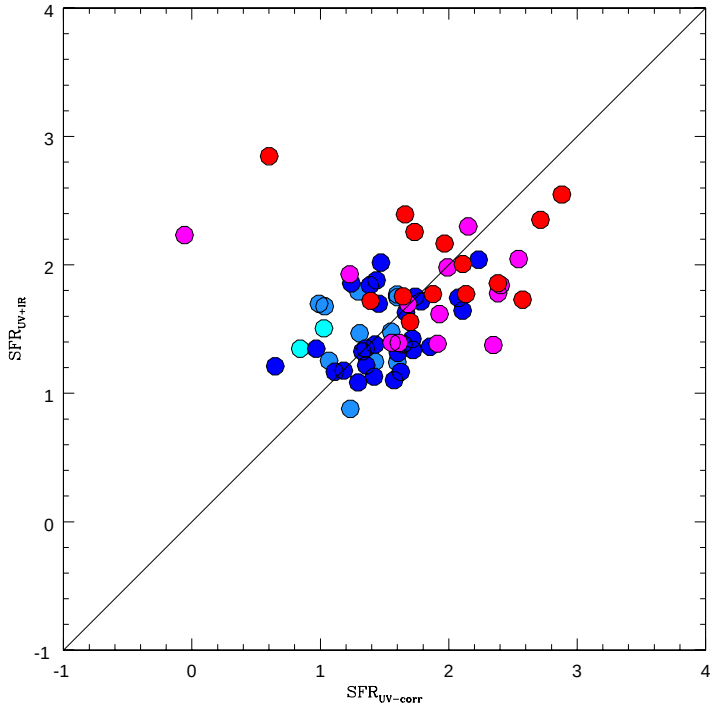

Fig. 5.21: $SFR_{UV-corr}$ vs. SFR_{IR+UV} for the 68 galaxies with at least 7 UV continuum fitting windows and an available LIR. Points are colour coded with respect to the redshift of the galaxies. See Fig. 5.15 for the legend. The black line marks the 1-to-1 relation.

The effective UV attenuation should correct SFR_{UV} to SFR_{total}, that we have assumed to be $SFR_{IR+UV} = SFR_{IR} + SFR_{UV}$, i.e. $log(SFR_{IR+UV}) = log(SFR_{UV}) + 0.4A_{IRX}$.

A_{IRX} is then defined as:
$A_{IRX} = 2.5\ log(\frac{SFR_{IR}}{SFR_{UV}}) + 1.$

Fig. 5.22 shows the A_{IRX} vs. β plot for our sub-sample of galaxies. A linear fit to our

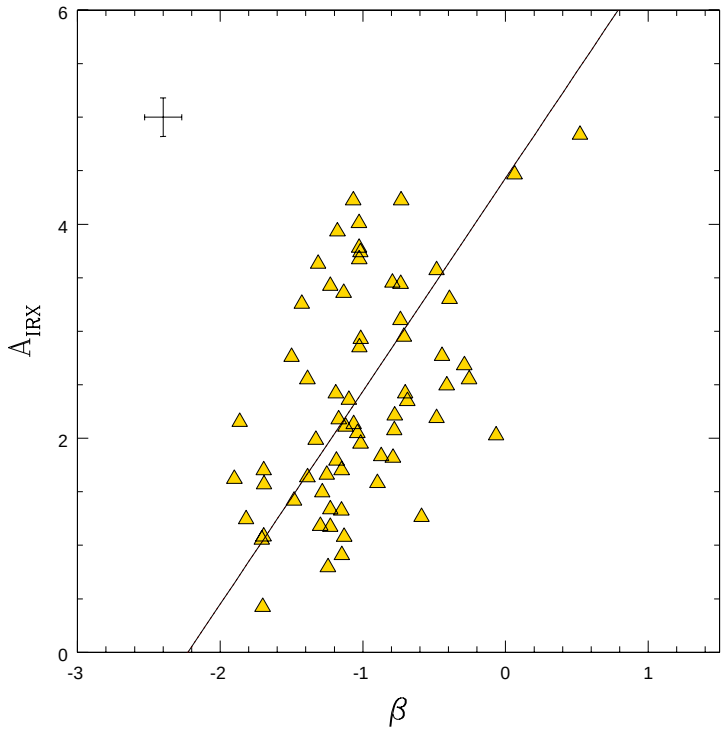

Fig. 5.22: A_{IRX} vs. β. The black line indicates the linear fit to the data, that coincides with the Meurer et al. (1999) relation.

data produced exactly the Meurer et al. (1999) relation, but the scatter from the relation is quite large ($\sigma = 1.38$).

Nordon et al. (2012) found the scatter in the A_{IRX} vs. β relation to be correlated with the position of a galaxy in the SFR vs. mass diagram, in particular, the distance from the so-called *main sequence* ($\Delta log(SFR)_{MS}$). They found that main sequence galaxies tend to form a tighter sequence than the full population in the A_{IRX} vs. β diagram.

To test this effect in our sample, we plotted SFR_{IR+UV} vs. Mass (Fig. 5.23). For the total sample of 201 galaxies with an available LIR, a linear fit to the data gave a slope of $\alpha = 1.12 \pm 0.05$, which agrees with the relations found for other $z \sim 2$ samples, for example Daddi et al. (2007), who quote a slope of ~ 0.9 using UV-derived SFRs, and Pannella et al. (2009), who report a slope 0.95 ± 0.07 and whose SFRs were computed from radio luminosity. We notice that a linear fit to the 68 galaxies of the sub-sample analysed in this section gave a consistent result: $\alpha = 1.19 \pm 0.12$.

Nordon et al. (2012) used redshift dependent main sequence curves from Rodighiero et al. (2010), with a slope, in the sSFR vs. mass plane, which is steeper than the one derived

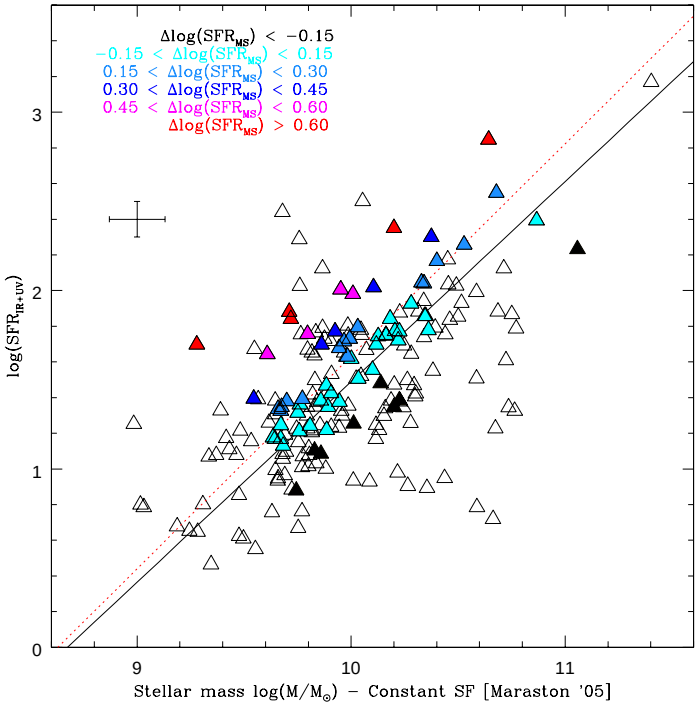

Fig. 5.23: SFR_{IR+UV} vs. stellar mass. Masses from SED fitting, with constant SF. Empty points: all galaxies with LIR available, from the *326-SFGs sample*; filled points: *Lyα sample*, with at least 7 UV continuum fitting windows. The black line marks the linear fit to the data of the bigger sample (main sequence). The red dotted line marks the linear fit to the data of the *Lyα sample*. Points are colour coded with respect to their distance from the main sequence.

from our sample. In particular, they quote $\gamma = -0.50$, while we derived $\gamma = -1.00 \pm 0.05$. Both curves are plotted in Fig. 5.24, over our data.

From the plot in Fig. 5.23 it can be seen that the majority of the galaxies in the sub-sample analysed in this section are very close to the main sequence. This means that we are probably not able to appreciate the correlation between $\Delta log(SFR)_{MS}$ and the scatter in the A_{IRX} vs. β relation. Comparing our Fig. 5.25 with the Nordon et al. (2012) corresponding plot, it is evident that in our sample we are missing galaxies with very high A_{IRX}, i.e. with very high SFR_{IR}/SFR_{UV} ratios, a selection bias effect already discussed in the previous section. However, an effect of the $\Delta log(SFR)_{MS}$ dependence of the A_{IRX} vs. β relation may be seen as well. Along with the Meurer et al. (1999) relation, that was verified to coincide perfectly with a linear fit to our data, we plot the relation between A_{IRX} and β computed for the group of galaxies lying closer to the main sequence:

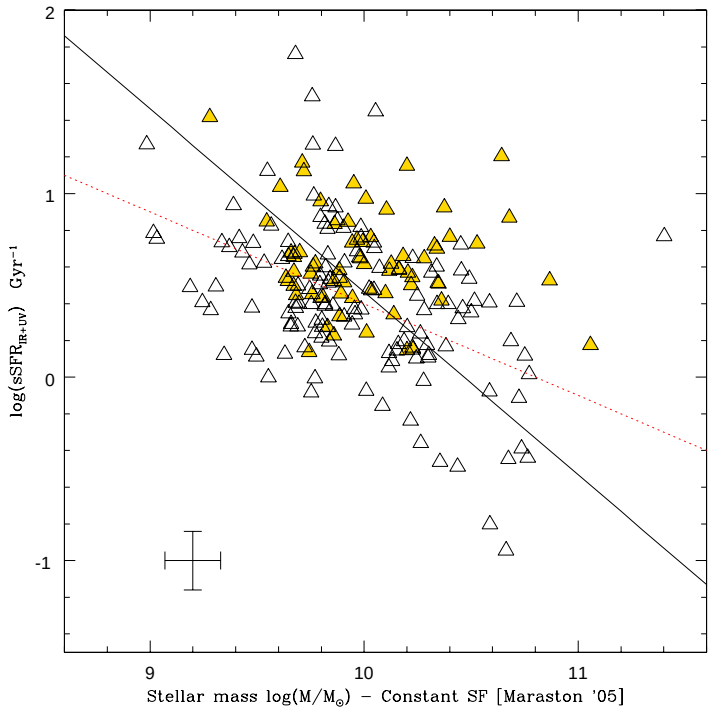

Fig. 5.24: $sSFR_{IR+UV}$ vs. stellar mass. Empty points: all galaxies with LIR available, from the *326-SFGs sample*; filled points: *Lyα sample*, with at least 7 continuum fitting windows. The black line marks the linear fit to the data of the bigger sample. The red dotted line is the main sequence curve, for galaxies at $1.5 < z < 2.0$, from Rodighiero et al. (2010).

$-0.15 < \Delta log(SFR)_{MS} < 0.15$. This second relation is flatter that the one referred to the total sample, an effect also reported by Nordon et al. (2012). For comparison, the relation for main sequence galaxies quoted by Nordon et al. (2012) is also reported. The difference between their curve and ours is probably due to the different slope of the used main sequence curves.

In conclusion, $\Delta log(SFR)_{MS}$ is surely related to the scatter in the A_{IRX} vs. β relation, but there must be also some other ingredient, since also when considering main sequence galaxies only, the scatter in the relation is still quite large.

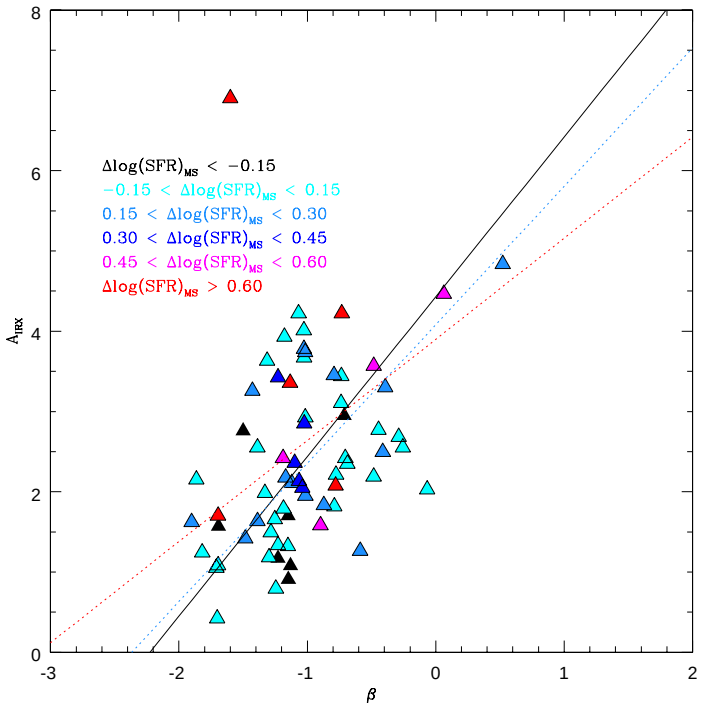

Fig. 5.25: A_{IRX} vs. β. Points are colour coded with respect to their distance from the main sequence. See Fig. 5.15 for the legend. The black line marks the linear fit to the data, that coincides with the Meurer et al. (1999) relation. The blue dotted line marks the linear fit to the points of galaxies that lie more closely to the main sequence, in the SFR vs. Mass diagram ($-0.15 < \Delta log(SFR)_{MS} < 0.15$). The red dotted line marks the relation of main sequence galaxies in Nordon et al. (2012).

5.4.3 $SFR_{[OII]}$ vs. SFR_{IR+UV}

The last SFR estimator to be considered was the flux of a forbidden line[10]: [OII] λ3727. As pointed out by Kennicutt (1998), the luminosities of forbidden lines are not directly coupled to the ionizing luminosity, and their excitation is sensitive to abundance and the ionization state of the gas. The excitation of [OII] is sufficiently well behaved that it can be calibrated empirically (through H_α) as a quantitative SFR tracer. However, the SFRs derived from [OII] are less precise than those from H_α because the mean [OII]/H_α ratios in individual galaxies vary considerably.

[10]A forbidden line is a spectral line emitted by atoms undergoing energy transitions not normally allowed by the selection rules of quantum mechanics. Although the transitions are nominally forbidden, there is a certain probability that an excited atom will make a forbidden transition to a lower energy state, per unit time. Forbidden emission lines are observed in space environments, where the densities are so low that de-excitation via atomic collisions are less likely. Under such conditions, once an atom or molecule

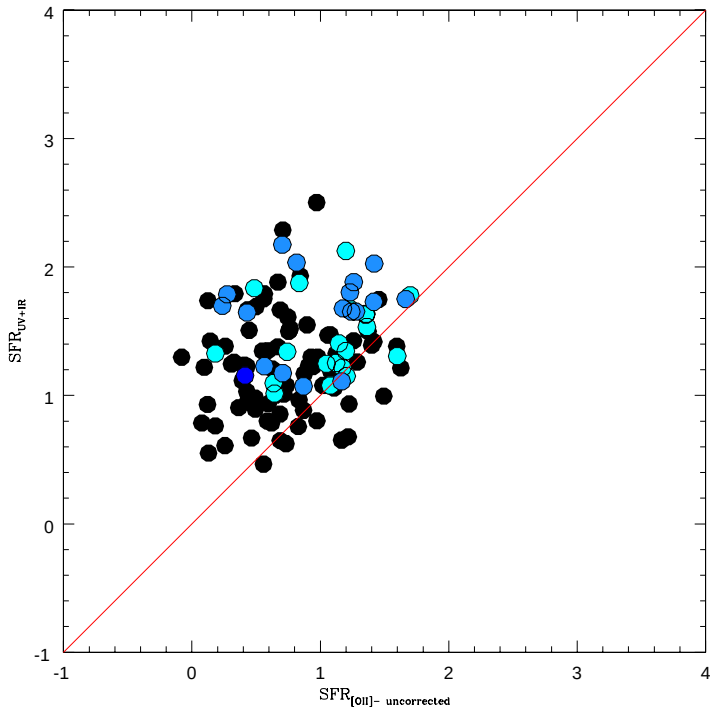

Fig. 5.26: SFR_{IR+UV} vs. $SFR_{[OII-uncorr]}$. $SFR_{[OII-uncorr]}$ is not corrected for extinction. Points are colour coded with respect to the redshift of the galaxies. See Fig. 5.15 for the legend. The red line marks the 1-to-1 relation.

In the previous section the [OII] sample was already introduced, as the sample of galaxies whose spectra include the [OII]λ3727 line, which are all at $z < 1.7$, given the selection criteria of our data sample. The sub-sample that will be the object of the analysis in this section is the intersection between this sub-sample and the one of galaxies with an available LIR, and it counts 118 galaxies.

Integrated fluxes of the [OII]λ3727 line were measured in all galaxies of the sub-sample, corrected for slit-losses using the available photometry and finally converted into $SFR_{[OII]}$ using the relation from Kennicutt (1998), scaled for a Kroupa (2001) IMF:
$\mathrm{SFR}_{[OII]}$ ($\mathrm{M}_\odot$ yr^{-1}) = $0.9 \times 10^{-41} \times \mathrm{L}_{[OII]}$ [erg s^{-1}].

Fig. 5.26 shows the comparison between $\mathrm{SFR}_{[OII]}$ and SFR_{IR+UV}. The observed luminosities must be corrected for extinction, of course. In this case the extinction at H_α must be used, because of the manner in which the [OII] fluxes were calibrated.

We tried to different extinction recipes to correct the [OII] fluxes. First, we used the

has been excited into a meta-stable state, it can decay by emitting a forbidden-line photon.

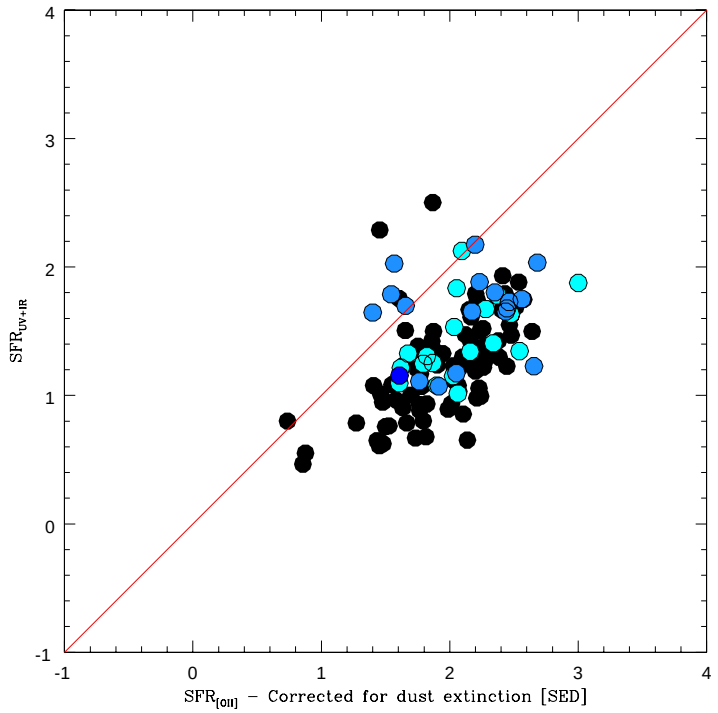

Fig. 5.27: SFR_{IR+UV} vs. $SFR_{[OII-uncorr]}$. $SFR_{[OII]}$ is corrected for extinction using $E(B-V)_{neb}$ from SED fitting (see the text for more details). Points are colour coded with respect to the redshift of the galaxies. See Fig. 5.15 for the legend. The red line marks the 1-to-1 relation.

A_v computed from SED fitting (M05 models and constant SF). The attenuation derived from SED fitting refers to the extinction of the stellar continuum. But in this case we are dealing with gas emission, therefore we applied the locally calibrated extra attenuation toward HII regions, compared to the continuum: $A_v(gas) = A_v(star)/0.44$ (Calzetti et al. 2000).

The second recipe was the local relation found by Domínguez et al. (2012) between LIR and A_v defined using the ratio between H_α and H_β lines. Measuring the lines ratios on stacked spectra, created by adding spectra of similar LIR, they found a linear relation between nebular extinction and LIR:
$E(B-V) = 0.289 \times log(LIR) - 2.54.$

We corrected the [OII] fluxes using the two methods given above and the Calzetti et al. (2000) law:
$F_{corr}([OII]) = F([OII]) \times 10^{0.4 \times 3.327\ E(B-V)}$

and the results are shown in Fig. 5.27 and 5.28.

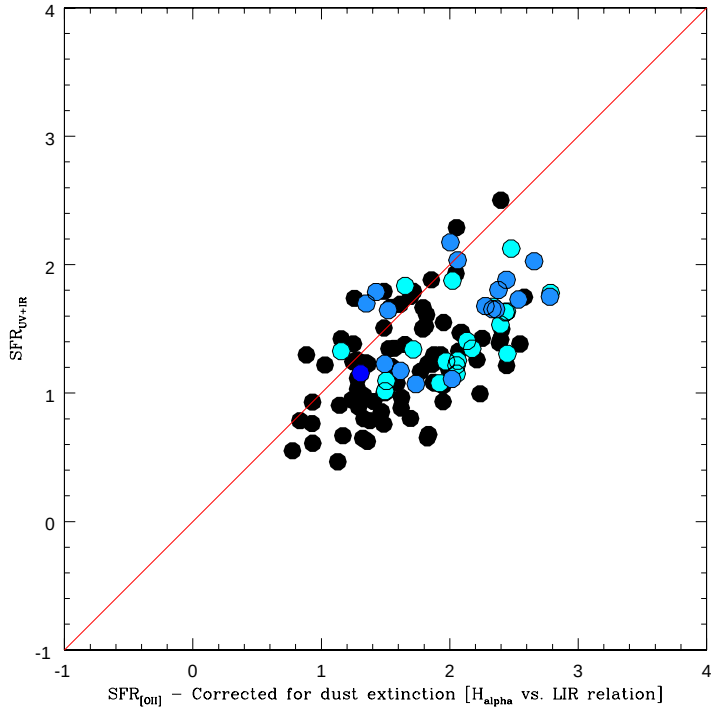

Fig. 5.28: SFR_{IR+UV} vs. $SFR_{[OII-uncorr]}$. $SFR_{[OII]}$ is corrected for extinction using the relation of Domínguez et al. (2012). Points are colour coded with respect to the redshift of the galaxies. See Fig. 5.15 for the legend. The red line marks the 1-to-1 relation.

We found that both correction methods are quite effective in correcting the [OII] flux, and also give similar results. In fact, in both cases the correlation coefficient between SFR_{OII} and SFR_{IR+UV} is $r_{xy} = 0.5$. The scatter from the 1-to-1 relation is instead smaller in the case of extinction calibrated from H_α/H_β vs. LIR ($\sigma = 0.62$), with respect to the SED fitting derived attenuation ($\sigma = 0.78$).

However, in both cases the corrected SFR_{OII} overestimates the SFR_{IR+UV}, similarly to what happens in the case of SFR_{SED}.

5.5 Conclusions

In this chapter we have conducted two analyses. First, we have computed IR luminosities for a sample of high-redshift star-forming galaxies. We used HERSCHEL data to test the robustness of the most commonly used synthetic SED libraries in recovering

the bolometric LIR when only one photometric point is available, and we computed the calibrations to correct the derived luminosities. Secondly, we compared different SFR estimators, taking SFR_{IR+UV} as yardstick. The results of our analysis may be summarized as follows.

1. When at least two IR points ($\lambda_{obs} \geq 24\mu m$) are available, the five analysed libraries are almost interchangeable, in terms of χ^2, to recover the bolometric LIR.

2. Three galaxies were found whose SED was not correctly reproduced by any SED library. Their SPIRE data, that reach seem to suggest that dust in these galaxies might be colder than the predictions of the models mostly calibrated on local sources.

3. When only one IR photometric points is available, CE01 library was found to be the most robust in recovering the total LIR, providing that some corrections were applied to the recovered LIR. We derived such corrections, by comparing LIR derived from $MIPS\,24\mu m$ only and LIR derived using all the available IR data.

4. Correction to LIR derived from $MIPS\,24\mu m$ only were computed also for DH02 libraries. LIR computed using CE01 or DH02 libraries, correcting the LIR_{MIPS} with our proposed relations, are strongly consistent with one another.

5. We took SFR_{IR+UV} as our main SFR estimator, i.e. the SFR obtained by adding the bolometric luminosity of the young stars (represented by LIR) and the UV radiation not reprocessed into the IR. The contribution of SFR_{UV} to the total SFR is smaller in galaxies with high SFRs, but in galaxies with low SFRs it may equal the contribution of SFR_{IR}.

6. Comparison between SFR_{SED} and SFR_{IR+UV}: for the majority of galaxies, the relation between the two estimates is quite tight, though synthetic models tend to systematically overestimate the SFR, with respect to SFR_{IR+UV}. But there is also a tail toward lower SED-modelled SFRs.

7. Assuming the extreme case of a constant star-formation history for all galaxies, the correspondence between the two estimators improves, in the sense that the tail at very low SFR_{SED} disappears, at the cost of a larger scatter in the overall relation between the two estimates.

8. A check of the SFR_{IR+UV}/SFR_{SED} and SFR_{IR}/SFR_{UV} diagram confirms that the spectroscopic selection biases our sample in the sense that we miss the galaxies, at $z \geq 2$, with a very low contribution of unattenuated UV emission to the total SFR, which are the galaxies for which the trend between the SFR ratio and the flux ratio is more evident.

9. We computed the UV continuum slope β of a sub-sample of star-forming galaxies whose spectra cover the wavelength range 1000 Å − 3000 Å, and found a mean value of $<\beta>= -1.11 \pm 0.57$ (r.m.s.).

10. A linear fit to our data in the A_{IRX} vs. β plane produced exactly the Meurer et al. (1999) relation, but with quite a large scatter of the data from the relation (σ = 1.38).

11. Comparison between SFR_{UV} and SFR_{IR+UV}: we corrected UV fluxes for extinction using the relation between A_{IRX} and β previously mentioned, before converting the flux to SFR. We found SFR_{UV} and SFR_{IR+UV} to agree reasonably well, but with a large scatter in the relation, due to the scatter in the A_{IRX} and β relation.

12. Investigating the SFR_{IR+UV} vs. stellar mass relation, we computed a slope of α = 1.12 ± 0.05, for our sample.

13. We found almost all the galaxies in our sample, with LIR and a rest-frame UV spectrum, to lie very close to the main sequence in the SFR_{IR+UV} vs. stellar mass plane.

14. The relation between A_{IRX} and β was derived also only for the group of galaxies lying closer to the main sequence: $-0.15 < \Delta log(SFR)_{MS} < 0.15$. This second relation is flatter that the one referred to the total sample. This is a hint that there may be a dependence of the scatter in the A_{IRX} vs. β on the distance of a galaxies from the main sequence.

15. Comparison between $SFR_{[OII]}$ and SFR_{IR+UV}: we tried two different methods for correcting observed [OII] fluxes for dust extinction. First, the attenuation derived from SED fitting; second, the attenuation derived from the relation between H_α/H_β and LIR. Both correction methods were found to be quite effective in correcting the [OII] flux, and also give similar results. In both cases, the corrected SFR_{OII} overestimates the SFR_{IR+UV}, similarly to what happens in the case of SFR_{SED}.

CHAPTER 6

Galactic-scale outflows

6.1 Introduction

In this chapter, the rest-frame UV spectra of 74 star-forming galaxies at $z > 1$, from the GMASS spectroscopic sample, will be analysed. By using composite spectra, we will study the properties of the absorption spectral lines associated with the inter-stellar medium, and investigate possible correlations with physical galaxy properties, such as stellar mass and star-formation rate.

6.2 The data sample: selection criteria and redshift refinement

To study galactic-scale outflows in high-redshift SFGs, first we had to select a representative sub-sample of SFGs with confirmed spectroscopic redshift and high-quality spectra for rest-frame wavelengths between 1100 Å and 2900 Å, where we can find the blueshifted absorption spectral lines that are tracers of the warm phase of galactic-scale outflows. We decided to use only spectra from the GMASS survey (and not from the other GOODS-S spectroscopic surveys), due to their very high quality. The criteria to select a clean sample of SFGs were already explained in the previous chapter. Here, we limited further our selection to the GMASS spectra that had been observed through a blue grism mask (B < 26.0), have a catalogue redshift $1.5 < z_{spec} < 2.8$, and have been spectroscopically classified as "star-forming". These criteria ensured the selection of SFGs with the required wavelength range. The selected objects, plotted on the *BzK* diagram developed by Daddi et al. (2004), lie in the star-forming region, as shown in Fig.6.1. The spectral features related to star-formation activity may be "contaminated" by the presence of nuclear activity but, as already explained in the previous chapter, objects with a spectrum showing AGN features had been excluded from the SFRs sample. After these preliminary selection steps, we ended up with an ensemble of 94 SFGs.

The next stage of our selection was based on the quality of the redshifts. Since the redshifts had been originally obtained using different measurement techniques, we decided to generate a more homogeneous set of redshifts by adopting a recursive procedure based on the cross-correlation of the single spectra with a template created from the sample itself (Tonry & Davis 1979). Briefly, the peak of the cross-correlation function between the spectrum of a galaxy and a given template provides the redshift and velocity dispersion of the galaxy with respect to the template. To quantify the significance of the results, a cross-correlation goodness parameter R was defined.[11] We then took the composite spectrum created by averaging the spectra from the preliminary sample of 94 SFGs, using catalogue redshifts, as a template. From the cross-correlation of the template with each single galaxy spectrum, a new set of redshifts was obtained. The difference between these new redshifts and the catalogue ones on average is $\Delta z \sim 2 \times 10^{-3}$. The goodness parameter R was then checked: too low a value of R means that only a low-quality redshift determination was possible, maybe due to a spectrum with a low signal-to-noise

[11] R is the ratio of the correlation peak height to the amplitude of the antisymmetric noise.

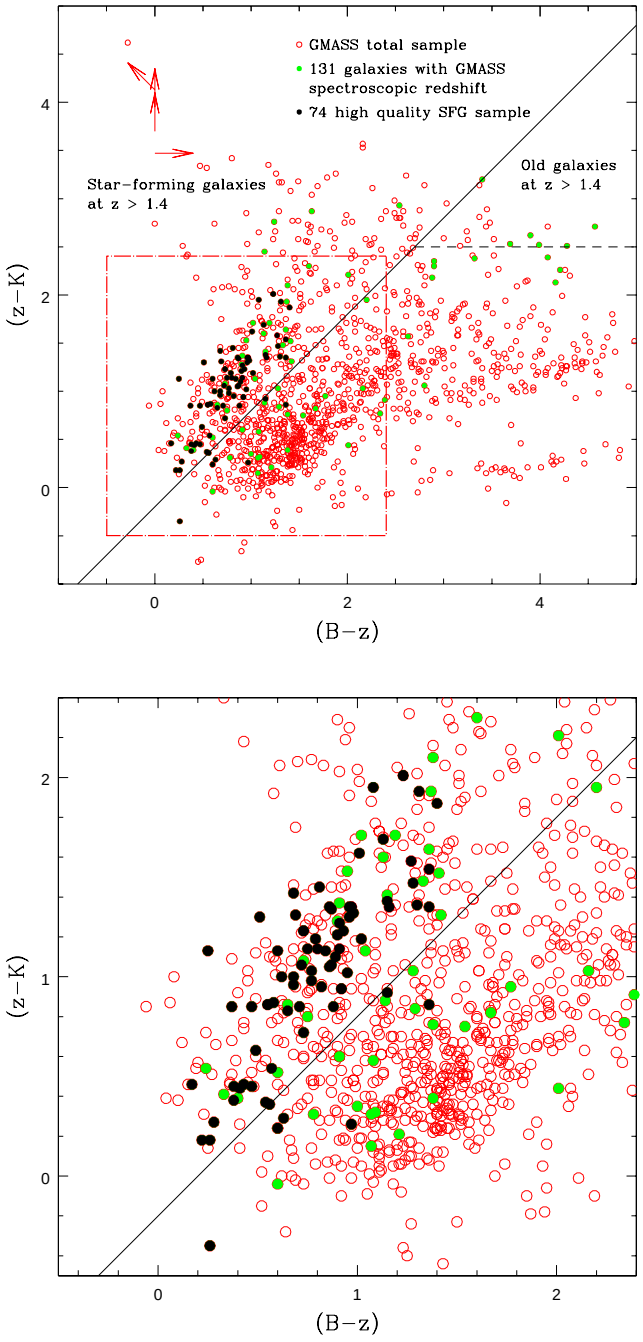

Fig. 6.1: Top panel: *BzK* plot for the objects in the GMASS total sample (red open circles). The green dots represent the 131 objects with a secure redshift determination from the GMASS spectroscopic sample. The black dots represent the 74 high-quality SFGs analysed in this work. Arrows indicate upper limits for objects undetected in one or more bands. Bottom panel: zoom on the 74 SFG sample.

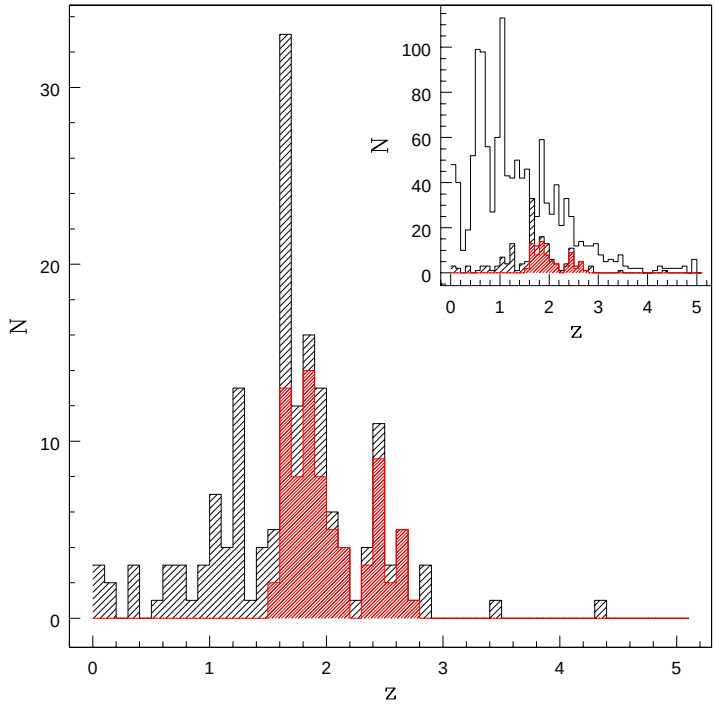

Fig. 6.2: Redshift distribution. The black shaded histogram represents secure spectroscopic redshifts of the observed full GMASS sample; the red shaded histogram represents redshifts for our sub-sample of 74 high-quality SFGs. In the inset, the distribution of photometric redshifts for the whole *GMASS total sample* is also shown (empty histogram).

ratio (S/N). After some tests, we decided to use R > 3 as the constraint determining that a redshift is reliable, and 20 objects, which did not satisfy this constraint, were excluded from the final high-quality sample.

The 74 remaining spectra were used to produce a new template, which was iteratively cross-correlated with each single spectrum until a round was reached when redshifts did not change significantly from the previous round. We reached convergence after five rounds and the final redshifts were the ones subsequently used in this work. Fig. 6.2 shows the redshift distribution of the final sample of 74 high-quality SFGs, with reliable redshifts measured as explained above, against the original spectroscopic GMASS sample of 131 extragalactic objects. Kurk et al. (2009) found that the peak at $z \sim 1.6$ represents a galaxy overdensity, possibly a cluster under assembly, where a significant portion of galaxies have a passive spectrum and hence are not included in our SFG sample.

The distributions of age, stellar mass, and SFR for the final sample of 74 SFGs, with

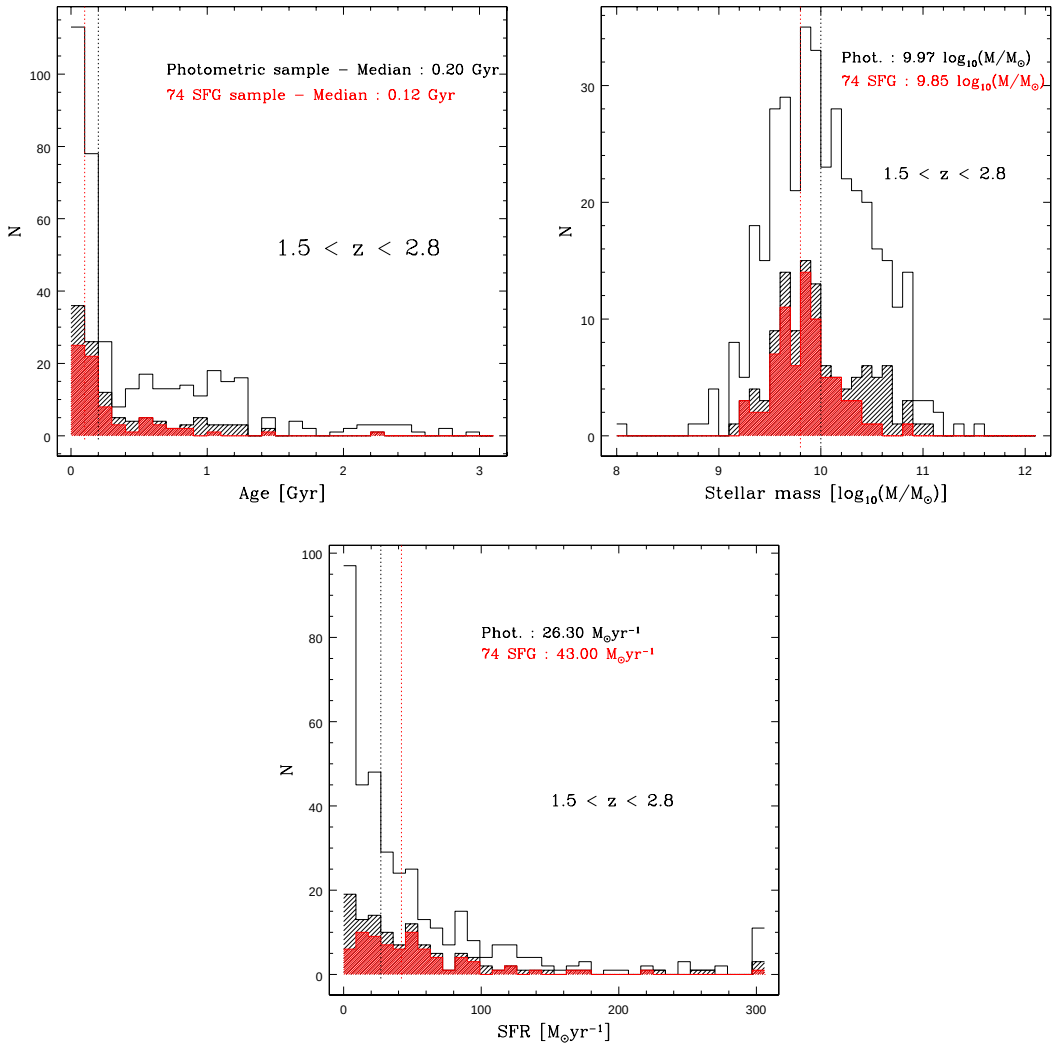

Fig. 6.3: Distributions, in the redshift range $1.5 < z < 2.8$, of stellar age, stellar mass, and SFR computed by SED fitting (using Maraston (2005) models with a Kroupa IMF) for: the final sample of 74 objects analysed in this chapter (shaded red histogram); the GMASS total sample (open histogram); and objects with a secure redshift determination from the GMASS spectroscopic sample (shaded black histogram). Medians of the photometric catalogue and the 74 SFG sample are also shown (vertical black and red lines, respectively).

respect to the GMASS total sample, are also shown in Fig. 6.3, in the redshift range $1.5 < z < 2.8$. We note that the adopted selection criteria, especially the cut in optical magnitude, led our sample to be biased towards younger ages and higher SFRs with respect to the parent galaxy population.

6.3 Rest-frame UV spectroscopic features

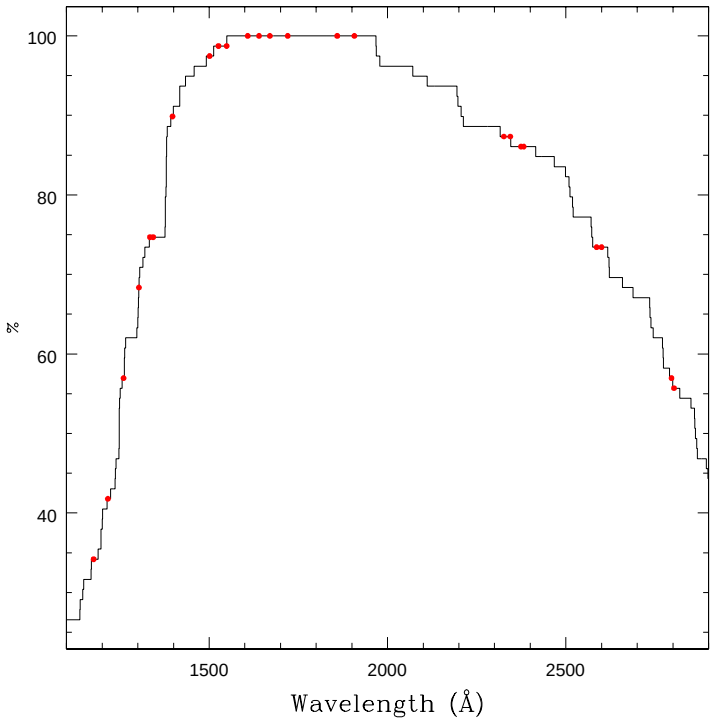

Fig. 6.4: Percentage of contributing objects per wavelength unit to the composite spectrum of the total sample (74 SFGs) (see Fig. 6.5). Red dots indicate the wavelengths of the most prominent spectral lines detectable in the spectrum.

The composite spectrum of the sample of 74 SFGs is shown in Fig. 6.5. It was generated by stacking the individual spectra, shifted into their rest-frame using the redshifts defined in the previous section, and then normalized for the wavelength range 1600-1800 Å and re-binned to a dispersion of 1 Å per pixel[12]. Fig. 6.4 shows the percentage of contributing objects per wavelength unit to the composite spectrum, with an indication of the most prominent spectral lines used in our analysis. The continuum slope of the composite spectrum, measured following Calzetti et al. (1994), is $\beta = -1.15 \pm 0.01$, which is in good agreement with the mean of the values measured for the individual spectra in the *326-SFGs sample* analysed in the previous chapter: $< \beta >= -1.11 \pm 0.57$ (r.m.s.). Several types of emission and absorption lines are recognizable. The most prominent ones are the lines due to absorption, by the interstellar medium, of the radiation coming from

[12]The dispersion of single spectra is 2.5 Å in the observed frame. The rest-frame dispersion of the composite was set to be 1 Å $\sim$ 2.5 Å $/1 + \bar{z}$, to match the observed pixel resolution.

stars, highlighted with red (low-ionization) and green (high-ionization) colours in Fig. 6.5. Information about the most prominent spectral lines detected in the spectrum is summarized in Tables 6.1 and 6.2.

6.3.1 Photospheric absorption stellar lines

Photospheric stellar lines generated by the absorption of radiation produced in the stellar interiors by the most external gas layers. Since they are very weak, these lines are almost undetectable in the single spectra of our sample, owing to the low S/N in the continuum (typical <5), but they can be both identified and measured in composite spectra, since the averaging procedure increases the S/N (>15) (see Fig. 6.9). As discussed later in more detail, stellar photospheric lines could be used to define the velocity zero point of the system, with respect to which the velocities of the outflowing interstellar gas were calculated. In our study here, we were able to identify five stellar lines: C III λ1176 Å, O IV λ1343 Å, S III λ1417 Å, S V λ1500 Å, and C III λ2297 Å.

6.3.2 Nebular emission lines

Two semi-forbidden carbon lines are detectable in our spectra: C III] λ1909 Å and C II] λ2326 Å, unresolved at our spectral resolution. These lines originate in nebular regions photo-ionized by radiation from massive O and B stars, hence can in principle be used, in addition to photospheric stellar lines, to determine the system rest-frame velocity.

The C III] λ1909 Å is known to be a doublet ($\lambda\lambda$1906.08, 1908.73 Å). The flux intensity ratio of the two lines depends on the physical conditions of the emitting gas, in particular the electron density (Keenan et al. 1992). For the electronic densities of local star-forming regions, the ratio varies between 0.5 and 1.5, with 1.5 being the most typical value and therefore the one we imposed in the line measurements.

Table 6.1: Spectral lines in a SFG rest-frame UV spectrum (1000-2000Å).

Ion	Vacuum wavelength (Å)	Rest-frame EW[a](Å)	Origin
C III	1175.71	1.70 ± 0.12	stellar (photospheric)
N V	1238.82, 1242.80	-1.11 ± 0.20	ISM
Si II	1260.42	1.47 ± 0.09	ISM
Si II*	1264.74	-0.36 ± 0.25	Fine-structure emission (ISM)
O I - Si II[b]	1302.17, 1304.37	2.43 ± 0.26[d]	ISM
Si II*	1309.28	-1.26 ± 0.25	Fine-structure emission (ISM)
C II	1334.53	2.09 ± 0.15	ISM
O IV	1343.35	0.27 ± 0.07	stellar (photospheric)
Si IV[c]	1393.76	2.02 ± 0.09	ISM + stellar wind (P-Cygni profile)
Si IV[c]	1402.77	1.42 ± 0.05	ISM + stellar wind (P-Cygni profile)
Si III	1417.24	0.72 ± 0.29	stellar (photospheric)
S V	1501.76	0.54 ± 0.13	stellar (photospheric)
Si II	1526.71	1.94 ± 0.08	ISM
C IV[b,c]	1548.20, 1550.78	3.24 ± 0.16[d]	ISM + stellar wind (P-Cygni profile)
Fe II	1608.45	1.31 ± 0.11	ISM
He II	1640.42	-1.02 ± 0.10	stellar wind
Al II	1670.79	1.54 ± 0.08	ISM
Ni II	1709.60	0.70 ± 0.35	ISM
N IV	1718.55	1.14 ± 0.18	stellar wind (P-Cygni profile)
Ni II	1741.55	0.25 ± 0.41	ISM
Ni II	1751.91	0.39 ± 0.41	ISM
Si II	1808.01	0.76 ± 0.09	ISM
Si I	1845.52	0.53 ± 0.21	ISM
Al III[c]	1854.72	1.20 ± 0.21	ISM + stellar wind (P-Cygni profile)
Al III[c]	1862.79	0.85 ± 0.11	ISM + stellar wind (P-Cygni profile)
C III][b,c]	1906.68, 1908.68	-1.02 ± 0.15[d]	nebular

[a] EW: negative for emission lines and positive for absorption lines.
[b] Blended at our spectral resolution.
[c] Doublet.
[d] The measurement of the EW refers to the blend of the two lines.
[e] Possible stellar wind contribution..
[f] Possible photospheric stellar contribution.

Table 6.2: Spectral lines in a SFG rest-frame UV spectrum (2000-3000Å).

Ion	Vacuum wavelength (Å)	Rest-frame EW[a](Å)	Origin
Fe II	2249.88	0.60 ± 0.22	ISM
Fe II	2260.78	0.50 ± 0.31	ISM
C III	2297.58	0.28 ± 0.24	stellar (photospheric)
C II]	2326.00	-1.24 ± 0.20	nebular
Fe II	2344.21	2.45 ± 0.13	ISM
Fe II*	2365.66	-0.74 ± 0.38	Fine-structure emission (ISM)
Fe II[c]	2374.46	1.87 ± 0.13	ISM
Fe II[c]	2382.76	2.22 ± 0.15	ISM
Fe II*	2396.15	-1.12 ± 0.18	Fine-structure emission (ISM)
Fe II[c]	2586.65	2.65 ± 0.17	ISM[e]
Fe II[c]	2600.17	2.77 ± 0.14	ISM[e]
Fe II*	2612.65	-1.07 ± 1.35	Fine-structure emission (ISM)
Fe II*	2626.45	-1.17 ± 0.41	Fine-structure emission (ISM)
Mg II[c]	2796.35	2.43 ± 0.10	ISM[f]
Mg II[c]	2803.53	2.07 ± 0.10	ISM[f]
Mg I	2852.96	1.75 ± 0.68	ISM

[a] EW: negative for emission lines and positive for absorption lines.
[b] Blended at our spectral resolution.
[c] Doublet.
[d] The measurement of the EW refers to the blend of the two lines.
[e] Possible stellar wind contribution..
[f] Possible photospheric stellar contribution.

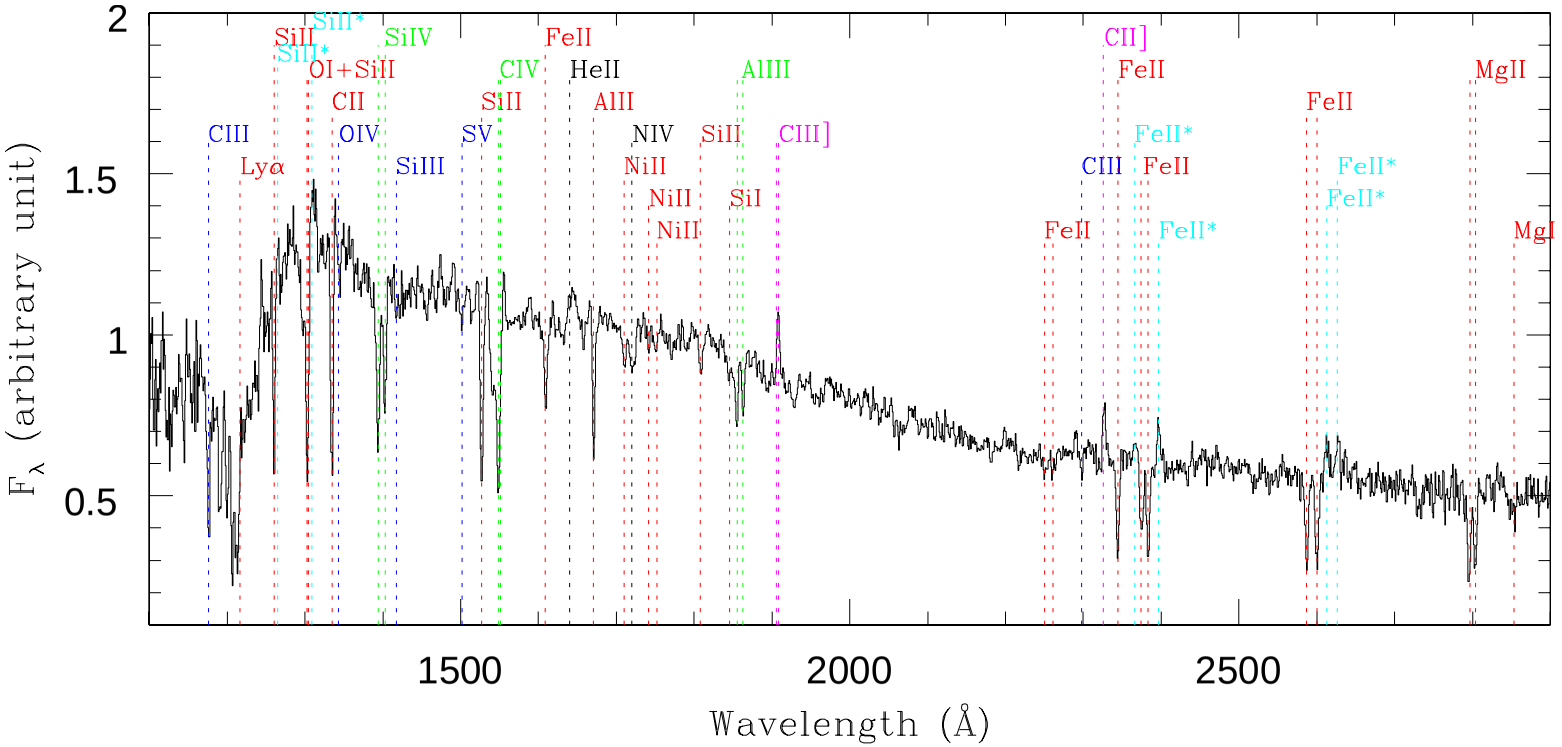

Fig. 6.5: Average spectrum of the total sample (74 SFGs). Spectral lines of interest are labelled. Blue: absorption stellar photospheric lines; red: interstellar absorption low-ionization lines; green: interstellar absorption high-ionization lines; magenta: emission nebular lines; black: emission and absorption lines associated with stellar winds; cyan: interstellar fine-structure emission lines.

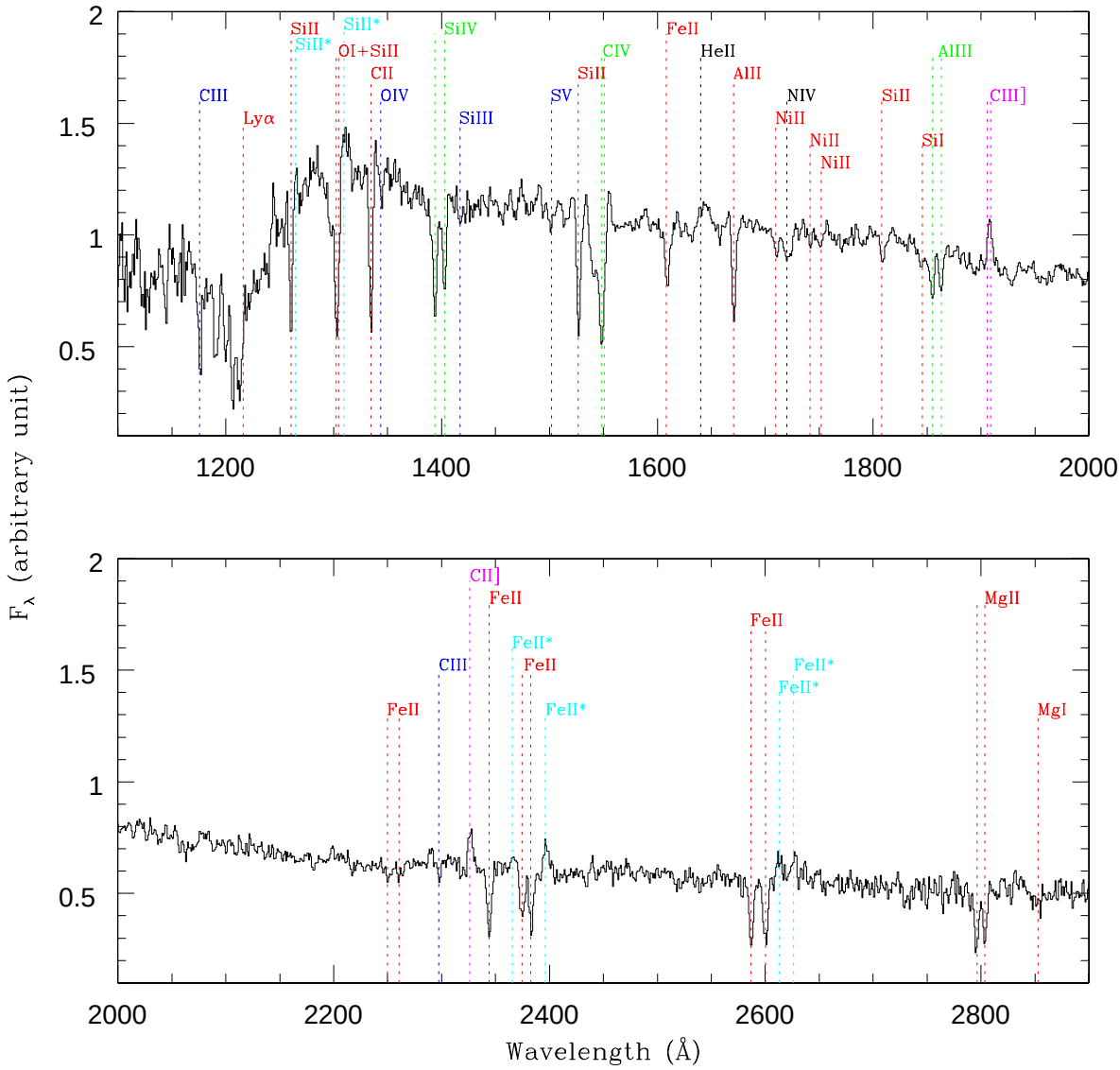

Fig. 6.6: Zoom of the composite spectrum, above and below 2000 Å. Spectral lines of interest are labelled. Blue: absorption stellar photospheric lines; red: interstellar absorption low-ionization lines; green: interstellar absorption high-ionization lines; magenta: emission nebular lines; black: emission and absorption lines associated with stellar winds; cyan: interstellar fine-structure emission lines.

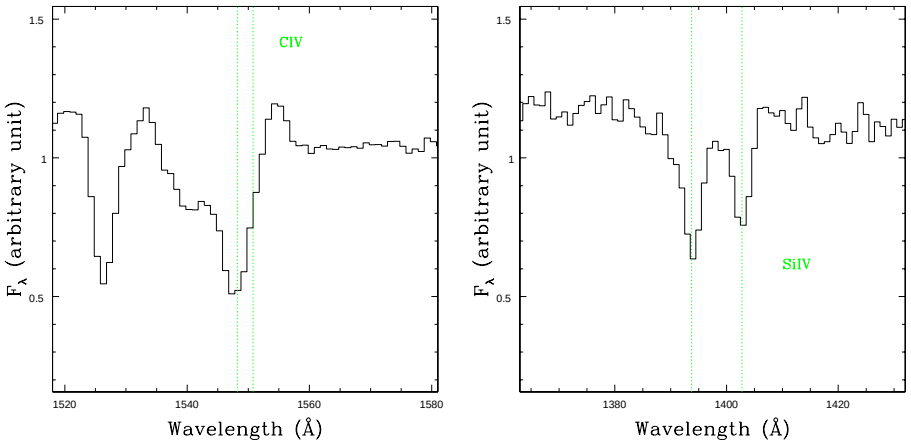

Fig. 6.7: Composite spectrum of the 74 spectra of the SFG sample (see Fig. 6.5): zoom-in of the regions close to the C IV and the Si IV doublets. The spectrum has been shifted into its stellar rest-frame. The vertical lines indicate the vacuum wavelength of the line.

6.3.3 Low- and high-ionization absorption lines associated with the ISM

The strongest lines detectable in the UV rest-frame spectrum of starburst galaxies are low- and high-ionization absorption interstellar lines. The first set of lines are associated with neutral gas regions and caused by the absorption of stellar radiation by the interstellar medium, which ensures that they are the optimal tools for detecting outflows in the host galaxy.

In particular, the strongest lines in our spectra are Si II λ1260 Å, C II λ1334 Å, Si II λ1526 Å, Fe II λ1608 Å, Al III λ1670 Å, Fe II λ2344 Å, Fe II λ2374 Å, Fe II λ2382 Å, Fe II λ2586 Å, Fe II λ2600 Å, plus the blend (at our spectral resolution) of O and Si II at λ1303 Å, and the doublet Mg II $\lambda\lambda$2796, 2803 Å. Some other weaker lines, which we identified as interstellar absorption lines, can be found in Tables 6.1 and 6.2.

High-ionization lines predominantly trace gas with T $> 10^4 K$. Three doublets are recognizable in our spectra, i.e., Si IV $\lambda\lambda$1393, 1402 Å, C IV $\lambda\lambda$1548, 1550 Å, and Al III $\lambda\lambda$1854, 1862 Å. Fig. 6.7 shows zoomed-in spectral regions of the composite spectrum, containing the CIV and SiIV doublets. The spectrum has been shifted into its stellar rest-frame and the expected position of the spectral lines is indicated by the dotted vertical lines. Unlike low-ionization lines, more than one process causes the formation of the high-ionization doublets, including the absorption of stellar radiation by the interstellar medium, as well as the contributions of stellar winds and photospheric stellar absorption,

but these different components are difficult to distinguish. A study of UV O-type stellar spectra by Walborn & Panek (1984) qualitatively showed that the Si IV doublet profile is dominated by the interstellar component, because only blue giant and super-giant stars contribute to the wind component, while the C IV doublet is dominated by the stellar wind feature, whose contribution to the line profile comes from stars belonging to all luminosity classes, from main-sequence to super-giant stars. The stellar wind component should display a P-Cygni profile, which is characterized by redshifted emission and blueshifted absorption. Since the spectral resolution is too low to allow a decomposition of the line profile into its components, high-ionization lines are poorly suited to the search and study of large-scale outflows.

6.3.4 Other notable spectral lines

Lyα

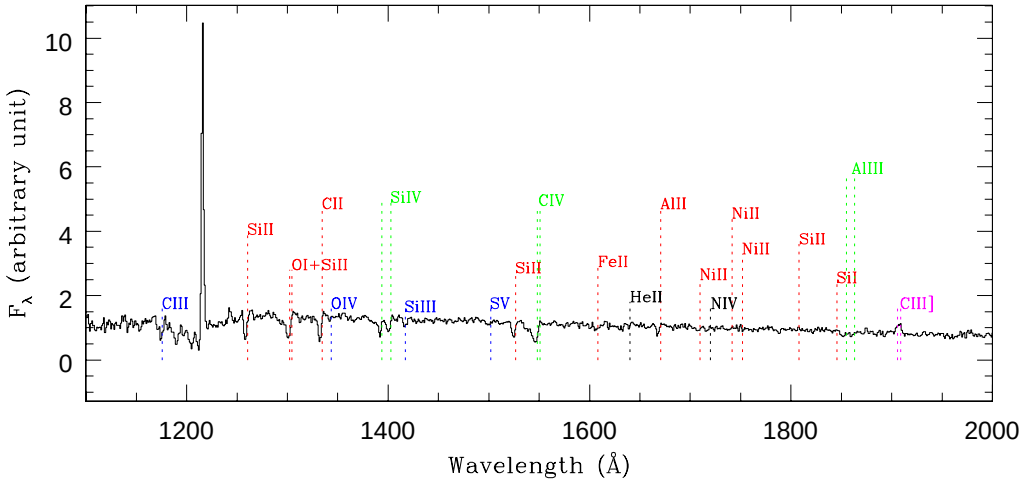

Fig. 6.8: Average spectrum of the six galaxies with Lyα line in emission. The spectrum has been shifted into the rest-frame given by the Lyα. The expected position of the most prominent spectral lines is indicated. See Fig. 6.5 for the colour legend.

The Lyα λ1216 Å spectral line originates from recombinations in H II regions and can be used to study the physical conditions within them. When detected in emission, it is the most prominent spectral feature in the spectra of high-redshift galaxies. When seen in absorption, the line has a very broad profile, often blueshifted. In our SFG sample, 32 spectra extend blueward to include the Lyα region: only in 8 cases the line is in

emission clearly. We measured the velocity offset between the Lyα in emission and the low-ionization interstellar absorption lines in the 6 spectra where both sets are detect A mean velocity offset $\Delta v_{em-abs} \sim 566 \pm 27$ km/s was found, which is consistent with the $\sim$ 650 km/s reported by Shapley et al. (2003) for their sample of $z \sim 3$ Lyman break galaxies.

Two composite spectra were then created, one with the spectra for which Lyα is in emission (see Fig. 6.8) and the other with the spectra for which Lyα is in absorption, and their continuum slope was measured following the procedure described in 5. We found that the emission Lyα spectrum has a bluer slope than in the other case (respectively, $\beta_{emLy\alpha} = -1.40 \pm 0.06$ and $\beta_{absLy\alpha} = -1.04 \pm 0.03$), thus confirming the relation between UV continuum slope, and therefore dust extinction, and the Lyα profile in SFGs, as already observed in LBGs at $z \sim 3$.

He II λ1640 Å

The He II λ1640 Å spectral line is a typical feature produced by winds from Wolf-Rayet (WR) stars or AGN. The WR stars are thought to represent a stage in the evolution of O-type stars with masses $M > 20M_{\odot}$. They are characterized by strong winds with velocities reaching thousands km/s, causing considerably mass losses. The strength of the broad He II λ1640 Å is likely to depend on the ratio of the number of WR to O-type stars, which in turn depends strongly on the metallicity (Schaerer & Vacca 1998; Meynet 1995; Brinchmann et al. 2008): at lower metallicities, O-type stars are less likely to evolve into WR, and the He II becomes intrinsically weaker. From the EW of He II λ1640 Å measured on the composite spectrum of our entire sample $EW_{HeII} = 1.02 \pm 0.10$ Å, we derived a WR/(WR+O) ratio of 0.05 ± 0.008 (Schaerer & Vacca 1998).

Quite a good agreement is found with the models of Brinchmann et al. (2008). For the case of a nearly constant SFR, with an age of $\sim$ 120 Myrs, which is the median age of our sample of galaxies, the predicted EW values range from $\sim$ 0.65 Å to $\sim$ 1.3 Å (see Brinchmann et al. 2008, Figure 2), depending on the metallicity ($0.4 < Z/Z_{\odot} < 1.0$). Since the metallicity of the SFGs in the GMASS sample were estimated to be $Z \sim 0.3Z_{\odot}$ by Halliday et al. (2008), our measured EW is fairly consistent with the model predictions.

Fe II*

In our composite spectrum, we were also able to identify some iron fine-structure emission lines between 2000Å and 3000Å namely Fe II* λ2365 Å, Fe II* λ2396 Å, Fe II* λ2612 Å, and Fe II* λ2626 Å. These lines have been proposed to be generated by photon scattering in large-scale outflows (Rubin et al. 2010), hence their detection can be considered as a confirmation of the presence of outflows.

6.4 Outflows

We searched for galactic-scale outflows in galaxy UV spectra by measuring the wavelength shift, in the centroid position, of spectral lines that originate from the absorption of the background stellar radiation by the interstellar medium. The most accurate estimate of the systemic rest-frame velocity of a galaxy is the one determined from spectral lines that are of stellar origin. The assumption that stellar spectral features are at rest with respect to their host galaxy is justified by considering that it is impossible to resolve stellar populations in high-redshift galaxies, and that the effects of stellar proper motions on a spectral line shift tend to statistically cancel out. The stellar lines observed in the galaxy UV rest-frame are extremely weak, and in the single GMASS spectra are almost undetectable because of the low S/N of the stellar continuum. It is possible to improve the S/N to identify the stellar spectral lines by working on composite spectra (see Fig. 6.9).

In Fig. 6.5, the composite spectrum of 74 high-quality SFGs is shown, where two stellar and two nebular lines can be detected and reliably measured: the absorption lines C III λ1176 Å, O IV λ1343 Å, and the semi-forbidden C III] $\lambda\lambda$1906, 1908 Å doublet and CII] λ2326 Å emission line. Since the redshifts of the single galaxies were determined from the strongest lines, which are the interstellar absorption ones, the composite spectrum does not appear to be at rest with respect to the stellar and nebular features (see Fig. 6.10). Therefore, to compute the velocity offsets of the lines tracers of the IS gas, first of all the composite spectrum was shifted into its rest-frame using the mean shift measured for the two chosen photospheric stellar lines and the two nebular carbon emission lines, weighted for their uncertainties (see Section 6.4.2), of $\sim 135 \pm 22$ km/s. [13].

[13]The error in a weighted mean is defined as $\sigma^2 = 1/\sum(1/\sigma_i^2)$, where σ_i are the measurement uncertainties associated with the stellar and nebular lines.

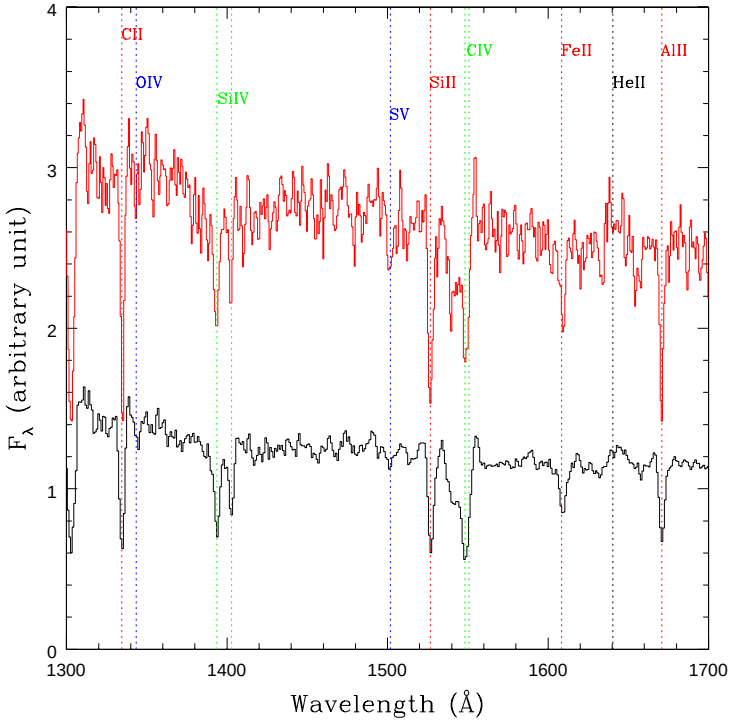

Fig. 6.9: Comparison of the total average spectrum (black, below; the same seen in Fig. 6.5) of our sample with the spectrum of a single galaxy (red, above). See Fig. 6.5 for the colour code adopted.

6.4.1 Velocity offset measurements

The different kinds of lines observed in the UV rest-frame spectrum of a SFG were already described in a previous section. Here we recall that, in the 1200 – 2900 Å range, seven strong low-ionization interstellar absorption lines, tracers of the large-scale winds, are detectable, one of which is a blend; three low-ionization doublets are also detectable (Fe II and Mg II), in addition to three high-ionization ones (Si IV, C IV, and Al III). The high-ionization doublets do not provide robust tools in the search for outflows, since at our spectral resolution an attempt to separate the ISM absorption from other components, such as the stellar wind P-Cygni profile, is impractical.

Therefore, in our analysis we concentrated only on the low-ionization interstellar absorption lines and doublets, particularly Si II λ1260 Å, C II λ1334 Å, Si II λ1526 Å, Fe II λ1608 Å, Al III λ1670 Å, and Fe II λ2344 Å, and the doublets Fe II λ2374, 2382 Å, Fe II λ2586, 2600 Å, and Mg II $\lambda\lambda$2796, 2803 Å. The O + Si II λ1303 Å feature was excluded because it was impossible to correctly determine the position of the centroids of the two

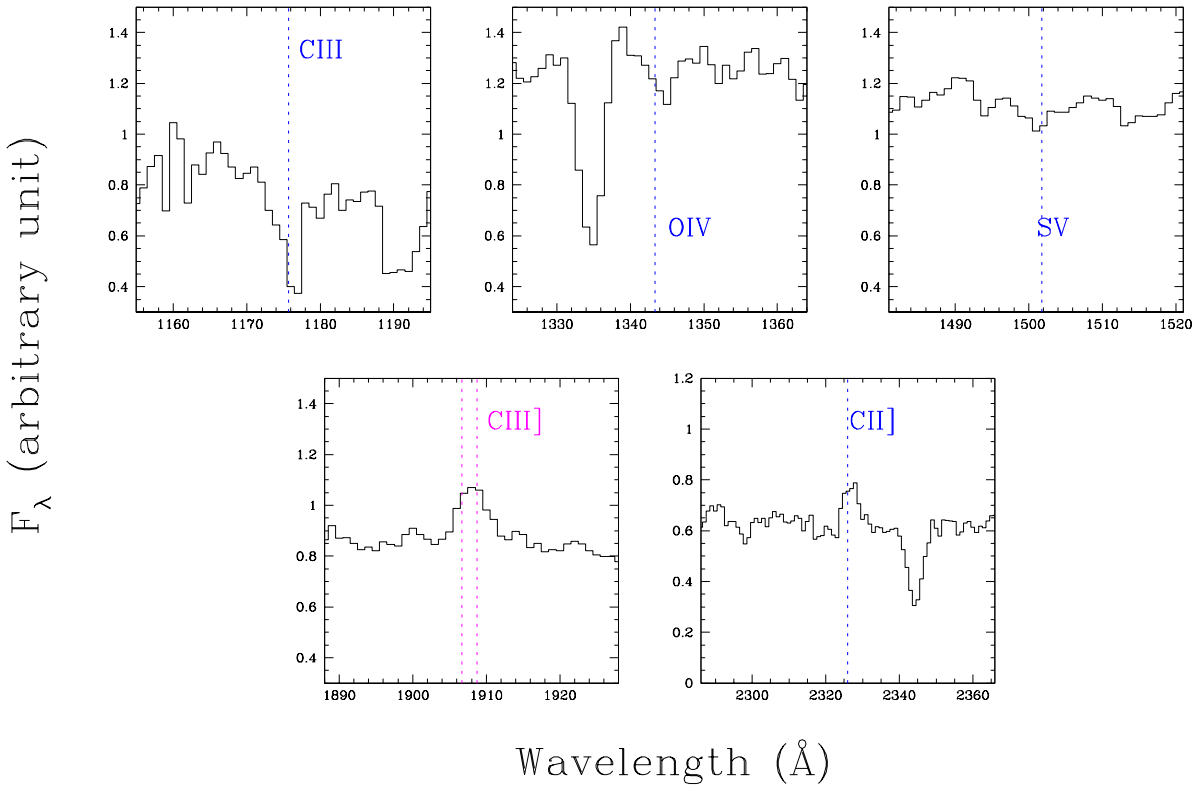

Fig. 6.10: Composite spectrum of the 74 spectra of the SFG sample (see Fig. 6.5): zoomed image of the three detectable stellar photospheric absorption lines (C III λ1176 Å, O IV λ1343 Å, S V λ1501 Å. The latter was not used in the analysis since it is too weak to be reliable measured), the C III] $\lambda\lambda$1906, 1908 Å nebular emission line doublet and the CII] λ2326 Å nebular line. The vertical lines indicate the vacuum wavelength of the line.

blended lines. The other cited interstellar lines were all detectable and strong enough to ensure a quite good determination of their centroid.

The Fe II λ1608 Å centroid is probably the least accurately determined, since it is the weakest of all the IS lines and its profile is broader and more asymmetric, which are all factors that may alter the position of the centroid during the fitting procedure. Moreover, we suspect that a blend of absorption features (Fe III, Al III, N II) typical of O and B stars in the 1600-1630 Å range (see Kinney et al. 1993) could play a major role in distorting the Fe II λ1608 Å line profile.

6.4.2 Uncertainties

For each line, two possible error sources related to the centroid measurement were estimated. The error caused by spectral noise was computed by creating an artificial template with a continuum slope similar to that of the real composite spectrum and perfect Gaussian spectral lines of similar intensities to those in the composite. Random noise was then added to the template until the S/N of the true composite spectrum was matched, and the centroids of the spectral lines of interest were measured. For each line, the r.m.s. of 30 repeated measurements, with respect to the input value, was then adopted as the measurement uncertainty. For the strongest absorption lines, the order of magnitude of this uncertainty is $\sim 15 - 20$ km/s; weaker lines have a larger measurement uncertainty with a maximum of ~ 100 km/s for the O IV λ1343 Å.

We then evaluated how slight variations in the number of constituents of the composite spectrum would affect the aspect of the spectral lines or the position of their centroid, by creating about a dozen composite spectra and omitting from the procedure a number of single spectra randomly chosen to be between 5 and 10. The lines of interest were then measured in all the spectra: the computed r.m.s. of the measurements for each line was eventually defined as the "galaxy sampling uncertainty" and added quadratically to the aforementioned measurement error. On average, the galaxy sampling uncertainty is ~ 10 km/s for the interstellar and nebular lines and ~ 35 km/s for the photospheric stellar ones.

Finally, for the unresolved C III] $\lambda\lambda$1906, 1908 Å doublet, as already mentioned, we fixed the intensities ratio of the two components to be 1.5, but added to the line measurement an error component of ~ 39 km/s to take into account the uncertainty in the flux intensity ratio. For example, Quider et al. (2009) measured a flux ratio $F(1906)/F(1908) = 1.1 \pm 0.2$ in the spectrum of the "Cosmic Horse Shoe", a gravitationally lensed SFG at $z \sim 2$, whose physical properties such as SFR, mass, and dust extinction are similar to the average ones computed for our sample. We note that using a flux ratio of 1.1 instead of 1.5, would not affect our results. The total uncertainty for each line is quoted in Table 6.3.

6.4.3 Results

Fig. 6.11 shows zoomed-in spectral regions containing the main low-ionization interstellar absorption lines whose offsets were measured. The spectrum has been shifted into its rest-frame defined by the velocity correction of ~ 135 km/s computed from the stellar

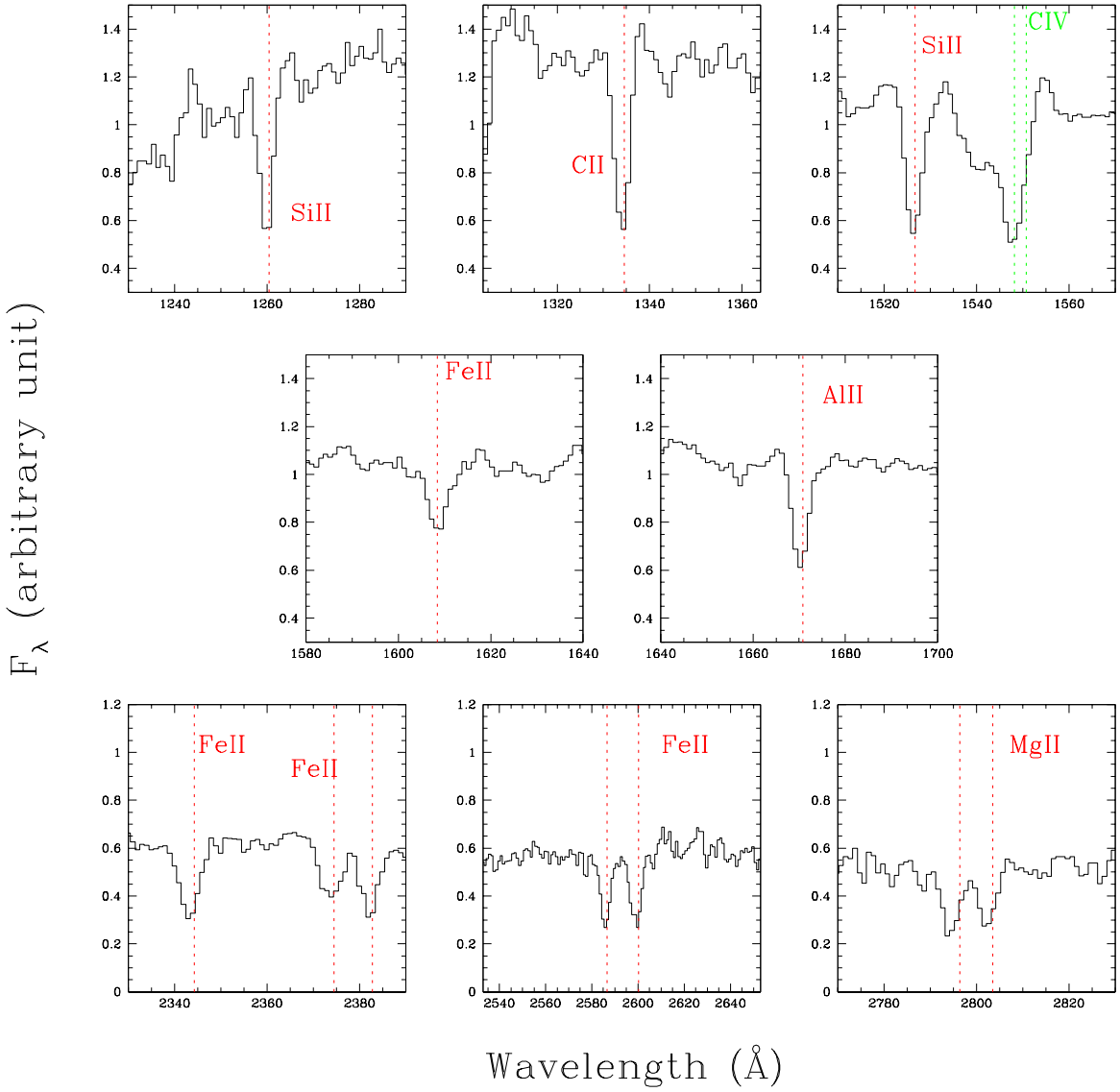

Fig. 6.11: Composite spectrum of the 74 spectra of the SFG sample (see Fig. 6.5): zoomed-in image of the strongest low-ionization interstellar absorption lines. The C IV high-ionization doublet is also labelled. The spectrum has been shifted into its rest-frame using the velocity correction derived from the stellar/nebular lines (~ 135 km/s). The vertical lines indicate the expected positions of the line.

and nebular lines.

Most of the lines are blueshifted with respect to their expected positions, as indicated by the vertical dashed lines: this confirms, at least on average, that outflows exist in the galaxies of our sample. These results, qualitatively shown in the figures, are presented in

Table 6.3: Velocity offsets and EWs of strong low-ionization lines, measured in the composite spectrum of the full SFG sample.

Ion	Vacuum wavelength (Å)	IE (eV)[a]	EW (Å)[b]		v (km/s)	
			GMASS	LBG[c]	GMASS	LBG[c]
Si II	1260.42	8.15	1.47 ± 0.09	1.63 ± 0.10	-79 ± 19	-110 ± 60[e]
O I - SiII[d]	1302.17, 1304.37	-	2.43 ± 0.26	2.20 ± 0.12	-123 ± 42	-270 ± 60[e]
C II	1334.53	11.26	2.09 ± 0.15	1.72 ± 0.11	-105 ± 33	-150 ± 60[e]
Si II	1526.71	8.15	1.94 ± 0.08	1.72 ± 0.18	-79 ± 19	-110 ± 60[e]
Fe II	1608.45	7.87	1.31 ± 0.11	0.91 ± 0.15	24 ± 40	-60 ± 60[e]
Al II	1670.79	5.99	1.54 ± 0.08	1.04 ± 0.15	-78 ± 27	-100 ± 60[e]
Fe II	2344.21	7.87	2.45 ± 0.13		-139 ± 27	
Fe II[f]	2374.46	7.87	1.87 ± 0.13		-72 ± 32	
Fe II[f]	2382.76	7.87	2.21 ± 0.15		-72 ± 27	
Fe II[g]	2586.65	7.87	2.65 ± 0.17		-108 ± 27	
Fe II[g]	2600.17	7.87	2.77 ± 0.14		-108 ± 28	
Mg II[h]	2796.35	7.65	2.43 ± 0.10		-176 ± 27	
Mg II[h]	2803.53	7.65	2.07 ± 0.10		-176 ± 27	

[a] Ionization energy.
[b] Rest-frame equivalent widths.
[c] Values from Shapley et al. (2003).
[d] All the measurements, both ours and Shapley's, refer to the blend of the two lines.
[e] Shapley et al. (2003) quotes only the mean error in the velocity offsets.
[f] ghDoublets.

Table 6.3. A mean velocity offset of $\sim$ 100 km/s was computed for all the interstellar lines in our composite. The shift velocities measured for the single low-ionization lines in the composite spectrum are listed, along with the results from Shapley et al. (2003) for the composite spectrum of a sample of Lyman-break selected galaxies (LBG) at $z \sim 3$. The EWs of all the lines were also measured, and presented. It was impossible to compare offsets and EWs of all the lines, since our composite spectrum extends more to the red than the LBG composite.

In the wavelength range sampled by both spectra, given the uncertainties, the two sets of velocities are fairly consistent, which demonstrates that gas outflows are a common phenomenon in SFGs at all redshifts.

However, the EWs measured in our composite are larger than in the LBG composite. Looking at the colour excess in the two samples, the LBG sample has $E(B-V)$ values that are, on average, $\sim$ 0.1 mag lower than the ones computed for our sample. This can be interpreted as evidence of the correlation between the interstellar absorption-line strength and dust extinction.

We also find that the kinematics of Mg II gas are often discrepant with respect to all the other lines, with Mg II preferentially tracing higher velocity gas. This result has been recently confirmed also by Kornei et al. (2012).

6.5 Searching for correlations between UV spectroscopic properties and galaxy physical properties

The spectral analysis of the composite spectrum has provided average information about our entire sample of $z \sim 2$ high-quality SFG spectra. The next step was to investigate possible correlations between galaxy UV spectral characteristics (EW, outflows) and galaxy general properties, in particular stellar mass, SFR, and dust-extinction.

Our sample was divided into two equally populated bins, for each property, and a composite spectrum of each group of galaxies was created, following the same procedure adopted in the creation of the composite of the total sample. We decided to work with only two bins because of the limited number of spectra at our disposal. As already stated, to have reliable measurements of centroids and EWs for the spectral lines of interest, a high S/N is needed in the composite spectra, and the composition procedure is the more effective in improving the S/N the larger the number of single spectra involved.

Fig. 6.12 shows the distribution of the chosen physical properties over our sample, with the binning division values marked and the median values of each bin reported. The composite spectrum of each bin was shifted into the rest-frame given by the stellar and nebular lines. We then measured the velocity offsets of the low-ionization absorption lines, which are presented in Tables 6.4, 6.5, and 6.6. Since these tables contain a large amount of information, the mean velocity offset and EW of the interstellar low-ionization absorption lines in each bin are also reported in Table 6.7.

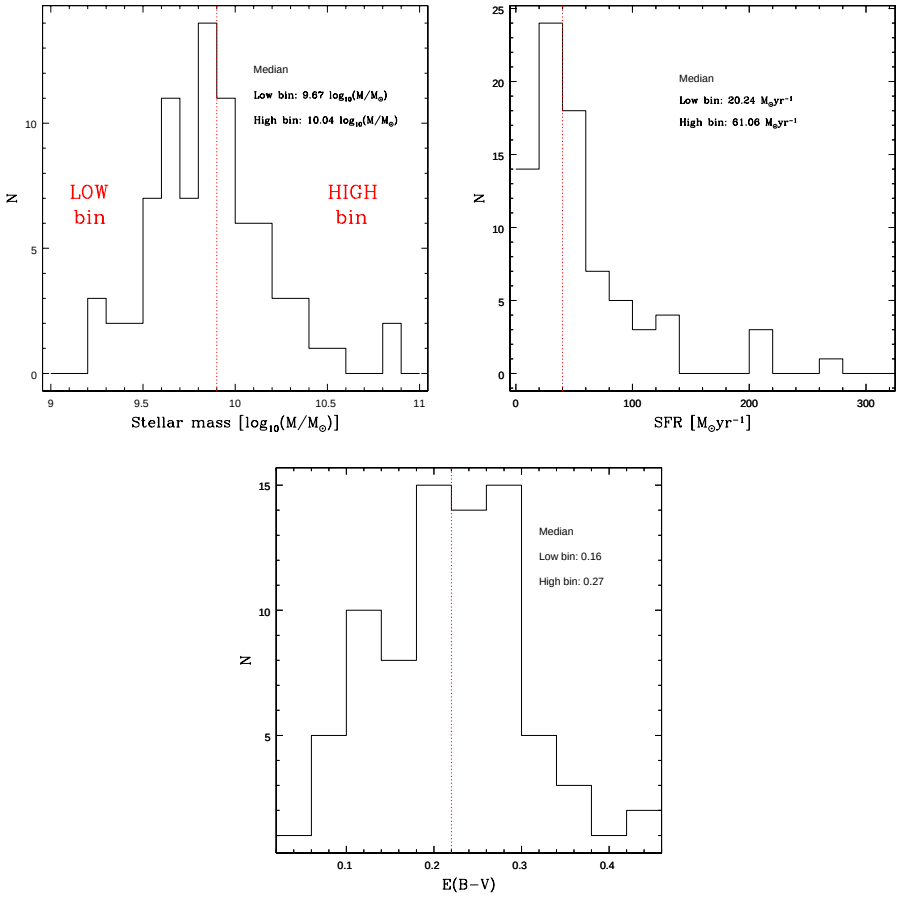

Fig. 6.12: Distribution over the sample of stellar mass, SFR (from 1500 Å luminosity measured in the spectra with dust extinction derived from the continuum slope), and E(B-V) (computed from the UV continuum slope). The median value of both the sub-samples is also reported in each panel.

Table 6.4: Equivalent widths and velocity offsets of the strongest interstellar absorption lines (plus the He II λ1640 Å emission line) measured in composite spectra (SFR).

Ion	Vacuum wavelength (Å)	EW (Å)	v (km/s)	EW (Å)	v (km/s)	EW_{ratio} [a] (Å)	Δv [b] (km/s)
SFR		Bin 1[c]: 20.24 $M_\odot$ yr^{-1}		Bin 2[c]: 61.06 $M_\odot$ yr^{-1}			
Si II	1260.42	0.97 ± 0.09	-97 ± 19	1.57 ± 0.09	-145 ± 19	1.62 ± 0.33	-49 ± 27
C II	1334.53	1.98 ± 0.15	-114 ± 33	2.17 ± 0.15	-138 ± 33	1.10 ± 0.33	-24 ± 47
Si II	1526.71	2.44 ± 0.08	-97 ± 19	3.73 ± 0.08	-145 ± 19	1.53 ± 0.27	-49 ± 27
Fe II	1608.45	1.09 ± 0.11	9 ± 40	1.21 ± 0.11	-47 ± 40	1.11 ± 0.25	-56 ± 57
He II	1640.42	-1.13 ± 0.10		-0.87 ± 0.10		0.77 ± 0.16	
Al II	1670.79	1.35 ± 0.08	-108 ± 27	1.77 ± 0.08	-95 ± 27	1.31 ± 0.22	13 ± 38
Fe II	2344.21	2.19 ± 0.13	-185 ± 27	3.02 ± 0.13	-120 ± 27	1.38 ± 0.38	65 ± 38
Fe II	2374.46	1.81 ± 0.13	-150 ± 32	2.77 ± 0.13	-89 ± 32	1.53 ± 0.43	61 ± 45
Fe II	2382.76	2.06 ± 0.15	-150 ± 27	2.28 ± 0.15	-89 ± 27	1.11 ± 0.33	61 ± 38
Fe II	2586.65	1.88 ± 0.17	-159 ± 27	3.74 ± 0.17	-87 ± 27	1.99 ± 0.84	72 ± 38
Fe II	2600.17	2.57 ± 0.14	-159 ± 28	3.33 ± 0.14	-87 ± 28	1.30 ± 0.38	72 ± 40
Mg II	2796.35	2.53 ± 0.10	-239 ± 27	2.18 ± 0.10	-137 ± 27	0.86 ± 0.17	101 ± 38
Mg II	2803.53	1.87 ± 0.10	-238 ± 27	2.37 ± 0.10	-137 ± 27	1.27 ± 0.26	101 ± 38

[a] $EW_{ratio} = EW_{HighBin} / EW_{LowBin}$

[b] $\Delta v = v_{HighBin} - v_{LowBin}$

[c] Median of each bin.

Table 6.5: Equivalent widths and velocity offsets of the strongest interstellar absorption lines (plus the He II λ1640 Å emission line) measured in composite spectra (stellar mass).

Ion	Vacuum wavelength (Å)	EW (Å)	v (km/s)	EW (Å)	v (km/s)	EW_{ratio} [a] (Å)	Δv [b] (km/s)
Stellar Mass		Bin 1[c]: 9.67 $\log(M_\odot)$		Bin 2[c]: 10.04 $\log(M_\odot)$			
Si II	1260.42	1.61 ± 0.09	-140 ± 19	1.89 ± 0.09	-138 ± 19	1.17 ± 0.21	2 ± 27
C II	1334.53	2.25 ± 0.15	-134 ± 33	2.34 ± 0.15	-91 ± 33	1.04 ± 0.31	43 ± 47
Si II	1526.71	2.47 ± 0.08	-140 ± 19	3.14 ± 0.08	-138 ± 19	1.27 ± 0.21	2 ± 27
Fe II	1608.45	1.17 ± 0.11	46 ± 40	1.28 ± 0.11	-13 ± 40	1.09 ± 0.24	-59 ± 57
He II	1640.42	-1.23 ± 0.10		-0.81 ± 0.10		0.66 ± 0.14	
Al II	1670.79	1.33 ± 0.08	-80 ± 27	1.87 ± 0.08	-92 ± 27	1.41 ± 0.24	-12 ± 38
Fe II	2344.21	2.37 ± 0.13	-149 ± 27	2.72 ± 0.13	-139 ± 27	1.15 ± 0.30	9 ± 38
Fe II	2374.46	1.68 ± 0.13	-82 ± 32	2.51 ± 0.13	-93 ± 32	1.49 ± 0.42	-11 ± 45
Fe II	2382.76	1.71 ± 0.15	-82 ± 27	2.90 ± 0.15	-93 ± 27	1.7 ± 0.58	-11 ± 38
Fe II	2586.65	2.59 ± 0.17	-139 ± 27	3.31 ± 0.17	-101 ± 27	1.28 ± 0.45	37 ± 38
Fe II	2600.17	2.88 ± 0.14	-139 ± 28	3.27 ± 0.14	-101 ± 28	1.14 ± 0.32	37 ± 40
Mg II	2796.35	2.24 ± 0.10	-183 ± 27	2.37 ± 0.10	-209 ± 27	1.06 ± 0.21	-26 ± 38
Mg II	2803.53	1.63 ± 0.10	-183 ± 27	2.66 ± 0.10	-209 ± 27	1.63 ± 0.37	-26 ± 38

[a] $EW_{ratio} = EW_{HighBin} / EW_{LowBin}$

[b] $\Delta v = v_{HighBin} - v_{LowBin}$

[c] Median of each bin.

Table 6.6: Equivalent widths and velocity offsets of the strongest interstellar absorption lines (plus the He II λ1640 Å emission line) measured in composite spectra (*E(B-V)*).

Ion	Vacuum wavelength (Å)	EW (Å)	v (km/s)	EW (Å)	v (km/s)	EW_{ratio} [a] (Å)	Δv [b] (km/s)
	E(B-V)	Bin 1[c] 0.16		Bin 2[c] 0.27			
Si II	1260.42	1.43 ± 0.09	-84 ± 19	2.25 ± 0.09	-38 ± 19	1.57 ± 0.31	46 ± 27
C II	1334.53	1.85 ± 0.15	-160 ± 33	2.18 ± 0.15	-58 ± 33	1.18 ± 0.36	102 ± 47
Si II	1526.71	1.70 ± 0.08	-84 ± 19	2.27 ± 0.08	-38 ± 19	1.34 ± 0.22	46 ± 27
Fe II	1608.45	1.25 ± 0.11	7 ± 40	1.61 ± 0.11	86 ± 40	1.29 ± 0.29	78 ± 57
He II	1640.42	-0.88 ± 0.10		-0.96 ± 0.10		1.10 ± 0.22	
Al II	1670.79	1.31 ± 0.08	-46 ± 27	1.81 ± 0.08	-51 ± 27	1.38 ± 0.23	-5 ± 38
Fe II	2344.21	2.28 ± 0.13	-103 ± 27	2.76 ± 0.13	-110 ± 27	1.21 ± 0.32	-7 ± 38
Fe II	2374.46	1.59 ± 0.13	-78 ± 32	2.15 ± 0.13	-21 ± 32	1.35 ± 0.37	57 ± 45
Fe II	2382.76	1.96 ± 0.15	-78 ± 27	2.40 ± 0.15	-21 ± 27	1.23 ± 0.38	57 ± 38
Fe II	2586.65	1.53 ± 0.17	-98 ± 27	3.89 ± 0.17	-58 ± 27	2.55 ± 1.28	39 ± 38
Fe II	2600.17	2.11 ± 0.14	-98 ± 28	3.58 ± 0.14	-58 ± 28	1.70 ± 0.54	39 ± 40
Mg II	2796.35	1.58 ± 0.10	-186 ± 27	3.04 ± 0.10	-124 ± 27	1.93 ± 0.47	63 ± 38
Mg II	2803.53	1.64 ± 0.10	-186 ± 27	2.32 ± 0.10	-123 ± 27	1.41 ± 0.30	63 ± 38

[a] $EW_{ratio} = EW_{HighBin} / EW_{LowBin}$

[b] $\Delta v = v_{HighBin} - v_{LowBin}$

[c] Median of each bin.

Table 6.7: Mean measured equivalent widths and velocity offsets.

	EW_{IS} (Å)		v_{IS} (km/s)		EW_{ratio} [b]	Δv [c]
SFR ($M_\odot$ yr^{-1})	Bin 1: 20.24	Bin 2: 61.06	Bin 1: 20.24	Bin 2: 61.06		
	1.90 ± 0.15	2.51 ± 0.24	-141 ± 19	-110 ± 9	1.33 ± 0.16	31 ± 21
Stellar Mass ($\log(M_\odot)$)	Bin 1: 9.67	Bin 2: 10.04	Bin 1: 9.67	Bin 2: 10.04		
	1.99 ± 0.16	2.52 ± 0.18	-117 ± 18	-118 ± 16	1.26 ± 0.13	-1 ± 24
E(B-V)	Bin 1: 0.16	Bin 2: 0.27	Bin 1: 0.16	Bin 2: 0.27		
	1.69 ± 0.09	2.52 ± 0.20	-99 ± 16	-51 ± 16	1.50 ± 0.14	48 ± 23

[a] Median of each bin.
[b] $EW_{ratio} = EW_{HighBin} / EW_{LowBin}$
[c] $\Delta v = v_{HighBin} - v_{LowBin}$

6.5.1 Outflow velocities

We found that the interstellar lines have a significant velocity shift in all the composite spectra ($\delta v_{IS} \sim 100$ km/s), but there seem to be no evident correlations between the velocity offsets of the interstellar absorption lines and the physical properties of the galaxies in our sample, apart from some weak differences to the colour excess and SFR.

However, our results do not completely exclude the existence of these correlations, since we are aware that factors may hide them. First of all, the magnitude of the uncertainties might be playing a significant role in obscuring some weak correlations. Moreover, the distributions of SFR, stellar mass, and colour excess do not help us to justify a division of the sample into two equally populated bins, since most of the galaxies are concentrated close to the threshold value, and the errors are large enough to cause confusion between the two bins. Finally, we should consider that there may also be absorption also from gas that is not outflowing, particularly in more massive galaxies (Steidel et al. 2010). This $v \sim 0$ component may affect the emergent line profile in the sense that the velocities computed from the centroid shift of the IS lines may be underestimated.

6.5.2 Equivalent widths of outflow-related absorption lines

The EW measurements differ significantly among those measured in the composite spectra of different sub-samples. There appears to be a positive trend between the EWs of the interstellar absorption lines and SFR, stellar mass, and E(B-V), which is the main result of this last part of our analysis.

In other samples of SFGs, at different redshifts but with comparable properties of stellar mass and SFR, interstellar absorption lines associated with large-scale outflows have been found to be stronger in galaxies with higher SFR, higher stellar mass, and more heavily extincted (Shapley et al. 2003; Weiner et al. 2009; Rubin et al. 2010). Given the correlations between these galaxy properties, it is not possible to establish the characteristic with which inter-stellar lines parameters are more strongly connected, even if the most significant of the three correlations appears to be the one with E(B-V).

From these results, it may be inferred that the EWs of the absorption interstellar lines are probably related to the velocity dispersion of the gas, to its geometry, or to a combination of the two effects, all of which are difficult to ascertain with the actual data.

Finally, we report the EW of He II λ1640 Å to be stronger in the composite spectra of the less massive and star-forming galaxies.

6.6 Conclusions

We have studied a sample of 74 SFGs at $z \sim 2$, selected from GMASS, by analysing their rest-frame UV spectra. In particular, we focused on large-scale gas-outflow-related properties. The main results can be summarized as follows:

1. A composite spectrum was created by averaging the high-quality spectra of 74 SFGs, to obtain average information about large-scale gas-outflow-related properties. The low-ionization absorption lines associated with the interstellar medium were found to be blueshifted, with respect to the rest frame of the system, indicating the presence of outflowing gas with velocities on the order of $\sim$ 100 km/s. Our measured velocity offsets were found to be fairly consistent with that obtained by Shapley et al. (2003) for the composite spectrum of a sample of LBGs at $z \sim 3$.

2. We measured the EWs of the low-ionization absorption lines associated with the interstellar medium: the EWs measured in our composite appear to be larger than in the LBG composite. This could be interpreted as evidence of a trend between the interstellar absorption-line strength and dust extinction, since the LBGs have $E(B-V)$ values that are, on average, $\sim$ 0.1 mag lower than the ones computed for our sample.

3. In the composite spectrum of 8 galaxies displaying *Ly*α in emission, a velocity difference of $\sim 566 \pm 27$km/s between this line and the interstellar absorption ones was measured. Moreover, the comparison of composite spectra of two sub-samples, one with *Ly*α in emission, the other with the feature in absorption, showed that the continuum slope is bluer in the first one (respectively, $\beta_{emLy\alpha} = -1.40 \pm 0.06$ and $\beta_{absLy\alpha} = -1.04 \pm 0.03$), confirming the existence of a relation between UV continuum slope, thus dust extinction, and the *Ly*α profile in SFGs.

4. Possible correlations between galaxy UV spectral characteristics (EW, outflows) and galaxy general properties, in particular stellar mass, SFR, and dust extinction, were investigated by dividing the sample into bins, for each of the aforementioned

properties. No evidence of a significant correlation was found between the velocity offsets of the interstellar absorption lines and the physical properties of the galaxies in our sample. However, this does not completely exclude the existence of these correlations, since the magnitude of the uncertainties in the velocity shift measurements may hide them.

5. The He II λ1640 Å emission line, a feature due to winds from WR stars, was measured in all the composite spectra and the values were compared with the predictions of the most recent stellar population synthesis models. Given the physical properties of the galaxies in our sample, the models predict EWs that are fairly consistent with our measurements. We also report that the He II λ1640 Å is stronger in the composite spectra of the less massive, star-forming galaxies, a puzzling result since a larger fraction of WR stars is expected at higher metallicities.

6. We have found a positive trend between the EWs of the interstellar absorption lines and SFR, stellar mass, and E(B-V), a trend previously reported to hold at different redshifts. The most significant appears to be the correlation with E(B-V), which suggests that the EWs of the absorption interstellar lines are probably related to the velocity dispersion of the gas, to its geometry, or to a combination of the two effects.

CHAPTER 7

Brief summary and future prospects

This thesis was devoted to the study of the properties of high-redshift galaxies, in order to answer some of the open questions in the topic of galaxy evolution. In particular, we selected a sample of galaxies at $1 < z < 3$ and studied their morphologies and their star-formation properties. Here we summarize the main results of this work, and briefly describe the possible future developments.

Morphologies

A sample of galaxies with HST/WFC3-IR imaging, was morphologically classified following two methods: a "by eye" classification, and non-parametric statistics. The classification was used to assess how the fraction of different morphological types changes with redshift.

We found that the fraction of regular morphologies (ellipticals and disks) drops going from $z = 1$ to $z \sim 4$; the high redshift galaxy population is, in fact, dominated by irregular galaxies. We can place the built up of the Hubble sequence around $z \sim 2 - 3$.

Since classification by eye is very difficult at high-redshift, it is important to calibrate other "automatic" methods. We tested some of the most commonly used non-parametric statistics, and found that the GvsM20 plane proves to be the more effective in segregating different morphological types.

By comparing WFC3 and ACS imaging, we explored the role of the morphological k-correction between the rest-frame UV and optical appearance of our galaxies. We concluded that, at $1 < z < 3$, there is no evidence of a significant morphological k-correction.

In our sample we confirm the existence of a rest-frame colour bimodality. Morphologies tend to follow the bimodality in the sense that almost all ellipticals fall under the red peak, while irregulars and compacts inhabit the blue one. Disks are a mixed category, showing a blue and a red peak in their distribution, but also populating the intermediate region.

We discovered a population of blue, star-forming galaxies with the same morphological properties of red ellipticals. The true nature, and possible evolution, of these objects is yet to be understood: they could be non-interacting low mass galaxies that are building up their stars and then will slowly passively evolve into local ellipticals, or major-merger remnant or disk-building systems.

We plan to extend our work by studying the links between morphologies and other properties of galaxies. In particular, their spectral features, their IR luminosities, and their X-ray properties. Then, the natural prosecution of the analyses here conducted will be to use the morphological informations to constrain the merger fraction at $z > 1$. The G-M20 plane effectively segregates merger candidates at low redshift, but at high redshift the locus of the plane where merger candidates fall has to be determined. We will use also a close pairs identification method, to search for merger candidates, and the results of the two methods will be compared. Finally, after the definition of a sample of merger candidates, the properties of these galaxies will be compared with the ones of the parent sample, in order to study the link between the occurrence of merger episodes and the star-formation history of a galaxy.

Star-formation rate and dust extinction

A sample of galaxies, with secure spectroscopic redshift, and a photometric coverage from optical to the far IR regime, was selected in order to study the SFR at $z > 1$.

We computed the SFR using different estimators, and compared the results. The first chosen estimator was the integrated luminosity between 8 and 1000 μm (LIR). We used HERSCHEL data to test the robustness of the most commonly used synthetic SED libraries in recovering the bolometric LIR when only one photometric point is available, and we computed the calibrations to correct the derived luminosities.

Since the SFR derived from LIR is related to the dust content of a galaxy, the comparison of this estimate with others derived at UV and optical wavelengths gives information about the effectiveness of methods to correct fluxes for dust extinction. Comparing the SFR derived from LIR with SFR from SED fitting, we found the latter estimate to be systematically higher. This result suggests that the treatment of dust obscuration in SED modelling needs to be refined. Also the star-formation history influences the relation between the two estimates. When an exponentially decaying star-formation is applied, in fact, some galaxies with low τ values have an excess of SFR_{IR+UV} with respect to SFR_{SED}. A better choice, for our sample of galaxies, seems to be a constant

star-formation.

The comparison between SFR_{IR+UV} and $SFR_{correctedUV}$ gives better results. The two estimates agree reasonably well, though with a large scatter. This scatter depends on the scatter in the relation between the ratio of IR over UV flux (A_{IRX}) and the rest-frame UV spectral slope (β). This relation is very tight, in the local Universe, but it becomes much more scattered at $z > 1$. This is another prove that the traditional way of addressing the dust obscuration problem does not work well at high-redshifts, and new models of dust geometry and composition are required.

Finally, we derived the SFR from the [OII]λ3727 forbidden line flux, trying two different methods of dust correction. First, the attenuation derived from SED fitting; second, the attenuation derived from a relation between H_α/H_β and LIR in low redsfhit galaxies. In both cases, the corrected SFR_{OII} overestimates the SFR_{IR+UV}, similarly to what happens in the case of SFR_{SED}.

We intend to continue our work on star-formation by examining more in depth the causes of the differences between the estimates at different wavelengths. In particular, we will use the SFR_{IR+UV} to calibrate new relations to correct for dust extinction the UV and optical estimators. Radiative transfer models will be also used in the process, to study the properties of dust. Once a "ladder" of cross-calibrated SFR indicators will have been established, we will use it to study the correlation between SFR and other galaxy properties, in particular mass and morphologies, using also of the results of our morphological analyses.

Galactic-scale outflows

A sub-sample of star-forming galaxies, with very high quality spectra, was used to study the galactic winds phenomenon. The rest-frame UV spectrum of a star-forming galaxy is characterized by many spectral lines, arising from the absorption of background stellar radiation by the inter-stellar medium. These lines can be used to study the kinematics of the inter-stellar gas.

Using stacking analyses, we found evidence of escaping gas at velocities of $\sim$ 100 km/s. We searched for correlations between the gas velocity and other properties of the galaxies, founding any. We found, instead, a positive trend between the equivalent width of the interstellar absorption lines and some galaxy properties, in particular SFR, stellar mass, and E(B-V).

The most significant of the three correlations appears to be the one with E(B-V), which

suggests that the equivalent widths of the absorption interstellar lines are probably related to the velocity dispersion of the gas, to its geometry, or to a combination of the two effects.

To improve our understanding of the phenomenon of large-scale outflows, deeper spectroscopic surveys would be needed in the future. In particular, it would be extremely useful to have multi-wavelength spectral data. High-quality spectra sampling not only the rest-frame UV range, but also longer wavelengths, could enable us to carry out a robust determination of the systemic velocities and, consequently, the study of the warm phase of large-scale outflows in single galaxies, a task that to date has only been attempted for lens-magnified objects. Meanwhile, the next step in our work on outflows will be the study of possible correlations between the spectral properties of the UV interstellar absorption lines and the morphology of star-forming galaxies.

Bibliography

Abraham, R., Tanvir, N., & Santiago, B. 1996, MNRAS, 279, L47

Abraham, R. G., Nair, P., McCarthy, P. J., et al. 2007, , 669, 184

Abraham, R. G., Valdes, F., Yee, H. K. C., & van den Bergh, S. 1994, , 432, 75

Abraham, R. G., van den Bergh, S., & Nair, P. 2003, , 588, 218

Balestra, I., Mainieri, V., Popesso, P., et al. 2010, , 512, A12

Bell, E. F., McIntosh, D. H., Barden, M., et al. 2004, , 600, L11

Bell, E. F., McIntosh, D. H., Katz, N., & Weinberg, M. D. 2003, , 149, 289

Bell, E. F., Phleps, S., Somerville, R. S., et al. 2006, , 652, 270

Bell, E. F., van der Wel, A., Papovich, C., et al. 2012, , 753, 167

Bershady, M. A., Jangren, A., & Conselice, C. J. 2000, , 119, 2645

Berta, S., Magnelli, B., Lutz, D., et al. 2010, , 518, L30

Bertin, E. & Arnouts, S. 1996, , 117, 393

Bertone, S. & Conselice, C. J. 2009, , 396, 2345

Bluck, A. F. L., Conselice, C. J., Bouwens, R. J., et al. 2009, , 394, L51

Bluck, A. F. L., Conselice, C. J., Buitrago, F., et al. 2012, , 747, 34

Blumenthal, G. R., Faber, S. M., Primack, J. R., & Rees, M. J. 1984, , 311, 517

Bolzonella, M., Miralles, J., & Pelló, R. 2000, , 363, 476

Bournaud, F., Duc, P.-A., & Emsellem, E. 2008, , 389, L8

Bouwens, R. J., Illingworth, G. D., Franx, M., et al. 2009, , 705, 936

Bouwens, R. J., Illingworth, G. D., Oesch, P. A., et al. 2011, , 737, 90

Brinchmann, J., Pettini, M., & Charlot, S. 2008, , 385, 769

Bruzual, G. & Charlot, S. 2003, , 344, 1000

Buitrago, F., Trujillo, I., Conselice, C. J., et al. 2008, , 687, L61

Bundy, K., Ellis, R. S., Conselice, C. J., et al. 2006, , 651, 120

Calzetti, D. 2001, , 113, 1449

Calzetti, D., Armus, L., Bohlin, R. C., et al. 2000, , 533, 682

Calzetti, D., Kinney, A. L., & Storchi-Bergmann, T. 1994, , 429, 582

Cappellari, M., di Serego Alighieri, S., Cimatti, A., et al. 2009, , 704, L34

Caputi, K. I., Dunlop, J. S., McLure, R. J., & Roche, N. D. 2005, , 361, 607

Carlberg, R. G., Cohen, J. G., Patton, D. R., et al. 2000, , 532, L1

Cassata, P., Cimatti, A., Franceschini, A., et al. 2005, , 357, 903

Cassata, P., Cimatti, A., Kurk, J., et al. 2008, , 483, L39

Cassata, P., Giavalisco, M., Guo, Y., et al. 2011, , 743, 96

Cassata, P., Guzzo, L., Franceschini, A., et al. 2007, , 172, 270

Chary, R. & Elbaz, D. 2001, , 556, 562

Chevalier, R. A. & Clegg, A. W. 1985, , 317, 44

Cimatti, A. 2009, in American Institute of Physics Conference Series, Vol. 1111, American Institute of Physics Conference Series, ed. G. Giobbi, A. Tornambe, G. Raimondo, M. Limongi, L. A. Antonelli, N. Menci, & E. Brocato, 191–198

Cimatti, A., Cassata, P., Pozzetti, L., et al. 2008, , 482, 21

Cimatti, A., Daddi, E., Renzini, A., et al. 2004, , 430, 184

Coil, A. L., Weiner, B. J., Holz, D. E., et al. 2011, , 743, 46

Cole, S., Norberg, P., Baugh, C. M., et al. 2001, , 326, 255

Conselice, C. J., Bershady, M. A., Dickinson, M., & Papovich, C. 2003, , 126, 1183

Conselice, C. J., Blackburne, J. A., & Papovich, C. 2005, , 620, 564

Conselice, C. J., Bluck, a. F. L., Ravindranath, S., et al. 2011, , 417, 2770

Conselice, C. J., Bundy, K., Trujillo, I., et al. 2007, , 381, 962

Conselice, C. J., Rajgor, S., & Myers, R. 2008, MNRAS, 386, 909

Conselice, C. J., Yang, C., & Bluck, A. F. L. 2009, , 394, 1956

Cowie, L. L., Songaila, A., Hu, E. M., & Cohen, J. G. 1996, , 112, 839

Daddi, E., Cimatti, A., Renzini, A., et al. 2004, , 617, 746

Daddi, E., Dickinson, M., Morrison, G., et al. 2007, , 670, 156

Dale, D. A. & Helou, G. 2002, , 576, 159

De Propris, R., Conselice, C. J., Liske, J., et al. 2007, , 666, 212

Dickinson, M., Papovich, C., Ferguson, H. C., & Budavári, T. 2003, , 587, 25

Domínguez, H., Mignoli, M., Pozzi, F., et al. 2012, ArXiv e-prints

Dove, J. B., Shull, J. M., & Ferrara, A. 2000, , 531, 846

Drory, N., Salvato, M., Gabasch, A., et al. 2005, , 619, L131

Elbaz, D., Dickinson, M., Hwang, H. S., et al. 2011, , 533, A119

Elbaz, D., Hwang, H. S., Magnelli, B., et al. 2010, , 518, L29

Ferrarese, L. & Merritt, D. 2000, , 539, L9

Finlator, K., Davé, R., & Oppenheimer, B. D. 2007, , 376, 1861

Fontana, A., Pozzetti, L., Donnarumma, I., et al. 2004, , 424, 23

Genzel, R., Burkert, A., Bouché, N., et al. 2008, , 687, 59

Genzel, R., Newman, S., Jones, T., et al. 2011, , 733, 101

Giavalisco, M., Ferguson, H. C., Koekemoer, A. M., et al. 2004, , 600, L93

Glazebrook, K., Abraham, R. G., McCarthy, P. J., et al. 2004, , 430, 181

Griffin, M. J., Abergel, A., Abreu, A., et al. 2010, , 518, L3

Grogin, N. A., Kocevski, D. D., Faber, S. M., et al. 2011, , 197, 35

Gruppioni, C., Pozzi, F., Andreani, P., et al. 2010, , 518, L27

Halliday, C., Daddi, E., Cimatti, A., et al. 2008, , 479, 417

Heckman, T. M. 2002, in Astronomical Society of the Pacific Conference Series, Vol. 254, Extragalactic Gas at Low Redshift, ed. J. S. Mulchaey & J. T. Stocke, 292

Heckman, T. M., Armus, L., & Miley, G. K. 1990, , 74, 833

Heckman, T. M., Lehnert, M. D., Strickland, D. K., & Armus, L. 2000, , 129, 493

Heckman, T. M., Robert, C., Leitherer, C., Garnett, D. R., & van der Rydt, F. 1998, , 503, 646

Heckman, T. M., Sembach, K. R., Meurer, G. R., et al. 2001a, , 558, 56

Heckman, T. M., Sembach, K. R., Meurer, G. R., et al. 2001b, , 554, 1021

Hogg, D. W., Blanton, M., Strateva, I., et al. 2002, , 124, 646

Hopkins, A. M. & Beacom, J. F. 2006, , 651, 142

Huertas-Company, M., Aguerri, J. A. L., Tresse, L., et al. 2010, , 515, A3

Im, M., Faber, S. M., Gebhardt, K., et al. 2001, , 122, 750

Jarosik, N., Bennett, C. L., Dunkley, J., et al. 2011, , 192, 14

Kannappan, S. J., Guie, J. M., & Baker, A. J. 2009, , 138, 579

Keenan, F. P., Feibelman, W. A., & Berrington, K. A. 1992, , 389, 443

Kennicutt, R. C. & Evans, N. J. 2012, , 50, 531

Kennicutt, Jr., R. C. 1998, , 36, 189

Kinney, A. L., Bohlin, R. C., Calzetti, D., Panagia, N., & Wyse, R. F. G. 1993, , 86, 5

Koekemoer, A. M., Faber, S. M., Ferguson, H. C., et al. 2011, , 197, 36

Komatsu, E., Smith, K. M., Dunkley, J., et al. 2011, , 192, 18

Kornei, K. A., Shapley, A. E., Martin, C. L., et al. 2012, , 758, 135

Kriek, M., van Dokkum, P. G., Franx, M., Illingworth, G. D., & Magee, D. K. 2009, , 705, L71

Kroupa, P. 2001, , 322, 231

Kulas, K. R., Shapley, A. E., Kollmeier, J. A., et al. 2012, , 745, 33

Kurk, J., Cimatti, A., Daddi, E., et al. 2013, , 549, A63

Kurk, J., Cimatti, A., Zamorani, G., et al. 2009, , 504, 331

Lagache, G., Dole, H., Puget, J.-L., et al. 2004, , 154, 112

Lanyon-Foster, M. M., Conselice, C. J., & Merrifield, M. R. 2012, , 424, 1852

Lauger, S., Burgarella, D., & Buat, V. 2005, , 434, 77

Law, D. R., Steidel, C. C., Shapley, A. E., et al. 2012a, , 759, 29

Law, D. R., Steidel, C. C., Shapley, A. E., et al. 2012b, , 745, 85

Le Fèvre, O., Abraham, R., Lilly, S. J., et al. 2000, , 311, 565

Le Fèvre, O., Vettolani, G., Garilli, B., et al. 2005, , 439, 845

Lee, J. H., Lee, M. G., & Hwang, H. S. 2006, , 650, 148

Lee, S.-K., Ferguson, H. C., Somerville, R. S., Wiklind, T., & Giavalisco, M. 2010, , 725, 1644

Leitherer, C. & Heckman, T. M. 1995, , 96, 9

Lilly, S. J., Le Fevre, O., Hammer, F., & Crampton, D. 1996, , 460, L1

Lotz, J. M., Jonsson, P., Cox, T. J., & Primack, J. R. 2008, , 391, 1137

Lotz, J. M., Primack, J., & Madau, P. 2004, , 128, 163

Lutz, D., Poglitsch, A., Altieri, B., et al. 2011, , 532, A90

Lynds, C. R. & Sandage, A. R. 1963, , 137, 1005

Madau, P., Ferguson, H. C., Dickinson, M. E., et al. 1996, , 283, 1388

Magnelli, B., Elbaz, D., Chary, R. R., et al. 2009, , 496, 57

Magnelli, B., Elbaz, D., Chary, R. R., et al. 2011, VizieR Online Data Catalog, 352, 89035

Maraston, C. 2005, , 362, 799

Maraston, C., Pforr, J., Renzini, A., et al. 2010, , 407, 830

Masjedi, M., Hogg, D. W., Cool, R. J., et al. 2006, , 644, 54

Mather, J. C., Cheng, E. S., Cottingham, D. A., et al. 1994, , 420, 439

Meurer, G. R., Heckman, T. M., & Calzetti, D. 1999, , 521, 64

Meynet, G. 1995, , 298, 767

Mignoli, M., Cimatti, A., Zamorani, G., et al. 2005, , 437, 883

Mukhanov, V. 2005, Physical Foundations of Cosmology

Nath, B. B. & Silk, J. 2009, , 396, L90

Noll, S., Mehlert, D., Appenzeller, I., et al. 2004, , 418, 885

Noll, S. & Pierini, D. 2005, , 444, 137

Nordon, R., Lutz, D., Saintonge, A., et al. 2012, ArXiv e-prints

Nordon, R., Lutz, D., Shao, L., et al. 2010, , 518, L24

Oliver, S. J., Wang, L., Smith, A. J., et al. 2010, , 518, L21

Oppenheimer, B. D. & Davé, R. 2006, , 373, 1265

Pannella, M., Carilli, C. L., Daddi, E., et al. 2009, , 698, L116

Papovich, C., Finkelstein, S. L., Ferguson, H. C., Lotz, J. M., & Giavalisco, M. 2011, , 412, 1123

Patton, D. R., Pritchet, C. J., Yee, H. K. C., Ellingson, E., & Carlberg, R. G. 1997, , 475, 29

Peng, C. Y., Ho, L. C., Impey, C. D., & Rix, H.-W. 2002, , 124, 266

Petrosian, V. 1976, , 209, L1

Pettini, M., Kellogg, M., Steidel, C. C., et al. 1998, , 508, 539

Pettini, M., Rix, S. A., Steidel, C. C., et al. 2002, , 569, 742

Pettini, M., Steidel, C. C., Adelberger, K. L., Dickinson, M., & Giavalisco, M. 2000, , 528, 96

Pilbratt, G. L., Riedinger, J. R., Passvogel, T., et al. 2010, , 518, L1

Poglitsch, A., Waelkens, C., Geis, N., et al. 2010, , 518, L2

Polletta, M., Tajer, M., Maraschi, L., et al. 2007, , 663, 81

Popesso, P., Dickinson, M., Nonino, M., et al. 2009, , 494, 443

Pozzetti, L., Bolzonella, M., Lamareille, F., et al. 2007, , 474, 443

Quider, A. M., Pettini, M., Shapley, A. E., & Steidel, C. C. 2009, , 398, 1263

Quider, A. M., Shapley, A. E., Pettini, M., Steidel, C. C., & Stark, D. P. 2010, , 402, 1467

Ravindranath, S., Ferguson, H. C., Conselice, C., et al. 2004, , 604, L9

Reddy, N., Dickinson, M., Elbaz, D., et al. 2012, , 744, 154

Reddy, N. A. & Steidel, C. C. 2009, , 692, 778

Renzini, A. 2009, , 398, L58

Rieke, G. H., Alonso-Herrero, A., Weiner, B. J., et al. 2009, , 692, 556

Rodighiero, G., Cimatti, A., Gruppioni, C., et al. 2010, , 518, L25

Rodighiero, G., Daddi, E., Baronchelli, I., et al. 2011, , 739, L40

Rubin, K. H. R., Weiner, B. J., Koo, D. C., et al. 2010, , 719, 1503

Rupke, D. S., Veilleux, S., & Sanders, D. B. 2005, , 160, 115

Salpeter, E. E. 1955, , 121, 161

Scannapieco, E., Silk, J., & Bouwens, R. 2005, , 635, L13

Schade, D., Lilly, S. J., Crampton, D., et al. 1995, , 451, L1

Schaerer, D. & Vacca, W. D. 1998, , 497, 618

Schwartz, C. M. & Martin, C. L. 2004, , 610, 201

Shapley, A. E., Steidel, C. C., Pettini, M., & Adelberger, K. L. 2003, , 588, 65

Shen, S., Mo, H. J., White, S. D. M., et al. 2003, , 343, 978

Steidel, C. C., Adelberger, K. L., Giavalisco, M., Dickinson, M., & Pettini, M. 1999, , 519, 1

Steidel, C. C., Erb, D. K., Shapley, A. E., et al. 2010, , 717, 289

Strateva, I., Ivezić, Ž., Knapp, G. R., et al. 2001, , 122, 1861

Strickland, D. K., Heckman, T. M., Colbert, E. J. M., Hoopes, C. G., & Weaver, K. A. 2004, , 606, 829

Strickland, D. K., Hornschemeier, A., Ptak, A., et al. 2009, in ArXiv Astrophysics e-prints, Vol. 2010, astro2010: The Astronomy and Astrophysics Decadal Survey, 289–+

Strickland, D. K. & Stevens, I. R. 2000, , 314, 511

Swinyard, B. M., Ade, P., Baluteau, J.-P., et al. 2010, , 518, L4

Talia, M., Mignoli, M., Cimatti, A., et al. 2012, , 539, A61

Taylor-Mager, V. A., Conselice, C. J., Windhorst, R. A., & Jansen, R. A. 2007, , 659, 162

Tenorio-Tagle, G., Silich, S. A., Kunth, D., Terlevich, E., & Terlevich, R. 1999, , 309, 332

Teplitz, H. I., Chary, R., Elbaz, D., et al. 2011, , 141, 1

Toft, S., Franx, M., van Dokkum, P., et al. 2009, , 705, 255

Tonry, J. & Davis, M. 1979, , 84, 1511

Trujillo, I., Conselice, C. J., Bundy, K., et al. 2007, , 382, 109

van Dokkum, P. G. 2005, , 130, 2647

Vanzella, E., Cristiani, S., Dickinson, M., et al. 2008, , 478, 83

Veilleux, S., Cecil, G., & Bland-Hawthorn, J. 2005, , 43, 769

Walborn, N. R. & Panek, R. J. 1984, , 280, L27

Wang, T., Huang, J.-S., Faber, S. M., et al. 2012, , 752, 134

Weiner, B. J., Coil, A. L., Prochaska, J. X., et al. 2009, , 692, 187

Weiner, B. J., Phillips, A. C., Faber, S. M., et al. 2005, , 620, 595

Whitaker, K. E., Labbé, I., van Dokkum, P. G., et al. 2011, , 735, 86

White, S. D. M. & Rees, M. J. 1978, , 183, 341

Wuyts, S., Förster Schreiber, N. M., Lutz, D., et al. 2011, , 738, 106

Xue, Y. Q., Luo, B., Brandt, W. N., et al. 2011, , 195, 10

Appendix: the morphological atlas

In the atlas, cutouts of all the galaxies of the *GMASS-wfc3 sample* are presented (see chapter 3 and chapter 4).

The cutouts are arranged in order of increasing redshift. ACS z_{850} and WFC3-IR H_{160} images (with their native pixel size and PSF) are shown side by side. The chosen display for the 4"x 4" cutouts is a square root scale with fixed minimum and maximum pixel count limits, in order to uniform the background. This means that some galaxies end up to being saturated; the classification by eye, however, was done looking also at the images in linear scale.

On each snapshot, galaxy GMASS identification number, redshift and visual classification are also marked, in different colours depending on the morphological type.

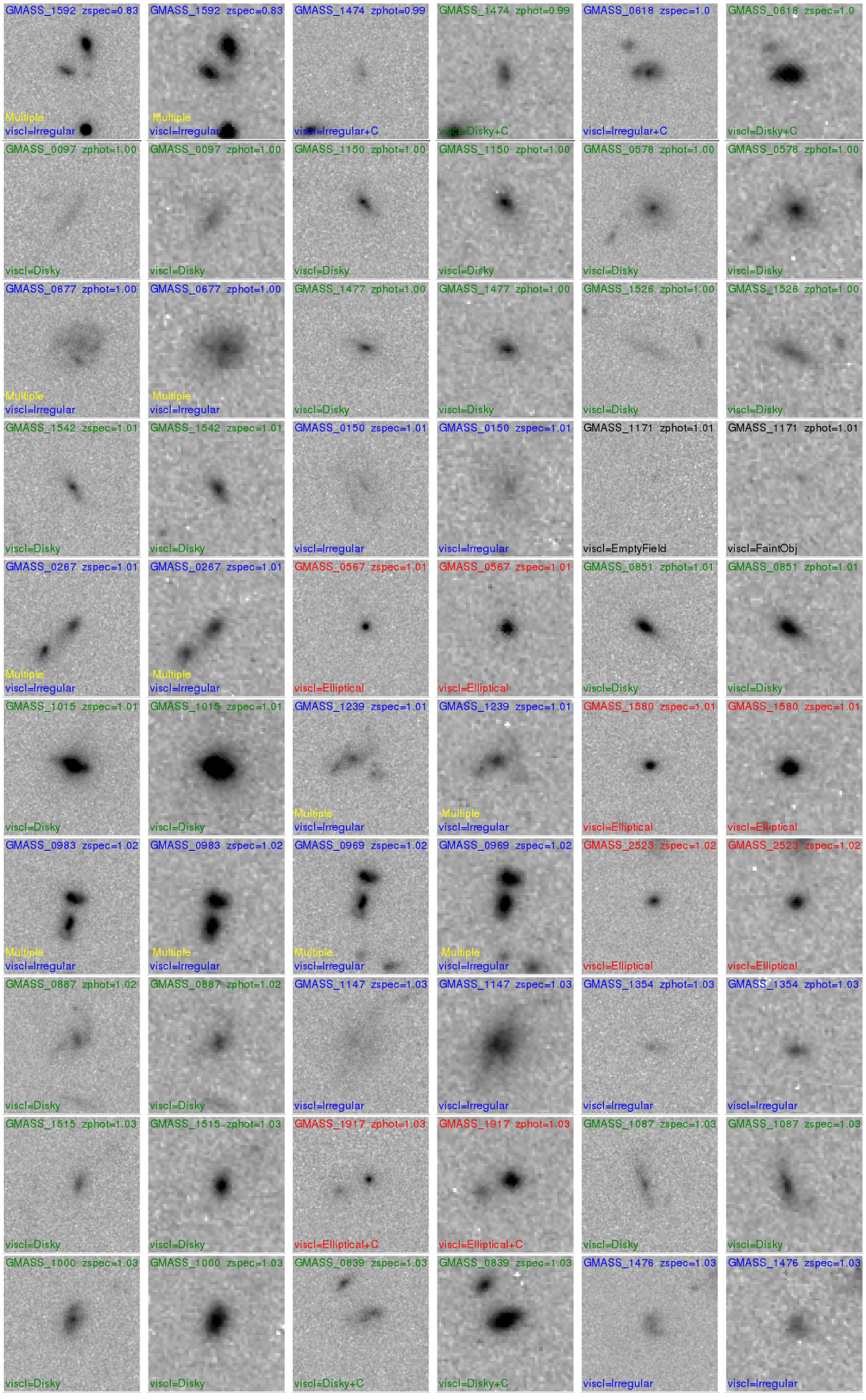
GMASS_1592 zspec=0.83
Multiple
viscl=Irregular
GMASS_1592 zspec=0.83
Multiple
viscl=Irregular
GMASS_1474 zphot=0.99
viscl=Irregular+C
GMASS_1474 zphot=0.99
viscl=Disky+C
GMASS_0618 zspec=1.0
viscl=Irregular+C
GMASS_0618 zspec=1.0
viscl=Disky+C
GMASS_0097 zphot=1.00
viscl=Disky
GMASS_0097 zphot=1.00
viscl=Disky
GMASS_1150 zphot=1.00
viscl=Disky
GMASS_1150 zphot=1.00
viscl=Disky
GMASS_0578 zphot=1.00
viscl=Disky
GMASS_0578 zphot=1.00
viscl=Disky
GMASS_0677 zphot=1.00
Multiple
viscl=Irregular
GMASS_0677 zphot=1.00
Multiple
viscl=Irregular
GMASS_1477 zphot=1.00
viscl=Disky
GMASS_1477 zphot=1.00
viscl=Disky
GMASS_1526 zphot=1.00
viscl=Disky
GMASS_1526 zphot=1.00
viscl=Disky
GMASS_1542 zspec=1.01
viscl=Disky
GMASS_1542 zspec=1.01
viscl=Disky
GMASS_0150 zspec=1.01
viscl=Irregular
GMASS_0150 zspec=1.01
viscl=Irregular
GMASS_1171 zphot=1.01
viscl=EmptyField
GMASS_1171 zphot=1.01
viscl=FaintObj
GMASS_0267 zspec=1.01
Multiple
viscl=Irregular
GMASS_0267 zspec=1.01
Multiple
viscl=Irregular
GMASS_0567 zspec=1.01
viscl=Elliptical
GMASS_0567 zspec=1.01
viscl=Elliptical
GMASS_0851 zphot=1.01
viscl=Disky
GMASS_0851 zphot=1.01
viscl=Disky
GMASS_1015 zspec=1.01
viscl=Disky
GMASS_1015 zspec=1.01
viscl=Disky
GMASS_1239 zspec=1.01
Multiple
viscl=Irregular
GMASS_1239 zspec=1.01
Multiple
viscl=Irregular
GMASS_1580 zspec=1.01
viscl=Elliptical
GMASS_1580 zspec=1.01
viscl=Elliptical
GMASS_0983 zspec=1.02
Multiple
viscl=Irregular
GMASS_0983 zspec=1.02
Multiple
viscl=Irregular
GMASS_0969 zspec=1.02
Multiple
viscl=Irregular
GMASS_0969 zspec=1.02
Multiple
viscl=Irregular
GMASS_2523 zspec=1.02
viscl=Elliptical
GMASS_2523 zspec=1.02
viscl=Elliptical
GMASS_0887 zphot=1.02
viscl=Disky
GMASS_0887 zphot=1.02
viscl=Disky
GMASS_1147 zspec=1.03
viscl=Irregular
GMASS_1147 zspec=1.03
viscl=Irregular
GMASS_1354 zphot=1.03
viscl=Irregular
GMASS_1354 zphot=1.03
viscl=Irregular
GMASS_1515 zphot=1.03
viscl=Disky
GMASS_1515 zphot=1.03
viscl=Disky
GMASS_1917 zphot=1.03
viscl=Elliptical+C
GMASS_1917 zphot=1.03
viscl=Elliptical+C
GMASS_1087 zspec=1.03
viscl=Disky
GMASS_1087 zspec=1.03
viscl=Disky
GMASS_1000 zspec=1.03
viscl=Disky
GMASS_1000 zspec=1.03
viscl=Disky
GMASS_0839 zspec=1.03
viscl=Disky+C
GMASS_0839 zspec=1.03
viscl=Disky+C
GMASS_1476 zspec=1.03
viscl=Irregular
GMASS_1476 zspec=1.03
viscl=Irregular

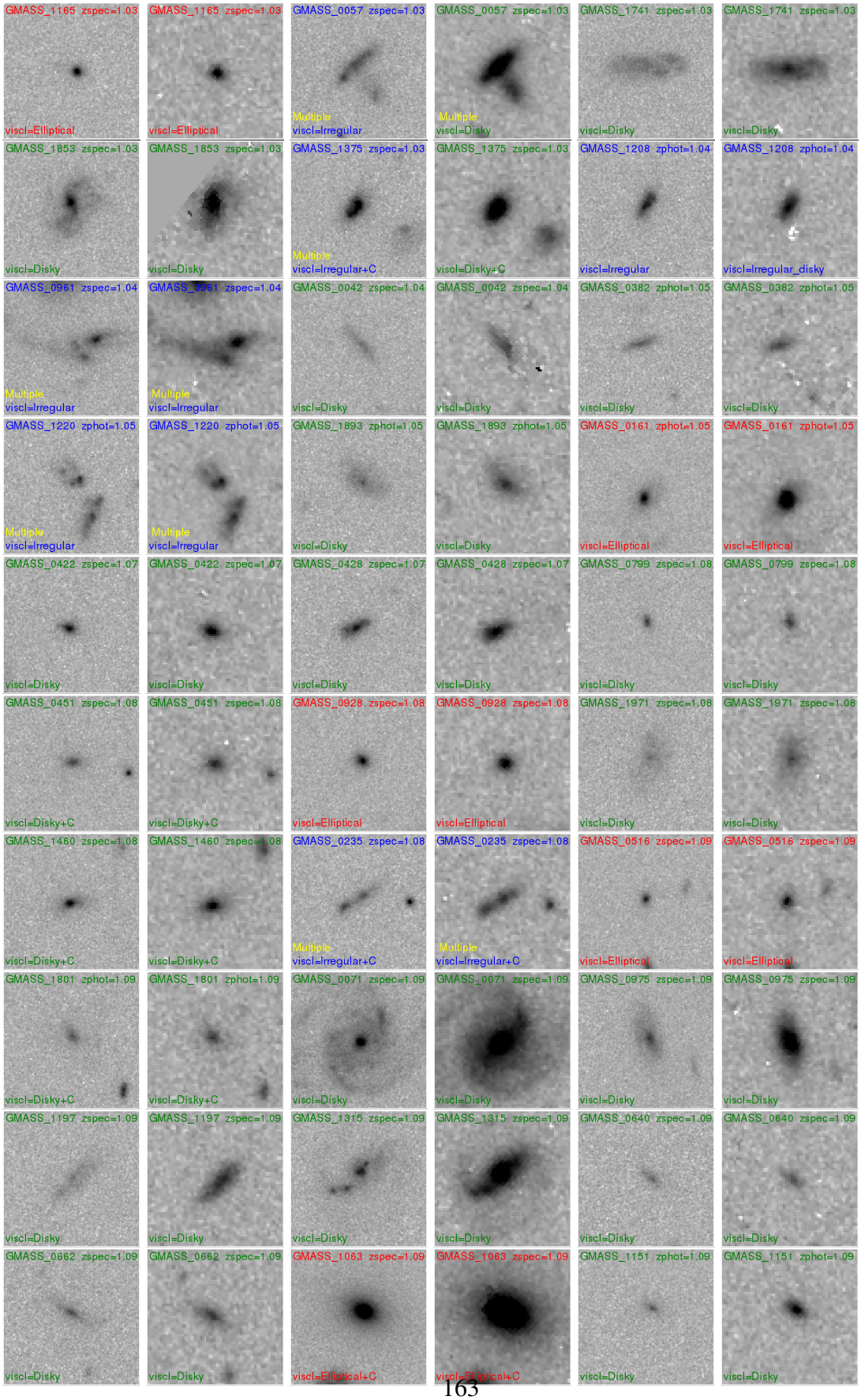
GMASS_1165 zspec=1.03
viscl=Elliptical
GMASS_1165 zspec=1.03
viscl=Elliptical
GMASS_0057 zspec=1.03
Multiple
viscl=Irregular
GMASS_0057 zspec=1.03
Multiple
viscl=Disky
GMASS_1741 zspec=1.03
viscl=Disky
GMASS_1741 zspec=1.03
viscl=Disky
GMASS_1853 zspec=1.03
viscl=Disky
GMASS_1853 zspec=1.03
viscl=Disky
GMASS_1375 zspec=1.03
Multiple
viscl=Irregular+C
GMASS_1375 zspec=1.03
viscl=Disky+C
GMASS_1208 zphot=1.04
viscl=Irregular
GMASS_1208 zphot=1.04
viscl=Irregular_disky
GMASS_0961 zspec=1.04
Multiple
viscl=Irregular
GMASS_0961 zspec=1.04
Multiple
viscl=Irregular
GMASS_0042 zspec=1.04
viscl=Disky
GMASS_0042 zspec=1.04
viscl=Disky
GMASS_0382 zphot=1.05
viscl=Disky
GMASS_0382 zphot=1.05
viscl=Disky
GMASS_1220 zphot=1.05
Multiple
viscl=Irregular
GMASS_1220 zphot=1.05
Multiple
viscl=Irregular
GMASS_1893 zphot=1.05
viscl=Disky
GMASS_1893 zphot=1.05
viscl=Disky
GMASS_0161 zphot=1.05
viscl=Elliptical
GMASS_0161 zphot=1.05
viscl=Elliptical
GMASS_0422 zspec=1.07
viscl=Disky
GMASS_0422 zspec=1.07
viscl=Disky
GMASS_0428 zspec=1.07
viscl=Disky
GMASS_0428 zspec=1.07
viscl=Disky
GMASS_0799 zspec=1.08
viscl=Disky
GMASS_0799 zspec=1.08
viscl=Disky
GMASS_0451 zspec=1.08
viscl=Disky+C
GMASS_0451 zspec=1.08
viscl=Disky+C
GMASS_0928 zspec=1.08
viscl=Elliptical
GMASS_0928 zspec=1.08
viscl=Elliptical
GMASS_1971 zspec=1.08
viscl=Disky
GMASS_1971 zspec=1.08
viscl=Disky
GMASS_1460 zspec=1.08
viscl=Disky+C
GMASS_1460 zspec=1.08
viscl=Disky+C
GMASS_0235 zspec=1.08
Multiple
viscl=Irregular+C
GMASS_0235 zspec=1.08
Multiple
viscl=Irregular+C
GMASS_0516 zspec=1.09
viscl=Elliptical
GMASS_0516 zspec=1.09
viscl=Elliptical
GMASS_1801 zphot=1.09
viscl=Disky+C
GMASS_1801 zphot=1.09
viscl=Disky+C
GMASS_0071 zspec=1.09
viscl=Disky
GMASS_0071 zspec=1.09
viscl=Disky
GMASS_0975 zspec=1.09
viscl=Disky
GMASS_0975 zspec=1.09
viscl=Disky
GMASS_1197 zspec=1.09
viscl=Disky
GMASS_1197 zspec=1.09
viscl=Disky
GMASS_1315 zspec=1.09
viscl=Disky
GMASS_1315 zspec=1.09
viscl=Disky
GMASS_0640 zspec=1.09
viscl=Disky
GMASS_0640 zspec=1.09
viscl=Disky
GMASS_0662 zspec=1.09
viscl=Disky
GMASS_0662 zspec=1.09
viscl=Disky
GMASS_1063 zspec=1.09
viscl=Elliptical+C
GMASS_1063 zspec=1.09
viscl=Elliptical+C
GMASS_1151 zphot=1.09
viscl=Disky
GMASS_1151 zphot=1.09
viscl=Disky

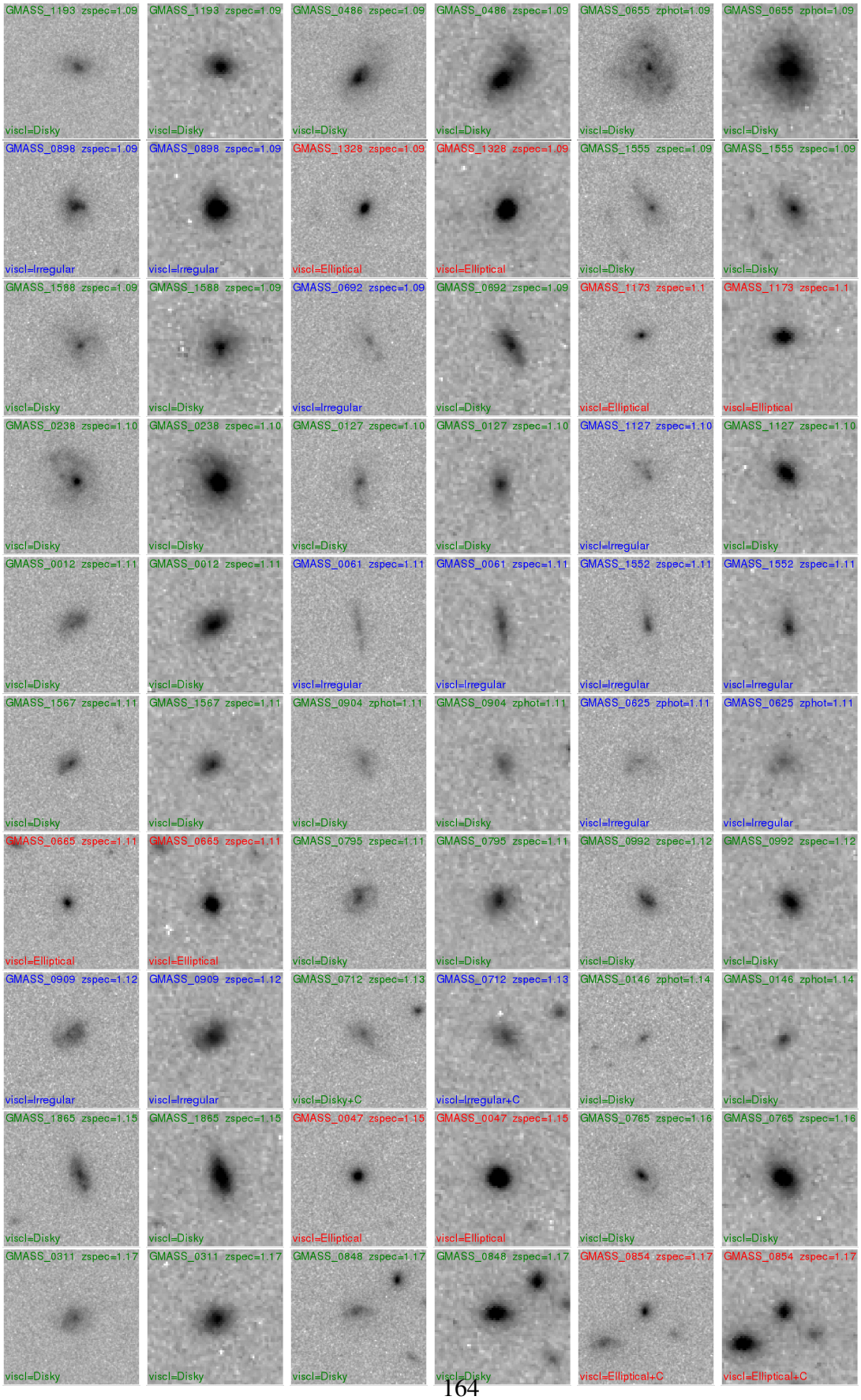
GMASS_1193 zspec=1.09
viscl=Disky
GMASS_1193 zspec=1.09
viscl=Disky
GMASS_0486 zspec=1.09
viscl=Disky
GMASS_0486 zspec=1.09
viscl=Disky
GMASS_0655 zphot=1.09
viscl=Disky
GMASS_0655 zphot=1.09
viscl=Disky
GMASS_0898 zspec=1.09
viscl=Irregular
GMASS_0898 zspec=1.09
viscl=Irregular
GMASS_1328 zspec=1.09
viscl=Elliptical
GMASS_1328 zspec=1.09
viscl=Elliptical
GMASS_1555 zspec=1.09
viscl=Disky
GMASS_1555 zspec=1.09
viscl=Disky
GMASS_1588 zspec=1.09
viscl=Disky
GMASS_1588 zspec=1.09
viscl=Disky
GMASS_0692 zspec=1.09
viscl=Irregular
GMASS_0692 zspec=1.09
viscl=Disky
GMASS_1173 zspec=1.1
viscl=Elliptical
GMASS_1173 zspec=1.1
viscl=Elliptical
GMASS_0238 zspec=1.10
viscl=Disky
GMASS_0238 zspec=1.10
viscl=Disky
GMASS_0127 zspec=1.10
viscl=Disky
GMASS_0127 zspec=1.10
viscl=Disky
GMASS_1127 zspec=1.10
viscl=Irregular
GMASS_1127 zspec=1.10
viscl=Disky
GMASS_0012 zspec=1.11
viscl=Disky
GMASS_0012 zspec=1.11
viscl=Disky
GMASS_0061 zspec=1.11
viscl=Irregular
GMASS_0061 zspec=1.11
viscl=Irregular
GMASS_1552 zspec=1.11
viscl=Irregular
GMASS_1552 zspec=1.11
viscl=Irregular
GMASS_1567 zspec=1.11
viscl=Disky
GMASS_1567 zspec=1.11
viscl=Disky
GMASS_0904 zphot=1.11
viscl=Disky
GMASS_0904 zphot=1.11
viscl=Disky
GMASS_0625 zphot=1.11
viscl=Irregular
GMASS_0625 zphot=1.11
viscl=Irregular
GMASS_0665 zspec=1.11
viscl=Elliptical
GMASS_0665 zspec=1.11
viscl=Elliptical
GMASS_0795 zspec=1.11
viscl=Disky
GMASS_0795 zspec=1.11
viscl=Disky
GMASS_0992 zspec=1.12
viscl=Disky
GMASS_0992 zspec=1.12
viscl=Disky
GMASS_0909 zspec=1.12
viscl=Irregular
GMASS_0909 zspec=1.12
viscl=Irregular
GMASS_0712 zspec=1.13
viscl=Disky+C
GMASS_0712 zspec=1.13
viscl=Irregular+C
GMASS_0146 zphot=1.14
viscl=Disky
GMASS_0146 zphot=1.14
viscl=Disky
GMASS_1865 zspec=1.15
viscl=Disky
GMASS_1865 zspec=1.15
viscl=Disky
GMASS_0047 zspec=1.15
viscl=Elliptical
GMASS_0047 zspec=1.15
viscl=Elliptical
GMASS_0765 zspec=1.16
viscl=Disky
GMASS_0765 zspec=1.16
viscl=Disky
GMASS_0311 zspec=1.17
viscl=Disky
GMASS_0311 zspec=1.17
viscl=Disky
GMASS_0848 zspec=1.17
viscl=Disky
GMASS_0848 zspec=1.17
viscl=Disky
GMASS_0854 zspec=1.17
viscl=Elliptical+C
GMASS_0854 zspec=1.17
viscl=Elliptical+C

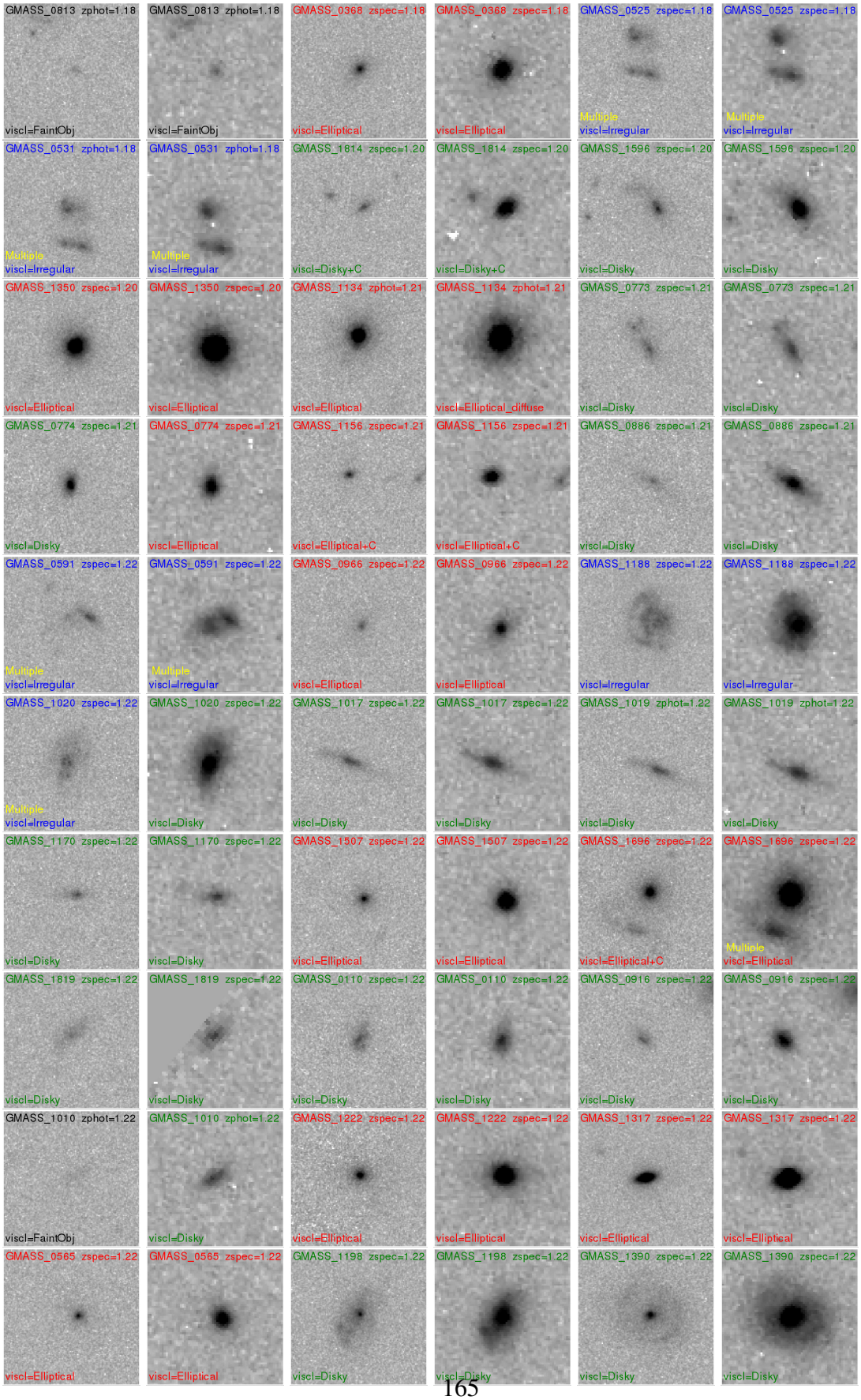
GMASS_0813 zphot=1.18
viscl=FaintObj
GMASS_0813 zphot=1.18
viscl=FaintObj
GMASS_0368 zspec=1.18
viscl=Elliptical
GMASS_0368 zspec=1.18
viscl=Elliptical
GMASS_0525 zspec=1.18
Multiple
viscl=Irregular
GMASS_0525 zspec=1.18
Multiple
viscl=Irregular
GMASS_0531 zphot=1.18
Multiple
viscl=Irregular
GMASS_0531 zphot=1.18
Multiple
viscl=Irregular
GMASS_1814 zspec=1.20
viscl=Disky+C
GMASS_1814 zspec=1.20
viscl=Disky+C
GMASS_1596 zspec=1.20
viscl=Disky
GMASS_1596 zspec=1.20
viscl=Disky
GMASS_1350 zspec=1.20
viscl=Elliptical
GMASS_1350 zspec=1.20
viscl=Elliptical
GMASS_1134 zphot=1.21
viscl=Elliptical
GMASS_1134 zphot=1.21
viscl=Elliptical_diffuse
GMASS_0773 zspec=1.21
viscl=Disky
GMASS_0773 zspec=1.21
viscl=Disky
GMASS_0774 zspec=1.21
viscl=Disky
GMASS_0774 zspec=1.21
viscl=Elliptical
GMASS_1156 zspec=1.21
viscl=Elliptical+C
GMASS_1156 zspec=1.21
viscl=Elliptical+C
GMASS_0886 zspec=1.21
viscl=Disky
GMASS_0886 zspec=1.21
viscl=Disky
GMASS_0591 zspec=1.22
Multiple
viscl=Irregular
GMASS_0591 zspec=1.22
Multiple
viscl=Irregular
GMASS_0966 zspec=1.22
viscl=Elliptical
GMASS_0966 zspec=1.22
viscl=Elliptical
GMASS_1188 zspec=1.22
viscl=Irregular
GMASS_1188 zspec=1.22
viscl=Irregular
GMASS_1020 zspec=1.22
Multiple
viscl=Irregular
GMASS_1020 zspec=1.22
viscl=Disky
GMASS_1017 zspec=1.22
viscl=Disky
GMASS_1017 zspec=1.22
viscl=Disky
GMASS_1019 zphot=1.22
viscl=Disky
GMASS_1019 zphot=1.22
viscl=Disky
GMASS_1170 zspec=1.22
viscl=Disky
GMASS_1170 zspec=1.22
viscl=Disky
GMASS_1507 zspec=1.22
viscl=Elliptical
GMASS_1507 zspec=1.22
viscl=Elliptical
GMASS_1696 zspec=1.22
viscl=Elliptical+C
GMASS_1696 zspec=1.22
Multiple
viscl=Elliptical
GMASS_1819 zspec=1.22
viscl=Disky
GMASS_1819 zspec=1.22
viscl=Disky
GMASS_0110 zspec=1.22
viscl=Disky
GMASS_0110 zspec=1.22
viscl=Disky
GMASS_0916 zspec=1.22
viscl=Disky
GMASS_0916 zspec=1.22
viscl=Disky
GMASS_1010 zphot=1.22
viscl=FaintObj
GMASS_1010 zphot=1.22
viscl=Disky
GMASS_1222 zspec=1.22
viscl=Elliptical
GMASS_1222 zspec=1.22
viscl=Elliptical
GMASS_1317 zspec=1.22
viscl=Elliptical
GMASS_1317 zspec=1.22
viscl=Elliptical
GMASS_0565 zspec=1.22
viscl=Elliptical
GMASS_0565 zspec=1.22
viscl=Elliptical
GMASS_1198 zspec=1.22
viscl=Disky
GMASS_1198 zspec=1.22
viscl=Disky
GMASS_1390 zspec=1.22
viscl=Disky
GMASS_1390 zspec=1.22
viscl=Disky

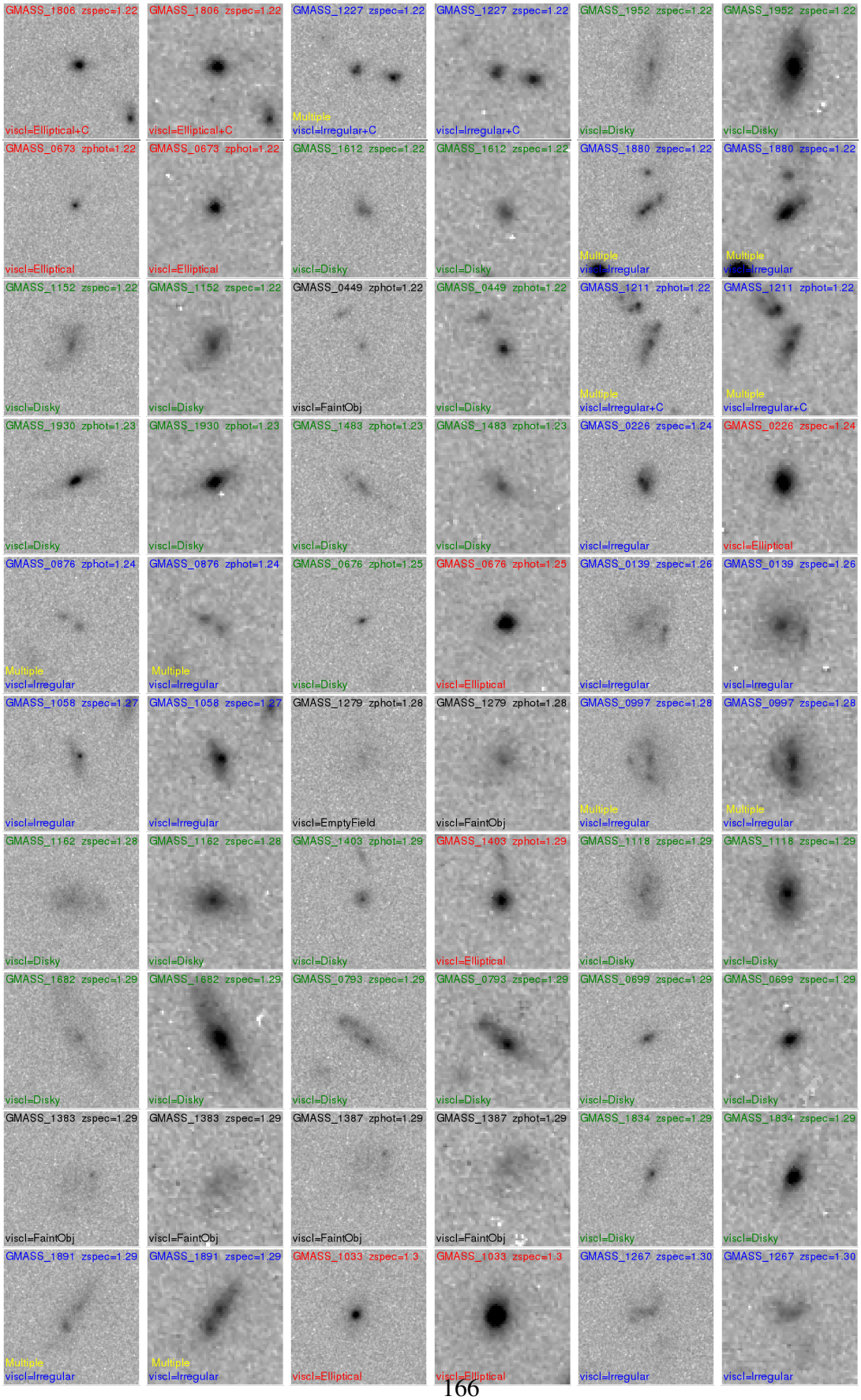
GMASS_1806 zspec=1.22
viscl=Elliptical+C
GMASS_1806 zspec=1.22
viscl=Elliptical+C
GMASS_1227 zspec=1.22
Multiple
viscl=Irregular+C
GMASS_1227 zspec=1.22
viscl=Irregular+C
GMASS_1952 zspec=1.22
viscl=Disky
GMASS_1952 zspec=1.22
viscl=Disky
GMASS_0673 zphot=1.22
viscl=Elliptical
GMASS_0673 zphot=1.22
viscl=Elliptical
GMASS_1612 zspec=1.22
viscl=Disky
GMASS_1612 zspec=1.22
viscl=Disky
GMASS_1880 zspec=1.22
Multiple
viscl=Irregular
GMASS_1880 zspec=1.22
Multiple
viscl=Irregular
GMASS_1152 zspec=1.22
viscl=Disky
GMASS_1152 zspec=1.22
viscl=Disky
GMASS_0449 zphot=1.22
viscl=FaintObj
GMASS_0449 zphot=1.22
viscl=Disky
GMASS_1211 zphot=1.22
Multiple
viscl=Irregular+C
GMASS_1211 zphot=1.22
Multiple
viscl=Irregular+C
GMASS_1930 zphot=1.23
viscl=Disky
GMASS_1930 zphot=1.23
viscl=Disky
GMASS_1483 zphot=1.23
viscl=Disky
GMASS_1483 zphot=1.23
viscl=Disky
GMASS_0226 zspec=1.24
viscl=Irregular
GMASS_0226 zspec=1.24
viscl=Elliptical
GMASS_0876 zphot=1.24
Multiple
viscl=Irregular
GMASS_0876 zphot=1.24
Multiple
viscl=Irregular
GMASS_0676 zphot=1.25
viscl=Disky
GMASS_0676 zphot=1.25
viscl=Elliptical
GMASS_0139 zspec=1.26
viscl=Irregular
GMASS_0139 zspec=1.26
viscl=Irregular
GMASS_1058 zspec=1.27
viscl=Irregular
GMASS_1058 zspec=1.27
viscl=Irregular
GMASS_1279 zphot=1.28
viscl=EmptyField
GMASS_1279 zphot=1.28
viscl=FaintObj
GMASS_0997 zspec=1.28
Multiple
viscl=Irregular
GMASS_0997 zspec=1.28
Multiple
viscl=Irregular
GMASS_1162 zspec=1.28
viscl=Disky
GMASS_1162 zspec=1.28
viscl=Disky
GMASS_1403 zphot=1.29
viscl=Disky
GMASS_1403 zphot=1.29
viscl=Elliptical
GMASS_1118 zspec=1.29
viscl=Disky
GMASS_1118 zspec=1.29
viscl=Disky
GMASS_1682 zspec=1.29
viscl=Disky
GMASS_1682 zspec=1.29
viscl=Disky
GMASS_0793 zspec=1.29
viscl=Disky
GMASS_0793 zspec=1.29
viscl=Disky
GMASS_0699 zspec=1.29
viscl=Disky
GMASS_0699 zspec=1.29
viscl=Disky
GMASS_1383 zspec=1.29
viscl=FaintObj
GMASS_1383 zspec=1.29
viscl=FaintObj
GMASS_1387 zphot=1.29
viscl=FaintObj
GMASS_1387 zphot=1.29
viscl=FaintObj
GMASS_1834 zspec=1.29
viscl=Disky
GMASS_1834 zspec=1.29
viscl=Disky
GMASS_1891 zspec=1.29
Multiple
viscl=Irregular
GMASS_1891 zspec=1.29
Multiple
viscl=Irregular
GMASS_1033 zspec=1.3
viscl=Elliptical
GMASS_1033 zspec=1.3
viscl=Elliptical
GMASS_1267 zspec=1.30
viscl=Irregular
GMASS_1267 zspec=1.30
viscl=Irregular

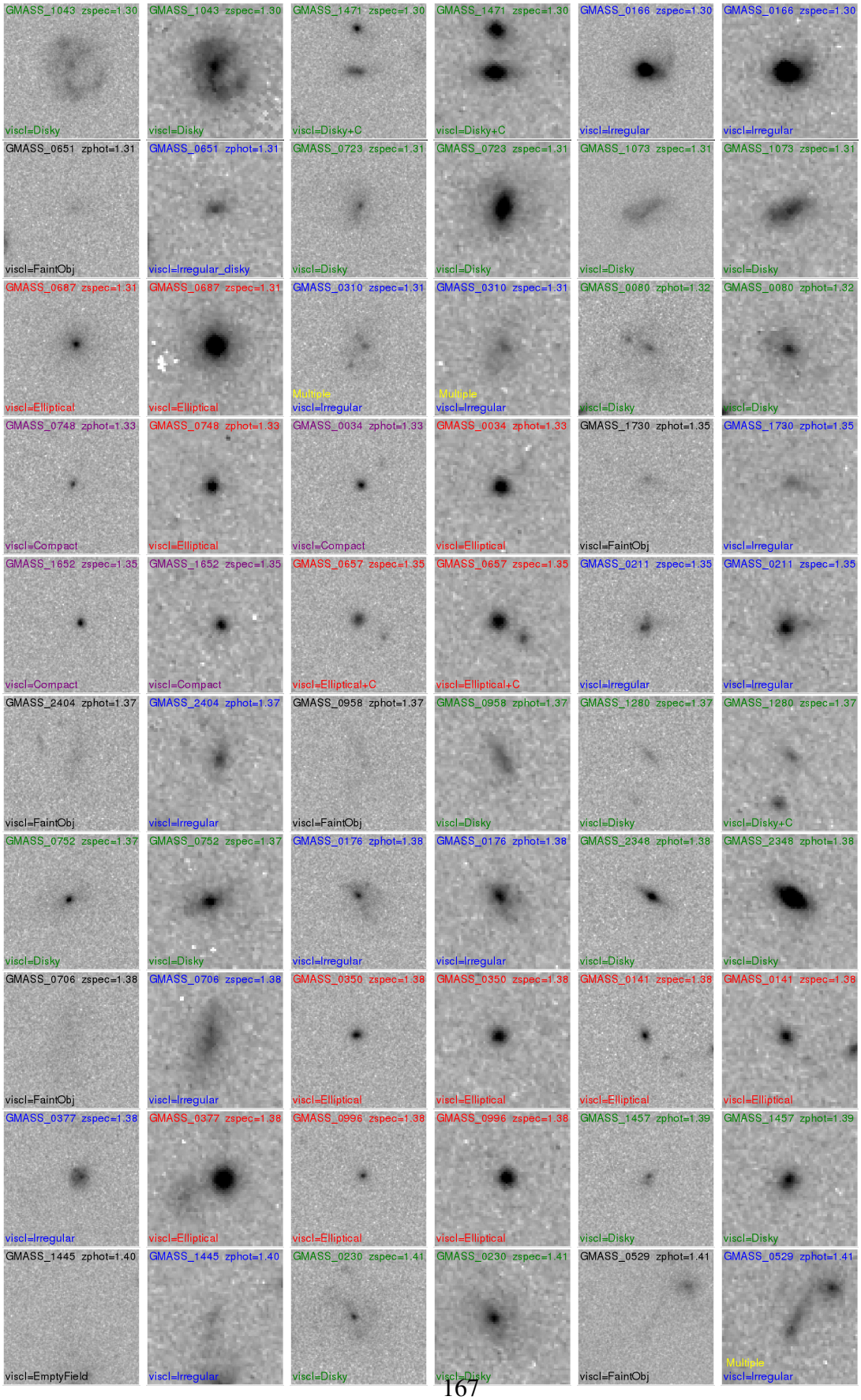
GMASS_1043 zspec=1.30
viscl=Disky
GMASS_1043 zspec=1.30
viscl=Disky
GMASS_1471 zspec=1.30
viscl=Disky+C
GMASS_1471 zspec=1.30
viscl=Disky+C
GMASS_0166 zspec=1.30
viscl=Irregular
GMASS_0166 zspec=1.30
viscl=Irregular
GMASS_0651 zphot=1.31
viscl=FaintObj
GMASS_0651 zphot=1.31
viscl=Irregular_disky
GMASS_0723 zspec=1.31
viscl=Disky
GMASS_0723 zspec=1.31
viscl=Disky
GMASS_1073 zspec=1.31
viscl=Disky
GMASS_1073 zspec=1.31
viscl=Disky
GMASS_0687 zspec=1.31
viscl=Elliptical
GMASS_0687 zspec=1.31
viscl=Elliptical
GMASS_0310 zspec=1.31
Multiple
viscl=Irregular
GMASS_0310 zspec=1.31
Multiple
viscl=Irregular
GMASS_0080 zphot=1.32
viscl=Disky
GMASS_0080 zphot=1.32
viscl=Disky
GMASS_0748 zphot=1.33
viscl=Compact
GMASS_0748 zphot=1.33
viscl=Elliptical
GMASS_0034 zphot=1.33
viscl=Compact
GMASS_0034 zphot=1.33
viscl=Elliptical
GMASS_1730 zphot=1.35
viscl=FaintObj
GMASS_1730 zphot=1.35
viscl=Irregular
GMASS_1652 zspec=1.35
viscl=Compact
GMASS_1652 zspec=1.35
viscl=Compact
GMASS_0657 zspec=1.35
viscl=Elliptical+C
GMASS_0657 zspec=1.35
viscl=Elliptical+C
GMASS_0211 zspec=1.35
viscl=Irregular
GMASS_0211 zspec=1.35
viscl=Irregular
GMASS_2404 zphot=1.37
viscl=FaintObj
GMASS_2404 zphot=1.37
viscl=Irregular
GMASS_0958 zphot=1.37
viscl=FaintObj
GMASS_0958 zphot=1.37
viscl=Disky
GMASS_1280 zspec=1.37
viscl=Disky
GMASS_1280 zspec=1.37
viscl=Disky+C
GMASS_0752 zspec=1.37
viscl=Disky
GMASS_0752 zspec=1.37
viscl=Disky
GMASS_0176 zphot=1.38
viscl=Irregular
GMASS_0176 zphot=1.38
viscl=Irregular
GMASS_2348 zphot=1.38
viscl=Disky
GMASS_2348 zphot=1.38
viscl=Disky
GMASS_0706 zspec=1.38
viscl=FaintObj
GMASS_0706 zspec=1.38
viscl=Irregular
GMASS_0350 zspec=1.38
viscl=Elliptical
GMASS_0350 zspec=1.38
viscl=Elliptical
GMASS_0141 zspec=1.38
viscl=Elliptical
GMASS_0141 zspec=1.38
viscl=Elliptical
GMASS_0377 zspec=1.38
viscl=Irregular
GMASS_0377 zspec=1.38
viscl=Elliptical
GMASS_0996 zspec=1.38
viscl=Elliptical
GMASS_0996 zspec=1.38
viscl=Elliptical
GMASS_1457 zphot=1.39
viscl=Disky
GMASS_1457 zphot=1.39
viscl=Disky
GMASS_1445 zphot=1.40
viscl=EmptyField
GMASS_1445 zphot=1.40
viscl=Irregular
GMASS_0230 zspec=1.41
viscl=Disky
GMASS_0230 zspec=1.41
viscl=Disky
GMASS_0529 zphot=1.41
viscl=FaintObj
GMASS_0529 zphot=1.41
Multiple
viscl=Irregular

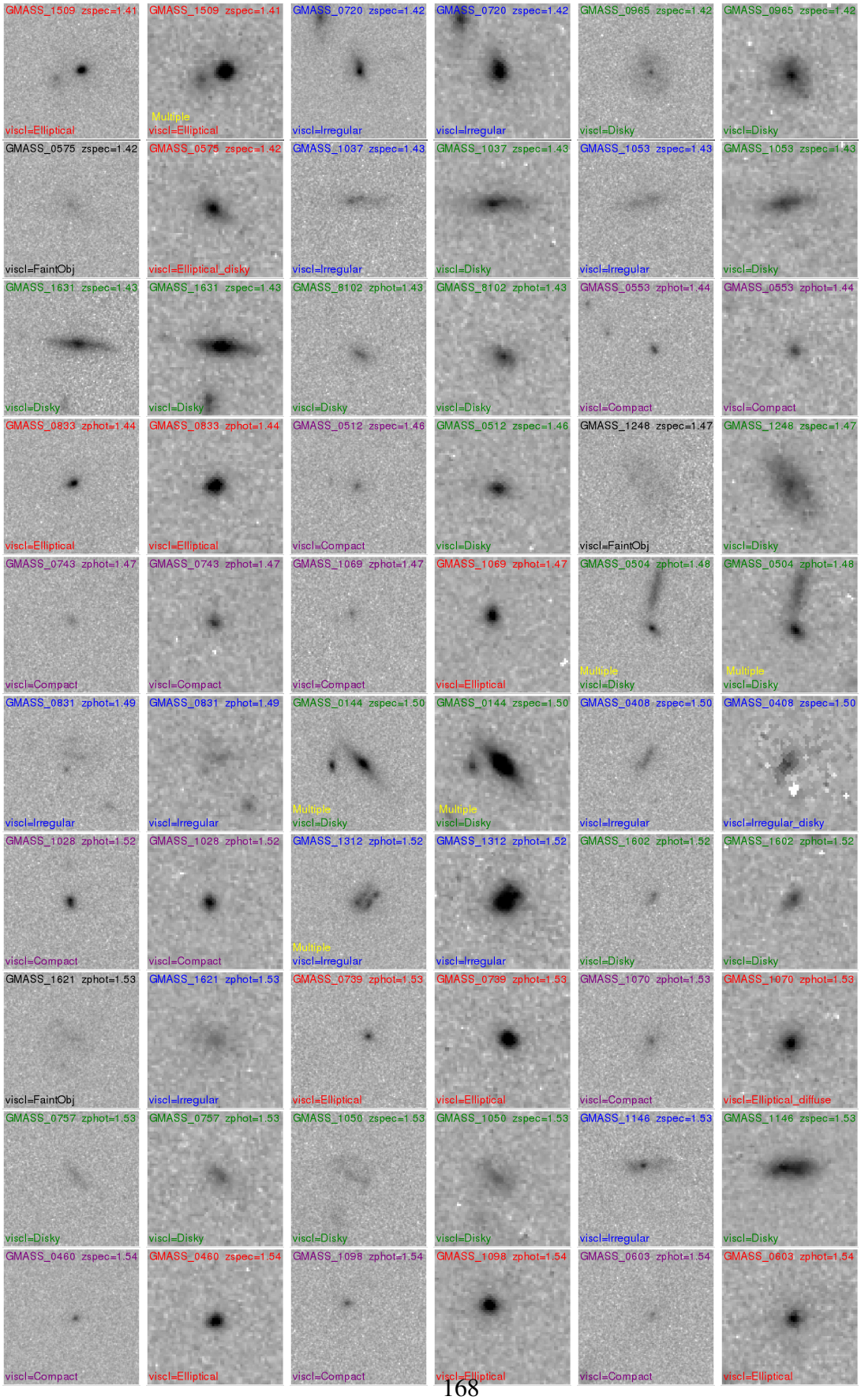
GMASS_1509 zspec=1.41
viscl=Elliptical
GMASS_1509 zspec=1.41
Multiple
viscl=Elliptical
GMASS_0720 zspec=1.42
viscl=Irregular
GMASS_0720 zspec=1.42
viscl=Irregular
GMASS_0965 zspec=1.42
viscl=Disky
GMASS_0965 zspec=1.42
viscl=Disky
GMASS_0575 zspec=1.42
viscl=FaintObj
GMASS_0575 zspec=1.42
viscl=Elliptical_disky
GMASS_1037 zspec=1.43
viscl=Irregular
GMASS_1037 zspec=1.43
viscl=Disky
GMASS_1053 zspec=1.43
viscl=Irregular
GMASS_1053 zspec=1.43
viscl=Disky
GMASS_1631 zspec=1.43
viscl=Disky
GMASS_1631 zspec=1.43
viscl=Disky
GMASS_8102 zphot=1.43
viscl=Disky
GMASS_8102 zphot=1.43
viscl=Disky
GMASS_0553 zphot=1.44
viscl=Compact
GMASS_0553 zphot=1.44
viscl=Compact
GMASS_0833 zphot=1.44
viscl=Elliptical
GMASS_0833 zphot=1.44
viscl=Elliptical
GMASS_0512 zspec=1.46
viscl=Compact
GMASS_0512 zspec=1.46
viscl=Disky
GMASS_1248 zspec=1.47
viscl=FaintObj
GMASS_1248 zspec=1.47
viscl=Disky
GMASS_0743 zphot=1.47
viscl=Compact
GMASS_0743 zphot=1.47
viscl=Compact
GMASS_1069 zphot=1.47
viscl=Compact
GMASS_1069 zphot=1.47
viscl=Elliptical
GMASS_0504 zphot=1.48
Multiple
viscl=Disky
GMASS_0504 zphot=1.48
Multiple
viscl=Disky
GMASS_0831 zphot=1.49
viscl=Irregular
GMASS_0831 zphot=1.49
viscl=Irregular
GMASS_0144 zspec=1.50
Multiple
viscl=Disky
GMASS_0144 zspec=1.50
Multiple
viscl=Disky
GMASS_0408 zspec=1.50
viscl=Irregular
GMASS_0408 zspec=1.50
viscl=Irregular_disky
GMASS_1028 zphot=1.52
viscl=Compact
GMASS_1028 zphot=1.52
viscl=Compact
GMASS_1312 zphot=1.52
Multiple
viscl=Irregular
GMASS_1312 zphot=1.52
viscl=Irregular
GMASS_1602 zphot=1.52
viscl=Disky
GMASS_1602 zphot=1.52
viscl=Disky
GMASS_1621 zphot=1.53
viscl=FaintObj
GMASS_1621 zphot=1.53
viscl=Irregular
GMASS_0739 zphot=1.53
viscl=Elliptical
GMASS_0739 zphot=1.53
viscl=Elliptical
GMASS_1070 zphot=1.53
viscl=Compact
GMASS_1070 zphot=1.53
viscl=Elliptical_diffuse
GMASS_0757 zphot=1.53
viscl=Disky
GMASS_0757 zphot=1.53
viscl=Disky
GMASS_1050 zspec=1.53
viscl=Disky
GMASS_1050 zspec=1.53
viscl=Disky
GMASS_1146 zspec=1.53
viscl=Irregular
GMASS_1146 zspec=1.53
viscl=Disky
GMASS_0460 zspec=1.54
viscl=Compact
GMASS_0460 zspec=1.54
viscl=Elliptical
GMASS_1098 zphot=1.54
viscl=Compact
GMASS_1098 zphot=1.54
viscl=Elliptical
GMASS_0603 zphot=1.54
viscl=Compact
GMASS_0603 zphot=1.54
viscl=Elliptical

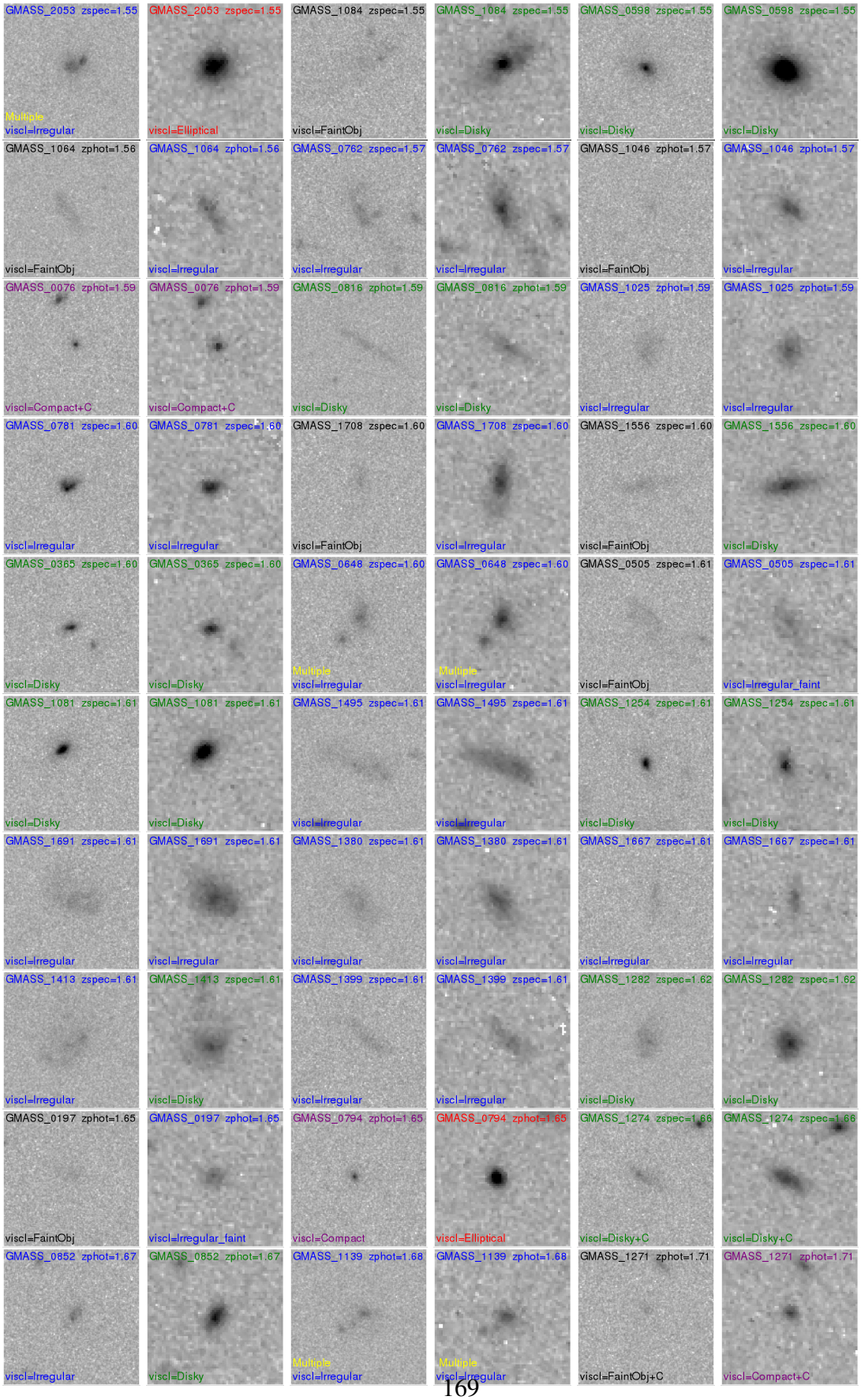
GMASS_2053 zspec=1.55
Multiple
viscl=Irregular
GMASS_2053 zspec=1.55
viscl=Elliptical
GMASS_1084 zspec=1.55
viscl=FaintObj
GMASS_1084 zspec=1.55
viscl=Disky
GMASS_0598 zspec=1.55
viscl=Disky
GMASS_0598 zspec=1.55
viscl=Disky
GMASS_1064 zphot=1.56
viscl=FaintObj
GMASS_1064 zphot=1.56
viscl=Irregular
GMASS_0762 zspec=1.57
viscl=Irregular
GMASS_0762 zspec=1.57
viscl=Irregular
GMASS_1046 zphot=1.57
viscl=FaintObj
GMASS_1046 zphot=1.57
viscl=Irregular
GMASS_0076 zphot=1.59
viscl=Compact+C
GMASS_0076 zphot=1.59
viscl=Compact+C
GMASS_0816 zphot=1.59
viscl=Disky
GMASS_0816 zphot=1.59
viscl=Disky
GMASS_1025 zphot=1.59
viscl=Irregular
GMASS_1025 zphot=1.59
viscl=Irregular
GMASS_0781 zspec=1.60
viscl=Irregular
GMASS_0781 zspec=1.60
viscl=Irregular
GMASS_1708 zspec=1.60
viscl=FaintObj
GMASS_1708 zspec=1.60
viscl=Irregular
GMASS_1556 zspec=1.60
viscl=FaintObj
GMASS_1556 zspec=1.60
viscl=Disky
GMASS_0365 zspec=1.60
viscl=Disky
GMASS_0365 zspec=1.60
viscl=Disky
GMASS_0648 zspec=1.60
Multiple
viscl=Irregular
GMASS_0648 zspec=1.60
Multiple
viscl=Irregular
GMASS_0505 zspec=1.61
viscl=FaintObj
GMASS_0505 zspec=1.61
viscl=Irregular_faint
GMASS_1081 zspec=1.61
viscl=Disky
GMASS_1081 zspec=1.61
viscl=Disky
GMASS_1495 zspec=1.61
viscl=Irregular
GMASS_1495 zspec=1.61
viscl=Irregular
GMASS_1254 zspec=1.61
viscl=Disky
GMASS_1254 zspec=1.61
viscl=Disky
GMASS_1691 zspec=1.61
viscl=Irregular
GMASS_1691 zspec=1.61
viscl=Irregular
GMASS_1380 zspec=1.61
viscl=Irregular
GMASS_1380 zspec=1.61
viscl=Irregular
GMASS_1667 zspec=1.61
viscl=Irregular
GMASS_1667 zspec=1.61
viscl=Irregular
GMASS_1413 zspec=1.61
viscl=Irregular
GMASS_1413 zspec=1.61
viscl=Disky
GMASS_1399 zspec=1.61
viscl=Irregular
GMASS_1399 zspec=1.61
viscl=Irregular
GMASS_1282 zspec=1.62
viscl=Disky
GMASS_1282 zspec=1.62
viscl=Disky
GMASS_0197 zphot=1.65
viscl=FaintObj
GMASS_0197 zphot=1.65
viscl=Irregular_faint
GMASS_0794 zphot=1.65
viscl=Compact
GMASS_0794 zphot=1.65
viscl=Elliptical
GMASS_1274 zspec=1.66
viscl=Disky+C
GMASS_1274 zspec=1.66
viscl=Disky+C
GMASS_0852 zphot=1.67
viscl=Irregular
GMASS_0852 zphot=1.67
viscl=Disky
GMASS_1139 zphot=1.68
Multiple
viscl=Irregular
GMASS_1139 zphot=1.68
Multiple
viscl=Irregular
GMASS_1271 zphot=1.71
viscl=FaintObj+C
GMASS_1271 zphot=1.71
viscl=Compact+C

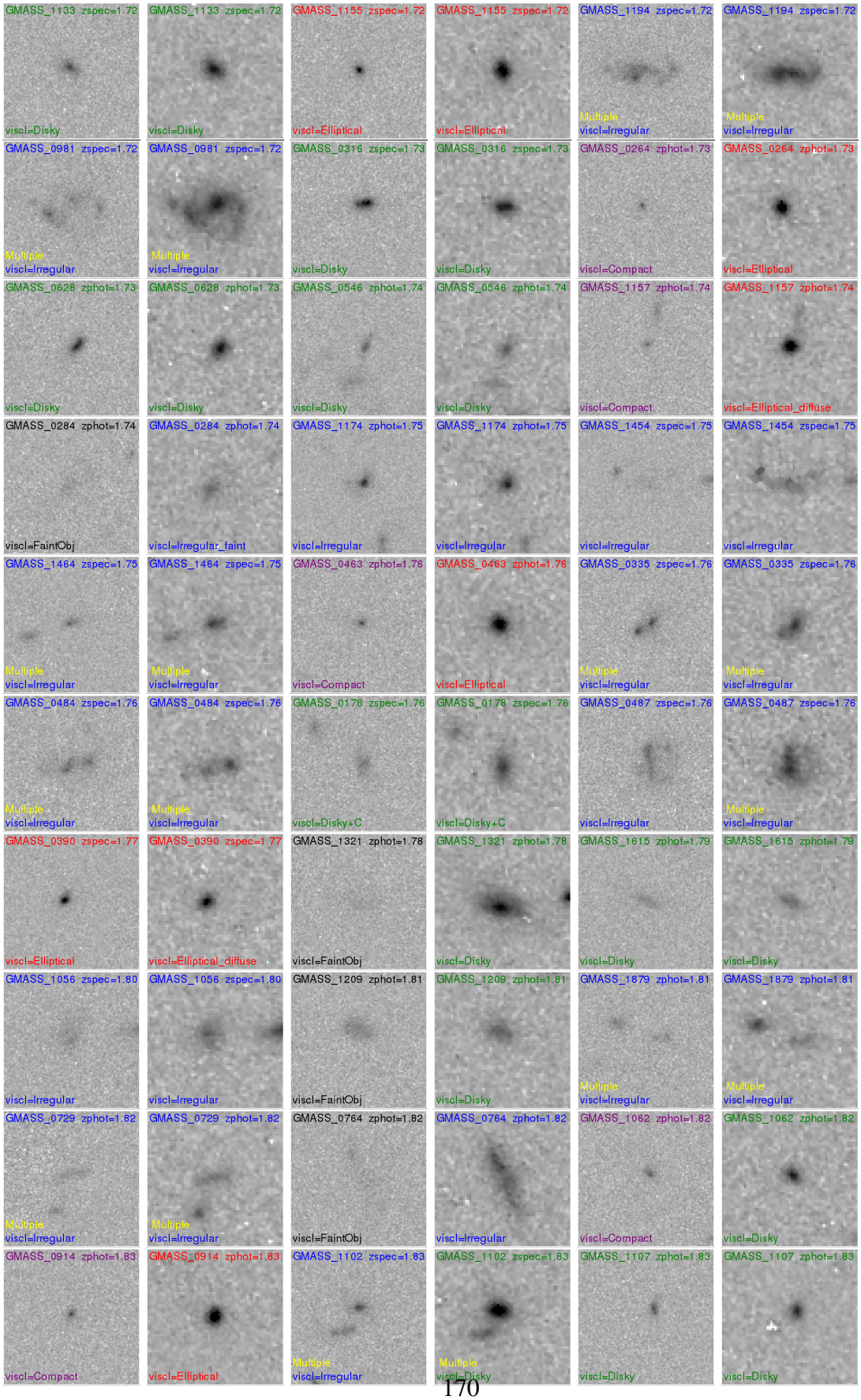
GMASS_1133 zspec=1.72
viscl=Disky
GMASS_1133 zspec=1.72
viscl=Disky
GMASS_1155 zspec=1.72
viscl=Elliptical
GMASS_1155 zspec=1.72
viscl=Elliptical
GMASS_1194 zspec=1.72
Multiple
viscl=Irregular
GMASS_1194 zspec=1.72
Multiple
viscl=Irregular
GMASS_0981 zspec=1.72
Multiple
viscl=Irregular
GMASS_0981 zspec=1.72
Multiple
viscl=Irregular
GMASS_0316 zspec=1.73
viscl=Disky
GMASS_0316 zspec=1.73
viscl=Disky
GMASS_0264 zphot=1.73
viscl=Compact
GMASS_0264 zphot=1.73
viscl=Elliptical
GMASS_0628 zphot=1.73
viscl=Disky
GMASS_0628 zphot=1.73
viscl=Disky
GMASS_0546 zphot=1.74
viscl=Disky
GMASS_0546 zphot=1.74
viscl=Disky
GMASS_1157 zphot=1.74
viscl=Compact
GMASS_1157 zphot=1.74
viscl=Elliptical_diffuse
GMASS_0284 zphot=1.74
viscl=FaintObj
GMASS_0284 zphot=1.74
viscl=Irregular_faint
GMASS_1174 zphot=1.75
viscl=Irregular
GMASS_1174 zphot=1.75
viscl=Irregular
GMASS_1454 zspec=1.75
viscl=Irregular
GMASS_1454 zspec=1.75
viscl=Irregular
GMASS_1464 zspec=1.75
Multiple
viscl=Irregular
GMASS_1464 zspec=1.75
Multiple
viscl=Irregular
GMASS_0463 zphot=1.76
viscl=Compact
GMASS_0463 zphot=1.76
viscl=Elliptical
GMASS_0335 zspec=1.76
Multiple
viscl=Irregular
GMASS_0335 zspec=1.76
Multiple
viscl=Irregular
GMASS_0484 zspec=1.76
Multiple
viscl=Irregular
GMASS_0484 zspec=1.76
Multiple
viscl=Irregular
GMASS_0178 zspec=1.76
viscl=Disky+C
GMASS_0178 zspec=1.76
viscl=Disky+C
GMASS_0487 zspec=1.76
viscl=Irregular
GMASS_0487 zspec=1.76
Multiple
viscl=Irregular
GMASS_0390 zspec=1.77
viscl=Elliptical
GMASS_0390 zspec=1.77
viscl=Elliptical_diffuse
GMASS_1321 zphot=1.78
viscl=FaintObj
GMASS_1321 zphot=1.78
viscl=Disky
GMASS_1615 zphot=1.79
viscl=Disky
GMASS_1615 zphot=1.79
viscl=Disky
GMASS_1056 zspec=1.80
viscl=Irregular
GMASS_1056 zspec=1.80
viscl=Irregular
GMASS_1209 zphot=1.81
viscl=FaintObj
GMASS_1209 zphot=1.81
viscl=Disky
GMASS_1879 zphot=1.81
Multiple
viscl=Irregular
GMASS_1879 zphot=1.81
Multiple
viscl=Irregular
GMASS_0729 zphot=1.82
Multiple
viscl=Irregular
GMASS_0729 zphot=1.82
Multiple
viscl=Irregular
GMASS_0764 zphot=1.82
viscl=FaintObj
GMASS_0764 zphot=1.82
viscl=Irregular
GMASS_1062 zphot=1.82
viscl=Compact
GMASS_1062 zphot=1.82
viscl=Disky
GMASS_0914 zphot=1.83
viscl=Compact
GMASS_0914 zphot=1.83
viscl=Elliptical
GMASS_1102 zspec=1.83
Multiple
viscl=Irregular
GMASS_1102 zspec=1.83
Multiple
viscl=Disky
GMASS_1107 zphot=1.83
viscl=Disky
GMASS_1107 zphot=1.83
viscl=Disky

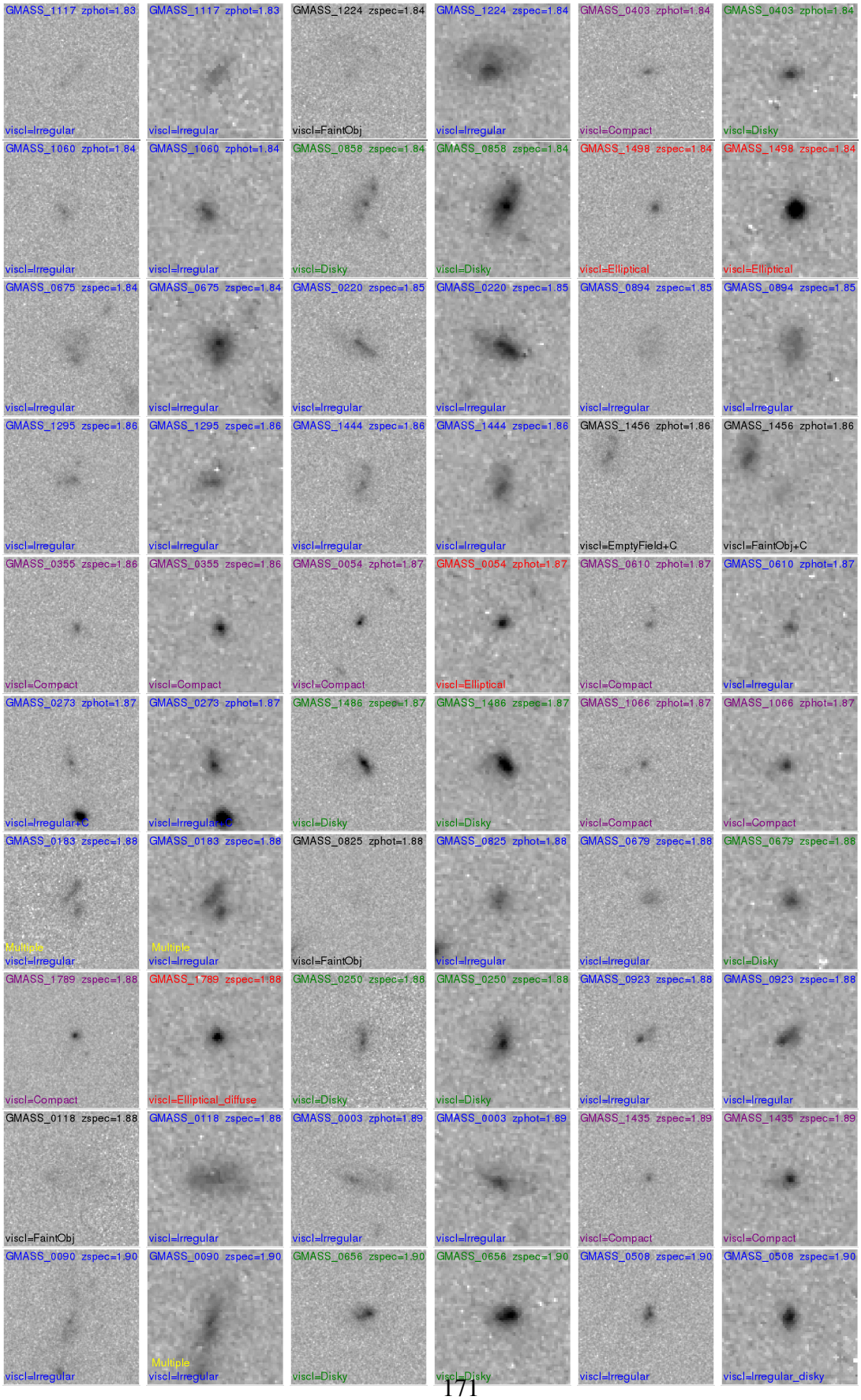
GMASS_1117 zphot=1.83
viscl=Irregular
GMASS_1117 zphot=1.83
viscl=Irregular
GMASS_1224 zspec=1.84
viscl=FaintObj
GMASS_1224 zspec=1.84
viscl=Irregular
GMASS_0403 zphot=1.84
viscl=Compact
GMASS_0403 zphot=1.84
viscl=Disky
GMASS_1060 zphot=1.84
viscl=Irregular
GMASS_1060 zphot=1.84
viscl=Irregular
GMASS_0858 zspec=1.84
viscl=Disky
GMASS_0858 zspec=1.84
viscl=Disky
GMASS_1498 zspec=1.84
viscl=Elliptical
GMASS_1498 zspec=1.84
viscl=Elliptical
GMASS_0675 zspec=1.84
viscl=Irregular
GMASS_0675 zspec=1.84
viscl=Irregular
GMASS_0220 zspec=1.85
viscl=Irregular
GMASS_0220 zspec=1.85
viscl=Irregular
GMASS_0894 zspec=1.85
viscl=Irregular
GMASS_0894 zspec=1.85
viscl=Irregular
GMASS_1295 zspec=1.86
viscl=Irregular
GMASS_1295 zspec=1.86
viscl=Irregular
GMASS_1444 zspec=1.86
viscl=Irregular
GMASS_1444 zspec=1.86
viscl=Irregular
GMASS_1456 zphot=1.86
viscl=EmptyField+C
GMASS_1456 zphot=1.86
viscl=FaintObj+C
GMASS_0355 zspec=1.86
viscl=Compact
GMASS_0355 zspec=1.86
viscl=Compact
GMASS_0054 zphot=1.87
viscl=Compact
GMASS_0054 zphot=1.87
viscl=Elliptical
GMASS_0610 zphot=1.87
viscl=Compact
GMASS_0610 zphot=1.87
viscl=Irregular
GMASS_0273 zphot=1.87
viscl=Irregular+C
GMASS_0273 zphot=1.87
viscl=Irregular+C
GMASS_1486 zspec=1.87
viscl=Disky
GMASS_1486 zspec=1.87
viscl=Disky
GMASS_1066 zphot=1.87
viscl=Compact
GMASS_1066 zphot=1.87
viscl=Compact
GMASS_0183 zspec=1.88
Multiple
viscl=Irregular
GMASS_0183 zspec=1.88
Multiple
viscl=Irregular
GMASS_0825 zphot=1.88
viscl=FaintObj
GMASS_0825 zphot=1.88
viscl=Irregular
GMASS_0679 zspec=1.88
viscl=Irregular
GMASS_0679 zspec=1.88
viscl=Disky
GMASS_1789 zspec=1.88
viscl=Compact
GMASS_1789 zspec=1.88
viscl=Elliptical_diffuse
GMASS_0250 zspec=1.88
viscl=Disky
GMASS_0250 zspec=1.88
viscl=Disky
GMASS_0923 zspec=1.88
viscl=Irregular
GMASS_0923 zspec=1.88
viscl=Irregular
GMASS_0118 zspec=1.88
viscl=FaintObj
GMASS_0118 zspec=1.88
viscl=Irregular
GMASS_0003 zphot=1.89
viscl=Irregular
GMASS_0003 zphot=1.89
viscl=Irregular
GMASS_1435 zspec=1.89
viscl=Compact
GMASS_1435 zspec=1.89
viscl=Compact
GMASS_0090 zspec=1.90
viscl=Irregular
GMASS_0090 zspec=1.90
Multiple
viscl=Irregular
GMASS_0656 zspec=1.90
viscl=Disky
GMASS_0656 zspec=1.90
viscl=Disky
GMASS_0508 zspec=1.90
viscl=Irregular
GMASS_0508 zspec=1.90
viscl=Irregular_disky

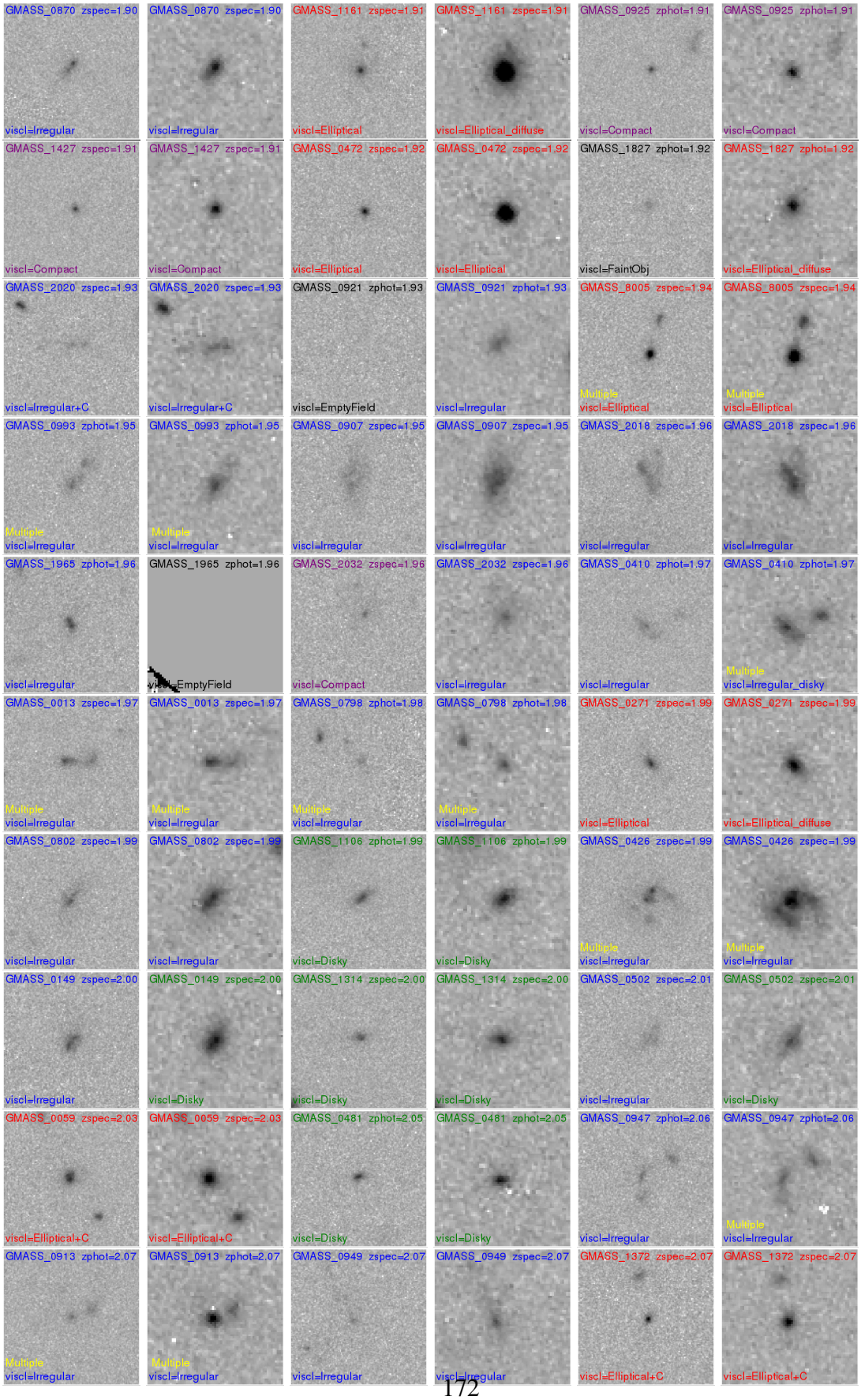
GMASS_0870 zspec=1.90
viscl=Irregular
GMASS_0870 zspec=1.90
viscl=Irregular
GMASS_1161 zspec=1.91
viscl=Elliptical
GMASS_1161 zspec=1.91
viscl=Elliptical_diffuse
GMASS_0925 zphot=1.91
viscl=Compact
GMASS_0925 zphot=1.91
viscl=Compact
GMASS_1427 zspec=1.91
viscl=Compact
GMASS_1427 zspec=1.91
viscl=Compact
GMASS_0472 zspec=1.92
viscl=Elliptical
GMASS_0472 zspec=1.92
viscl=Elliptical
GMASS_1827 zphot=1.92
viscl=FaintObj
GMASS_1827 zphot=1.92
viscl=Elliptical_diffuse
GMASS_2020 zspec=1.93
viscl=Irregular+C
GMASS_2020 zspec=1.93
viscl=Irregular+C
GMASS_0921 zphot=1.93
viscl=EmptyField
GMASS_0921 zphot=1.93
viscl=Irregular
GMASS_8005 zspec=1.94
Multiple
viscl=Elliptical
GMASS_8005 zspec=1.94
Multiple
viscl=Elliptical
GMASS_0993 zphot=1.95
Multiple
viscl=Irregular
GMASS_0993 zphot=1.95
Multiple
viscl=Irregular
GMASS_0907 zspec=1.95
viscl=Irregular
GMASS_0907 zspec=1.95
viscl=Irregular
GMASS_2018 zspec=1.96
viscl=Irregular
GMASS_2018 zspec=1.96
viscl=Irregular
GMASS_1965 zphot=1.96
viscl=Irregular
GMASS_1965 zphot=1.96
viscl=EmptyField
GMASS_2032 zspec=1.96
viscl=Compact
GMASS_2032 zspec=1.96
viscl=Irregular
GMASS_0410 zphot=1.97
viscl=Irregular
GMASS_0410 zphot=1.97
Multiple
viscl=Irregular_disky
GMASS_0013 zspec=1.97
Multiple
viscl=Irregular
GMASS_0013 zspec=1.97
Multiple
viscl=Irregular
GMASS_0798 zphot=1.98
Multiple
viscl=Irregular
GMASS_0798 zphot=1.98
Multiple
viscl=Irregular
GMASS_0271 zspec=1.99
viscl=Elliptical
GMASS_0271 zspec=1.99
viscl=Elliptical_diffuse
GMASS_0802 zspec=1.99
viscl=Irregular
GMASS_0802 zspec=1.99
viscl=Irregular
GMASS_1106 zphot=1.99
viscl=Disky
GMASS_1106 zphot=1.99
viscl=Disky
GMASS_0426 zspec=1.99
Multiple
viscl=Irregular
GMASS_0426 zspec=1.99
Multiple
viscl=Irregular
GMASS_0149 zspec=2.00
viscl=Irregular
GMASS_0149 zspec=2.00
viscl=Disky
GMASS_1314 zspec=2.00
viscl=Disky
GMASS_1314 zspec=2.00
viscl=Disky
GMASS_0502 zspec=2.01
viscl=Irregular
GMASS_0502 zspec=2.01
viscl=Disky
GMASS_0059 zspec=2.03
viscl=Elliptical+C
GMASS_0059 zspec=2.03
viscl=Elliptical+C
GMASS_0481 zphot=2.05
viscl=Disky
GMASS_0481 zphot=2.05
viscl=Disky
GMASS_0947 zphot=2.06
viscl=Irregular
GMASS_0947 zphot=2.06
Multiple
viscl=Irregular
GMASS_0913 zphot=2.07
Multiple
viscl=Irregular
GMASS_0913 zphot=2.07
Multiple
viscl=Irregular
GMASS_0949 zspec=2.07
viscl=Irregular
GMASS_0949 zspec=2.07
viscl=Irregular
GMASS_1372 zspec=2.07
viscl=Elliptical+C
GMASS_1372 zspec=2.07
viscl=Elliptical+C

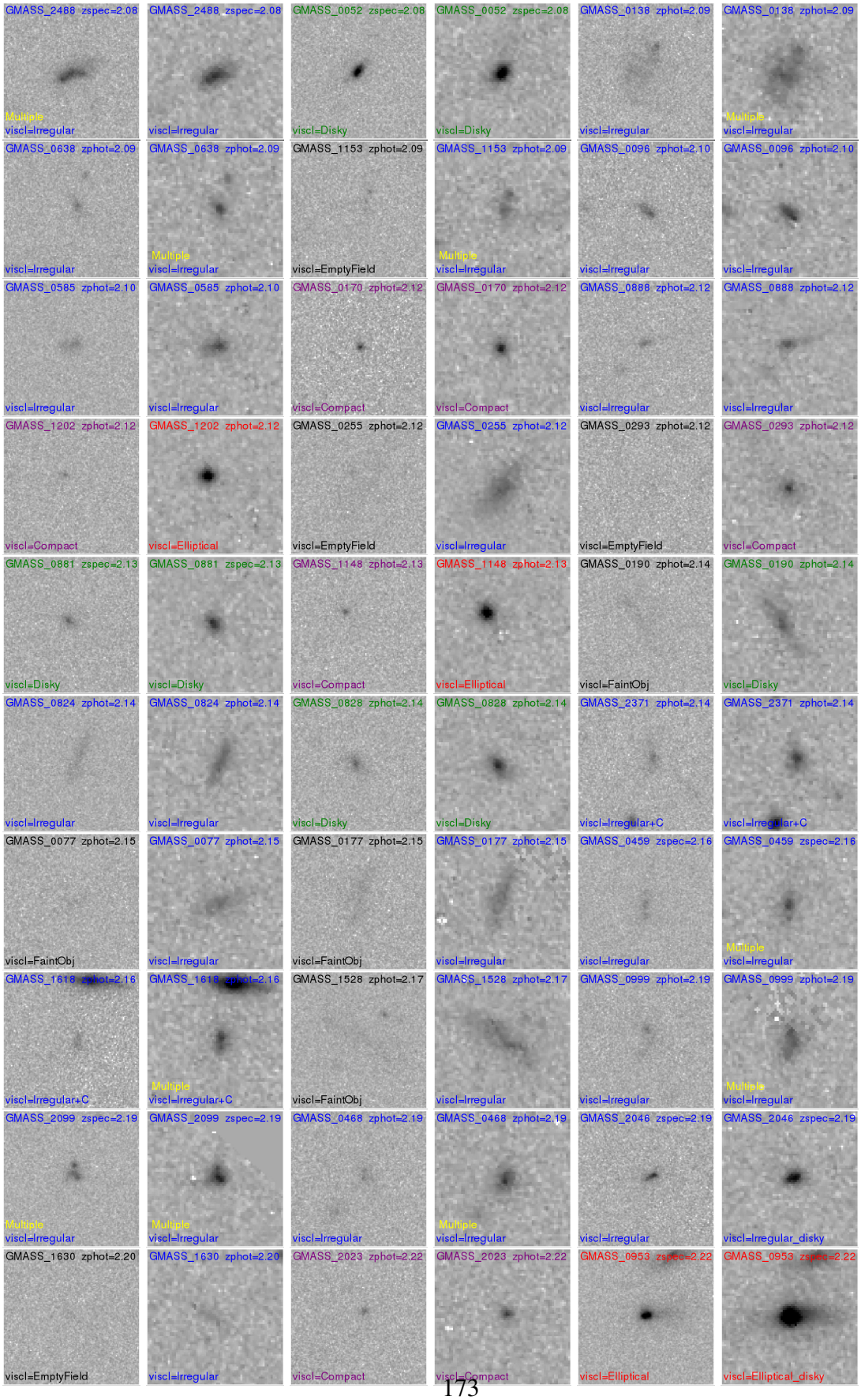
GMASS_2488 zspec=2.08
Multiple
viscl=Irregular
GMASS_2488 zspec=2.08
viscl=Irregular
GMASS_0052 zspec=2.08
viscl=Disky
GMASS_0052 zspec=2.08
viscl=Disky
GMASS_0138 zphot=2.09
viscl=Irregular
GMASS_0138 zphot=2.09
Multiple
viscl=Irregular
GMASS_0638 zphot=2.09
viscl=Irregular
GMASS_0638 zphot=2.09
Multiple
viscl=Irregular
GMASS_1153 zphot=2.09
viscl=EmptyField
GMASS_1153 zphot=2.09
Multiple
viscl=Irregular
GMASS_0096 zphot=2.10
viscl=Irregular
GMASS_0096 zphot=2.10
viscl=Irregular
GMASS_0585 zphot=2.10
viscl=Irregular
GMASS_0585 zphot=2.10
viscl=Irregular
GMASS_0170 zphot=2.12
viscl=Compact
GMASS_0170 zphot=2.12
viscl=Compact
GMASS_0888 zphot=2.12
viscl=Irregular
GMASS_0888 zphot=2.12
viscl=Irregular
GMASS_1202 zphot=2.12
viscl=Compact
GMASS_1202 zphot=2.12
viscl=Elliptical
GMASS_0255 zphot=2.12
viscl=EmptyField
GMASS_0255 zphot=2.12
viscl=Irregular
GMASS_0293 zphot=2.12
viscl=EmptyField
GMASS_0293 zphot=2.12
viscl=Compact
GMASS_0881 zspec=2.13
viscl=Disky
GMASS_0881 zspec=2.13
viscl=Disky
GMASS_1148 zphot=2.13
viscl=Compact
GMASS_1148 zphot=2.13
viscl=Elliptical
GMASS_0190 zphot=2.14
viscl=FaintObj
GMASS_0190 zphot=2.14
viscl=Disky
GMASS_0824 zphot=2.14
viscl=Irregular
GMASS_0824 zphot=2.14
viscl=Irregular
GMASS_0828 zphot=2.14
viscl=Disky
GMASS_0828 zphot=2.14
viscl=Disky
GMASS_2371 zphot=2.14
viscl=Irregular+C
GMASS_2371 zphot=2.14
viscl=Irregular+C
GMASS_0077 zphot=2.15
viscl=FaintObj
GMASS_0077 zphot=2.15
viscl=Irregular
GMASS_0177 zphot=2.15
viscl=FaintObj
GMASS_0177 zphot=2.15
viscl=Irregular
GMASS_0459 zspec=2.16
viscl=Irregular
GMASS_0459 zspec=2.16
Multiple
viscl=Irregular
GMASS_1618 zphot=2.16
viscl=Irregular+C
GMASS_1618 zphot=2.16
Multiple
viscl=Irregular+C
GMASS_1528 zphot=2.17
viscl=FaintObj
GMASS_1528 zphot=2.17
viscl=Irregular
GMASS_0999 zphot=2.19
viscl=Irregular
GMASS_0999 zphot=2.19
Multiple
viscl=Irregular
GMASS_2099 zspec=2.19
Multiple
viscl=Irregular
GMASS_2099 zspec=2.19
Multiple
viscl=Irregular
GMASS_0468 zphot=2.19
viscl=Irregular
GMASS_0468 zphot=2.19
Multiple
viscl=Irregular
GMASS_2046 zspec=2.19
viscl=Irregular
GMASS_2046 zspec=2.19
viscl=Irregular_disky
GMASS_1630 zphot=2.20
viscl=EmptyField
GMASS_1630 zphot=2.20
viscl=Irregular
GMASS_2023 zphot=2.22
viscl=Compact
GMASS_2023 zphot=2.22
viscl=Compact
GMASS_0953 zspec=2.22
viscl=Elliptical
GMASS_0953 zspec=2.22
viscl=Elliptical_disky

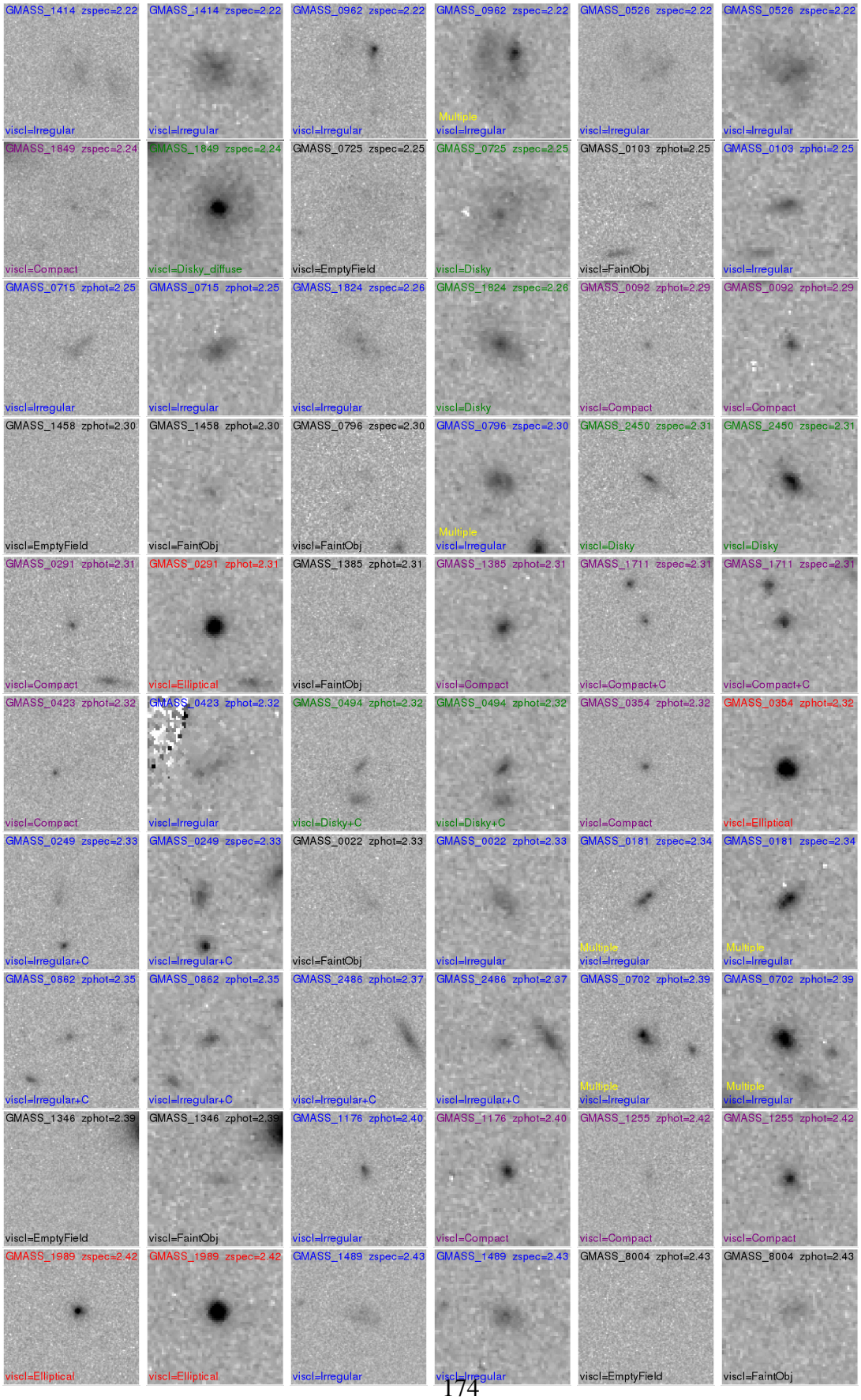
GMASS_1414 zspec=2.22
viscl=Irregular
GMASS_1414 zspec=2.22
viscl=Irregular
GMASS_0962 zspec=2.22
viscl=Irregular
GMASS_0962 zspec=2.22
Multiple
viscl=Irregular
GMASS_0526 zspec=2.22
viscl=Irregular
GMASS_0526 zspec=2.22
viscl=Irregular
GMASS_1849 zspec=2.24
viscl=Compact
GMASS_1849 zspec=2.24
viscl=Disky_diffuse
GMASS_0725 zspec=2.25
viscl=EmptyField
GMASS_0725 zspec=2.25
viscl=Disky
GMASS_0103 zphot=2.25
viscl=FaintObj
GMASS_0103 zphot=2.25
viscl=Irregular
GMASS_0715 zphot=2.25
viscl=Irregular
GMASS_0715 zphot=2.25
viscl=Irregular
GMASS_1824 zspec=2.26
viscl=Irregular
GMASS_1824 zspec=2.26
viscl=Disky
GMASS_0092 zphot=2.29
viscl=Compact
GMASS_0092 zphot=2.29
viscl=Compact
GMASS_1458 zphot=2.30
viscl=EmptyField
GMASS_1458 zphot=2.30
viscl=FaintObj
GMASS_0796 zspec=2.30
viscl=FaintObj
GMASS_0796 zspec=2.30
Multiple
viscl=Irregular
GMASS_2450 zspec=2.31
viscl=Disky
GMASS_2450 zspec=2.31
viscl=Disky
GMASS_0291 zphot=2.31
viscl=Compact
GMASS_0291 zphot=2.31
viscl=Elliptical
GMASS_1385 zphot=2.31
viscl=FaintObj
GMASS_1385 zphot=2.31
viscl=Compact
GMASS_1711 zspec=2.31
viscl=Compact+C
GMASS_1711 zspec=2.31
viscl=Compact+C
GMASS_0423 zphot=2.32
viscl=Compact
GMASS_0423 zphot=2.32
viscl=Irregular
GMASS_0494 zphot=2.32
viscl=Disky+C
GMASS_0494 zphot=2.32
viscl=Disky+C
GMASS_0354 zphot=2.32
viscl=Compact
GMASS_0354 zphot=2.32
viscl=Elliptical
GMASS_0249 zspec=2.33
viscl=Irregular+C
GMASS_0249 zspec=2.33
viscl=Irregular+C
GMASS_0022 zphot=2.33
viscl=FaintObj
GMASS_0022 zphot=2.33
viscl=Irregular
GMASS_0181 zspec=2.34
Multiple
viscl=Irregular
GMASS_0181 zspec=2.34
Multiple
viscl=Irregular
GMASS_0862 zphot=2.35
viscl=Irregular+C
GMASS_0862 zphot=2.35
viscl=Irregular+C
GMASS_2486 zphot=2.37
viscl=Irregular+C
GMASS_2486 zphot=2.37
viscl=Irregular+C
GMASS_0702 zphot=2.39
Multiple
viscl=Irregular
GMASS_0702 zphot=2.39
Multiple
viscl=Irregular
GMASS_1346 zphot=2.39
viscl=EmptyField
GMASS_1346 zphot=2.39
viscl=FaintObj
GMASS_1176 zphot=2.40
viscl=Irregular
GMASS_1176 zphot=2.40
viscl=Compact
GMASS_1255 zphot=2.42
viscl=Compact
GMASS_1255 zphot=2.42
viscl=Compact
GMASS_1989 zspec=2.42
viscl=Elliptical
GMASS_1989 zspec=2.42
viscl=Elliptical
GMASS_1489 zspec=2.43
viscl=Irregular
GMASS_1489 zspec=2.43
viscl=Irregular
GMASS_8004 zphot=2.43
viscl=EmptyField
GMASS_8004 zphot=2.43
viscl=FaintObj

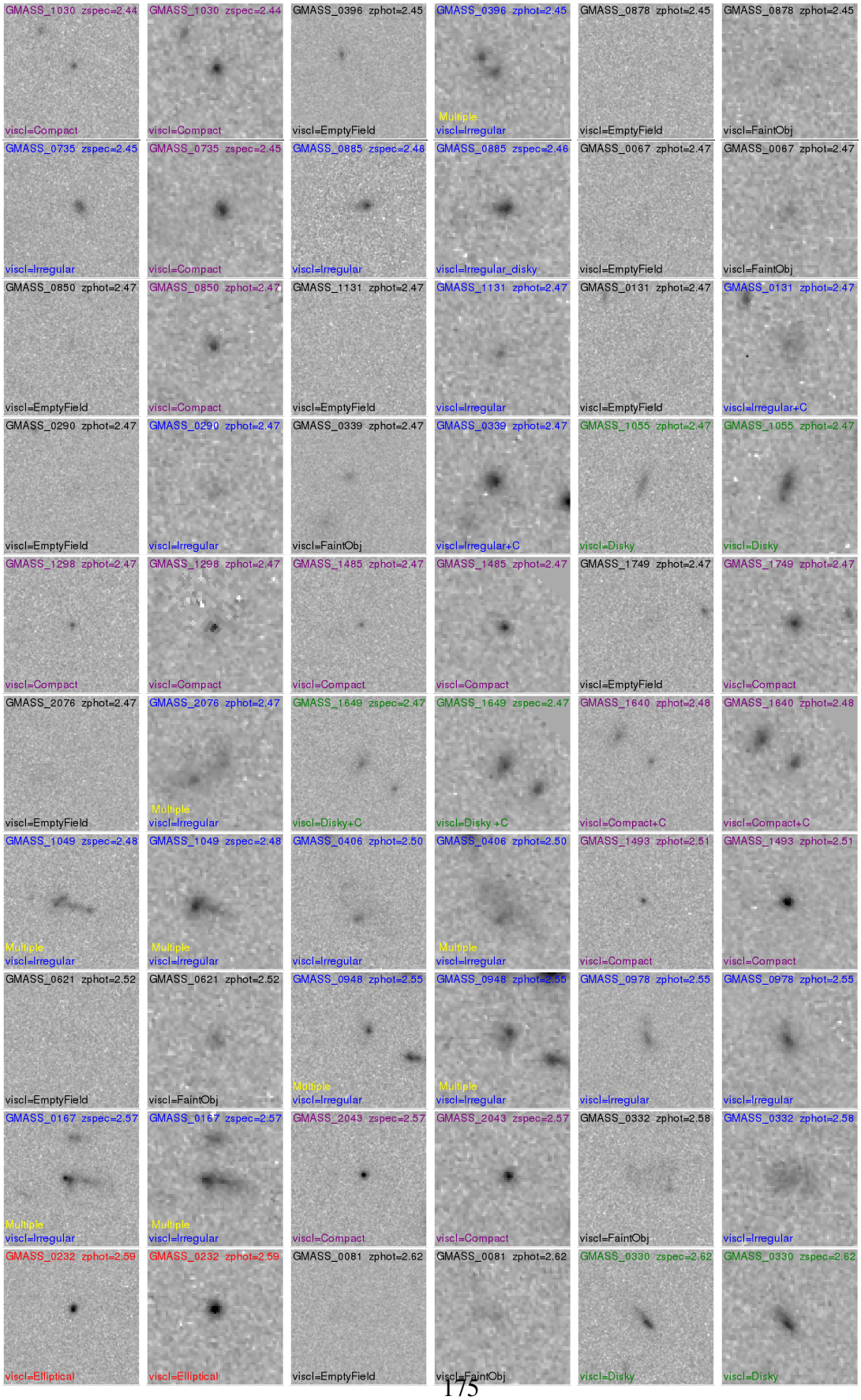
GMASS_1030 zspec=2.44
viscl=Compact
GMASS_1030 zspec=2.44
viscl=Compact
GMASS_0396 zphot=2.45
viscl=EmptyField
GMASS_0396 zphot=2.45
Multiple
viscl=Irregular
GMASS_0878 zphot=2.45
viscl=EmptyField
GMASS_0878 zphot=2.45
viscl=FaintObj
GMASS_0735 zspec=2.45
viscl=Irregular
GMASS_0735 zspec=2.45
viscl=Compact
GMASS_0885 zspec=2.46
viscl=Irregular
GMASS_0885 zspec=2.46
viscl=Irregular_disky
GMASS_0067 zphot=2.47
viscl=EmptyField
GMASS_0067 zphot=2.47
viscl=FaintObj
GMASS_0850 zphot=2.47
viscl=EmptyField
GMASS_0850 zphot=2.47
viscl=Compact
GMASS_1131 zphot=2.47
viscl=EmptyField
GMASS_1131 zphot=2.47
viscl=Irregular
GMASS_0131 zphot=2.47
viscl=EmptyField
GMASS_0131 zphot=2.47
viscl=Irregular+C
GMASS_0290 zphot=2.47
viscl=EmptyField
GMASS_0290 zphot=2.47
viscl=Irregular
GMASS_0339 zphot=2.47
viscl=FaintObj
GMASS_0339 zphot=2.47
viscl=Irregular+C
GMASS_1055 zphot=2.47
viscl=Disky
GMASS_1055 zphot=2.47
viscl=Disky
GMASS_1298 zphot=2.47
viscl=Compact
GMASS_1298 zphot=2.47
viscl=Compact
GMASS_1485 zphot=2.47
viscl=Compact
GMASS_1485 zphot=2.47
viscl=Compact
GMASS_1749 zphot=2.47
viscl=EmptyField
GMASS_1749 zphot=2.47
viscl=Compact
GMASS_2076 zphot=2.47
viscl=EmptyField
GMASS_2076 zphot=2.47
Multiple
viscl=Irregular
GMASS_1649 zspec=2.47
viscl=Disky+C
GMASS_1649 zspec=2.47
viscl=Disky +C
GMASS_1640 zphot=2.48
viscl=Compact+C
GMASS_1640 zphot=2.48
viscl=Compact+C
GMASS_1049 zspec=2.48
Multiple
viscl=Irregular
GMASS_1049 zspec=2.48
Multiple
viscl=Irregular
GMASS_0406 zphot=2.50
viscl=Irregular
GMASS_0406 zphot=2.50
Multiple
viscl=Irregular
GMASS_1493 zphot=2.51
viscl=Compact
GMASS_1493 zphot=2.51
viscl=Compact
GMASS_0621 zphot=2.52
viscl=EmptyField
GMASS_0621 zphot=2.52
viscl=FaintObj
GMASS_0948 zphot=2.55
Multiple
viscl=Irregular
GMASS_0948 zphot=2.55
Multiple
viscl=Irregular
GMASS_0978 zphot=2.55
viscl=Irregular
GMASS_0978 zphot=2.55
viscl=Irregular
GMASS_0167 zspec=2.57
Multiple
viscl=Irregular
GMASS_0167 zspec=2.57
Multiple
viscl=Irregular
GMASS_2043 zspec=2.57
viscl=Compact
GMASS_2043 zspec=2.57
viscl=Compact
GMASS_0332 zphot=2.58
viscl=FaintObj
GMASS_0332 zphot=2.58
viscl=Irregular
GMASS_0232 zphot=2.59
viscl=Elliptical
GMASS_0232 zphot=2.59
viscl=Elliptical
GMASS_0081 zphot=2.62
viscl=EmptyField
GMASS_0081 zphot=2.62
viscl=FaintObj
GMASS_0330 zspec=2.62
viscl=Disky
GMASS_0330 zspec=2.62
viscl=Disky

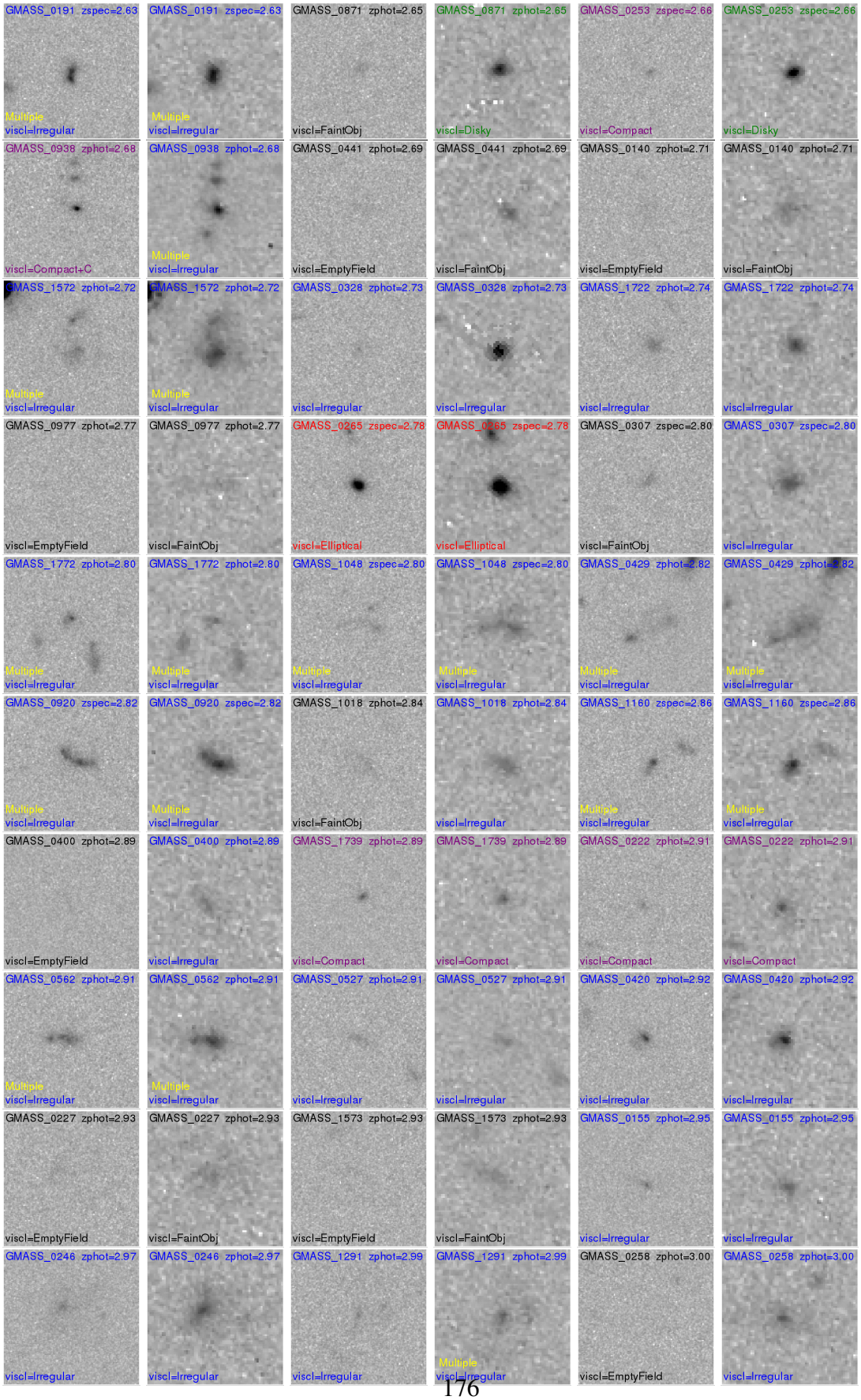
GMASS_0191 zspec=2.63
Multiple
viscl=Irregular
GMASS_0191 zspec=2.63
Multiple
viscl=Irregular
GMASS_0871 zphot=2.65
viscl=FaintObj
GMASS_0871 zphot=2.65
viscl=Disky
GMASS_0253 zspec=2.66
viscl=Compact
GMASS_0253 zspec=2.66
viscl=Disky
GMASS_0938 zphot=2.68
viscl=Compact+C
GMASS_0938 zphot=2.68
Multiple
viscl=Irregular
GMASS_0441 zphot=2.69
viscl=EmptyField
GMASS_0441 zphot=2.69
viscl=FaintObj
GMASS_0140 zphot=2.71
viscl=EmptyField
GMASS_0140 zphot=2.71
viscl=FaintObj
GMASS_1572 zphot=2.72
Multiple
viscl=Irregular
GMASS_1572 zphot=2.72
Multiple
viscl=Irregular
GMASS_0328 zphot=2.73
viscl=Irregular
GMASS_0328 zphot=2.73
viscl=Irregular
GMASS_1722 zphot=2.74
viscl=Irregular
GMASS_1722 zphot=2.74
viscl=Irregular
GMASS_0977 zphot=2.77
viscl=EmptyField
GMASS_0977 zphot=2.77
viscl=FaintObj
GMASS_0265 zspec=2.78
viscl=Elliptical
GMASS_0265 zspec=2.78
viscl=Elliptical
GMASS_0307 zspec=2.80
viscl=FaintObj
GMASS_0307 zspec=2.80
viscl=Irregular
GMASS_1772 zphot=2.80
Multiple
viscl=Irregular
GMASS_1772 zphot=2.80
Multiple
viscl=Irregular
GMASS_1048 zspec=2.80
Multiple
viscl=Irregular
GMASS_1048 zspec=2.80
Multiple
viscl=Irregular
GMASS_0429 zphot=2.82
Multiple
viscl=Irregular
GMASS_0429 zphot=2.82
Multiple
viscl=Irregular
GMASS_0920 zspec=2.82
Multiple
viscl=Irregular
GMASS_0920 zspec=2.82
Multiple
viscl=Irregular
GMASS_1018 zphot=2.84
viscl=FaintObj
GMASS_1018 zphot=2.84
viscl=Irregular
GMASS_1160 zspec=2.86
Multiple
viscl=Irregular
GMASS_1160 zspec=2.86
Multiple
viscl=Irregular
GMASS_0400 zphot=2.89
viscl=EmptyField
GMASS_0400 zphot=2.89
viscl=Irregular
GMASS_1739 zphot=2.89
viscl=Compact
GMASS_1739 zphot=2.89
viscl=Compact
GMASS_0222 zphot=2.91
viscl=Compact
GMASS_0222 zphot=2.91
viscl=Compact
GMASS_0562 zphot=2.91
Multiple
viscl=Irregular
GMASS_0562 zphot=2.91
Multiple
viscl=Irregular
GMASS_0527 zphot=2.91
viscl=Irregular
GMASS_0527 zphot=2.91
viscl=Irregular
GMASS_0420 zphot=2.92
viscl=Irregular
GMASS_0420 zphot=2.92
viscl=Irregular
GMASS_0227 zphot=2.93
viscl=EmptyField
GMASS_0227 zphot=2.93
viscl=FaintObj
GMASS_1573 zphot=2.93
viscl=EmptyField
GMASS_1573 zphot=2.93
viscl=FaintObj
GMASS_0155 zphot=2.95
viscl=Irregular
GMASS_0155 zphot=2.95
viscl=Irregular
GMASS_0246 zphot=2.97
viscl=Irregular
GMASS_0246 zphot=2.97
viscl=Irregular
GMASS_1291 zphot=2.99
viscl=Irregular
GMASS_1291 zphot=2.99
Multiple
viscl=Irregular
GMASS_0258 zphot=3.00
viscl=EmptyField
GMASS_0258 zphot=3.00
viscl=Irregular

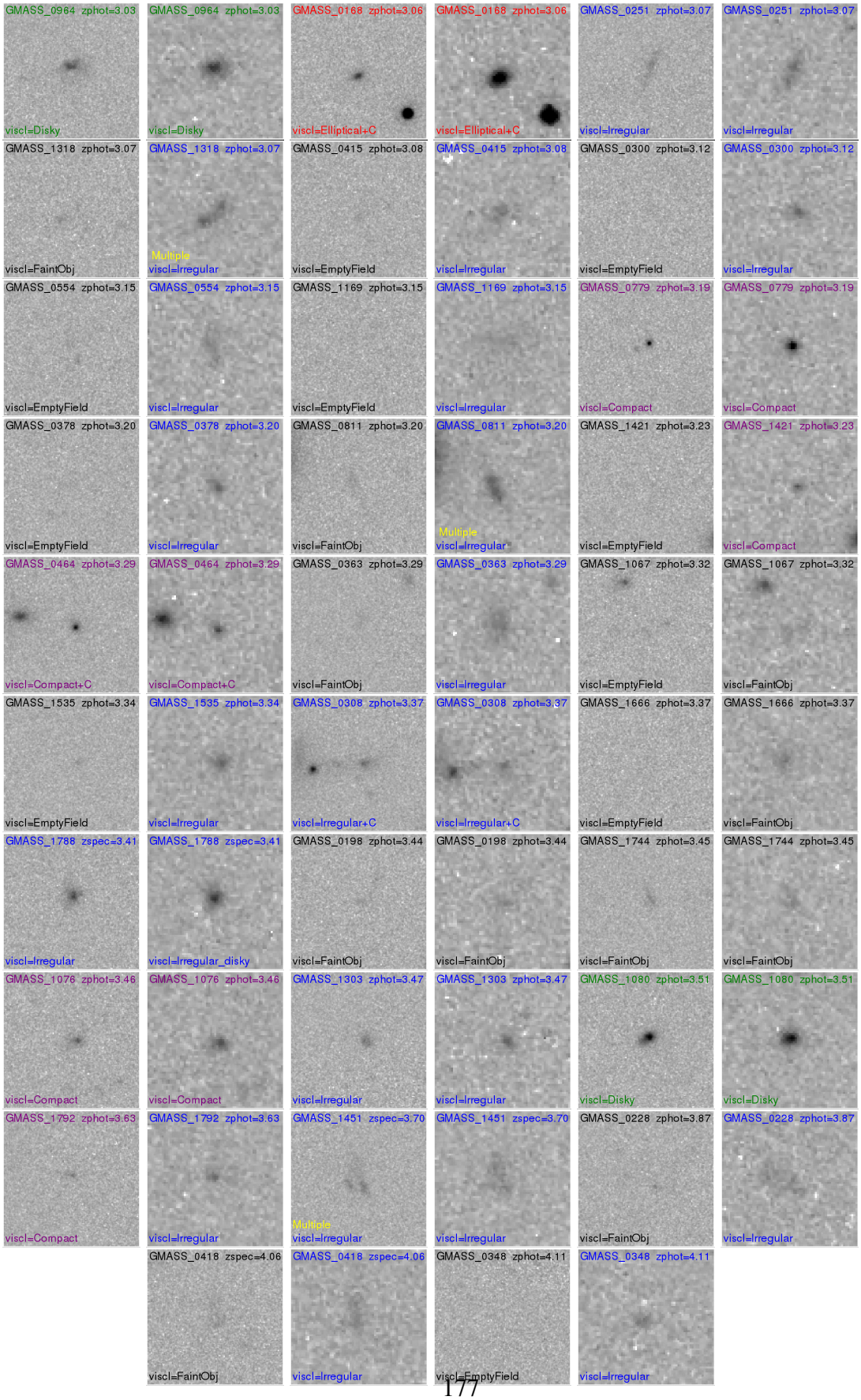
GMASS_0964 zphot=3.03
viscl=Disky
GMASS_0964 zphot=3.03
viscl=Disky
GMASS_0168 zphot=3.06
viscl=Elliptical+C
GMASS_0168 zphot=3.06
viscl=Elliptical+C
GMASS_0251 zphot=3.07
viscl=Irregular
GMASS_0251 zphot=3.07
viscl=Irregular
GMASS_1318 zphot=3.07
viscl=FaintObj
GMASS_1318 zphot=3.07
Multiple
viscl=Irregular
GMASS_0415 zphot=3.08
viscl=EmptyField
GMASS_0415 zphot=3.08
viscl=Irregular
GMASS_0300 zphot=3.12
viscl=EmptyField
GMASS_0300 zphot=3.12
viscl=Irregular
GMASS_0554 zphot=3.15
viscl=EmptyField
GMASS_0554 zphot=3.15
viscl=Irregular
GMASS_1169 zphot=3.15
viscl=EmptyField
GMASS_1169 zphot=3.15
viscl=Irregular
GMASS_0779 zphot=3.19
viscl=Compact
GMASS_0779 zphot=3.19
viscl=Compact
GMASS_0378 zphot=3.20
viscl=EmptyField
GMASS_0378 zphot=3.20
viscl=Irregular
GMASS_0811 zphot=3.20
viscl=FaintObj
GMASS_0811 zphot=3.20
Multiple
viscl=Irregular
GMASS_1421 zphot=3.23
viscl=EmptyField
GMASS_1421 zphot=3.23
viscl=Compact
GMASS_0464 zphot=3.29
viscl=Compact+C
GMASS_0464 zphot=3.29
viscl=Compact+C
GMASS_0363 zphot=3.29
viscl=FaintObj
GMASS_0363 zphot=3.29
viscl=Irregular
GMASS_1067 zphot=3.32
viscl=EmptyField
GMASS_1067 zphot=3.32
viscl=FaintObj
GMASS_1535 zphot=3.34
viscl=EmptyField
GMASS_1535 zphot=3.34
viscl=Irregular
GMASS_0308 zphot=3.37
viscl=Irregular+C
GMASS_0308 zphot=3.37
viscl=Irregular+C
GMASS_1666 zphot=3.37
viscl=EmptyField
GMASS_1666 zphot=3.37
viscl=FaintObj
GMASS_1788 zspec=3.41
viscl=Irregular
GMASS_1788 zspec=3.41
viscl=Irregular_disky
GMASS_0198 zphot=3.44
viscl=FaintObj
GMASS_0198 zphot=3.44
viscl=FaintObj
GMASS_1744 zphot=3.45
viscl=FaintObj
GMASS_1744 zphot=3.45
viscl=FaintObj
GMASS_1076 zphot=3.46
viscl=Compact
GMASS_1076 zphot=3.46
viscl=Compact
GMASS_1303 zphot=3.47
viscl=Irregular
GMASS_1303 zphot=3.47
viscl=Irregular
GMASS_1080 zphot=3.51
viscl=Disky
GMASS_1080 zphot=3.51
viscl=Disky
GMASS_1792 zphot=3.63
viscl=Compact
GMASS_1792 zphot=3.63
viscl=Irregular
GMASS_1451 zspec=3.70
Multiple
viscl=Irregular
GMASS_1451 zspec=3.70
viscl=Irregular
GMASS_0228 zphot=3.87
viscl=FaintObj
GMASS_0228 zphot=3.87
viscl=Irregular
GMASS_0418 zspec=4.06
viscl=FaintObj
GMASS_0418 zspec=4.06
viscl=Irregular
GMASS_0348 zphot=4.11
viscl=EmptyField
GMASS_0348 zphot=4.11
viscl=Irregular

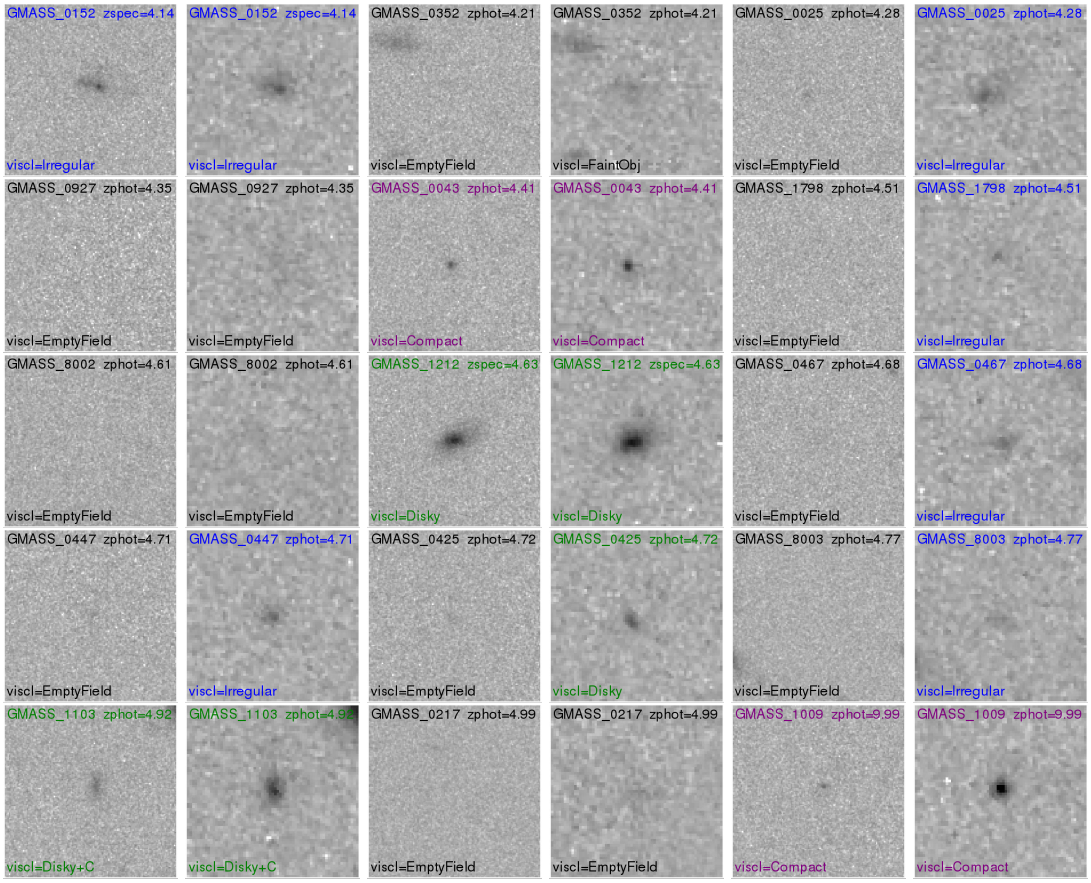
GMASS_0152 zspec=4.14
viscl=Irregular
GMASS_0152 zspec=4.14
viscl=Irregular
GMASS_0352 zphot=4.21
viscl=EmptyField
GMASS_0352 zphot=4.21
viscl=FaintObj
GMASS_0025 zphot=4.28
viscl=EmptyField
GMASS_0025 zphot=4.28
viscl=Irregular
GMASS_0927 zphot=4.35
viscl=EmptyField
GMASS_0927 zphot=4.35
viscl=EmptyField
GMASS_0043 zphot=4.41
viscl=Compact
GMASS_0043 zphot=4.41
viscl=Compact
GMASS_1798 zphot=4.51
viscl=EmptyField
GMASS_1798 zphot=4.51
viscl=Irregular
GMASS_8002 zphot=4.61
viscl=EmptyField
GMASS_8002 zphot=4.61
viscl=EmptyField
GMASS_1212 zspec=4.63
viscl=Disky
GMASS_1212 zspec=4.63
viscl=Disky
GMASS_0467 zphot=4.68
viscl=EmptyField
GMASS_0467 zphot=4.68
viscl=Irregular
GMASS_0447 zphot=4.71
viscl=EmptyField
GMASS_0447 zphot=4.71
viscl=Irregular
GMASS_0425 zphot=4.72
viscl=EmptyField
GMASS_0425 zphot=4.72
viscl=Disky
GMASS_8003 zphot=4.77
viscl=EmptyField
GMASS_8003 zphot=4.77
viscl=Irregular
GMASS_1103 zphot=4.92
viscl=Disky+C
GMASS_1103 zphot=4.92
viscl=Disky+C
GMASS_0217 zphot=4.99
viscl=EmptyField
GMASS_0217 zphot=4.99
viscl=EmptyField
GMASS_1009 zphot=9.99
viscl=Compact
GMASS_1009 zphot=9.99
viscl=Compact